Phenomenology of the Higgs and Flavour Physics In the Standard Model and Beyond

D I S S E R T A T I O N

zur Erlangung des akademischen Grades

doctor rerum naturalium
(Dr. rer. nat.)
im Fach Physik

eingereicht an der
Mathematisch-Wissenschaftlichen Fakultät
Humboldt-Universität zu Berlin

von
M.Sc. Lina Alasfar
geboren am 27. 09. 1994 in Riad

Präsidentin der Humboldt-Universität zu Berlin:
Prof. Dr.-Ing. Dr. Sabine Kunst

Dekan der Mathematisch-Wissenschaftlichen Fakultät:
Prof. Dr. Elmar Kulke

Gutachter:
1. Prof. Dr. R. Gröber, Humboldt-Universität zu Berlin
2. Prof. Dr. Dr. M. Musterman, Potsdam-Institut fur Klimafolgenforschung
3. Prof. Dr. M. Mustermann2, Heidelberg

Tag der mündlichen Prüfung: 06. November 2013

Abstract

The precise determination of the Higgs boson properties is one of the main focus of the Large Hadron Collider (LHC) physics programme.

Since the discovery of the Higgs boson in 2012 at the Large Hadron Collider (LHC), most of its properties have been already measured with increasing accuracy. However, few of the Higgs's main properties are yet to be probed. The future runs of the LHC hold a lot of potential for further understanding of the Higgs boson's properties.

Many of Higgs production processes are plagued by large theoretical uncertainties. In order to reduce them, these processes need to be computed at higher precision. One of such processes is the production of the Higgs with he Z boson. This is a key process in measuring both the Higgs mass and its couplings with more precision. My collaborators and I have preformed such calculation using a novel method that can be used alongside other calculations via Padé approximants and then incorporated into Monte Carlo event simulations [1].

In an another project, we have studied the correlations between the Higgs self-interaction and other set of interactions involving four heavy quarks. Both interaction classes are equally weakly constrained from current LHC data. Using Markov-chain Monte Carlo (MCMC) Bayesian analysis, we have seen that there is a strong correlations amongst these observables. Revealing many challenges to probing Higgs self-coupling using current Higgs measurements [**?**].

The only direct way to study the Higgs self-coupling is to search for Higgs bosons produced in pairs. A process that is sought after in the High-Luminosity (HL)-LHC. We have used interpretable machine learning to improve upon the expected sensitivity of the HL-LHC and future colliders to this process. We were able to constrain both the Higgs's self interaction and its interaction with light quarks, and show that they are uncorrelated from this process [2**?**].

Since 2015, experimental data was hinting towards an anomaly involving the decay of composite particles known as B-mesons that could be a result of new physics beyond the Standard Model. We have used (MCMC) Bayesian analysis to show that the parameters characterising new physics in these decays are strongly related to other set of parameters in the Standard Model related to the interaction between the Z and Higgs bosons, and muons [3].

Keywords: Higgs Physics, Standard Model Effective Field Theory, Flavour observables, Statistical data analysis

Zusammenfassung

Schlagwörter: Higgs Physik, Standardmodell Effektive Feldtheorie, Flavour Anomalies, Statistische Datenanalyse

Contents

List of abbreviations

Colliders and working groups .

CERN Conseil européen pour la recherche nucléaire.

LHC Large Hadron Collider

HL-LHC High-Luminosity LHC

CMS Compact Muon Solenoid

ATLAS A Toroidal LHC ApparatuS

LEP Large Electron-Positron Collider

ALEPH Apparatus for LEp PHysics

SLC Stanford Linear Collider

FCC Future circular collider

HXSWG Higgs cross-section working group

PDG Particle data group

Higgs and Standard Model physics.

SM Standard Model

QCD Quantum chromodynamics

QED Quantum electrodynamics

EFT Effective field theory

SMEFT Standard Model effective field theory

HEFT Higgs effective field theory

EW Electroweak

VEV/ vev Vacuum expectation value

EWSB Electroweak symmetry breaking

EWPO Electroweak precision observables

EWChL Electroweak chiral Lagrangian

SSB Spontanious symmetry breaking

$SU(N)$	Special unitary (group) of dimension N
ggF	Gluon fusion (processes)
$q\bar{q}$A	Quark anti-quark anhitation (processes)
PDF	Parton distribution functions
STXS	Simplified template cross-sections

Higher order computations.

RGE	Renormalisation group equation or evolution
LO, NLO ...	Leading order, Next to leading order etc.
HTL	Heavy top limit
HPL	Harmonic polylogarithms
GPL	Generalised polylogarithms
HE	High energy expantion

Flavour.

CKM	Cabibbo-Kobayashi-Maskawa-Matrix
$\mathcal{CP}$	Charge conjugation and parity
MFV	Minimal flavour violation
AFV	Aligned flavour violation
SFV	Spontanious flavour violation
PDD	Phenomenological data-driven
PMD	Phenomenological model-driven
FCNC	Flavour-changing neutral currents
LUV	Lepton universality violation

Data analysis/statistics.

MC	Monte Carlo (simulation)
ML	Machine learning
BDT	Boosted decision tree
XGBoost	EXtreme gradient boosted decision tree

DNN Deep Neural Networks

MCMC Markov chain Monte Carlo (Bayesian analysis)

PCo Principle component

FDR False discovery rate

ANOVA Analysis of variation

HDPI Highest density posterior interval

CI Crediable interval (Bayesian statistics)

CL Confidence interval (Frequentiststatistics)

New Physics.

4F Four-fermion

NP New physics

BSM Beyond the Standard Model

VLQ Vector-like quarks

LQ Leptoquarks

2HDM Two-Higgs-doublet model

CHM Composite Higgs model

MSSM Minimal supersymmetric Standard Model

SILH Strongly interacting light Higgs

Part I

Higgs Physics

Part II

Single Higgs Processes at the LHC

1 Overview of Higgs production at colliders

The production of the Higgs boson at the LHC is mediated by four distinct processes: gluon fusion (ggF), vector boson fusion (VBF), veector bosons Higgsstrahlung (Vh) and the production with top (and anti-top) pair ($th/t\bar{t}h$). It should be noted that sometimes the ggF category will include the quark anti-quark annihilation, but this is negligible in the SM, but becomes important for significant modifications of light Yukawa couplings. These process are illustrated in Figure 1.1, and their details were summarised in Table 1.1. All of these four channels have been observed at the LHC with $> 5\sigma$ precision.
Since the experimental measurements of this Higgs were discussed previously in **??**, the aim of this chapter is to provide an overview of the current theoretical status of these channels.

Process	Cross-section 13 TeV (pb)	Theo. accuracy	Exp. uncertainty (%)	Contribution (%)
ggF	48.51	N3LO QCD & NLO EW	6.5	88
tth & th	0.58	NLO QCD & NLO EW	20.0	1
VBF	3.78	NNLO QCD* & NLO EW	10.0	7
Vh	2.25	NNLO QCD & NLO EW	15.0	4

Table 1.1. Summary of the Higgs production processes at the LHC.

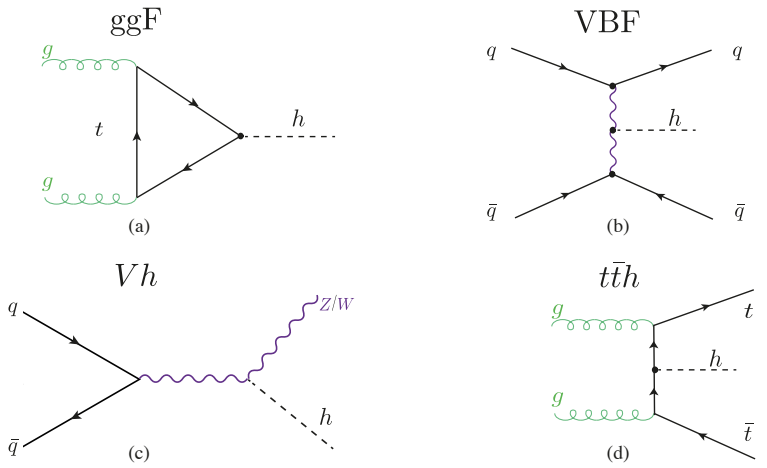

Figure 1.1. Feynman-diagram examples of the leading Higgs production processes at the LHC.

1.1 Current status of the Higgs production channels

1.1.1 Gluon fusion process

The Higgs production via gluon fusion (ggf) has the highest cross-section amongst the Higgs production channels, and consequently has the lowest experimental uncertainty. The current state-of-the-art theoretical computation for the Higgs inclusive cross-section is N^{3}LO in QCD and NLO in EW [4]. A full differential cross-section for the final state $gg \to h \to \gamma\gamma$ has been computed recently to N^{3}LO in QCD, also for the kinematic variables y_h, y_{γ_1}, y_{γ_2}, $\Delta y_{1,2}$ using the projection-to-born method [5].In addition to the fiducial differential cross-section in p_T with experimental cuts has been computed up to third re-summed and fixed order, i.e. N^{3}LL$'$ N^{3}LO dependence [6]. The theoretical computation of this fiducial cross-section with different orders compared to the experimental measurement by ATLAS [7] is shown in Figure 1.2, we can see that the resummed result has significantly smaller theoretical uncertainties. The current total theoretical uncertainty with this order calculation is 5.4%, with only 2.7% of it coming from the perturbation order cut-off of the calculation, while the rest comes from the branching fraction, PDF+α_s, EW corrections and mass uncertainties. When compared to **??**, the projected experimental uncertainty of this final states at the HL-LHC is 4.2%, we see that the uncertainties will become comparable, and if the PDF uncertainties are reduced. The predictions can be further improved by the computation of mixed QCD-

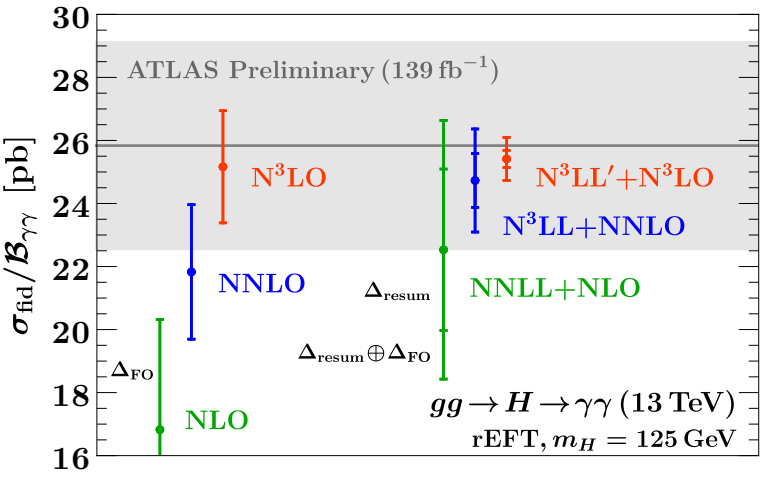

Figure 1.2. The total fiducial cross-section for the final state $gg \to h \to \gamma\gamma$ at both fixed and resumed third order compared to the experimental ATLAS measurement [7] this figure is taken from [6].

EW effects. These computations invokes three-loop integrals with both gluons and EW bosons, computed in [8] or two-loop ones with two particle final states appearing in the real corrections with the process $gg \to hg$ computed in [9] using differential equations. The computation was completed by inclusion of light quark initial states for the real corrections in [10] with exact quark mass dependence, reducing the EW uncertainty from

2% to $\sim 0.6\%$.
The computation of the three-loop form-factors with full top-mass dependence were carried out by [11, 12]. However, there remains an intricate interplay between the mass effects of gg, qg and qq initial states for the real matrix elements that cannot be fully controlled due to the light quark mass effects.
NLO corrections to the $h + j$ and $h + 2j$ processes were computed by [13] in the FT approximation, which used exact born and real correction amplitudes, and approximates the two-loop virtuals by

$$|\mathcal{A}^{2-\text{loop}}(m_t, \mu_R^2)|^2 \approx |\mathcal{A}^{1-\text{loop}}(m_t \to \infty, \mu_R^2)|^2 \frac{|\mathcal{A}^{1-\text{loop}}(m_t)|^2}{A^{(0)}(m_t) \to \infty|^2}. \tag{1.1}$$

This approximation works superbly even for $p_T \gg m_t$. Later, the full top mass effects computations have been carried out in [14–16] using the high energy (HE) expiation technique.

1.1.2 Vector boson fusion

The VBF channel has a very distinctive signature, making it a bona fide channel for Higgs signal extraction. The suppressed colour exchange between the quarks result in a little jet activity in the central rapidity region, and the quarks will be scattered into two forward jets, such that the decay products of the Higgs are found in the region between them. These features allows for excellent measurement of Higgs couplings, observation of challenging decays, and $\mathcal{CP}$ properties determination. Some of these features are also shared with the Vh production channel . Both of these channels contain the VVh vertex which could be written generally as [17]

$$T^{\mu\nu}(p_1, p_2) = a_1 g^{\mu\nu} + a_2 \left(g^{\mu\nu} - 2\frac{p_2^\mu p^\nu}{p_1 \cdot p_2} \right) + a_3 \frac{p_1^\alpha p_2^\beta}{p_1 \cdot p_2} \epsilon^{\mu\nu\alpha\beta}. \tag{1.2}$$

In the SM only $a_1 \neq 0$, while the rest of the coefficients represent the anomalous coupling, for example if $a_3 \neq 0$ then the Higgs is $\mathcal{CP}$ odd. The study of the azimuthal angle distribution $d\sigma_{VBF}/d\Delta\phi_{jj}$ allows for the determination of these coefficients, with very little dependence on the Higher order corrections [18].
The NLO QCD inclusive cross-section is known since the 90's [19], and later these corrections were made for the differential distributions cf. [20, 21]. Unlike the ggF channel, that has an NLO K-factor of 1.6 at 13 TeV [22] , the VBF NLO corrections are small $\sim$ 10%. The two-loop NNLO QCD cross-section has been also computed, the most recent results of the two-loop computation were calculated via the structure function approach [23] in addition to STXS level 1.2 bins with EW corrections [24]. These calculation are implemented in the MC event generator `HAWK`. Despite these corrections being small, they are non-negligible and their inclusion is important for uncertainties reduction.

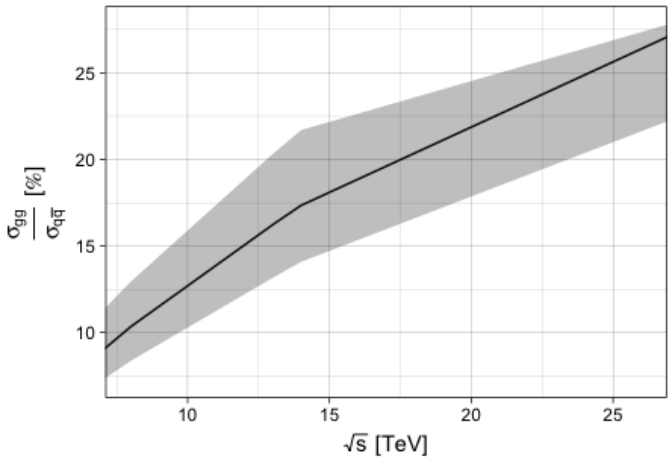

Figure 1.3. The ratio of the LO gluon fusion production cross-section $gg \to Zh$ (σ_{gg}) with respect to the NLO Drell-Yan process $q\bar{q} \to Zh$ cross-section ($\sigma_{q\bar{q}}$) at a pp collider with centre-of-mass energy $\sqrt{s}$. The error band captures the total theoretical uncertainties on both cross-sections dominated by σ_{gg} .

1.1.3 Associated production with EW bosons

The vecctor boson Higgsstrahlung channels $pp \to Wh/Zh$ at LO are quark-initiated tree-level processes interpreted as **Drell-Yan process** [25, 26]. They have been computed up to NNLO in QCD ($\sim \alpha_s^2$), and NLO EW ($\sim \alpha^2$) [27].

Despite arising for the first time at NLO, the gluon fusion channel $gg \to Zh$ has a non-negligible contribution to the total hadronic cross-section $pp \to Zh$, which could reach $> 16\%$ of the total cross-section contribution at 14 TeV [28], see Figure 1.3. The contribution becomes more significant when looking at large invariant mass bins of the differential cross-section. This is due to the significant abundance of gluonic PDF's at the LHC and the extra enhancement coming from the top quark initiated contribution near the $t\bar{t}$ threshold to boot [29], but also it has a higher scale uncertainty than the quark anti-quark annihilation $q\bar{q}$A channel. With these points in mind, and the absence of gluon fusion channel for Wh channel, the Zh channel has higher theoretical uncertainties than Wh. This motivates the need for calculation of the $gg \to Zh$ channel to higher orders in perturbation theory in order to reduce these uncertainties. The inclusion of the two-loop calculations for the ggF part would facilitate the precision measurement of the Zh channel at the future LHC runs, which in term provides better constraints on several observables, such as sign and magnitude of the top Yukawa and ZZh couplings amongst others [30].

The leading order (LO) contribution to the $gg \to Zh$ amplitude, given by one-loop diagrams, was computed exactly in refs.[31, 32]. For the NLO computations, the virtual corrections contain multi-scale two-loop integrals some of which are still not known analytically, making these computations a formidable task to accomplish. The first com-

putation of the NLO terms has been done by [33], where the HTL asymptotic expansion, and setting $m_b = 0$. The HTL NLO computations pointed to a large K-factor of about ~ 2. Later, the computation has been improved via soft gluon resummation, including NLL terms found in ref.[34]. The NLL matching to the fixed-order NLO computation can be found in ref. [33]. Top quark mass effects were first implemented using a combination of HTL and Padé approximants [35]. A data-driven approach to extract the gluon fusion dominated non-Drell-Yan part of Zh production using the known relation between Wh and Zh associated production when only the Drell-Yan component of the two processes is considered has been investigated in ref.[36]. The differential distributions of $gg \to Zh$ at NLO was studied in ref.[37] via LO matrix element matching.

More recent studies of the NLO virtual corrections to this process were based on the high-energy (HE) expansion improved by Padé approximants with the LME, which extended the validity range of the HE expansion [38]. However, this expansion is only valid for in the invariant mass region $\sqrt{\hat{s}} \gtrsim 750\,\text{GeV}$ and $\sqrt{\hat{s}} \lesssim 350\,\text{GeV}$, which only covers $\sim 32\%$ of the hadronic cross-section. Additionally, numerical computation of the two-loop virtual corrections, though implemented exactly in [39], are rather slow for practical use in MC simulations. This highlights the importance of an analytical method that can cover the remaining region of the cross-section and can be merged with the HE expansion via Padé approximants. Fortunately, the two-loop corrections to the triangle diagrams can be computed exactly. And the loop integrals appearing in the box correction having no analytic expression can be expanded in small Z (or Higgs) transverse momentum, p_T. This method was first used for Higgs pair production in [40], to compute the NLO virtual corrections to the box diagrams in the forward kinematics. In **??**, I will discuss the calculation preformed by my collaborators and myself and published in [1], which includes the full top mass dependence of the virtual two-loop correction to $gg \to Zh$ in an analytic form using the same p_T expansion technique.

1.1.4 Associated production with top quarks

The largest part of the $t\bar{t}h/th$ uncertainty budget comes from the theoretical modelling of this process's backgrounds, mainly $t\bar{t}b\bar{b}$, $t\bar{t}W$ as backgrounds for $t\bar{t}(h \to b\bar{b})$ and $t\bar{t}(h \to \text{multileptons})$, respectively. There have been several theoretical developments regarding these backgrounds. Starting with $t\bar{t}W$, the differential cross-section at NNL+NLO QCD calculation of this channel has been done in [41, 42] including EW corrections. The fully decayed final state at NLO QCD [43–45] and at NLO-EW [46] have been computed. Additionally, these calculations were implemented in `POWHEG-BOX` [47]. The comparison between the NLO-QCD with parton showering vs on-shell can be found in [48]. As for $t\bar{t}b\bar{b}$, the progress in obtaining higher order corrections is faced with challenges posed by the complexity of this channel. However, progress has been made, for instance the off-shell effects in the fully decayed $pp \to 2\ell 2\nu 4b$ with NLO corrections was studied in [49, 50]. Further discussion of the theoretical developments of these channels is beyond the scope of this thesis.
Regarding the higher order corrections to the $t\bar{t}h/th$ channel itself, the NLO QCD+EW effects on the off-shell multileptons final state were studied in [51], while the NLO cor-

rections including SMEFT operators were calculated in[52]. The NLO QCD+EW with parton showering is available in all event generators, and the SMEFT operators at NLO are available in `MadGraph5_aMC@NLO` . As of the time of writing this thesis, there is no NNLO calculation of $t\bar{t}h/th$ available.

1.2 Concluding remarks

The precision-era of Higgs measurements requires developments on both experimental and theoretical levels. Though the experimental precision can be improved with Higher luminosities and energies, better detectors and improved analysis techniques. Theoretical uncertainties require higher-order calculations, inclusion of mixed EW and QCD terms, inclusion of mass effects and suitable parton distribution functions with Higher order in QCD. A lot of effort is being put into improving the theoretical predictions of Higgs production channels. Moreover, a plethora of computer tools have been made available to facilitate the computation of these cross-sections, for example `iHixs2` [53] or to generate full events, like `POWHEG` [54–60] and `MadGraph5_aMC@NLO` [61], and many others can be found with greater detail in the LHC-HXWG Twiki page[62].
Sometimes, in order to improve the measurement of the process, it is not sufficient to include Higher order terms of the channel itself, but also its backgrounds, which is particularly important for $t\bar{t}h$. Hence, higher order calculations of processes like $t\bar{t}W$ with parton-shower effects as well as improved analysis to distinguish $t\bar{t}(h \to b\bar{b})$ have a significant impact on $t\bar{t}h$ measurements. Event generator tools with SMEFT implementation for Higgs processes with patron showing interface capabilities have been implemented in a `MadGraph5_aMC@NLO` model `SMEFTatNLO` [63] which enabled loop computations with SMEFT operators and consequently fits of the SMEFT Wilson coefficients with Higgs data at NLO as we have seen in **??**.
There is plenty of room for future improvements in the reduction of theory uncertainty budget, and providing better theoretical prediction of the Higgs processes in the SM and beyond. From inclusion of patron shower matching , merging and validation to inclusion of two-loop calculations of gluon fusion Zh and EW NLO effects of $t\bar{t}h$, all in preparation to the HL-LHC Higgs precision era !

2 Four top operator in Higgs production and decay

In **??**, the SM effective field theory has been portrayed as a pragmatic yet robust parametrisation of potential NP degrees of freedom for LHC searches, with the ansatz that these degrees of freedom have masses that are higher than the LHC reach. From the discussion and overview of Higgs-related SMEFT operator in that chapter, the operator $\mathcal{O}_\phi$ stood out as one of the weakly constrained amongst them. This is due to the current low experimental sensitivity on the Higgs self-coupling as shown in **??**.

The physics of the top quark is deeply intertwined with Higgs physics, and when one starts looking at the operators entering at NLO of Higgs processes, and by restricting oneself to pure Higgs or EW operators, one would miss the full picture in a global fit. Namely, the top quark operators. Though many of these operators are strongly constraint from top observables, a subset of them remain as weakly constraint as the trilinear Higgs self-coupling. These operators are four-fermion operators involving the third generation quarks. They would be constrained directly from the production of four tops observation. However, this process has small cross-section at the LHC of $\sim$ 12 fb [64], which is more or less comparable to the Higgs pair production signal strength. In addition, we have seen in the previous chapter that the theoretical predictions of $t\bar{t}b\bar{b}$ remain limited. Experimental searches for the production of four top quarks has been first made by CMS [65] combining different LHC runs, followed by ATLAS [66], the latter reporting a 4.3σ observation of this processes with cross-section of 24^{+7}_{-6} fb. When the whole third generation quarks is included, one sees the same story with $t\bar{t}b\bar{b}$ contact interaction which require the observation of $t\bar{t}b\bar{b}$ production for a direct constraint, see [67, 68] for experimental searches and [69, 70] for SMEFT fits. It should be noted that for the production of four tops, or two tops two beauty quarks in SMEFT, the contact terms do not interfere with the SM process, and only appear proportional to $\mathcal{O}(1/\Lambda^4)$. This makes the SMEFT global analysis of these operators depend highly on the EFT truncation scheme used, i.e. whether to keep quadratic terms or not.

These four-fermion operators enter in single Higgs processes at NLO, in a similar manner as the Higgs self-coupling. In this chapter, the exact NLO corrections to the Higgs rates, i.e. production and decay, due to these four-fermion operators have been competed, and it was found to be significantly larger or at the same scale as the corrections from C_ϕ. Since the four-fermions operators are weakly constrained they should be included in fits involving Higgs data. We shall demonstrate that, there is a significant correlation amongst the Higgs self-coupling and the four-fermion operators.

As the direct bounds for $t\bar{t}t\bar{t}$ and $t\bar{t}b\bar{b}$ contact interactions are weak, single Higgs data provides competitive bounds of there operators alongside other alternative constraints

like top quark pair production [63] and electroweak precision data [71] .

The chapter is based on a the paper [72] and structured as follows: in **??** the full NLO calculation of Higgs rates due to the four-fermion operators is illustrated. Afterwards, in section 2.2, a fit from Higgs data combining the Higgs trilinear coupling and the four-fermion operators is presented, for both Run-II and HL-LHC, with more elaborate results for the latter is found in **??**. The results are further discussed in section 2.3.

2.1 Contribution of four-fermion operators to Higgs rates at NLO

We will consider the following dimension-six SMEFT operators in the NLO calculations

Four-Heavy-quarks SMEFT operators modifying Higgs rates at NLO

Operators with homogenous chiral structure, i.e. (RR)(RR) or (LL)(LL)

$$\mathcal{O}_{tt},\ \mathcal{O}_{bb},\ \mathcal{O}_{tb}^{(1)},\ \mathcal{O}_{tb}^{(8)},\ \mathcal{O}_{QQ}^{(1)},\ \mathcal{O}_{QQ}^{(3)}. \tag{2.1}$$

Operators with heterogeneous chiral structure, i.e. (LR)(LR) or (LL)(RR)

$$\mathcal{O}_{Qt}^{(1)},\ \mathcal{O}_{Qt}^{(8)},\ \mathcal{O}_{Qb}^{(1)},\ \mathcal{O}_{Qb}^{(8)},\ \mathcal{O}_{QtQb}^{(1)},\ \mathcal{O}_{QtQb}^{(8)} \tag{2.2}$$

The explicit definition of these operators can be found in **??**. However, the notation is slightly modified from the standard Warsaw basis one. The flavour indices were suppressed since only the the third generation is considered throughout this chapter. Adopting the same notation from previous chapters, Q denotes the (heavy) left-handed $SU(2)_L$ doublet quarks while t and b refer to the right-handed singlets. In studies involving SMEFT fits, such as [73] the $SU(3)_C$ singlet and octet left-handed operators $\mathcal{O}_{QQ}^{(1),SU(3)}$, $\mathcal{O}_{QQ}^{(8)}$ are used instead of the singlet and triplet of $SU(2)_L$ appearing in the stabdard Warsaw basis. These two conventions' Wilson coefficients are related via the relations

$$\begin{aligned} C_{QQ}^{(1),SU(3)} &= 2C_{QQ}^{(1)} - \frac{2}{3}C_{QQ}^{(3)}, \\ C_{QQ}^{(8)} &= 8C_{QQ}^{(3)}. \end{aligned} \tag{2.3}$$

Additionally, all of these Wilson coefficients are assumed to be real.

From here on, only operators that induce sizeable NLO correction to Higgs processes are taken into account. These operators turns out to be the ones that introduce loop corrections to the top or beauty Yukawa, top or beauty masses and finite corrections from top loops. Such corrections will be proportional to the top mass. On the contrary, corrections from beauty loops are highly suppressed by m_b. Also, operators that have chiral structure that does not enable them to enter in the Yukawa renormalisation group

equation (RGE)'s will not be constrained from Higgs data as they would only contribute through small finite terms, as we shall see later. Hence, only four top and the $\mathcal{O}_{QtQb}^{(1),(8)}$ operators will be considered, as they will possess corrections with top quark loops.

This section will demonstrate the calculation of NLO Higgs production and decay rates from the four-heavy-quarks operators discussed above. For the production of Higgs via gluon fusion or Higgs decay to gluon, photons and beauty quarks, the results were computed fully analytically and presented in this section. However, for the associated production of the Higgs with top pair $t\bar{t}h$, the corrections were computed numerically, due to the length of the the analytic expressions if the result.

2.1.1 Analytic calculations

The NLO corrections to gluon fusion, $h \to gg$, $h \to \gamma\gamma$ and $h \to b\bar{b}$ all come from the sub-diagrams listed in Table 2.1, with top loops entering in the mass renormalisation or to/beauty Yukawa vertex correction. Where $N_c = 3$ the number of colours, and $c_F = (N_c^2 - 1)/(2N_c) = 4/3$ the $SU(3)$ quadratic Casimir in the fundamental representation. The effect of beauty loops coming from for $C_{QtQb}^{(1/8)}$, can be easily read from this table by

Diagram	colour factor		mass/coupling
	singlet	octet	
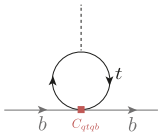	$2N_c + 1$	c_F	$y_t\, m_b\, m_t^2$
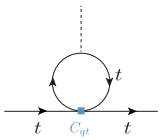	1	c_F	$y_t\, m_t^3$
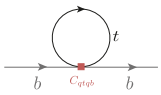	$2N_c + 1$	c_F	m_t^3
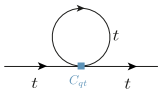	1	c_F	m_t^3

Table 2.1. The sub diagrams contributing to the NLO corrections of gluon fusion Higgs production higgsdecasy to gluon, photon and beauty quarks.

exchanging $t \leftrightarrow b$, which is significantly smaller than the corrections coming from top loops.

We see that these corrections correspond to the Wilson coefficients appearing in the RGE's include them in the appendix, and operators with (LL)(LL) or (RR(RR)) chiral structures do not contribute to these processes.
By considering the two-loop corrections to the gluon fusion illustrated in Figure 2.1 we find that such correction contain the sub-diagrams shown in Table 2.1, except for diagram (e), which is found to be vanishing for on-shell gluons. Additionally, these diagrams indicated that the two-loop corrections will be reduced to a product of two one-loop functions after the integral reduction.
Following the Feynman rules derived in ref. [74] for the four-fermion operators of interest here, the *ggtoh* two-loop amplitude was calculated, then Dirac algebra and further algebraic manipulations were preformed in Mathematica using `PackageX` [75]. Reduction of the resulting two-loop to Master integrals has been preformed using `KIRA` [76], all of the resulting master integrals were indeed products on one-loop functions as expected. The computation has been cross-checked independently by my collaborators, using a different pipeline : `FeynArts` [77], for amplitude generation then `FeynRules` [78] and `Fire` [79] for algebraic manipulation and loop-integral reduction.

The sub-diagrams appearing in the two-loop calculation, correspond to mass and vertex renormalisation, hence they contain poles that require counter-terms. A mixture of on-shell (OS) and $\overline{\text{MS}}$ – schemes has been used for the mass and $hq\bar{q}$ coupling renormalisation, respectively. The renormalisation of SM quantities in the OS and NP ones in the $\overline{\text{MS}}$ scheme was proposed by [80], which provides consistency since the NP is assumed to be of a Higher scale than the SM.

The top/beauty mass renormalisation can be expressed as

$$m_{t/b}^{\text{OS}} = m_{t/b}^{(0)} - \delta m_{t/b}, \tag{2.4}$$

with the corresponding counter-terms

$$\begin{aligned}\delta m_t =& \frac{1}{16\pi^2}\frac{C_{Qt}^{(1)} + c_F C_{Qt}^{(8)}}{\Lambda^2} m_t^3 \left[\frac{2}{\bar{\epsilon}} + 2\log\left(\frac{\mu_R^2}{m_t^2}\right) + 1\right] \\ &+ \frac{1}{16\pi^2}\frac{(2N_c+1)C_{QtQb}^{(1)} + c_F C_{QtQb}^{(8)}}{\Lambda^2}\left[\frac{1}{\bar{\epsilon}} + \log\left(\frac{\mu_R^2}{m_b^2}\right) + 1\right] m_b^3\,,\end{aligned} \tag{2.5}$$

$$\delta m_b = \frac{1}{16\pi^2}\frac{(2N_c+1)C_{QtQb}^{(1)} + c_F C_{QtQb}^{(8)}}{\Lambda^2}\left[\frac{1}{\bar{\epsilon}} + \log\left(\frac{\mu_R^2}{m_t^2}\right) + 1\right] m_t^3\,, \tag{2.6}$$

with $\bar{\epsilon}^{-1} = \epsilon^{-1} - \gamma_E + \log(4\pi)$, in dimensional regularization with $d = 4 - 2\epsilon$. It is possible

to convert from OS to the $\overline{\text{MS}}$ – scheme for mass counter-terms via the following relations

$$\delta m_t^{\overline{\text{MS}}} = \frac{1}{8\pi^2}\frac{C_{Qt}^{(1)} + c_F C_{Qt}^{(8)}}{\Lambda^2} m_t^3 \frac{1}{\bar{\epsilon}} + \frac{1}{16\pi^2}\frac{(2N_c+1)C_{QtQb}^{(1)} + c_F C_{QtQb}^{(8)}}{\Lambda^2}\frac{1}{\bar{\epsilon}} m_b^3 \,, \tag{2.7}$$

$$\delta m_b^{\overline{\text{MS}}} = \frac{1}{16\pi^2}\frac{(2N_c+1)C_{QtQb}^{(1)} + c_F C_{QtQb}^{(8)}}{\Lambda^2}\frac{1}{\bar{\epsilon}} m_t^3 \,. \tag{2.8}$$

The effect of changing to the mass renormalisation scheme is small for the top mass but rather significant, up to 100% for the beauty mass.
The top/beauty Higgs coupling in SMEFT, is written as

$$g_{ht\bar{t}/hb\bar{b}} = \frac{m_{t/b}}{v} - \frac{v^2}{\Lambda^2}\frac{C_{t\phi/b\phi}}{\sqrt{2}} \,. \tag{2.9}$$

Hence, a modification of the Higgs couplings to bottom and top quarks is generated by operator mixing, even if $C_{t\phi/b\phi}$ are zero at Λ. From this, the $\overline{\text{MS}}$ counter-term should take the form

$$\delta g_{ht\bar{t}/hb\bar{b}} = \frac{m_{t/b}}{v}\delta m_{t/b} - \frac{v^2 \delta C_{t\phi/b\phi}}{\sqrt{2}}, \tag{2.10}$$

where $\delta C_{t\phi/b\phi}$ is directly read from the anomalous dimension, see App for the explicit expression of the RGE's.

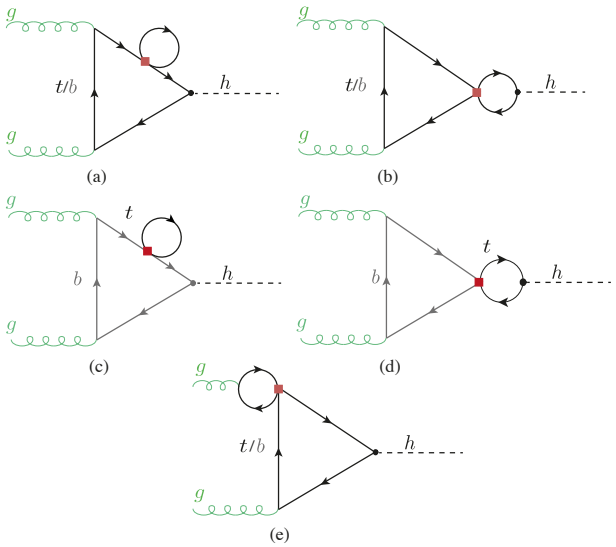

Figure 2.1. Example Feynman diagrams for four-fermion-operator contributions to the Higgs production via gluon fusion. The red box indicates the four-fermion operator.

Correction to gluon fusion and $h \to gg$

The modification of the Higgs production via gluon fusion can be written as

$$\frac{\sigma_{ggF}}{\sigma_{ggF}^{\mathrm{SM}}} = 1 + \frac{\sum_{i=t,b} 2\mathrm{Re}\left(F_{\mathrm{LO}}^{i} F_{\mathrm{NLO}}^{*}\right)}{\left|F_{\mathrm{LO}}^{t} + F_{\mathrm{LO}}^{b}\right|^{2}} \tag{2.11}$$

with

$$F_{\mathrm{LO}}^{i} = -\frac{8m_i^2}{m_h^2}\left[1 - \frac{1}{4}\log^2(x_i)\left(1 - \frac{4m_i^2}{m_h^2}\right)\right] \tag{2.12}$$

and

$$\begin{aligned} F_{\mathrm{NLO}} =& \frac{1}{4\pi^2\Lambda^2}(C_{Qt}^{(1)} + c_F C_{Qt}^{(8)}) F_{\mathrm{LO}}^{t}\left[2m_t^2 + \frac{1}{4}(m_h^2 - 4m_t^2)\left(3 + 2\sqrt{1 - \frac{4m_t^2}{m_h^2}}\log(x_t)\right)\right. \\ &\left. + \frac{1}{2}(m_h^2 - 4m_t^2)\log\left(\frac{\mu_R^2}{m_t^2}\right)\right] \\ &+ \frac{1}{32\pi^2\Lambda^2}((2N_c+1)C_{QtQb}^{(1)} + c_F C_{QtQb}^{(8)})\left[F_{\mathrm{LO}}^{b}\frac{m_t}{m_b}\left(4m_t^2 - 2m_h^2\right.\right. \\ &\left.\left. -(m_h^2 - 4m_t^2)\sqrt{1 - \frac{4m_t^2}{m_h^2}}\log(x_t) - (m_h^2 - 4m_t^2)\log\left(\frac{\mu_R^2}{m_t^2}\right)\right) + (t \leftrightarrow b)\right]. \end{aligned} \tag{2.13}$$

Only top quark loops contribute to the parts proportional to $C_{Qt}^{(1),(8)}$. The variable x_i for a loop particle with mass m_i is given by

$$x_i = \frac{-1 + \sqrt{1 - \frac{4m_i^2}{m_h^2}}}{1 + \sqrt{1 - \frac{4m_i^2}{m_h^2}}}\,. \tag{2.14}$$

Using the same amplitudes, the $h \to gg$ partial width modification can be written as

$$\frac{\Gamma_{h\to gg}}{\Gamma_{h\to gg}^{\mathrm{SM}}} = 1 + \frac{\sum_{i=t,b} 2\mathrm{Re}\left(F_{\mathrm{LO}}^{i} F_{\mathrm{NLO}}^{*}\right)}{|F_{\mathrm{LO}}^{t} + F_{\mathrm{LO}}^{b}|^{2}} \tag{2.15}$$

Correction to Higgs decays to photons

Analogously, since the decay $h \to \gamma\gamma$ contains the same topologies as gluon fusion, we could use the result from the above calculation to calculate the correction to the partial width for this decay

$$\frac{\Gamma_{h\to\gamma\gamma}}{\Gamma_{h\to\gamma\gamma}^{\mathrm{SM}}} = 1 + \frac{2\mathrm{Re}\left(F_{\mathrm{LO},\gamma} F_{\mathrm{NLO},\gamma}^{*}\right)}{|F_{\mathrm{LO},\gamma}|^{2}}. \tag{2.16}$$

However, one should pay attention to the change in the prefactors, and the extra

EW contributions for $h \to \gamma\gamma$

$$F_{\mathrm{LO},\gamma} = N_C\, Q_t^2 F_{\mathrm{LO}}^t + N_C\, Q_b^2 F_{\mathrm{LO}}^b + F_{\mathrm{LO}}^W + F_{LO}^G, \tag{2.17}$$

and $F_{\mathrm{NLO},\gamma}$ is obtained from F_{NLO} by replacing the LO form factor that appears inside of it by $F_{\mathrm{LO}}^i \to N_c\, Q_i^2 F_{\mathrm{LO}}^i$, with the charges $Q_t = 2/3$ and $Q_b = -1/3$. The W boson contribution

$$F_{\mathrm{LO}}^W = 2\left(1 + 6\frac{m_W^2}{m_h^2}\right) - 6\frac{m_W^2}{m_h^2}\left(1 - 2\frac{m_W^2}{m_h^2}\right)\log^2(x_W), \tag{2.18}$$

with m_W the W mass, and the Goldstone contribution

$$F_{\mathrm{LO}}^G = 4\frac{m_W^2}{m_h^2}\left(1 + \frac{m_W^2}{m_h^2}\,\log^2(x_W)\right). \tag{2.19}$$

Four-fermion operators also affect the $h \to Z\gamma$ partial width. However, as in the diphoton case, the effect is expected to be small due to the dominance of the W boson loop. Because of this, and given the smallness of the $h \to Z\gamma$ branching ratio and the relatively low precision expected in this channel at the LHC, the effects of four-fermion interactions in this decay are neglected.

Correction to Higgs decays to $b\bar{b}$

The dominant four-fermion contributions to decay channel $h \to b\bar{b}$ come from the operators with Wilson coefficients $C_{QtQb}^{(1),(8)}$. The corresponding diagram at NLO is shown in fig 2.2. Adopting the same renormalisation procedure as outlined in the previous subsection, we obtain the following expression for the correction to the $h \to b\bar{b}$ decay rate in the presence of $\mathcal{O}_{QtQb}^{(1),(8)}$,

$$\begin{aligned}\frac{\Gamma_{h\to b\bar{b}}}{\Gamma_{h\to b\bar{b}}^{\mathrm{SM}}} =& 1 + \frac{1}{16\pi^2}\frac{m_t}{m_b}(m_h^2 - 4m_t^2)\frac{(2N_c+1)C_{QtQb}^{(1)} + c_F C_{QtQb}^{(8)}}{\Lambda^2} \\ &\times\left[2 + \sqrt{1 - \frac{4m_t^2}{m_h^2}}\log(x_t) - \log\left(\frac{m_t^2}{\mu_R^2}\right)\right],\end{aligned} \tag{2.20}$$

which carries an enhancement factor of m_t/m_b and is hence expected to be rather large.

The results of the NLO effects from the four-fermion operators reported above, do not take into an account the running of the Wilson coefficients. This would be based on the assumption that these coefficients are defined at the process scale. Nevertheless, when we want to compare different process or assume that the four-fermion operators are defined at the UV scale, i.e. Λ, for example after matching with some UV model. One has take into an account the running of these Wilson coefficients from Λ down to the process scale Those running effects can be included via the renormalisation group

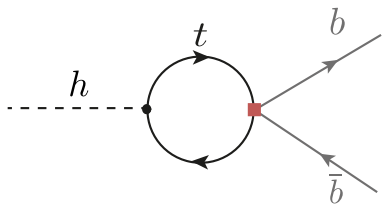

Figure 2.2. Feynman diagram contributing to the NLO $h \to b\bar{b}$ process.

equation (RGE) for the operators with Wilson coefficient $C_{t\phi}$ and $C_{b\phi}$ [81, 82], that lead approximatively to

$$\begin{aligned} C_{t\phi}(\mu_R) - C_{t\phi}(\Lambda) =& \frac{1}{16\pi^2 v^2}\left[-2y_t(m_h^2 - 4m_t^2)(C_{Qt}^{(1)} + c_F C_{Qt}^{(8)})\log\left(\frac{\mu_R^2}{\Lambda^2}\right)\right. \\ &\left. + \frac{y_b}{2}(m_h^2 - 4m_b^2)\left((2N_c+1)C_{QtQb}^{(1)} + c_F C_{QtQb}^{(8)}\right)\log\left(\frac{\mu_R^2}{\Lambda^2}\right)\right] \end{aligned} \tag{2.21}$$

and

$$C_{b\phi}(\mu_R) - C_{b\phi}(\Lambda) = \frac{y_t}{32\pi^2 v^2}\left[(m_h^2 - 4m_t^2)\left((2N_c+1)C_{QtQb}^{(1)} + c_F C_{QtQb}^{(8)}\right)\log\left(\frac{\mu_R^2}{\Lambda^2}\right)\right], \tag{2.22}$$

where $y_{t/b} = \sqrt{2}m_{t/b}/v$. Note that the combinations of Wilson coefficients appearing in (2.21)(2.22) are the same as in F_{NLO} in (2.13). Effectively, we can then obtain the result under the assumption that the four-fermion operators are the only non-zero ones at the high scale by replacing in (2.13) $\mu_R \to \Lambda$, noting that we have renormalised the top and beauty quark masses in the OS scheme. Including the leading logarithmic running of $C_{b\phi}$ of (2.22) from the high scale Λ to the electroweak scale is achieved by setting in (2.20) $\mu_R \to \Lambda$. The expression in (2.20) agrees with results obtained from the full calculation of the NLO effects in the dimension-six SMEFT, first computed in [83].

2.1.2 SMEFT-NLO calculation of $t\bar{t}h$

Unlike the previous processes, the associated production of the Higgs with top quark pair involves new topologies not limited to Yukawa vertex or mass renormalisation. At the LHC, there are two sub-processes responsible for the $t\bar{t}h$ production: gluon-initiated process illustrated in Figure 2.3 and quark-initiated one, see in Figure 2.4. We see the new *finite* topologies induced by the four-fermion operator corrections in (d) triangle and (e) box topologies in Figure 2.3 and (b) triangle topology in Figure 2.4. Additionally, the $t\bar{t}g$ vertex correction in the quark-initiated process (diagram (c)) of Figure 2.4 is non-vanishing as the gluon is off-shell. This vertex correction has a UV pole that requires a

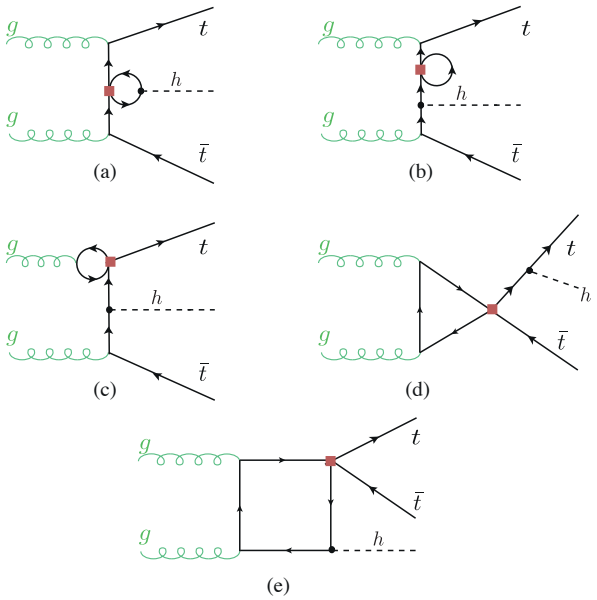

Figure 2.3. Feynman diagrams including the four-fermion loop contributions to the $gg \to t\bar{t}h$ subprocess.

counter-term for its cancellation

$$= \frac{ig_s}{12\pi^2\Lambda^2} T^A_{ij} p_g^2 \gamma^\mu \left(C_{tt} P_R + \left(C^{(1)}_{QQ} + C^{(3)}_{QQ} \right) P_L + \frac{C^{(8)}_{Qt}}{4} \right) \left(\frac{1}{\bar{\epsilon}} - 1 \right). \quad (2.23)$$

Another difference between $t\bar{t}h$ and the rest of the processes considered, is that this process has multiple colour projectors, as the quark anti quark triplets or the gluon pairs do not have to recombine to only a singlet state rather to both a singlet and an octet, according to the expansion of product $\mathbf{3} \otimes \overline{\mathbf{3}} \to \mathbf{1} + \mathbf{8}$. This breaks the degeneracy between the singlet and octet Wilson coefficients. Lastly, due to the new topologies and $t\bar{t}g$ vertex correction, operators with single chirality will contribute to NLO corrections, namely Ctt and $C^{(1,3)}_{QQ}$.

All of the four-fermion operators are implemented in the loop-capable UFO model `SMEFTatNLO` [63] and their contribution to NLO corrections of $t\bar{t}h$ can hence be computed via `Madgraph_aMCNLO` [61] (version 3.1.0) with some tweaking to remove the NLO QCD corrections. This is done via a use-defined loop filter function in Madgraph. The results were reproduced by an analytic computation based on the reduction of one-loop amplitudes via the method developed by G. Ossola, C.G. Papadopoulos and R. Pittau (OPP reduction) [84]. The OPP reduction was done using the `CutTools` programme [85]. This programme take the full one-loop amplitude and then reduces it to terms with 1,2,3 and 4-point loop functions in four dimensions, keeping spurious terms from the ϵ part of the amplitude. To correct for such terms, one needs to compute the divergent UV counter-

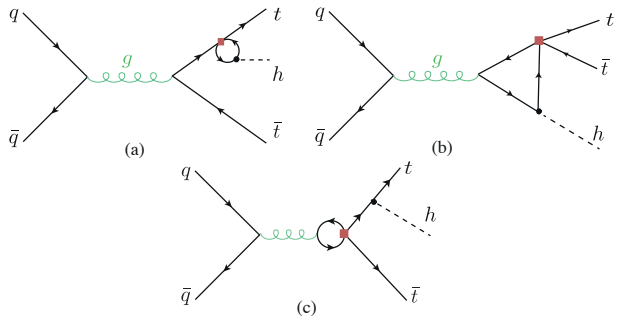

Figure 2.4. Feynman diagrams including the four-fermion loop contributions to the $q\bar{q} \to t\bar{t}h$ subprocess.

term as well as a finite rational terms, denoted R_2 as in Ref. [86].[1] The amplitudes were generated in the same way as for gluon fusion. The UV and R_2 counter-terms, that need to be supplemented to `CutTools`, were computed manually following the method detailed in [86]. For both codes, the NNPDF23 parton distribution functions set at NLO [87] was used.

The singlet and octet operators $\mathcal{O}_{QtQb}^{(1),(8)}$ contribute to $t\bar{t}h$ only via beauty loops and in principle, could be directly dismissed like the other beauty quark operators mentioned above. However, it is instructive to investigate their effect albeit it is expected to be small. Since the `SMEFTatNLO` model does not have these operators, it was needed to implement them manually in that model. This is simply done by include the vertices generated by these operators as well as their UV and R_2 counter-terms, only relevant for $t\bar{t}th$ calculation. The calculation of the NLO correction by these operators was done both in Madgraph using a modified UFO model and with the code based on `CutTools`. The effects where comparable to the leading log effects computed using `SMEFTsim` package [88] of $\sim 10^{-6}$. Hence confirming the expectation that beauty quark loops have a negligible effect.

In order to take the effect of Wilson coefficients' running, the relevant contribution for the gluon-initiated process as the same as the stated for the gluon fusion in (2.21). While for the quark-initiated process, one needs to consider the operator mixing in the running, particularly between operators that contain second and third generation quarks mixed together. These corrections can be obtained from the RGEs in refs. [81, 82, 89].

2.1.3 Results

The NLO correction from the four-fermion operators of the third generation quarks on the Higgs rates i.e., partial width Γ or cross-section σ., is extracted from the above

[1] Another rational term R_1 appears due to the mismatch between the four and d dimensional amplitudes, but this is computed automatically in `CutTools`.

computation using the formula

$$\delta R(C_i) = R/R^{\rm SM} - 1, \tag{2.24}$$

here effect from the operator with Wilson coefficient C_i on the Higgs rate R is denoted by $\delta R(C_i)$. Only contributions linear in the Wilson coefficients are considered. In order to isolate the finite terms from the ones coming from the RGE leading log approximation, the correction is further expanded to finite $\delta R^{fin}_{C_i}$ and leading log terms $\delta R^{log}_{C_i}$ as follows

$$\delta R(C_i) = \frac{C_i}{\Lambda^2}\left(\delta R^{fin}_{C_i} + \delta R^{log}_{C_i} \log\left(\frac{\mu_R^2}{\Lambda^2}\right)\right). \tag{2.25}$$

Using this formula, one can obtain the correction at any NP scale Λ, though in the remainder of this chapter this scale is set to 1 TeV. In Table 2.2, the finite and logarithmic corrections for the operators considered in this study is reported. Using this table in filling the formula (2.25) will give the correction to Higgs rates. However, since some of the rates are Higgs partial widths, the Higgs total width Γ_h will be affected and therefore all of Higgs rates are changed. An important observation from Table 2.2 is that the finite terms, are either larger or at the same order than the leading log ones, except for $h \to b\bar{b}$ corrections from $C^{(1),(8)}_{QtQb}$. This highlights the importance of thee full NLO calculation for these corrections in constraining these four-fermion operators, in particular $\mathcal{O}^{(1),(8)}_{Qt}$.

As mentioned earlier, there is a degeneracy amongst the singlet and octet operators, seen clearly in the analytic result for gluon fusion and Higgs decays considered. This degeneracy is though broken for $\mathcal{O}^{(1),(8)}_{Qt}$ due to $t\bar{t}h$. Since, the effect of $\mathcal{O}^{(1),(8)}_{QtQb}$ is negligible for this process, thee true degree of freedom for these operators' Wilson coefficients is the linear combination

$$C^{+}_{QtQb} = (2N_c + 1)C^{(1)}_{QtQb} + c_F C^{(8)}_{QtQb}. \tag{2.26}$$

2.2 Fit to Higgs observables

Using the results from the previous NLO calculations, and combining them with the calculations of NLO Higgs rates from the trilinear Higgs self-coupling λ_3,preformed in refs. [90–94] we could expand on the previous fits for λ_3 from Higgs data, to include four-fermion SMEFT Wilson coefficients as well. In order to examine the true sensitivity of single Higgs observables to λ_3. Although combined fits from Higgs data including λ_3 and SMEFT operators modifying Higgs rates at LO has been preformed [95]. Such fits would not be sufficient in determine the actual sensitivity for λ_3, in particular when the SMEFT operators are weakly constraint and possess significant modifications to Higgs rates as we have seen in Table 2.2. This chapter does not include a global SMEFT fit, but merely motivates it by illustrating how thee sensitivity for probing the Higgs-self coupling from single Higgs data gets diluted when the four-fermion operators are included, and how these two are correlated.

Operator	Process	μ_R	$\delta R_{C_i}^{fin}$ [TeV^2]	$\delta R_{C_i}^{log}$ [TeV^2]
$\mathcal{O}_{Qt}^{(1)}$	ggF	$\frac{m_h}{2}$	$9.91 \cdot 10^{-3}$	$2.76 \cdot 10^{-3}$
	$h \to gg$	m_h	$6.08 \cdot 10^{-3}$	$2.76 \cdot 10^{-3}$
	$h \to \gamma\gamma$		$-1.76 \cdot 10^{-3}$	$-0.80 \cdot 10^{-3}$
	$t\bar{t}h$ 13 TeV	$m_t + \frac{m_h}{2}$	$-4.20 \cdot 10^{-1}$	$-2.78 \cdot 10^{-3}$
	$t\bar{t}h$ 14 TeV		$-4.30 \cdot 10^{-1}$	$-2.78 \cdot 10^{-3}$
$\mathcal{O}_{Qt}^{(8)}$	ggF	$\frac{m_h}{2}$	$1.32 \cdot 10^{-2}$	$3.68 \cdot 10^{-3}$
	$h \to gg$	m_h	$8.11 \cdot 10^{-3}$	$3.68 \cdot 10^{-3}$
	$h \to \gamma\gamma$		$-2.09 \cdot 10^{-3}$	$-1.07 \cdot 10^{-3}$
	$t\bar{t}h$ 13 TeV	$m_t + \frac{m_h}{2}$	$6.81 \cdot 10^{-2}$	$-2.40 \cdot 10^{-3}$
	$t\bar{t}h$ 14 TeV		$7.29 \cdot 10^{-2}$	$-2.48 \cdot 10^{-3}$
$\mathcal{O}_{QtQb}^{(1)}$	ggF	$\frac{m_h}{2}$	$2.84 \cdot 10^{-2}$	$9.21 \cdot 10^{-3}$
	$h \to gg$		$1.57 \cdot 10^{-2}$	$9.21 \cdot 10^{-3}$
	$h \to \gamma\gamma$	m_h	$-1.30 \cdot 10^{-3}$	$-0.78 \cdot 10^{-3}$
	$h \to b\bar{b}$		$9.25 \cdot 10^{-2}$	$1.68 \cdot 10^{-1}$
$\mathcal{O}_{QtQb}^{(8)}$	ggF	$\frac{m_h}{2}$	$5.41 \cdot 10^{-3}$	$1.76 \cdot 10^{-3}$
	$h \to gg$		$2.98 \cdot 10^{-3}$	$1.76 \cdot 10^{-3}$
	$h \to \gamma\gamma$	m_h	$-0.25 \cdot 10^{-3}$	$-0.15 \cdot 10^{-3}$
	$h \to b\bar{b}$		$1.76 \cdot 10^{-2}$	$3.20 \cdot 10^{-2}$
$\mathcal{O}_{QQ}^{(1)}$	$t\bar{t}h$ 13 TeV	$m_t + \frac{m_h}{2}$	$1.75 \cdot 10^{-3}$	$1.84 \cdot 10^{-3}$
	$t\bar{t}h$ 14 TeV		$1.65 \cdot 10^{-3}$	$1.76 \cdot 10^{-3}$
$\mathcal{O}_{QQ}^{(3)}$	$t\bar{t}h$ 13 TeV	$m_t + \frac{m_h}{2}$	$1.32 \cdot 10^{-2}$	$5.48 \cdot 10^{-3}$
	$t\bar{t}h$ 14 TeV		$1.24 \cdot 10^{-2}$	$5.30 \cdot 10^{-3}$
$\mathcal{O}_{tt}$	$t\bar{t}h$ 13 TeV	$m_t + \frac{m_h}{2}$	$4.60 \cdot 10^{-3}$	$1.82 \cdot 10^{-3}$
	$t\bar{t}h$ 14 TeV		$4.57 \cdot 10^{-3}$	$1.74 \cdot 10^{-3}$

Table 2.2. The NLO effects of the four.heavy-quarks operators on the Higgs rates. The effects are separated into finite $\delta R_{C_i}^{fin}$ and leading log parts, in correspondence with (**??**). Effects of $\mathcal{O}(10^{-5} - 10^{-6})$ TeV^{-2} have been omitted from this table. This table has been published in [72]

In the previous references, the modification to Higgs self coupling was reported in terms of the κ-formalism, for the consistency of this analysis, the NLO corrections from the trilinear self-coupling will be converted from this formalism to the SMEFT notation, in terms of the Wilson coefficient C_ϕ. For more details on the conversion between SMEFT and κ-formalism see **??**. In order to keep track of power counting (in terms of Λ) in SMEFT, we expand the results of [91] after converting it to SMEFT , to get

$$\delta R_{\lambda_3} \equiv \frac{R_{\rm NLO}(\lambda_3) - R_{\rm NLO}(\lambda_3^{\rm SM})}{R_{\rm LO}} = -2\frac{C_\phi v^4}{\Lambda^2 m_h^2} C_1 + \left(-4\frac{C_\phi v^4}{\Lambda^2 m_h^2} + 4\frac{C_\phi^2 v^8}{m_h^4 \Lambda^4}\right) C_2. \tag{2.27}$$

In (2.27), the coefficient C_1 corresponds to the contribution of the trilinear coupling to the single Higgs processes at one loop, adopting the same notation as [91]. The values of C_1 for the different processes of interest for this paper are given in **??**. The coefficient

C_2 describes universal corrections and is given by

$$C_2 = \frac{\delta Z_h}{1 - \left(1 - \frac{2C_\phi v^4}{\Lambda^2 m_h^2}\right)^2 \delta Z_h}\,, \tag{2.28}$$

where the constant δZ_h is the SM contribution from the Higgs loops to the wave function renormalisation of the Higgs boson,

$$\delta Z_h = -\frac{9}{16}\frac{G_F m_h^2}{\sqrt{2}\pi^2}\left(\frac{2\pi}{3\sqrt{3}} - 1\right). \tag{2.29}$$

The coefficient C_2 thus introduces additional $\mathcal{O}(1/\Lambda^4)$ (and higher order) terms in δR_{λ_3}. In ref. [91] considering the κ formalism the full expression of (2.28) is kept, while we define two different descriptions: one in which we expand δR_{λ_3} up to linear order and an alternative scheme in which we keep also terms up to $\mathcal{O}(1/\Lambda^4)$ in the EFT expansion. Keeping the full expression in (2.28) and including terms up to $\mathcal{O}(1/\Lambda^4)$ in C_2 lead to nearly the same results as the simple $\mathcal{O}(1/\Lambda^4)$ fit.

Process	C_1	$\delta R^{fin}_{C_\phi}$
ggF/ $gg \to h$	$6.60 \cdot 10^{-3}$	$-3.10 \cdot 10^{-3}$
$t\bar{t}h$ 13 TeV	$3.51 \cdot 10^{-2}$	$-1.64 \cdot 10^{-2}$
$t\bar{t}h$ 14 TeV	$3.47 \cdot 10^{-2}$	$-1.62 \cdot 10^{-2}$
$h \to \gamma\gamma$	$4.90 \cdot 10^{-3}$	$-2.30 \cdot 10^{-3}$
$h \to b\bar{b}$	0.00	0.00
$h \to W^+W^-$	$7.30 \cdot 10^{-3}$	$-3.40 \cdot 10^{-3}$
$h \to ZZ$	$8.30 \cdot 10^{-3}$	$-3.90 \cdot 10^{-3}$
$pp \to Zh$ 13 TeV	$1.19 \cdot 10^{-2}$	$-5.60 \cdot 10^{-3}$
$pp \to Zh$ 14 TeV	$1.18 \cdot 10^{-2}$	$-5.50 \cdot 10^{-3}$
$pp \to W^\pm h$	$1.03 \cdot 10^{-2}$	$-4.80 \cdot 10^{-3}$
VBF	$6.50 \cdot 10^{-3}$	$-3.00 \cdot 10^{-3}$
$h \to 4\ell$	$8.20 \cdot 10^{-3}$	$-3.80 \cdot 10^{-3}$

Table 2.3. The NLO dependence of single Higgs rate on C_ϕ, these results were computed in [94]. The C_1 coefficients are to be used in eq. (2.27), while for a direct comparison with the effect of the four-fermion operators, we quote the translated effect $\delta R^{fin}_{C_\phi}$, which can be used directly in eq. (2.25). If the value of $\sqrt{s}$ is not indicated the effect is the same for both 13 and 14 TeV. This table has been published in [72]

A Bayesian fit was preformed using Markov-chain Monte Carlo (MCMC) method. Using a flat prior s $\pi(C_i) = const.$ and a log likelihood of a Gaussian distribution

$$\log(L) = -\frac{1}{2}\left[(\vec{\mu}_{\text{Exp}} - \vec{\mu})^T \cdot \mathbf{V}^{-1} \cdot (\vec{\mu}_{\text{Exp}} - \vec{\mu})\right]. \tag{2.30}$$

Constructed as follows:

Experimental input $\vec{\mu}_{\text{Exp}}$ The signal strength from experimental measurements of single Higgs rates defined as

$$\mu_{\text{Exp}} \equiv \sigma_{\text{Obs}}/\sigma_{\text{SM}}. \tag{2.31}$$

These measurements as taken from LHC Run II for centre-of-mass energy of $\sqrt{s} = 13$ TeV and integrated luminosity of $139\,\text{fb}^{-1}$ for ATLAS and $137\,\text{fb}^{-1}$ for CMS. In addition to HL-LHC projections by CMS for $\sqrt{s} = 14$ TeV and integrated luminosity of $3000\,\text{fb}^{-1}$. Both of these input types have been already discussed in **??** and summarised in **??**.

Theoretical prediction $\vec{\mu}$ The corresponding theoretical predictions for each of the experimental measurement /projection have been built using the modification to the cross-sections and branching ratios coming from the SMEFT four-fermion operators and C_ϕ. To keep with the power-counting, the signal strength is also expanded in powers of Λ, keeping only Λ^{-2} terms.

$$\mu(C_\phi, C_i) = \frac{\sigma_{\text{Prod}}(C_\phi, C_i) \times \text{BR}(C_\phi, C_i)}{\sigma_{\text{Prod,SM}} \times \text{BR}_{\text{SM}}} \approx 1 + \delta\sigma(C_\phi, C_i) + \delta\Gamma(C_\phi, C_i) - \delta\Gamma_h(C_\phi, C_i). \tag{2.32}$$

Uncertainties and correlations V The correlation matrix $\mathbf{V}$ is build from thee experimental uncertainties found in **??**. For Run-II data, only ATLAS collaboration reported the correlation amongst different channels, and only correlations $> 10\%$ are considered. While for the HL-LHC, the whole correlation matrix found on the webpage [96]. The HL-LHC projections for the S2 scenario explained in [28] were used. These assume the improvement on the systematics that is expected to be attained by the end of the HL-LHC physics programme, and that theory uncertainties are improved by a factor of two with respect to current values. Theoretical uncertainties were not considered in this fit

The python package `pymc3` [97] was used to construct the posterior distribution. We use the `Arviz` Bayesian analysis package [98] to extract the credible intervals (CIs) from the highest density posterior intervals (HDPI) of the posterior distributions, where the intervals covering 95% (68%) of the posterior distribution are considered the 95% (68%) CIs. In the Gaussian limit, these 95% (68%) CIs should be interpreted as equivalent to the 95% (68%) Frequentist Confidence Level (CL) two-sided bounds. `HEPfit` [99] code was used to validate the fits. Given that current bounds on these operators are rather weak, one may wonder about the uncertainty in our fits associated to the truncation of the EFT. Note that, since the four-quark operators only enter into the virtual corrections at NLO, Higgs production and decay contain only linear terms in $1/\Lambda^2$ in the corresponding Wilson coefficients, i.e. the quadratic terms coming from squaring the amplitudes are technically of next-to-NLO. Hence, the quadratic effects in the signal strengths come from not linearising the corrections to the product $\sigma_{\text{Prod}} \times \text{BR}$. These effects have been investigated, and found to have a negligible effect on the fit. The operators of single

chirality $\mathcal{O}_{tt}$ and $\mathcal{O}_{QQ}^{(1)/(3)}$ were not included in the fit, as their effect on Higgs rates is limited to small δR for $t\bar{t}h$. Thus, they cannot be contained simultaneously with C_ϕ using single Higgs data.

2.2.1 Fit results

In Figure 2.5 and Figure 2.6 the 68% and 95% highest posterior density contours of the two-parameter posterior distributions and their marginalisation for the two-parameter fits involving C_ϕ and one of the four-heavy quark Wilson coefficients, evaluated at the scale $\Lambda = 1$ TeV for Run-II LHC measurements . Both linearised and quadratically truncated δR_{λ_3} fits are shown, and we observe that the 95% CI bounds (shown on top of the panels) and correlations depends on the truncation.

We observe that the four-fermion operators are strongly correlated with Higgs self-coupling modifier $\mathcal{O}_\phi$, in the linear fit. With Pearson's correlation of $\gtrsim 0.7$ with p-value $< 10^{-4}$. In the case of quadratic δR_{λ_3} fit, we observe diminished Pearson correlation, but in this scenario Pearson's correlation test is not particularly applicable, as we have non-linear relation between the variables.

The two-parameter fit results for thee four-fermion Wilson coefficients are mesmerised in the forest plots in Figure 2.7 marginalising the posteriors distributions over C_ϕ. The finite effects were isolated by preforming fits with δR^{fin} only. The finite effects are small for $O_{QtQb}^{(1)/(8)}$ but dominant for the four-top operators $O_{Qt}^{(1)/(8)}$mainly coming from $t\bar{t}h$. The effect of EFT truncations of δR_{λ_3} can also be observed as shifts in the mean value for the Wilson coefficients, but the 95% CI's themselves are not significantly affected. In these plots, the fits results from this study are also confronted with the limits obtained from fits to top data [69, 70, 73, 100–102] and EWPO fits from [103]. Showing that when the Wilson coefficient running is taken into an account, the 95% CI bounds obtained from Higgs data are consistently stronger than the ones from top data.

In Figure 2.8 the fit results for C_ϕ after marginalising over the four-fermion Wilson coefficients in both EFT truncations schemes of δR_{λ_3}. In addition to a single parameter fit for C_ϕ. Additionally the current 95 % CL bound on C_ϕ extracted from Higgs pair production search using th final state $b\bar{b}\gamma\gamma$ preformed by ATLAS using Run-II data [104], translated from κ formalism.
The mean values and the 95%CI's change depending on the four-fermion Wilson coefficient that was paired with C_ϕ in the two.-parameter fit. As expected, the single parameter fits for C_ϕ yield stronger bound on C_ϕ than the two-parameter fits, thus the inclusion of the four-fermion operators in single Higgs data dilutes C_ϕ bounds . Additionally, the truncation order of δR_{λ_3} appears to have a significant effect on the length of the CI's, with quadratic fits giving more stringent constraint on C_ϕ. Instead, for Higgs pair production is makes only a negligible effect if linear or up to quadratic terms in the EFT expansion are kept for the $C_\phi > 0$ bound, while the bound weakens at linear order in $1/\Lambda^2$ for $C_\phi < 0$ [105]. For instance, the quadratic single parameter fit for C_ϕ is comparable to the direct bound from Higgs pair production. However, this changes dramatically, when one includes the four-fermion operators in a combined fit, and the

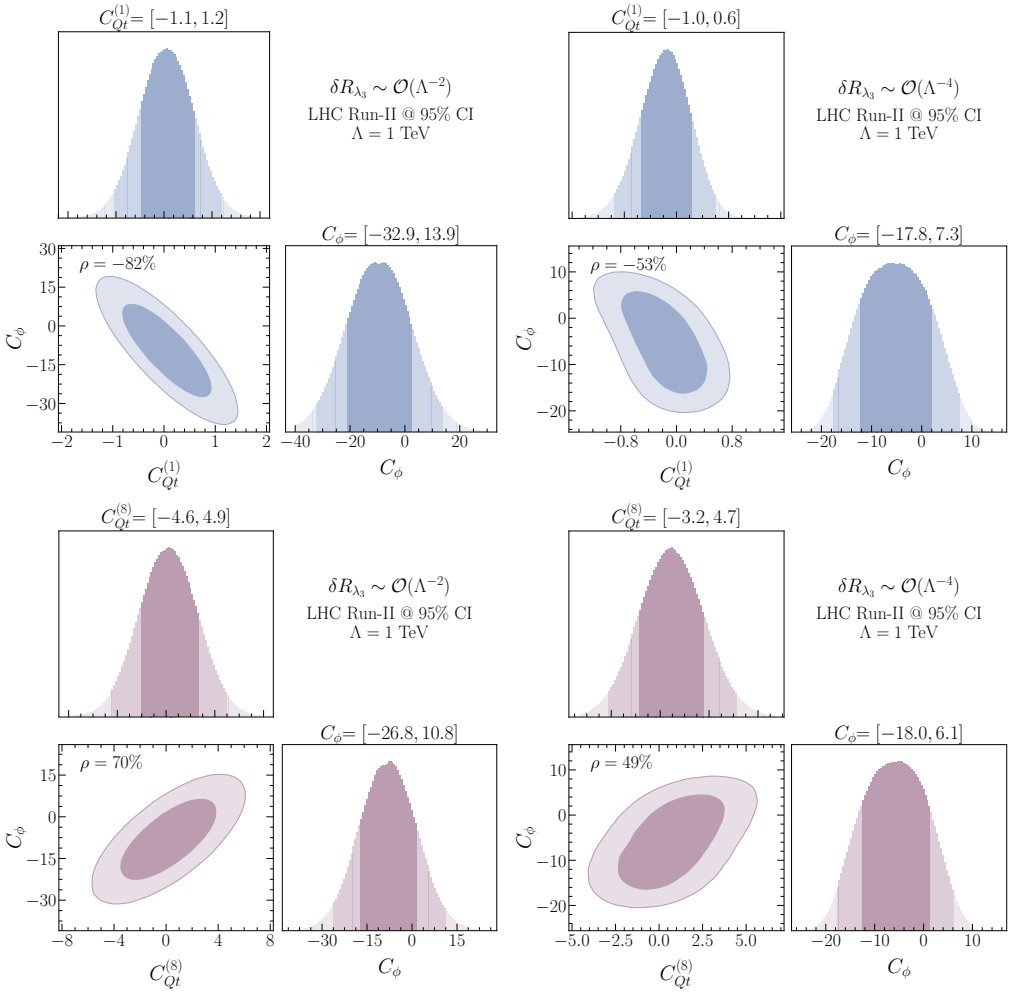

Figure 2.5. The posterior distributions of the Run-II data fits for C_ϕ with $C_{Qt}^{(1)}$ (up) and C_ϕ with $C_{Qt}^{(8)}$ (down). With 68% and 95% highest density posterior contours indicated. The limits shown on top of the plots indicate the 95% CI's. Plots on the left are made for the fully linearised n δR_{λ_3}, while the ones on the right include the quadratic effects. This figure has been published in [72].

single Higgs data constraints on C_ϕ become less significant compared to the direct hh bounds.
It should be noted that the strongest bound on the Higgs self-coupling currently comes from the perturbative unitarity bound of ref. [106], as discussed in chapter.

One of the important aspects of multivariate studies is the correlation among variables. Apart from the two-parameter fits discussed above, here we also consider a four-parameter fit to C_ϕ plus the three directions in the four heavy-quark operator parameter space that the Higgs rates are mostly sensitive too, i.e. neglecting $C_{QQ}^{(1),(3)}$ and C_{tt}, and

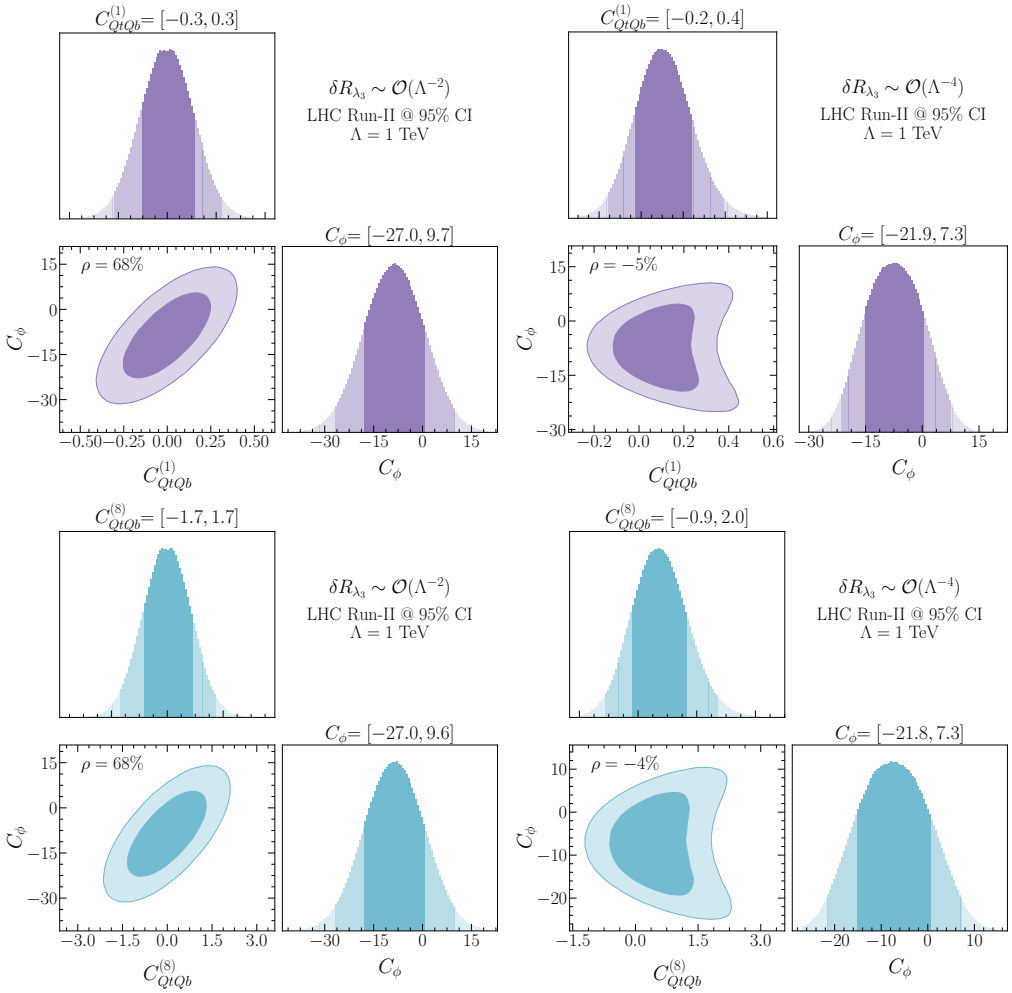

Figure 2.6. The posterior distributions of the Run-II data fits for C_ϕ with $C^{(1)}_{QtQb}$ (up) and C_ϕ with $C^{(8)}_{QtQb}$ (down). With the same annotations as in Figure 2.5. This figure has been published in [72].

trading $C^{(1)}_{QtQb}$ and $C^{(8)}_{QtQb}$ by C^{+}_{QtQb}. When considering two- or four-parameter fits of C_ϕ and the four-heavy-quark Wilson coefficients, we observe a non-trivial correlation patterns amongst these coefficients. Figure 2.9 illustrates these correlation patterns clearly for the four-parameter fit. We observe that the Wilson coefficients $C^{(1),(8)}_{Qt}$ are strongly correlated because, in analogy to $C^{(1),(8)}_{QtQb}$, they only appear in certain linear combination whenever correcting the Yukawa coupling. However, unlike $C^{(1),(8)}_{QtQb}$ they are not completely degenerate because the main part of the NLO correction to $t\bar{t}h$ does not contain the aforementioned linear combination. The four-parameter fit also reveals that the Wilson coefficients $C^{(1),(8)}_{Qt}$ have a large correlation with C^{+}_{QtQb} because all of the

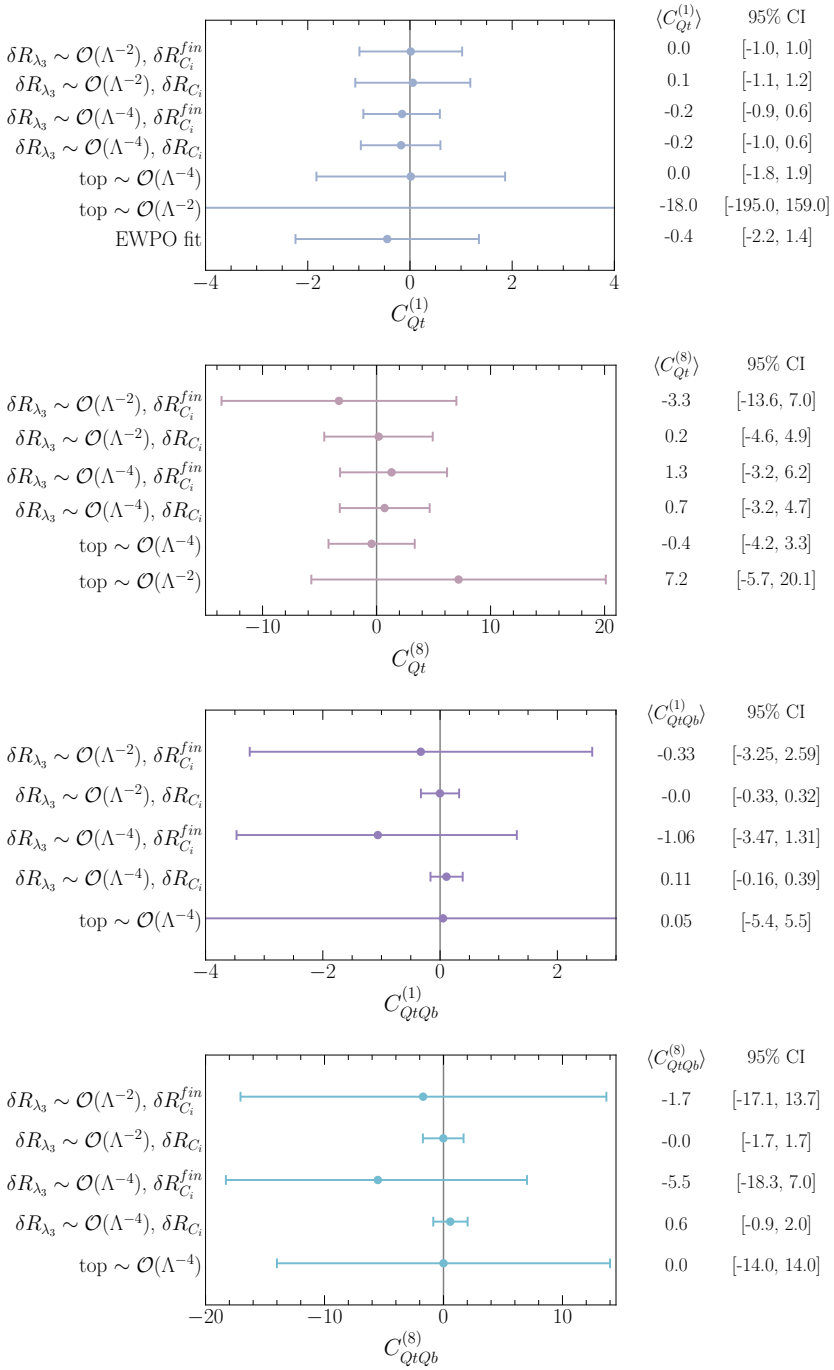

Figure 2.7. Forest plots illustrating the means and 95% CI's constraints on the four-heavy-quark Wilson coefficients C_i from Run-II data. These bounds are obtained from two-parameter fits including the aforementioned coefficients along with C_ϕ, then marginalising over the latter. The different fits with only the finite part of the NLO correction included VS the full results, as well as the EFT truncation scheme for the trilinear coupling, linear vs quadratic. Fits from top data [73] for $C^{(1),(8)}_{Qt}$ and [70] for $C^{(1),(8)}_{QtQb}$ as well as EWPO fits from [103] were included for comparison.This figure has been published in [72].

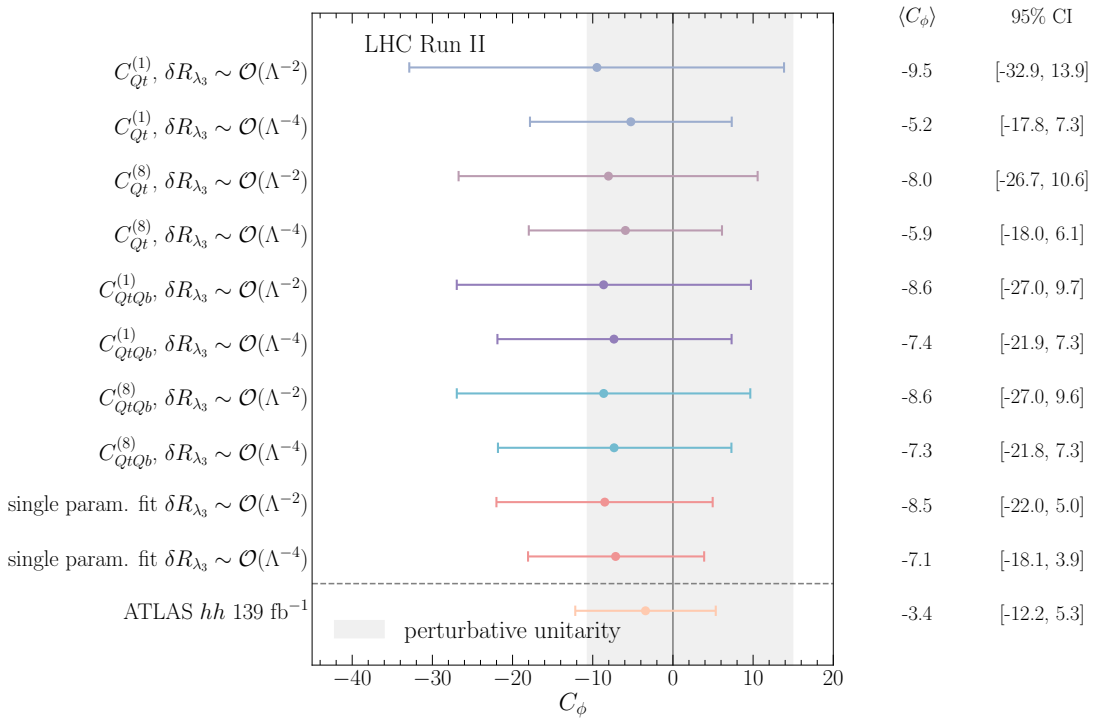

Figure 2.8. A forest plot illustrating the means and 95% CI's bounds for C_ϕ from the two-parameter fit with the four-fermion operators marginalised. The fits results for C_ϕ from full run-II Higgs data keeping terms up to $\mathcal{O}(1/\Lambda^2)$ or $\mathcal{O}(1/\Lambda^4)$ in δR_{λ_3} are shown. For comparison, also the 95% CI and means for the single parameter fit for C_ϕ with the same single Higgs data is shown as well as the bounds on C_ϕ from the 139 fb^{-1} search for Higgs pair production [104]. The horizontal grey band illustrates the perturbative unitarity bound [106]. This figure has been published in [72].

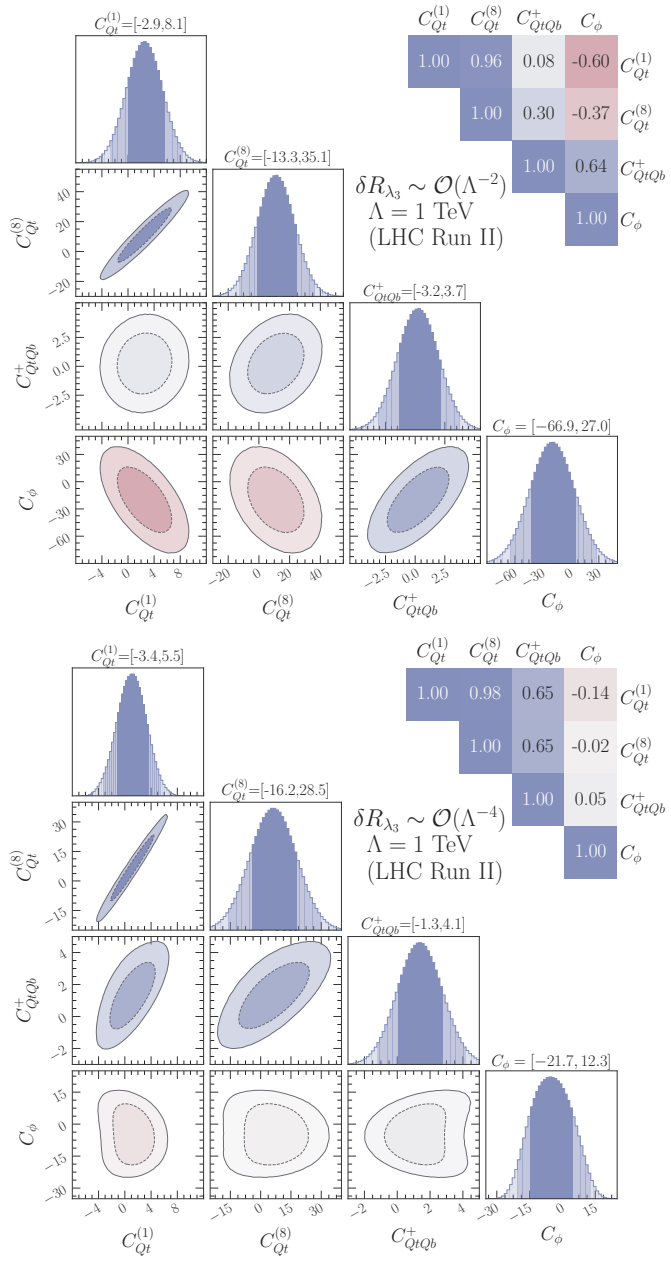

Figure 2.9. The marginalised 68% and 95% Highest density posterior contours for the four-parameter fits including the different four-quark Wilson coefficients and C_ϕ. The numbers above the plots show the 95% CI bounds while the correlations are given on the top-right side. The correlation between each pair of the Wilson coefficients is highlighted as a heatmap. The upper panel shows the fit including up to $\mathcal{O}(1/\Lambda^2)$ in δR_{λ_3} while the lower one shows the fit with including also $\mathcal{O}(1/\Lambda^4)$. This figure has been published in [72].

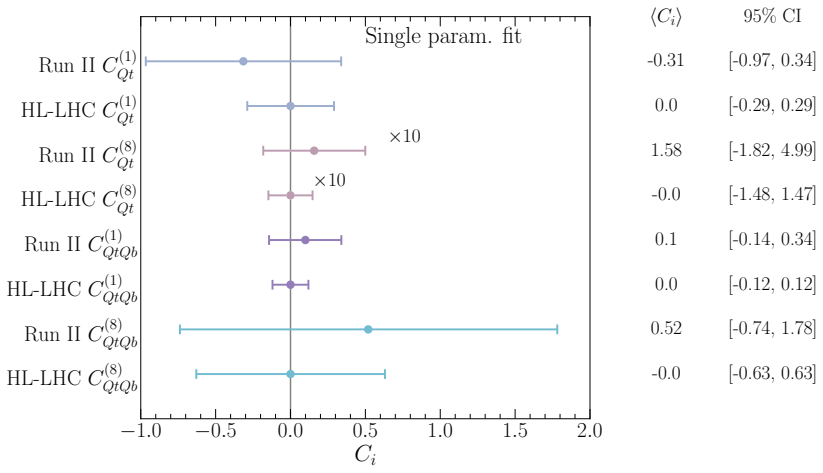

Figure 2.10. Results of a single parameter fit showing the improvement in constraining power of the HL-LHC over the current bounds from Run-2 data. This figure has been published in [72].

four Wilson coefficients appear in a linear combination in the NLO corrections except for $h \to b\bar{b}$ and $t\bar{t}h$. However, this correlation is not as strong due to the large NLO correction of the Higgs decay $h \to b\bar{b}$ from $C_{QtQb}^{(1),(8)}$. Moreover, the correlation between the four-heavy-quark Wilson coefficients and C_ϕ depends on the δR_{λ_3} truncation.

2.2.2 Prospects for HL-LHC

Using the CMS Higgs signal strength measurement projections for the HL-LHC in refs. [96, 107] for a centre-of-mass energy of $\sqrt{s} = 14$ TeV and integrated luminosity of $3\,\text{ab}^{-1}$, it is possible to repeat the fits done for Run-II. The projections for the S2 scenario explained in [28] were used. These assume the improvement on the systematics that is expected to be attained by the end of the HL-LHC physics programme, and that theory uncertainties are improved by a factor of two with respect to current values. These projections are assumed to have their central values in the SM prediction with the total uncertainties summarised in table **??** in Appendix **??**.

In Figure 2.10 I show the comparison between the fit results of Run-II data and the projections for the HL-LHC for single parameter fits. For the operators $\mathcal{O}_{Qt}^{(1),(8)}$ the constraining power of the HL-LHC is roughly a factor two better as the current bounds we could set from single Higgs data, while for the operators $\mathcal{O}_{QtQb}^{(1),(8)}$ the improvement is a little less. While in Figure 2.11 the limits on C_ϕ in a single parameter fit for Run-2 and the projections for the HL-LHC are shown. including in δR_{λ_3} up to order $\mathcal{O}(1/\Lambda^2)$ or $\mathcal{O}(1/\Lambda^4)$. While for Run-II data the inclusion of $\mathcal{O}(1/\Lambda^4)$ made a significant difference, this is less pronounced for the HL-LHC projections. These results are very similar to the projections presented in a κ_λ fit in [108]. The results were also confronted with data from searches for Higgs pair production 139 fb^{-1} [104] and HL-LHC projections [109] on

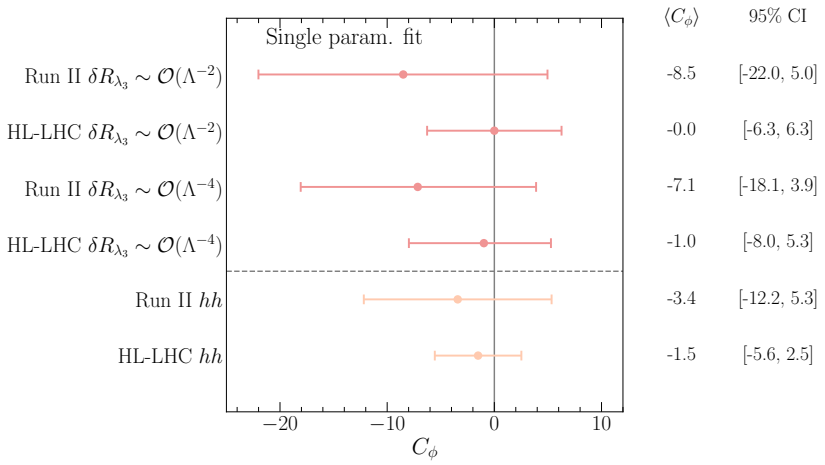

Figure 2.11. A forest plot illustrating the means and 95% CI's of the posteriors built from the C_ϕ in a single-parameter fit, showing also the differences in including terms of $\mathcal{O}(1/\Lambda^2)$ or up to $\mathcal{O}(1/\Lambda^4)$ in the definition of δR_{λ_3}. For comparison, also the limits and projections from searches for Higgs pair production are shown. This figure has been published in [72].

Higgs pair production, showing that Higgs pair production will still allow to set stronger limits on C_ϕ.

2.3 Conclusion

In this chapter, the calculations of the NLO corrections depending on four-heavy-quark operators to single Higgs rates have been calculated. We have seen that operators both homogenous and heterogeneous chirality structures contribute to Higgs rates at NLO. Though, the operators with heterogeneous chirality structure have more sizeable effects as they would contribute to $hf\overline{f}$ vertex renormalisation in SMEFT and therefore appear in more channels compared to the operators baring homogenous chirality structure. Using the calculation results, fits using Higgs data have been preformed. The operators with the same chirality structure will not be constrained strongly by the Higgs data, and hence their results were not included. This applies to the operators that contribute only via beauty quarks loops, like $\mathcal{O}_{Qb}^{(1),(8)}$.
Two processes stood out in this calculation in terms of their sensitivity to these operators. The decay of the Higgs to beauty quarks, which had strong sensitivity to $\mathcal{O}_{QtQb}^{(1),(8)}$, Moreover, the associated production of the Higgs with top pair $t\bar{t}h$, which had large finite corrections coming from $\mathcal{O}_{Qt}^{(1),(8)}$. These corrections were depending on the colour factor and thus broke the degeneracy between the singlet and octet operators.
Using these calculations combined Higgs measurements using complete Run-II data as well as HL-LHC projections, fits for constraining these operators have been preformed. These fits also included the SMEFT operator modifying the Higgs self-coupling C_ϕ which

is weakly constrained, and only appears at NLO in single Higgs rates; like the group of four-heavy-quark operators considered. One can observe from the fits, that the constrains on C_ϕ from single Higgs data will become significantly diluted compared to the fits preformed with this operator alone, or even with ones that enter at LO [90–94]. This is due to the strong correlation patters amongst C_ϕ and the four-fermion operators in question. On the contrary, The fits yielded overall stronger bounds on the four-heavy-quark operators than the ones obtained from top data [70, 73]. Comparable bounds can be also seen when EWPO data is considered [103], which these operators also enter at NLO in these observables. Additionally, the authors of ref. [110] have shown that these operators could also be constrained from flavour observables involving $\Delta F = 2$, in particular $B_s - -\overline{B}_s$ mixing. Although these bounds depend on the flavour ansatz of the New Physics, and not completely model independent.
The results of these calculations and consequent fits further emphasize the interconnectivity of SMEFT operators and experimental observables, which was discussed in**??**.
Then remains the question: *How this interconnectivity would manifest in a NP model ?*. Particularly, one might wonder if the strong correlation between these four-fermion operators and $\mathcal{O}_\phi$ could appear in a UV complete model. In fact, large effective couplings involving four top quarks are expected in many NP models, for example partial compositness [111]. These models would also generate sizeable modifications to the Higgs self-interaction. Similar effects could be obtained from models containing new scalars such as an additional Higgs doublet $\varphi \sim (1,2)_{\frac{1}{2}}$, or other scalars with non-singlet representation under $SU(3)_c$ like $(6,1)_{\frac{1}{3}}$ and $(8,2)_{\frac{1}{2}}$. For further details on these models and their matching see [112]. In addition, for NLO matching to SMEFT see [113].

Part III

Higgs Pair Production

3 Overview of Higgs pair production at colliders

The determination of the shape of the Higgs potential is an essential part of the LHC physics programme. Unlike the determination of most properties of the Higgs and its couplings to heavy particles, the light Yukawa and Higgs-self couplings are exceptionally hard to probe. This is particularly evident from the conclusion of chapter 2. When we have seen that the effectiveness of the utilisation of single Higgs signals in order to probe the Higgs trilinear coupling is challenged with the fact that other weakly constrained operators also affect these signals. Thus, Higgs pair production remains as thee only direct way to access this elusive interaction.
The production of Higgs in pairs has roughly 10^{-4} the signal of producing a single Higgs at the LHC. The Higgs pair production with Higgs pair decays considered have a cross-section of $\sim$ 1fb, in the SM. This would make it inaccessible from Run-II or Run-III data, but should be accessed using the whole luminosity of the HL-LHC [28, 114, 115]. As for the quartic coupling, which would require NLO corrections to Higgs pair, which are currently unknown, or triple Higgs production, both of which are beyond the sensitivity of the LHC [116]. The measurement potentials for the light Yukawa couplings shall be discussed in the Next chapter. The main advantages for Higgs pair production in determining the Higgs trilinear self-coupling comes from the dependence of the cross-section of λ_3 at the LO level, as well as the fact that the rest of SMEFT operators entering in this process (see eq (**??**)) can be strongly constraint from other processes, breaking any potential correlations that might appear between them and the trilinear coupling using only di-Higgs data. However, the inclusion of light quark Yukawa couplings modifiers e.g.$C_{u\phi}$ and $C_{d\phi}$ would complicate things as we shall see in **??**.
This chapter will start by reviewing the theoretical status of the dominant process for Higgs pair production, the gluon fusion, in section 3.1. Then, the other subdominant channels will be briefly reviewed in section 3.2. I will afterwards overview the experimental efforts in probing this rare yet fascinating processes in section 3.3. Finally, I will present in section 3.4 a summery of the trilinear Higgs-self coupling constraints.

3.1 Higgs pair production by gluon fusion

The dominant process for Higgs pair production at the LHC (and hadron colliders in general) is the gluon gluon fusion (ggF) via a heavy quark loop Q, mainly the top and beauty quark, with the latter contributing only to about 1%, as shown in Figure 3.1. This process is well-studied at leading order (LO) analytically [117–120]. The higher or-

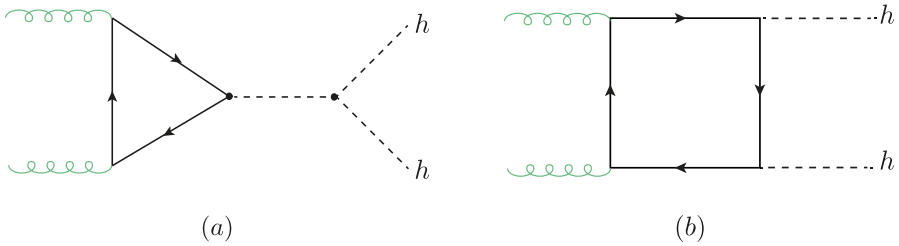

Figure 3.1. Feynman diagrams for the ggF process of Higgs pair production in the SM.

der computations are significantly more complicated to preform compared to the gluon fusion production of a single Higgs. This is due to the fact that multi-scale amplitudes at two-loops (and more) cannot be always computed analytically using the current computational techniques. The first attempt to compute the NLO corrections to di-Higgs were via the infinite top limit (HTL/LME) approximation [33, 121, 122] and implemented in `HPAIR` [120]. These corrections were found to be large, with a K-factor of ~ 2. This prompted more calculations with inclusion of top mass effects [13, 123–126], which improved the stability of the LME expansion as well as corrected the cross-section by $\sim 10\%$. In addition, the threshold resummation effects of the LME has been included in [127]. This approach, however, is not sufficient to produce corrections to the differential cross-section, as the LME fails for $m_{hh}^2/4m_t^2 \lesssim 1$. Using numerical evaluation of the two-loop integrals, it is possible to obtain exact results with full top mass dependence, see refs. [128–130]. But this comes at the cost of computational power required to evaluate the cross-section. Hence, approximation methods were imperative in obtaining more flexible results for use at simulations and BSM Higgs pair production predictions. These approximations methods are analogous, and sometimes connected to the ones used for Zh production discussed in **??**. This includes, small final particle transverse momentum [40], and high energy (HE) expansions [**?**]. In addition to a method developed in refs. [131, 132] which considers both $\hat{s}, \hat{t}$ and m_t as large quantities while keeping the Higgs mass as small one. This method has a wide coverage of the m_{hh} spectrum. The use of Padé approximation to improve the p_T–expanded amplitude coverage as well as to obtain a description for the three-loop (NNLO) form factors was demonstrated in [133]. The NNLO cross section with top mass effects has been computed numerically in [134] and also at differential level [135], and analytically only in the LME [136]. Also, NLO+ NNL analytic results have been obtained by [137]. Parton shower matching for NLO Higgs pair production has been computed in [138, 139], which was essential for the `POWHEG` implementation for di-Higgs, with NLO corrections computed from a grid has been made available by [139–141]. Figure 3.2 shows the Higgs pair virtual partonic cross-section defined in eq.(**??**) vs the p_T and HE expansions bridged using Padé approximants [142]. The matching between the results across low and high energy intervals of m_{hh} shows the strength of Padé approximants technique. This is the most recent analytic higher order correction result for Higgs pair production.
The LO Higgs pair production with SMEFT operators is available in `SMEFTatNLO` model [63] for `MadGraph`.

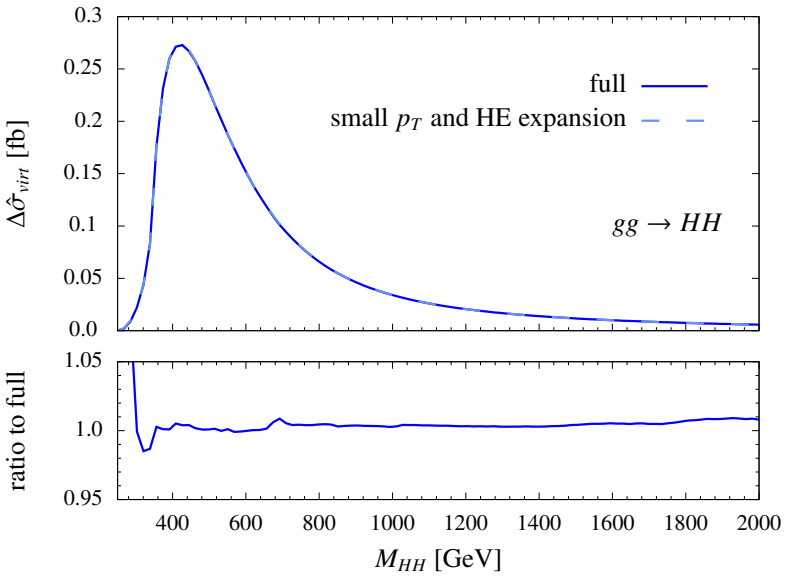

Figure 3.2. Combination of the HE and p_T expansions of the virtual two-loop NLO corrections using Padé approximants, confronted with the NLO results from a numerical grid. This plot is taken from [142].

Calculation of LO in addition to Higher order corrections to Higgs pair production in EFT, MSSM and composite Higgs models can be found in [143–147].
The NNLO correction were used according to the Higgs cross section working group recommended values [148, 149]:

$$K = \frac{\sigma_{NNLO}}{\sigma_{LO}}, \qquad K_{14\text{TeV}} \approx 1.71. \tag{3.1}$$

3.1.1 Theoretical uncertainties

There are four main sources of theoretical uncertainties for Higgs pair production:

1. Scale uncertainty: coming form the arbitrariness of scales choice.
2. PDF uncertainties : coming form the uncertainty in the PDF fitting and model.
3. α_s running uncertainty: originating from the initial value (i.e. $\alpha_s(M_Z)$).
4. Top mass renormalisation scheme, which involves m_t appearing in the loop propagators and in the top Yukawa.

The computation of the uncertainties is described in [150, 151]. for PDF and α_s uncertainties. In order to calculate the scale uncertainties, the cross-section was computed

	σ [fb]	Scale [fb]	PDF+α_s [fb]	Total [fb]
SM HEFT (LO)	18.10	–	–	–
SM running mass (LO)	16.96	–	–	–
SM (LO)	21.45	$^{+4.29}_{-3.43}$	± 1.46	$^{+4.53}_{-3.73}$
SM (NLO) [155]	33.89	$^{+6.17}_{-4.98}$	$^{+2.37}_{-2.01}$	$^{+6.61}_{-5.37}$
SM (NNLO) [134]	36.69	$^{+0.77}_{-1.83}$	± 1.10	$^{+1.66}_{-6.43}$ (incl. m_t uncertainty [152])

Table 3.1. Gluon fusion (ggF) Higgs pair production cross-section at 14 TeV with theoretical uncertainties, the HTL/LME is computed using (SM HEFT), top running mass, LO, NLO and NNLO QCD corrections. The NLO and NNLO results are taken from the references cited in the table. The LO results are computed via a FORTRAN code.

with different μ_R and μ_F values ranging between:

$$\frac{M_{hh}}{4} \leq \mu_R/\mu_F \leq M_{hh} \tag{3.2}$$

As for the m_t renormalisation uncertainty, one uses the $\overline{\text{MS}}$ running of the top mass formula at N^{3}LO [152]

$$\overline{m_t}(m_t^{pole}) = m_t^{pole}\left(1 + \frac{4}{3\pi}\alpha_s(m_t^{pole}) + 10.9\frac{\alpha_s^2(m_t^{pole})}{\pi^2} + 107.11\frac{\alpha_s^3(m_t^{pole})}{\pi^3}\right)^{-3} \tag{3.3}$$

The total 14 TeV ggF hh, cross-section at different orders in computation with its uncertainties are shown in Table 3.1, which indicates that the uncertainties are dominated by the m_t renormalisation scheme of $\sim -18\%$ uncertainty in the lower envelope. This is significant part of the uncertainty budget and needs to be resolved by including N^{3}LO corrections to ggF hh, such corrections are available in the HTL [153, 154].

3.2 Other processes

Like the single Higgs production at hadron colliders, the production of Higgs pairs has the same subdominant channels VBF, di-Higgsstrahlung Vhh and associates production of Higgs pair with tops $t\bar{t}hh/tjhh$. Their cross-sections and uncertainties at 14 TeV are shown in Table 3.2, while in Figure 3.3 their cross-sections as a function of the centre-of-mass energy $\sqrt{s}$ is shown [108].

3.2.1 VBF hh

Vector boson fusion hh production has the second largest cross-section after ggF hh, which is calculated up to N^{3}LO [155–157] inclusively and differentially at NNLO [158]. The dominant diagrams are analigious to the single Higgs VBF, which involve the W/Z bosons exchanged in the $t-$channel. The process has the same topology as the -off shell-

Process	Cross-section 14 TeV (fb)	Theo. accuracy	Theo. uncertainty (%)	Contribution (%)
1. ggF hh	36.690	NNLO QCD	12.3	90.1
2. VBF hh	2.050	N³LO QCD	2.1	5.0
3. Zhh	0.415	NNLO QCD	3.6	1.0
4. W^+hh	0.369	NNLO QCD	2.1	0.9
5. W^-hh	0.198	NNLO QCD	3.0	0.5
6. tthh & tjhh	0.986	NLO QCD	5.1	2.4

Table 3.2. Summery of the Higgs pair production processes at 14 TeV LHC.

single Higgs VBF, with the off-shell Higgs giving two final states ones via the trilinear self-coupling.

3.2.2 Di-Higgsstrahlung

The associated production of Higgs pair with W and Z bosons has a small cross-section compared to ggF and VBF, this process is known up to NNLO QCD accuracy, which includes the gluon-fusion component in the full computation [159**?** , 160].

3.2.3 Associated Higgs pair production with t-quarks

Sometimes called the di-Higgs bremsstrahlung off top quarks [108], this channel has a steeper dependence on $\sqrt{s}$ than the single Higgs bremsstrahlung $t\bar{t}h$. One can see, for example, from Figure 3.3 that its cross-section becomes at roughly the same values as the VBF's. Only NLO computations for this channels have been carried out [161].
All of the three channels have a relatively small NLO correction, compared to gluon fusion. Which ranges from 10-30%.

3.3 Experimental overview for Higgs pair production

The search for Higgs pair production can be divided into two categories, resonant and non-resonant searches. The first searches for a heavy scalar or spin-2 resonance that decays into a Higgs pair. While the latter is concerned about the SM or if the new particle has a mass beyond the reach of the LHC, i.e. when the EFT limit is valid. In this review, I shall focus on the non-resonant searches, as these are the ones relevant to focus of this thesis, for detailed overview of the resonant searches, and non-resonant ones, see [108].
Figure 3.4 shows the current searches for non-resonant Higgs pair production by both ATLAS and CMS. The searches are summarised according to the final state:

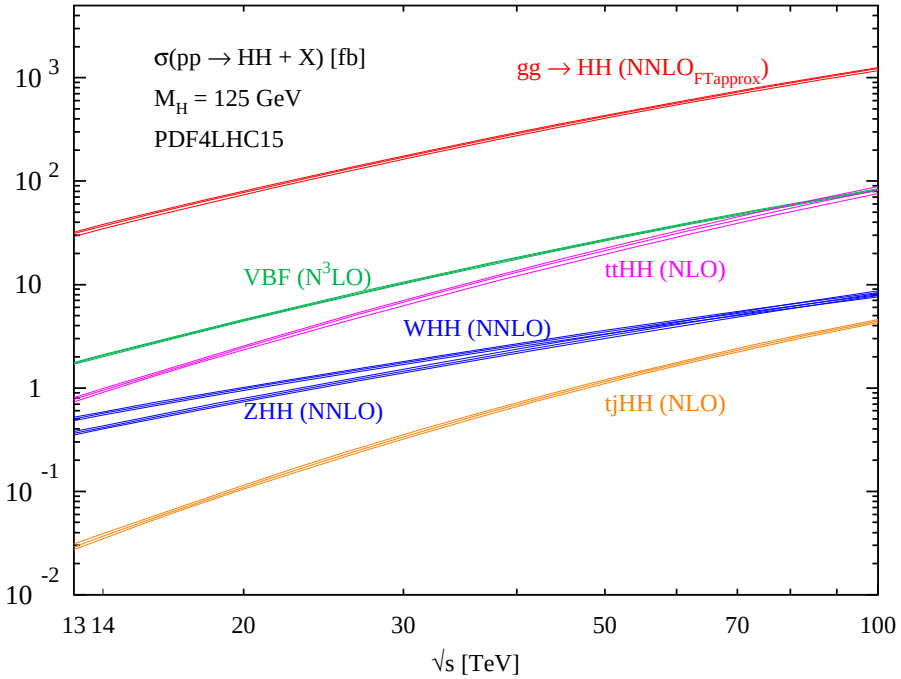

Figure 3.3. The cross-section of all di-Higgs processes at the highest available perturbation order as a function of centre-of-mass energy $\sqrt{s}$.The bands show the uncertainties without the top-mass renormalisation scheme. This plot is taken from [108].

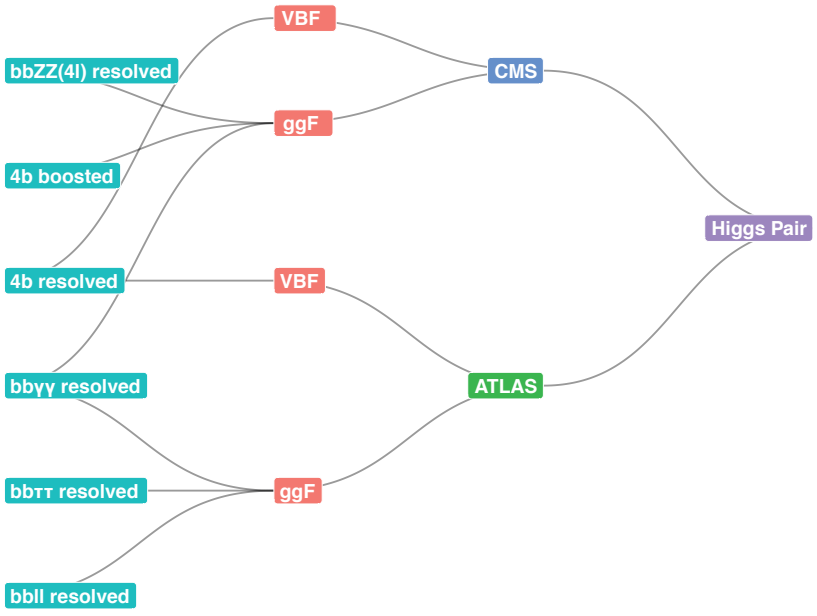

Figure 3.4. The non-resonant Higgs pair searches conducted by ATLAS and CMS using the full Run-II data.

$hh \to b\bar{b}b\bar{b}$

The final state $hh \to b\bar{b}b\bar{b}$ has the highest cross-section possible for Higgs pair, but poses a difficulty due to the large QCD background coming from production of 4 b-tagged jets. CMS [162] has used Boosted decision trees (BDT) for studying this final state for ggF and VBF channels, separated. This allowed for sinsitivity for the trilinear and $hhVV$ coupling. This analysis lead to 95% CL bounds on $\kappa_\lambda \in [-2.3; 9.4]$ and $\kappa_{2V} \in [-0.1; 2.2]$. They have also preformed boosted analysis for the VBF channel, by defining two large jets with jet radius of $\Delta R = 0.8$. This analysis is not sensitive to the trilinear self-coupling, but it is sensitive to both κ_V and κ_{2V}, which leads to the most stringent bound on the latter coupling modifier so far $\kappa_{2V} \in [0.6; 1.4]$. The $\kappa_{2V} = 0$ hypothesis is excluded with $p < 0.001$ [163]. On the other hand, ATLAS has preformed only a resolved analysis for this final state and only for the VBF production channel [164], hence they were able to only report bounds on $hhVV$ coupling $\kappa_{2V} \in [-0.43; 2.56]$.

$hh \to b\bar{b}VV$

ATLAS has considered the gluon fusion final state $hh \to b\bar{b}\ell\ell$, with the leptons coming from WW/ZZ decays [165]. This states covers around 90% of the total $hh \to b\bar{b}VV$ signal. Their analysis was divided into two categorise, same-flavour and different-flavour leptons. The observed signal strength were higher than the expected one. Hence, no bounds on the self-coupling could be extracted from this search. Similar analysis has been carried out by CMS, but with a requirement to observe four leptons instead of two, hence they searched for the final state$hh \to b\bar{b}(ZZ^* \to 4\ell)$. The 95% CL upper limit on the signal strength was 30 times the SM one, with bounds on Higgs self-coupling of $\kappa_\lambda \in [-9; 14]$ [166].

$hh \to b\bar{b}\tau\tau$

This channel has backgrounds coming from real τ's, such as $t\bar{t}$ and Zj with heavy jets. Also, fake τ's coming from QCD multijet process. A neural network has been used by ATLAS [167] for this channel's search, using resolved b jets. The extracted bounds on κ_λ are $[-2.4; 9.2]$.

$hh \to b\bar{b}\gamma\gamma$

This final is the most promising for Higgs pair searches and observation. Despite having a lower cross-section that the previous final states with BR of 0.27% in the SM, it has the highest selection efficiency. This is due to the low backgrounds and the ability to fully reconstruct the photons. The dominant non-reducible background is $b\bar{b}\gamma\gamma$ which has a cross-section of ~ 13fb at the 14 TeV LHC, more details about the backgrounds of this final states are stated in Table 3.3.

Both ATLAS and CMS have published searches of this channel using resolved b-jets and BDT and neural networks [104, 168]. With ATLAS reporting the strongest 95% CL

Channel	LO σ [fb]	NLO K-fact	$6\,\text{ab}^{-1}$ [#evt @ NLO]
$b\bar{b}h, y_b^2$	0.0648	1.5	583
$b\bar{b}h, y_b y_t$	-0.00829	1.9	-95
$b\bar{b}h, y_t^2$	0.123	2.5	1,840
Zh	0.0827	1.3	645
$\sum b\bar{b}h$	0.262	-	2,970
$b\bar{b}\gamma\gamma$	12.9	1.5	116,000
$t\bar{t}h$	1.156	1.2	6,938

Table 3.3. SM cross-section for the main background processes at 14 TeV with $6\,\text{ab}^{-1}$ data at the HL-LHC. For $b\bar{b}h$ production, the Higgs boson is decayed to a pair of photons. The total production of Higgs associated with $b\bar{b}$ is denoted by $\sum b\bar{b}h$ and is the sum of the top four channels.

bound on κ_λ yet, which was used in the comparisons in Figure 2.11. While CMS has reported bounds on κ_λ and κ_{2V} : $\kappa_\lambda \in [-3.3; 8.5]$ and $\kappa_{2V} \in [-1.3; 3.5]$.

3.3.1 Prospects for the HL-LHC

The highlight of the HL-LHC programme is the search for the Higgs pair production. It is projected that the Higgs pair signal to be observed at $\sim 4 - 4.5\sigma$ level. The use of machine learning techniques in the event analysis of hh searches will be a key factor in the potential discovery of this process [28]. In **??** the interpretable machine learning technology will be exploited in improving the sensitivity for hh signals at the HL-LHC. With the main focus on the $b\bar{b}\gamma\gamma$ final state. As this channel has the highest potential for discovery of di-Higgs production [155, 169–174]. The expected bounds on κ_λ at the HL-LHC for combined ATLAS and CMS is $\kappa_\lambda \in [0.1, 2.3]$ [28, 108]

3.4 Summary

The Higgs pair production is a missing key measurement of the SM, it is essential for the determination of the Higgs potential by directly constraining the Higgs trilinear self-coupling. Moreover, this channel is sensitive to non-linear couplings with the Higgs, like $hhVV$ and $hhf\overline{f}$. Due to the small cross-section of this channel, current searches obtain rather weak bounds on κ_λ that are comparable with the perturbative unitarity bounds [106]. Hence, the need for higher luminosity is imperative. Consequently, the HL-LHC is expected to result in an observation or even discovery of this process. Particularly with the help of advanced machine learning techniques.
The observation of Higgs pair production is expected to provide a direct measurement on one of the two " difficult" couplings of the Higgs, which is the trilinear self-coupling. However, as we shall explore in the upcoming chapters, it could also provide a window for observing the second difficult coupling discussed in the first chapter; the coupling between the Higgs and light quarks.

4 Higgs pair as a probe for light Yukawa couplings

The vast hierarchy of quark (and lepton) masses that we have seen in **??** is one of the unsolved mysteries of the SM. One might wonder whether the Higgs is actually responsible for the light quarks masses or there exist other physics that interplays with the Higgs in generating the light quark mass terms. In fact, one of Weinberg's last papers was exactly addressing this question [175], in this paper he proposed that only the third generation fermions obtain their masses from Yukawa coupling, while the rest acquire theirs via loop-level interactions. Despite his models being only illustrative, his paper is a proof that even the pioneers of the SM theory still reflect upon this mystery.
The pragmatic approach to unravelling this puzzle, is to directly measure the Higgs interaction with light fermions. Ideally, this would be via Higgs decay to first and second generation fermions. This is feasible for the muon case [176, 177] and rather challenging for the charm quarks [178–180] but almost impossible with the current technologies for the electron [181], strange and first generation quarks. Although, lepton colliders might have potential for *strange tagging* [182]. The difficulties here is twofold, first, the SM predicts that these couplings to be extremely small effectually making these decay channels vanishing even at few ab^{-1} luminosity. Additionally, even if NP would enhance the Higgs coupling to these fermions, the resolution of the LHC, would not be sufficient for reconstructing the Higgs from electron pairs, and it is not possible to distinguish up, down or gluon jets at the LHC form an overwhelming QCD background . This means that the search for these couplings ought to take a non-trivial path. Enhancements of light quark Yukawa couplings would open the tree-level quark anti-quark inhalation Higgs production channel $q\bar{q}$A, which is enhanced by the presence of light quarks in the PDF's. Moreover breaking the degeneracy amongst the strange up and down quarks, by having a *production tagging* coming form the different distributions of the PDF's amongst quark flavours. For sufficiently large enhancement of the light quark Yukawa couplings, this channel would even become dominant over the loop-induced gluon fusion, as seen in Figure 4.2. Working strictly in the SMEFT paradigm, the $q\bar{q}$A channel would contain a $hhq\bar{q}$ contact interaction illustrated in Figure 4.1, this interaction enhances the Higgs pair production more than the single Higgs $q\bar{q}$A, thus making Higgs pair production more sensitive to light quark Yukawa enhancement, as Figure 4.2 indicates.
Although the ggF Higgs pair production channel in SMEFT contains diagrams with contact $hhq\bar{q}$ interaction shown in Figure 4.3, the contribution of this diagram topology is suppressed by the kinematic mass of the quarks appearing inside the loops, hence the ggF channel is not affected by enhanced light quark Yukawa couplings in a significant way.

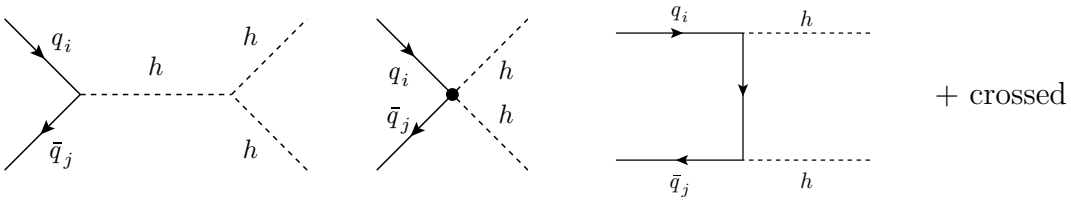

Figure 4.1. Feynman diagrams for the $q\bar{q}$A Higgs pair production in the SMEFT paradigm. The middle diagram shows a contact $hhq\bar{q}$ interaction, that contributes to significant enhancement of this channel compared to its single Higgs counterpart.

This chapter aims to exploit the potential for Higgs pair production as a direct measurement channel for light quark Yukawa. Focusing on the first generation quarks. I will start by introducing the inclusion of light quark couplings to the Higgs in the SMEFT framework in section 4.1. Then the NLO QCD calculation of the $q\bar{q}$A channel will be shown in section 4.2. section 4.4 will outline a cut-based analysis of the di-Higgs final state $b\bar{b}\gamma\gamma$ in order to estimate the sensitivity of this channel for the HL-LHC. Later, in section 4.5 an optimised approach for enhancing the sensitivity based on multi-variant analysis and interpretable machine learning will be showcased. The results of both analysis techniques will be discussed and compared in section 4.6 While in section 4.7 I will overview the other searches for light Yukawa couplings comparing it the Higgs pair production expected sensitivity. This chapter will be concluded in section 4.8.
The cut-based analysis has been published in [2], while the interpretable machine-learning one is an undergoing project with R. Gröber, C. Grojean, A. Paul, and Z. Qian.

4.1 SMEFT and light Yukawa couplings

Including the flavour indices ij of the SMEFT operators introduced in refs. [183, 184] and **??**, we would get light quark -Higgs coupling enhancement from the operators

$$\Delta\mathcal{L}_y = \frac{\phi^\dagger\phi}{\Lambda^2}\left(C^{ij}_{u\phi}\overline{Q}^i_L\tilde{\phi}u^j_R + C^{ij}_{d\phi}\overline{Q}^i_L\phi d^j_R + h.c.\right), \tag{4.1}$$

The mass matrices of the up- and down-type quarks obtained from the Yukawa and the new SMEFT coupling are

$$\begin{aligned} M^u_{ij} =& \frac{v}{\sqrt{2}}\left(y^u_{ij} - \frac{1}{2}(C_{u\phi})_{ij}\frac{v^2}{\Lambda^2}\right), \\ M^d_{ij} =& \frac{v}{\sqrt{2}}\left(y^d_{ij} - \frac{1}{2}(C_{d\phi})_{ij}\frac{v^2}{\Lambda^2}\right), \end{aligned} \tag{4.2}$$

where y^q_{ij} are the SM Yukawa matrix elements introduced in eq. (**??**). Since the quark masses are measured quantities, one would naturally rotate to the mass basis using bi-

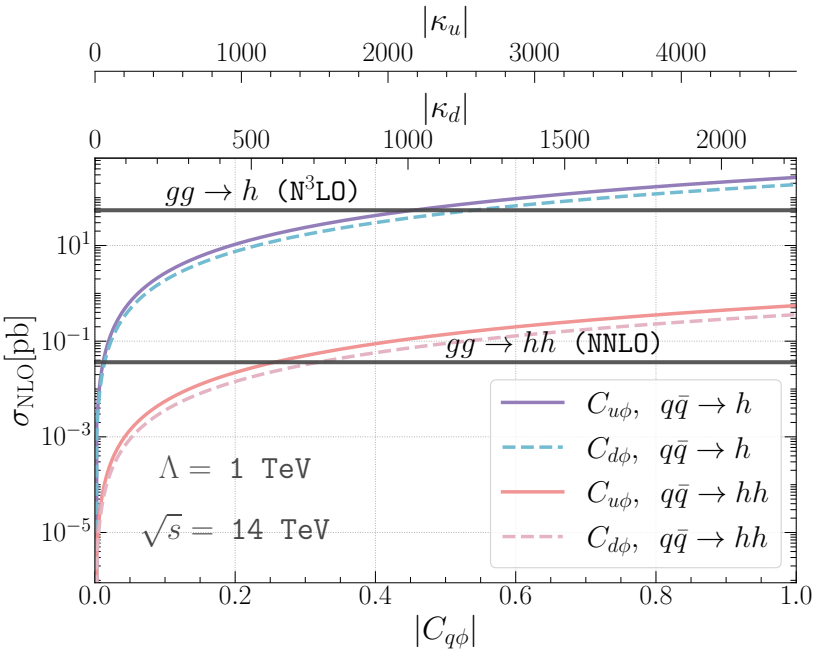

Figure 4.2. *The production cross-section of single Higgs and di-Higgs at* 14 *TeV from the quark anti-quark annihilation* $q\bar{q}A$ *as a function of the Wilson coefficients* $C_{u\phi}$ *and* $C_{d\phi}$ *versus the SM gluon fusion cross-sections (the horizontal solid line for* $gg \to h$ *and the dashed-dotted one for* $gg \to hh$*). One can observe that for values of* $C_{u\phi} = 0.22\,(0.43)$ *and* $C_{d\phi} = 0.26\,(0.47)$ *the* $q\bar{q}A$ *channel becomes the dominant di-Higgs (single Higgs) production channel. The UV scale is set to* $\Lambda = 1$ *TeV.*

unitary transformation represented by the matrices $\mathcal{V}_q, \mathcal{U}_q$, like in the SM. The Wilson coefficients matrix elements in the flavour space in the mass basis can be written as

$$\tilde{C}^{ij}_{q\phi} = (\mathcal{V}_q)^*_{ni}\, C^{nm}_{q\phi}\, (\mathcal{U}_q)_{mj}\,, \quad \text{with} \quad q = u, d\,. \tag{4.3}$$

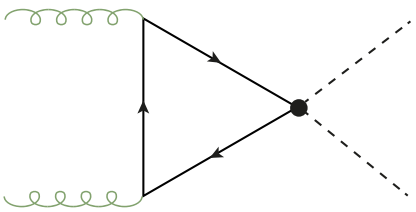

Figure 4.3. The new diagram for ggF emerging from the $hhq\bar{q}$ coupling stemming from an effective dim-6 operator.

n order to match these Wilson coefficients to Higgs couplings to quarks, we use the Lagrangian operator describing these couplings

$$\mathcal{L} \supset g_{h\bar{q}_i q_j}\bar{q}_i q_j h + g_{h\bar{q}_i q_j}\bar{q}_i q_j h^2 \tag{4.4}$$

Then the matching results in identifying the SMEFT couplings of Higgs and quarks

$$g_{h\bar{q}_i q_j} := \quad \frac{m_{q_i}}{v}\delta_{ij} - \frac{v^2}{\Lambda^2}\frac{\tilde{C}^{ij}_{q\phi}}{\sqrt{2}}, \qquad\qquad g_{hh\bar{q}_i q_j} := \quad -\frac{3}{2\sqrt{2}}\frac{v}{\Lambda^2}\tilde{C}^{ij}_{q\phi}. \tag{4.5}$$

We observe that, in the general case, we will be having non-diagonal couplings. However, such couplings are strongly constraint by flavour observables , particularly neutral meson mixing [185].

$$|\tilde{C}^{12}_{q\phi}| \lesssim 10^{-5}\Lambda^2/v^2| \qquad\qquad |\tilde{C}^{13/23}_{d\phi}| \lesssim 10^{-4}\Lambda^2/v^2 \tag{4.6}$$

Due to these strong constraints, it is typical to consider SMEFT with minimal flavour violation (MFV) [186], in which the SM Yukawa matrices y_q^{ij} are the only spurions breaking the global $SU(3)_Q \otimes SU(3)_U \otimes SU(3)_D \to U^6(1)$ flavour symmetry. This implies that the Wilson coefficients matrices in the mass basis are simultaneously diagonalisable with the SM Yukawa matrices. This make the Wilson coefficients maintain the hierarchy of the couplings seen in the SM, thus MFV is not a viable scheme when one wants to consider significant enhancements to the couplings for first and second generations, but keep the third generation couplings unchanged.

In order to bypass the constraints of MFV and yet avoid flavour changing neutral currents (FCNC) that are prohibited by flavour observables, one needs to turn to flavour alignment [187, 188] or its generalisation aligned flavour violation (AFV) [189] .

With flavour alignment, the NP flavour parameters (here the Wilson coefficients) are aligned with the SM Yukawa, such that both can be simultaneously diagonalised, hence preventing tree-level FCNCs. But unlike MFV, the constraint on making these new parameters proportional to the SM Yukawas is lifted. This would induce radiative FCNCs, as this formalism in unstable under quantum corrections [190–192]. This alignment breaking would not be seen in the SMEFT, but rather when UV-complete models are considered. AFV resolves this instability, by ensuring that any NP Spurion breaking the flavour symmetry will transform trivially under the quark phases transformations $U^6(1)$, keeping the CKM matrix as the only flavour object that has non-trivial transformations. Thereby the CKM will have physical flavour changing currents as well as a $\mathcal{CP}$-violating phase. This constraint on the NP flavour spurions k_q, allows them to be written as a series in powers of the CKM matrix, known as the alignment expansion

$$k_u = K_{0,u} + K_{1,u}V^*_{CKM}K_{2,u}V^T_{CKM}K_{3,u} + \mathcal{O}(V^4_{CKM}) + \ldots, \tag{4.7}$$

$$(k_d)^\dagger = K_{0,d} + K_{1,d}V^T_{CKM}K_{2,d}V^*_{CKM}K_{3,d} + \mathcal{O}(V^4_{CKM}) + \ldots, \tag{4.8}$$

where $K_{i,u}$ and $K_{i,d}$ are complex 3×3 diagonal matrices invariant under flavour transformations. This formalism is stable under renormalisation group evolution as any linear

combinations or tensor product of the spurions will remain flavour aligned.
For simplicity, I shall only consider the first term in the alignment expansion, such that only diagonal $C_{q\phi}$ are investigated, as the other terms are already CKM-suppressed and not of particular phenomenological interest. With this in mind, and using the translation between SMEFT and κ-formalism discussed in **??**, it is possible to identify the couplings in SMEFT with the κ's

$$g_{h\bar{q}_i q_i} = \kappa_q g^{\text{SM}}_{h\bar{q}_i q_i}\,, \qquad\qquad g_{hh\bar{q}_i q_i} = -\frac{3}{2}\frac{1-\kappa_q}{v} g^{\text{SM}}_{h\bar{q}_i q_i}\,, \tag{4.9}$$

in a slight abuse of language of the κ-framework used often in experimental analyses, as the $hhq\bar{q}$ coupling also depends on the light quarks coupling modifier κ_q.

Higgs pair production offers an extra advantage for probing light Yukawa interactions, as it is particularly sensitive to the $hhq\bar{q}$ interaction, one could also consider the non-linear HEFT, by extending it to include Wilson coefficients c_q and c_{qq} for the first and second generation quarks, in analogy to ones defined for the top quark in eq. (**??**) [193]. The analysis preformed on these HEFT parameters is published in [2].

4.2 Higgs pair production and Higgs decays with modified light Yukawa couplings

As we have briefly discussed in the introduction, the gluon fusion channel Higgs pair production is affected by enhanced light Yukawa couplings in two ways. First, the inclusion of light quark loops in the triangle and box diagrams. Second, the new diagrams introduced by the contact $hhq\bar{q}$ coupling shown in Figure 4.3. However, these effects are negligible, due to the mass-suppression of these diagrams by the light quark appearing in the loops. Therefore, effectively, one could consider the ggF channel as purely derived by third generation quarks, and only affected by the trilinear coupling C_ϕ as far as this analysis is concerned.

4.2.1 Higgs pair production via quark anti-quark annihilation

Contrary to the ggF, the $q\bar{q}$A channel does not exist in the SM, except for $b\bar{b} \to hh$, following the assumptions of 4(or 5)-flavour scheme, that the these quarks are massless. This channel contains four-diagrams shown in Figure 4.1, and its differential partonic cross-section is given by

$$\frac{d\hat{\sigma}_{q_i\bar{q}_j}}{d\hat{t}} = \frac{1}{16\pi}\frac{1}{12\hat{s}}\left[\left|2g_{hhq_i\bar{q}_j} + \frac{g_{hhh}\, g_{hq_i\bar{q}_j}}{\hat{s} - m_h^2 - i m_h \Gamma_h}\right|^2 + \mathcal{O}(g^4_{hq_i\bar{q}_j})\right], \tag{4.10}$$

where the $\mathcal{O}(g^4_{hq_i\bar{q}_j})$ terms stem from the $\hat{t}$ and $\hat{u}$ channel diagrams, and their contribution is typically only $\sim 0.1\%$ of the total cross-section. The hadronic cross section is then

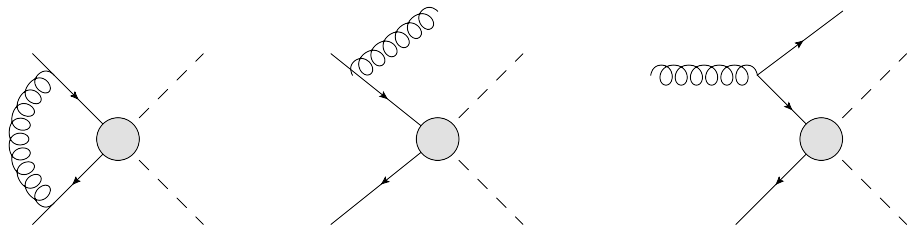

Figure 4.4. Generic form of the QCD corrections of order $\mathcal{O}(\alpha_s)$ to the $q\bar{q}$A Higgs pair production.

obtained by

$$\sigma_{\text{hadronic}} = \int_{\tau_0}^{1} d\tau \int_{\hat{t}_-}^{\hat{t}_+} d\hat{t} \sum_{i,j} \frac{d\mathcal{L}^{q_i\bar{q}_j}}{d\tau} \frac{d\hat{\sigma}_{q_i\bar{q}_j}}{d\hat{t}} \,, \tag{4.11}$$

with $\tau_0 = 4\,m_h^2/s$, $\hat{s} = \tau s$ and

$$\hat{t}_\pm = m_h^2 - \frac{\hat{s}(1 \mp \beta)}{2} \qquad \text{and} \qquad \beta = \sqrt{1 - \frac{4m_h^2}{\hat{s}}} \,. \tag{4.12}$$

The parton luminosity is given by

$$\frac{d\mathcal{L}^{q_i\bar{q}_j}}{d\tau} = \int_{\tau}^{1} \frac{dx}{x} \left[f_{q_i}(x/\tau, \mu_F^2) f_{\bar{q}_j}(x, \mu_F^2) + f_{\bar{q}_j}(x/\tau, \mu_F^2) f_{q_i}(x, \mu_F^2) \right] . \tag{4.13}$$

All the kinematic masses were neglected, in accordance with the 5-flavour scheme of the PDF's while the coupling of the Higgs boson to the light quarks (for flavour diagonal couplings) is

$$g_{hq_i\bar{q}_j} = \frac{m_q^{\overline{MS}}(\mu_R)}{v} \kappa_q \delta_{ij} \,, \tag{4.14}$$

and analogously for the $g_{hhq_i\bar{q}_j}$ coupling. It is worth noting that there is no inconsistency with such an assumption since in scenarios of modified Yukawa couplings, the masses of the quarks need not to be generated by electroweak symmetry breaking.

NLO QCD correction

Since the ggF NLO QCD corrections are sizeable, it is reasonable to assume that the same would apply to the $q\bar{q}$A. Computing the NLO QCD corrections to this channel is a relatively straight-forward task, as they are only one-loop. More simplifications can be made by neglecting the NLO corrections of the $\hat{t}$ and $\hat{u}$ channels because they are strongly suppressed. This enables us to use the NLO QCD corrections results from $b\bar{b} \to h$ in the 5-flavour scheme [194–196][1] by some adjustments taking into account the modified LO cross section and the different kinematics of the process. The Feynman diagrams at NLO QCD are shown in fig. 4.4. For convenience and in order to make our

[1] Note that the NLO and NNLO QCD corrections for $b\bar{b}hh$ have been given in [197, 198].

adjustments explicit we report here the formulae from [199]

$$\sigma(q\bar{q} \to h) = \sigma_{LO} + \Delta\sigma_{q\bar{q}} + \Delta\sigma_{qg} \tag{4.15a}$$

$$\Delta\sigma_{q\bar{q}} = \frac{\alpha_s(\mu_R)}{\pi} \int_{\tau_0}^1 d\tau \sum_q \frac{d\mathcal{L}^{q\bar{q}}}{d\tau} \int_\tau^1 dz\ \hat{\sigma}_{LO}(Q^2 = z\tau s)\ \omega_{q\bar{q}}(z) \tag{4.15b}$$

$$\Delta\sigma_{qg} = \frac{\alpha_s(\mu_R)}{\pi} \int_{\tau_0}^1 d\tau \sum_{q,\bar{q}} \frac{d\mathcal{L}^{qg}}{d\tau} \int_\tau^1 dz\ \hat{\sigma}_{LO}(Q^2 = z\tau s)\ \omega_{qg}(z) \tag{4.15c}$$

and

$$\hat{\sigma}_{LO}(Q^2) = \int_{\hat{t}_-}^{\hat{t}_+} \frac{d\hat{\sigma}_{q_i\bar{q}_j}}{d\hat{t}} \tag{4.16}$$

with $z = \tau_0/\tau$, $\sigma_{LO} = \sigma_{\text{hadronic}}$ of eq. (4.11), and the ω factors are given by

$$\omega_{q\bar{q}}(z) = -P_{qq}(z) \ln\frac{\mu_F^2}{\tau s} + \frac{4}{3}\left\{\left(2\zeta_2 - 1 + \frac{3}{2}\ln\frac{\mu_R^2}{M_{hh}^2}\right)\delta(1-z)\right. \tag{4.17a}$$
$$\left. + (1+z^2)\left[2\mathcal{D}_1(z) - \frac{\ln z}{1-z}\right] + 1 - z\right\},$$

$$\omega_{qg}(z) = -\frac{1}{2}P_{qg}(z)\ln\left(\frac{\mu_F^2}{(1-z)^2\tau s}\right) - \frac{1}{8}(1-z)(3-7z), \tag{4.17b}$$

with $\zeta_2 = \frac{\pi^2}{6}$. The Altarelli Parisi splitting functions $P_{qq}(z)$ and $P_{qg}(z)$ [200–202] are given by

$$P_{qq}(z) = \frac{4}{3}\left[2\mathcal{D}_0(z) - 1 - z + \frac{3}{2}\delta(1-z)\right], \tag{4.18a}$$

$$P_{qg} = \frac{1}{2}\left[z^2 + (1-z)^2\right], \tag{4.18b}$$

and the 'plus' distribution is

$$\mathcal{D}_n(z) := \left(\frac{\ln(1-z)^n}{1-z}\right)_+. \tag{4.19}$$

The renormalisation scale $\mu_R = M_{hh}$ and the factorisation scale $\mu_F = M_{hh}/4$, were chosen as central values.
The NLO $q\bar{q}$A cross-section as well as the LO ggF were implemented in a private FORTRAN code utilising the `VEGAS` integration algorithm, and NNPDF30 parton distribution functions (PDF's)[203] implemented via the `LHAPDF-6` package [204]. For the one-loop integrals appearing in the form factors of the box and triangle diagrams, we have used the COLLIER library [205] to ensure numerical stability of the loop integral calculation

for massless quarks inside the loops [2]. The resulting NLO K-factor was found to be

$$K_{NLO} = \frac{\sigma_{NLO}}{\sigma_{LO}} = 1.28 \pm 0.02\,, \tag{4.20}$$

with the error denoting the theoretical uncertainty. The K-factor does not depend on the scaling of the couplings, nor the flavour of the initial $q\bar{q}$ since the LO cross section factors out (with exception of the different integration in the real contributions).
The $q\bar{q}$A channel will enhance the overall Higgs pair production cross-section, but if one considers the ggF as a SM background for the Yukawa enhancement "signal" $q\bar{q}$A channel, it would be interesting to estimate qualitatively when this signal becomes dominant. This estimates how sensitive is Higgs pair to enhanced light Yukawa couplings as **??** demonstrates. The dominant term for $q\bar{q}$A comes from the $hhq\bar{q}$ vertex diagram, such that the $q\bar{q}$A cross-section behaves for large values of κ as (assuming that $\sigma_{SM}^{qqA} \sim 0$)

$$(\sigma^{qqA} - \sigma_{SM}^{qqA}) \sim g^2_{hhq\bar{q}} \sim v^{-4}\, m_q^2\, \kappa_q^2. \tag{4.21}$$

The ggF cross-section instead gets contributions from light quark loops interfering with top quark loops in the triangle SM diagram, leading to a scaling of

$$(\sigma^{ggF} - \sigma_{SM}^{ggF}) \sim \kappa_q\, \frac{m_q^2}{v^2\, M_{hh}^2}\, \ln^2\left(\frac{M_{hh}}{m_q}\right). \tag{4.22}$$

Taking the ratio we get

$$\frac{(\sigma^{qqA} - \sigma_{SM}^{qqA})}{(\sigma^{ggF} - \sigma_{SM}^{ggF})} \sim \frac{\kappa_q}{v^2\left(\frac{\ln^2\left(\frac{M_{hh}}{m_q}\right)}{M_{hh}^2}\right)}. \tag{4.23}$$

This ratio approaches one (neglecting effects from different PDFs) when

$$\kappa_q^{qqA=ggF} \sim \frac{v^2\, \ln^2\left(\frac{M_{hh}}{m_q}\right)}{M_{hh}^2}\,. \tag{4.24}$$

Using this order of magnitude estimate, we see that the two cross sections are roughly equal if $\kappa_c^{qqA=ggF} \sim 1$, $\kappa_s^{qqA=ggF} \sim 10$ and $\kappa_u^{qqA=ggF} \sim \kappa_d^{qqA=ggF} \sim 10^3$. The actual values of $\kappa_q^{qqA=ggF}$ for the first generation quarks can be read from fig. **??**.It is interesting to point out to the pact that these κ_q values are not yet excluded.

4.2.2 Higgs decays

The same way hh production squires additional channels due to enhanced Yukawa couplings, also Higgs decays to light quarks will become significant compared to the SM

[2] I have expanded code to include other SMEFT operators, and it can be found in the `GitHub` repository `https://github.com/alasfar-lina/HH_XS_in_SMEFT`

case with Higgs decays to first generation BR'S being $< \mathcal{O}(10^{-9})$ [149]. In addition to the contribution of light quarks in the loop-level decays $h \to \gamma\gamma/Z\gamma$ and $h \to gg$, though this effect is small. Since the $h \to q\bar{q}$ decay are near impossible to detect with the current technologies, the effect of opening these decay channels is reduction in the branching ratios of the Higgs final states that are typically sought after, like $h \to b\bar{b}$ and $h \to \gamma\gamma$.
In order to compute the Higgs partial widths and branching ratios (BR) at higher orders in QCD, I have modified the FORTRAN programme `HDECAY` [206, 207] to include the light fermion decay channels and loops in the above-mentioned decays [3]. The overall change of the Higgs total width is given by

$$\Gamma_H \approx \Gamma_{\text{SM}} + \sum_{q=c,s,u,d} \frac{g^2_{h\bar{q}_i q_i}}{(g^{\text{SM}}_{h\bar{q}_i q_i})^2} \Gamma_q \,, \tag{4.25}$$

where Γ_q can be obtained at NLO QCD from the modified `HDECAY` code. Detailed results for the Branching ratios for the final states of interest have been published in [2]. In order to have a preliminary estimate about the sensitivity of Higgs pair production to light Yukawa enhancements, it is important to consider both production and decay effects in terms of signal strength

$$\mu_i := \frac{\sigma \, \text{BR}_i}{\sigma^{\text{SM}} \, \text{BR}_i^{\text{SM}}}. \tag{4.26}$$

Comparing the production of single Higgs vs. Higgs pair signal strengths, for any final state of interest, we could see in Figure 4.5 that for first generation $C_{q\phi} \lesssim 0.8$ Higgs pair production has a higher signal strength than single-Higgs production despite having double the reduction in the signal strength from the decays of two Higgs bosons as opposed to a single one. In fact, and as we shall see in section 4.7, values of $C_{q\phi} > 0.4$ have been already excluded by multiple searches.

4.3 Event generation for the final state $hh \to b\bar{b}\gamma\gamma$

For this study, the final state $b\bar{b}\gamma\gamma$ is considered, as this channel has the most potential for Higgs pair searches [28]. It has the "clean" $h \to \gamma\gamma$ decay, but also the other Higgs decay to b-quark pair is a channel with large branching ratio $\sim 58\%$ and b-tagging capabilities for ATLAS and CMS are continuously improving.

For the cut-based analysis, the FORTRAN codes used to compute the hh cross-section and decay have been interfaced with `Pythia` 6.4 [208], where the $q\bar{q}$A process was generated at NLO and the ggF at NLO, then multiplied with the NLO k-factor. The generated events were written to a ROOT file via `RootTuple` tool [209] for further

[3] The modified `HDECAY` code can be found in the `GitHub` repository `https://github.com/alasfar-lina/hdecay_lightflavour`

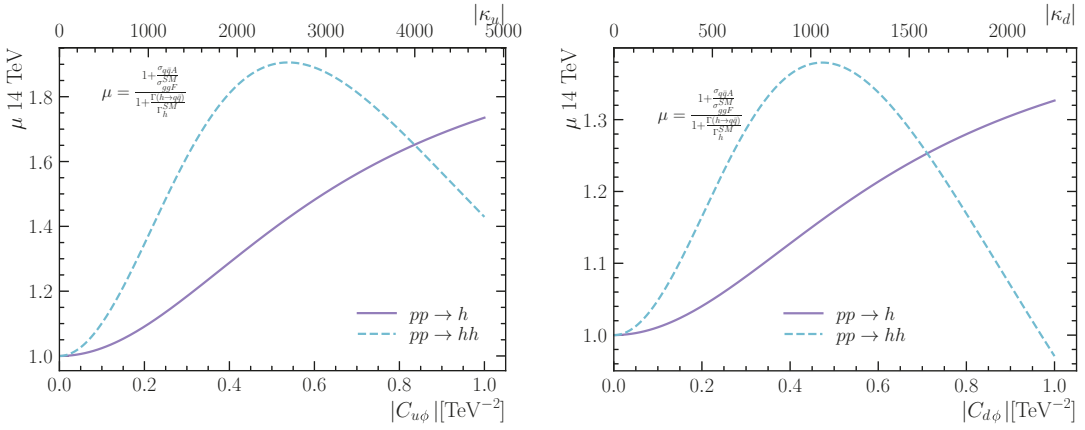

Figure 4.5. Signal strength at 14 TeV LHC, of the single Higgs (purple solid line) vs. Higgs pair (blue dashed line) as functions of $C_{u\phi}$ (left) and $C_{d\phi}$ (right). Both plots show that for $C_{q\phi} \lesssim 0.8$ the signal strength of Higgs pair production is higher than the single Higgs one. This implies that Higgs pair production is more sensitive to enhancements of light quark Yukawa in SMEFT. This is independent of the final state (except for $h \to q\bar{q}$).

analysis.
The backgrounds were not simulated for this analysis, rather, the results from [169] were used, because we have used the same cuts as this reference.

For the improved analysis which is based on interpretable BDT, the backgrounds and signal events needed to be generated. The backgrounds described in Table 3.3 were generated using `MadGraph_aMC@NLO` [61], then showered via `Pythia 8.3` [210] and a detector simulation is done using `Delphes 3` [211], the QED/QCD background $b\bar{b}\gamma\gamma$, Zh and $b\bar{b}h$ events were taken from the analysis data of Ref. [212], while $t\bar{t}h$ events were generated specifically for this analysis.In order to obtain the NLO cross-section for these process, the events were multiplied by their respective K-factors that have been obtained from $t\bar{t}h$ [213], $b\bar{b}\gamma\gamma$ [214], Zh [215] and the remaining part of the $b\bar{b}h$ processes from [216].
The Higgs pair signals were generated in a slightly different pipeline, the ggF channel events were simulated first using `POWHEG` [139–141], which has been modified to separate the individual contributions from the box, triangle and their interference individually. This is done in order to easily scale by κ_λ (or C_ϕ), as the box does not depend on it, while the triangle and the interference have quadratic and linear dependence on the trilinear coupling, respectively. The $q\bar{q}$A channel events were generated via `MadGraph_aMC@NLO` using a UFO model created with `FeynRules` [78]. Samples for both up- and down-quark initiated $q\bar{q}$A processes have been generated. Parton showering and fast detector simulation for both Higgs pair processes were run thorough the same pipeline as the backgrounds, this also goes for the scaling by the NLO of $q\bar{q}$A and NNLO for ggF K-factors after the event generation. The Higgs bosons were decayed with the assumption of narrow width approximation, and the BR values were computed in the modified

Channel	LO σ [fb]	K-fact.	Order	$6\,\text{ab}^{-1}$ [#evt @ order]
$hh^{gg\text{F}}_{\text{tri}}$	$7.288 \cdot 10^{-3}$	2.28	NNLO	96
$hh^{gg\text{F}}_{\text{box}}$	0.054	1.98		680
$hh^{gg\text{F}}_{\text{int}}$	-0.036	2.15		-460
$u\bar{u}\text{A}$ $(C_{d\phi} = 0.1)$	2.753	1.29	NLO	28
$d\bar{d}\text{A}$ $(C_{u\phi} = 0.1)$	4.270	1.30		43

Table 4.1. The LO cross-section for Higgs pair production processes (including the decay $hh \to b\bar{b}\gamma\gamma$) for $6\,\text{ab}^{-1}$ 14 TeV HL-LHC.

`HDECAY` code.
To be inclusive and to explore the capabilities and importance of the full detector coverage, no generator-level cuts were applied on these processes except for the $b\bar{b}\gamma\gamma$ processes to avoid divergences. These minimal generator-level cuts for $b\bar{b}\gamma\gamma$ are

$$\text{generator level cuts:} \quad \begin{aligned} & Xp_T^b > 20 \text{ GeV}, \\ & \eta_\gamma < 4.2,\ \Delta R_{b\gamma} > 0.2, \\ & 100 < m_{\gamma\gamma}\,(\text{GeV}) < 150. \end{aligned} \tag{4.27}$$

Here Xp_T implies a minimum p_T cut for at least one b-jet. After the showering and detector simulation, further basic selection cuts were applied to select events with

$$\text{basic cuts:} \quad \begin{aligned} & n_{\text{eff}}^{bjet} \geq 1,\ n_{eff}^{\gamma jet} \geq 2, \\ & p_T^{bjet} > 30 \text{ GeV},\ p_T^{\gamma jet} > 5 \text{ GeV}, \\ & \eta_{bjet,\gamma jet} < 4,\ 110 \text{ GeV} < m_{\gamma_1\gamma_2} < 140 \text{ GeV}, \end{aligned} \tag{4.28}$$

and $n_{eff}^{b/\gamma jet}$ representing the number of b/γ-jets that pass the basic selection. The cross-section, K-factors, number of events with 6ab^{-1} luminosity at 14 TeV are given in Table 3.3 for the background and in Table 4.1 for the Higgs pair signals. Both analysis methods included sensitivity analysis for the HL-LHC, i.e. 14 TeV and $6\,\text{ab}^{-1}$ [4] luminosity and projections for a future hadron circular collider (FCC-hh), with 100 TeV and the luminosity of 30 ab^{-1} has been done for the ML based analysis, the results for the FCC can be foun in the **??**

4.4 Cut-based analysis

A cut and count analysis has been preformed mainly as a "proof of concept", in order to demonstrate the sensitivity of Higgs pair production for probing light quark Yukawa couplings. The analysis used the same cuts and m_{hh} binning as ref. [169] such that their

[4] In the published cut-based analysis [2] $3\,\text{ab}^{-1}$ luminosity for the HL-LHC was used. However, here I used $6\,\text{ab}^{-1}$ when reporting fit results

background events counts can be used.

4.4.1 Analysis strategy

In order to derive sensitivity bounds, the number of expected background N_b and signal N_s events needs to be estimated from simulated events. Since N_b is taken from [169], the task is to estimate N_s for the $q\bar{q}$A process as a function of $C_{q\phi}$, and to reproduce N_s of the ggF SM process published in the reference as a cross-check.
Since the cross-section, branching fraction and the integrated luminosity, it is only needed to estimate the selection efficiency ϵ_{SEL} from the applied cuts appearing in eq (**??**) to obtain the number of signal events.
The basic cuts of trigger-level selection are jets and photons with minimal p_T and maximal η.

$$p_T(\gamma/j) > 25\,\text{GeV}\,, \quad |\eta(\gamma/j)| < 2.5\,. \tag{4.29}$$

Additionally, a veto on the events with hard leptons is applied

$$p_T(\ell) > 20\,\text{GeV}, \quad |\eta(\ell)| < 2.5\,, \tag{4.30}$$

Jets were clustered using `fastjet` [217] with the anti-kt algorithm with a radius parameter of $R = 0.5$.
The b-tagging efficiency of $\epsilon_b = 0.7$, as well as the photon identification efficiency $\epsilon_\gamma = 0.8$ have been simulated, in accordance with the ATLAS and CMS performance [218–220, 220, 221]. The selection cuts we used are the same ones as in [169], starting with the cuts of the transverse momentum p_T of the photons and b-tagged jets. The two hardest photons/b-tagged jets, with transverse momentum $p_{T>}$, and the softer ones with $p_{T<}$ are selected to satisfy

$$p_{T>}(b/\gamma) > 50\,\text{GeV}, \quad \text{and} \quad p_{T<}(b/\gamma) > 30\,\text{GeV}\,. \tag{4.31}$$

In order to ensure well-separation of the photons and b-jets, we require the following cuts on the jet radius,

$$\Delta R(b,b) < 2, \quad \Delta R(\gamma,\gamma) < 2, \quad \Delta R(b,\gamma) > 1.5\,. \tag{4.32}$$

The mass windows used used are about three times the photon resolution of ATLAS and CMS [220, 221], such wide windows were used in order to avoid significant signal loss.

$$105\,\text{GeV} < m_{b\bar{b}} < 145\,\text{GeV}, \quad 123\,\text{GeV} < m_{\gamma\gamma} < 130\,\text{GeV}\,. \tag{4.33}$$

The selection cuts are summarised in table Table 4.2 with their corresponding efficiency. The total selection efficiency for the ggF channel was found to be $\epsilon_{ggF} = 0.044$, consistent with the results of [169], while the $q\bar{q}$A channel efficiency is slightly higher $\epsilon_{qq} = 0.05 \pm 0.001$ for the up and down quark initiated $q\bar{q}$A, results for second generation quarks can be found in [2].

cut	ϵ_{cut}	$\delta\epsilon_{\text{cut}}$
Trigger-level in eq. (4.29) and (4.30)	0.71	0.04
p_T cuts in eq. (4.31)	0.35	0.07
ΔR cuts in eq. (4.32)	0.69	0.21
total	0.11	0.06

Table 4.2. The cuts used in the analysis with their efficiency ϵ_{cut} and uncertainties on these efficiencies $\delta\epsilon_{\text{cut}} = \sqrt{\epsilon(1-\epsilon)\,N}$, where N is the total number of events. The analysis was performed on 100K SM simulated events. This table is published in [2].

4.4.2 Statistical analysis

The likelihood ratio test statistic q_μ was used in order to estimate the HL-LHC sensitivity, and set projected limits on the SMEFT Wilson coefficients $C_{q\phi}$, with and without the modifier of the trilinear coupling C_ϕ. Additionally to the HEFT parameters c_q and c_{qq}. The likelihood function was constructed from the signal and background events in each bin of the m_{hh} distribution described in [169]

$$-\ln \mathscr{L}(\mu) = \sum_{i\in\text{bins}} (N_{bi} + \mu\, N_{si}) - n_i \,\ln(N_{bi} + \mu\, N_{si}), \tag{4.34}$$

with N_{bi} and N_{si} being the number of background and signal events in the ith m_{hh} distribution, respectively. In order to include the theoretical uncertainties on the expected number of signal events, the above likelihood was extended by a Gaussian distribution for N_{si} in which the mean equals to the central value of the bin values and standard deviation σ equals to its theoretical uncertainty. The signal strength μ was then estimated by minimising $-\ln \mathscr{L}(\mu)$ to obtain the estimator for $\hat{\mu}$ by injecting SM signal + background events n_i. The test statistic is then given by

$$q_\mu = 2(\ln \mathscr{L}(\mu) - \ln \mathscr{L}(\hat{\mu})), \tag{4.35}$$

following the procedure described in [222], and using the Python package `pyhf` [223, 224]. The expected 6 ab^{-1}HL-LHC sensitivity for the signal strength at 95% (68 %) CL is found to be $\mu = 1.5(1.1)$.

4.5 Optimised search for Higgs pair via Interpretable machine learning

When dealing with a multi-variate problem, such as the separation of the Higgs pair signal from its backgrounds, the use of "simple" cuts is not the most efficient method for accomplishing this task. This is mainly due to the fact that in multivariate analysis, the various features used in the classification correlate with each other. This is not captured with the cut and count method. With boasted decision tree (BDT) classifier,

it is possible to capture these correlations and introduce highly non-trivial cuts .

4.5.1 Constructing features

The simulated events of the signal and background described in the event selection section are required to contain at least two reconstructed photons and at a b-tagged jet. From these events, the following high-level features were constructed

- $p_T^{b_1}$, $p_T^{b_2}$, $p_T^{\gamma_1}$, $p_T^{\gamma\gamma}$,
- $\eta_{b_{j1}}$, $\eta_{b_{j2}}$, η_{γ_1}, $\eta_{\gamma\gamma}$,
- n_{bjet}, n_{jet}, $\Delta R^{b\gamma}_{\text{min}}$, $\Delta\varphi^{bb}_{\text{min}}$,
- $m_{\gamma\gamma}$, m_{bb}, $m_{b_1 h}$, $m_{b\bar{b}h}$, H_T.

$p_T^{b/\gamma_{1,2}}$ and $\eta^{b/\gamma_{1,2}}$ are the p_T and pseudorapidity for the tagged leading and sub-leading b/γ-jets (in our definition the subleading b-jet could be a null four-vector since we require one b-jet inclusive), n_{bj} is the number of tagged and passed b-jets. $\Delta R^{b\gamma}_{\text{min}}$ and $\Delta\varphi^{bb}_{\text{min}}$ are the minimum R-distance and φ-angle between a tagged b-jet and a photon jet. The remaining variables are the invariant masses and H_T is the scalar sum of the transverse mass of the system.
These features are the same as the ones studied in ref.. [212] for $b\bar{b}h$. However, they are, by no means, unique. It is possible to run the analysis with another set of features and obtain the same results, as long as these features are independent and highly correlated. Figure 4.6 shows the distributions four most important features from this list, the $m_{\gamma\gamma}$ is very important in distinguishing the large $b\bar{b}\gamma\gamma$ background from the signal and $t\bar{t}h$ (or other background that contain $h \to \gamma\gamma$). While the rest, particularly H_T distinguishes the different hh channels and also hh from other Higgs channels backgrounds.

4.5.2 Exploratory network analysis

The aim of this analysis is to explore how the kinematic variables constructed in the previous section are related to each other. Moreover, we are interested in examining their variation from channel to channel. This can be achieved by calculating the intra-feature correlations stratified according to the signal channels (ggF, $u\bar{u}$A, ddA) and background. Then draw them as network diagrams that can be seen in (a) of Figure 4.7. The Pearson's correlation networks show some differences amongst the different signal strata.[5]. These differences can be further investigated by a post-hoc hypothesis test, based on a linear mixed effects model for each pair of the features X_i, X_j stratified according to the processes (ggF, $u\bar{u}$A, $d\bar{d}$A and background) S_k, given as follows

$$X_i = \beta_{ij} X_j + \beta_k S_k + \beta_0, \tag{4.36}$$

[5] for network plots of the backgrounds see [212]

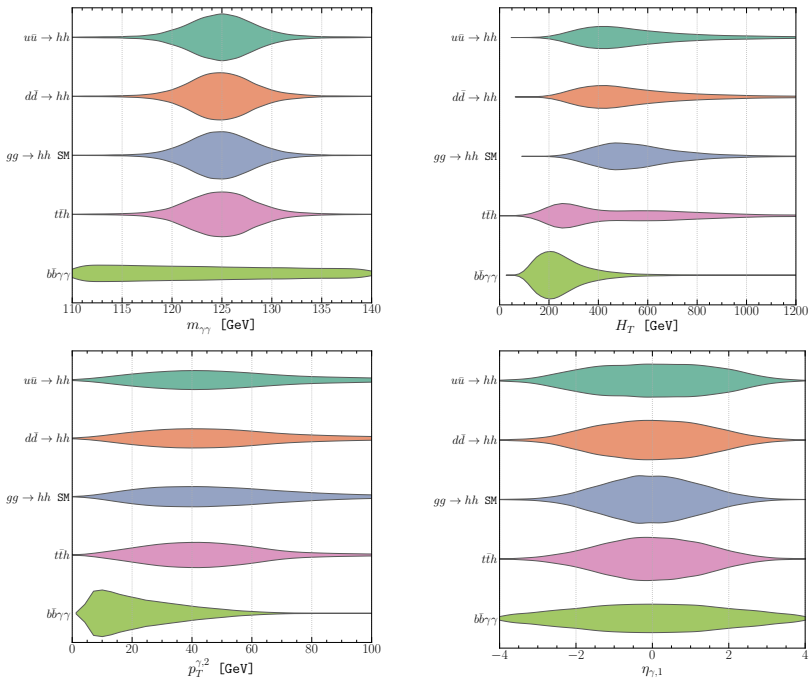

Figure 4.6. violin plots of the most significant features used by the BDT classifier for the signal channels, and the two most significant backgrounds $b\bar{b}\gamma\gamma$.

where β_{ij}, β_k and β_0 are the constants for the fit . The hypothesis test is therefore preformed by taking the ratio of log likelihood for the linear model of eq. (4.36), defined as

$$t = \frac{\mathscr{L}(\beta_{ij}, \beta_k, \beta_0)}{\mathscr{L}(\beta_{ij}, \beta_k = 0, \beta_0)}. \tag{4.37}$$

This analysis of variation (ANOVA) yields a p-value for each feature pair, these p-values are false discovery rate (FDR)-corrected, and the correlation difference amongst the strata is considered significant if the FDR-corrected p-values pass the threshold $p < 0.001$ or $p > 0.01$ when comparing $u\bar{u}$A against $d\bar{d}$A [6]. The result of these comparisons can be seen in sub-figures (b). We can see that many of the features do not have significant variation across the strata.This indicates that these features are not important in the separation of the signal from the background. The most significant variation is between the ggF (equivalently $q\bar{q}$A) and the background. While for the $q\bar{q}$A channels, the correlation patters are almost identical except for the correlation between the observables related to the PDF's, which is expected since the only kinematic difference between the up- and down- initiated $q\bar{q}$A emerges from the PDF's of the up and down quarks.

[6] The threshold for this comparison is related due to the high degree of similarity between the two channels.

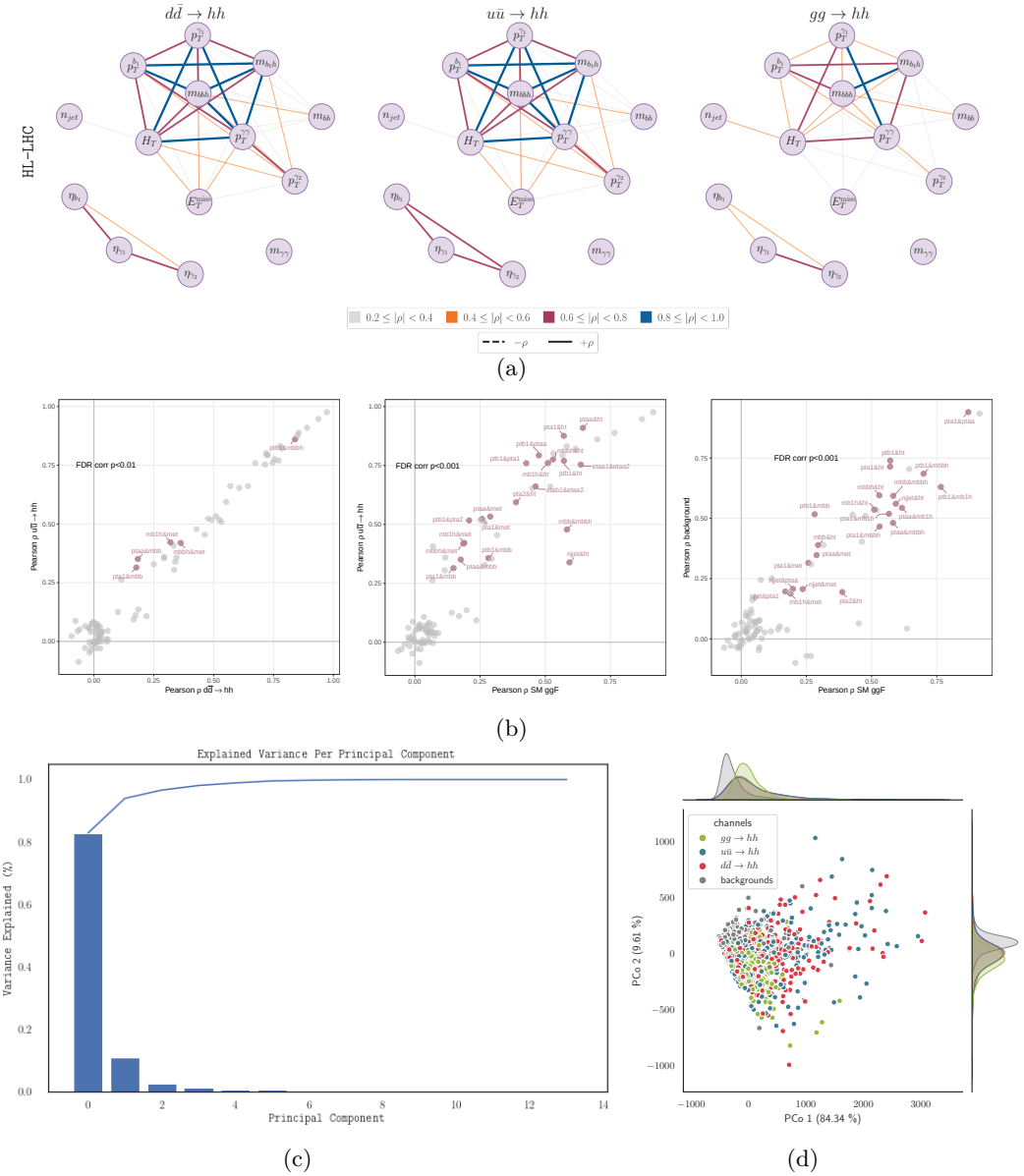

Figure 4.7. (a) Network diagrams of the signal channels of their Pearson correlation ρ between the features, showing slightly different patterns of correlation amongst these channels. (b) The same Pearson correlations of figure (a) plotted against each other for the different signals, with the colouring indicating whether the difference between the correlation passes the hypothesis testing (ANOVA) passes the threshold FDR-corrected p-value indicated at each figure. (c) Scree plot of the Principal-component clustering (PCo) of the the signal channels and the backgrounds, almost full variance coverage is obtained by the first four PCo's .(d) The clustering in the first two PCo's, one can see that even with unsupervised clustering the di-Higgs signals have a significantly different distribution than the background. However, it is hard to see an marked clustering for the different signal channels.

This network analysis allows for better understanding of the feature set at hand. When considering that many intra-feature correlations do not vary much across the channels as seen in (b) of Figure 4.7 and the features themselves cluster into four groups according to their correlations, it is tempting to further reduce the dimensionality of the feature space by preforming an unsupervised clustering via Principle Component analysis (PCoA). Panel (c) in Figure 4.7 contains a scree plot showing that the variance explained by the first few PCo's is very high, thus reducing the dimensionality of our feature space significantly. When the first two PCo's are plotted (d), the clustering of signal and the background channels can be seen. The distinction between the signals vs. backgrounds is visible, but less marked between the signal channel themselves, in particular $u\overline{u}$A against $d\overline{d}$A . The first PCo contains, from highest weight to lowest, $m_{\gamma\gamma}, H_T, n_{jet}, m_{bb}$ and $p_T^{\gamma_1}$. The rest of the of features have a negligible weight.
It is not surprising to see these feature contribute the most in the clustering of events given how they are distributed as we have seen in Figure 4.6. In the next step of the analysis we will see then appear once more.

4.5.3 Classification analysis

The unsupervised clustering and network analysis merely offers a method to explore how the Higgs pair signal is different from the backgrounds. It is useful to reduce the dimensionality of the feature space and offer "hints" on which subset of features has the highest discriminant power. However, for analysis of the sensitivity and full resolution of the signal against backgrounds, the gold standard is rule-based machine learning. The use of BDT's and random forests in particle physics analysis has been explored since early LHC era, nowadays it became widespread, their popularity becomes evident when one examines the literature-review of this thesis for instance. Many of the recent Higgs experimental analyses were preformed using some rule-based ML algorithm. [7]
In this analysis, the EXtreme gradient BDT (XGBoost), with its Python implementation [225], has been used as the classifier algorithm. The standard procedure for training and testing the classifier was followed, starting with the complete list of features listed in subsection 4.5.1 and then the most important features were shortlisted to improve the efficiency and performance of the classifier. This was possible due to the introduction of interpretability to the ML analysis, which provided variable importance measures, by which features with low importance index can be removed.
Interpretability is achieved by incorporating a mathematically robust measure from game theory known as **Shapley values** [226]. This measure formulate an axiomatic prescription for fairly distributing the payoff of a game amongst the players in a n-player cooperative game. When applied to ML, Shapley values estimate the significance of the features used in the classification. The process naturally and mathematically lends itself to examining the correlations amongst the features used in the classification, since all possible combinations of variables can be taken out of the game to check the outcome.

[7] Rule-based ML algorithms outperform deep neural networks (DNN) in terms of simplicity of implementation and computational requirements. In addition, rule-based algorithms, such as decision trees, are more transparent as far as the signal vs. background separation is concerned

Actual no. of events	Predicted no. of events at HL-LHC					
Channel	hh_{tri}^{ggF}	hh_{tri}^{ggF}	hh_{box}^{ggF}	$Q\overline{Q}h$	$b\bar{b}\gamma\gamma$	total
hh_{tri}^{ggF}	28	14	18	38	10	108
hh_{int}^{ggF}	89	80	129	178	41	517
hh_{box}^{ggF}	77	105	266	265	50	763
$Q\overline{Q}h$	177	98	191	5,457	1,835	7,758
$b\bar{b}\gamma\gamma$	1,743	845	1,074	30,849	287,280	321,791

Table 4.3. The confusion matrix output of the trained BDT five-channel classifier. The separation between the ggF topologies allows for setting constraints on C_ϕ. The number of events shown are for the HL-LHC at 14 TeV and integrated luminosity of 6 ab^{-1}, assuming the SM signal.

Further information regarding the application of Shapley values in particle physics analysis can be found in refs. [212, 227, 228]. For Higgs pair production study presented here, the same procedure described in [212] was followed, The importance of a variable in determining the outcome of a classification will be quantified by the mean of the absolute Shapley value, $\overline{|S_v|}$, larger values signifying higher importance. The SHAP (SHapley Additive exPlanations) [229] package implemented in Python was used. This package computes the feature importance using Shapley values calculated exactly from tree-explainers [230, 231].

Classifier output

The trained BDT's outputs are extracted in terms of confusion matrices, with number of events as entries. The diagonal elements of these matrices represent the true positive (TP) identification of the signal and true negative (TN) rejection of the background, while the upper triangular part represents the signal loss, or false negative counts (FN) . Finally the lower triangular part shows the remaining background contamination of the signal, or the false positive counts (FP). Using these counts it is possible to estimate the accuracy score ACC of the classifiers

$$ACC = \frac{TP + TN}{TP + TN + FP + FN} \approx 0.7, \tag{4.38}$$

And the sensitivity $TP/P \approx 0.2$, which corresponds to the ϵ_{SEL} of the cut-based analysis. Here we see that the ML- based analysis yielded a four- to five-fold increase in ϵ_{SEL} compared to the cut and count method. Table 4.3 shows one of these matrices from the classification of the ggF SM signal separated into the topologies according to their dependence on C_ϕ. For up- and down-quark $q\bar{q}$A, the same matrices were constructed, and sense the number of events for these processes scale with $C_{q\phi}^2$ it is only required to produce one matrices for each classification procedure, like the case of the ggF channel. For the fitting procedure, a Bayesian framework based on an MCMC method was used, analogous to the procedure described in section 2.2
The full analysis code, including the BDT training and fits as well as the confusion ma-

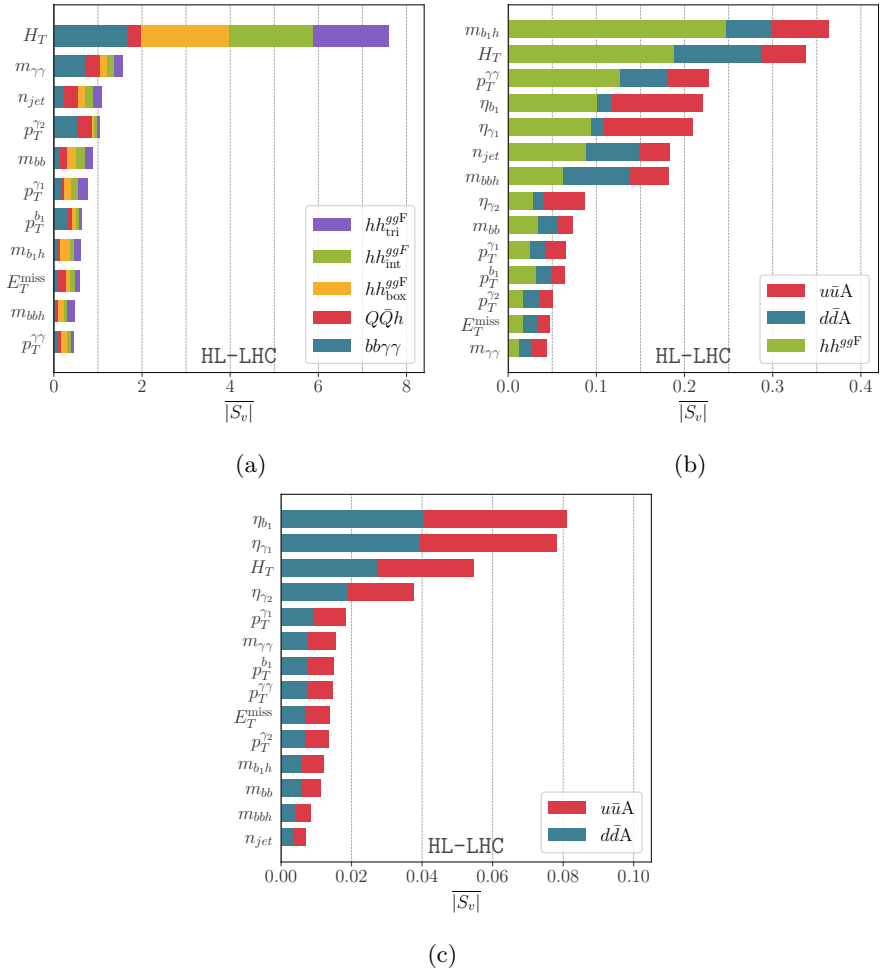

Figure 4.8. The feature importance output in terms of $\overline{|S_v|}$. The higher the value of $\overline{|S_v|}$, the more important the kinematic variable is in separating the different channels : (a) The hierarchy of variables important for the separation of hh^{ggF}_{tri} from hh^{ggF}_{int} events from hh^{ggF}_{box}, $Q\overline{Q}h$ and $b\bar{b}\gamma\gamma$ QCD-QED background (b) The hierarchy of variables important for the separation of hh^{ggF}, $u\bar{u}$A and $d\bar{d}$A events. (c) The hierarchy of variables important for the separation of $u\bar{u}$A from $d\bar{d}$A events.

trices for the classification procedures preformed can be found in the `Github` repository: https://github.com/talismanbrandi/IML-diHiggs.git.

Feature importance and Shapley values

Another output of the interpretable BDT is the SHAP scores for the features used in the classification. The $\overline{|S_v|}$ values are used to order the features used for the classification. The most important features in different classifiers used in this analysis is seen in Figure 4.8. Panel (a) shows the hierarchy of the features used for the separation of the SM ggF signal from the backgrounds, the same features that showed the most

significant change in the network analysis and unsupervised clustering appear in the top of the list. However, the BDT was able to distinguish between the the different signals, a task the unsupervised clustering was unable to fulfil. Figure (b) shows the list of feature importance for the ggF vs $q\bar{q}$A classification, while (c) demonstrates the full strength of the BDT in distinguishing $u\bar{u}$A from $d\bar{d}$A despite having very little variation of their kinematic distributions. As expected, $u\bar{u}$A vs $d\bar{d}$A classification, the features appeared on top of the list, are related to the different PDF's but their ranking was unintuitive because this classification is a truly a multivariate problem, where the intra-variable correlations and differences have been fully extorted.

4.6 Fit results

The fit from the cut-bases analysis was originally made for $3\,\text{ab}^{-1}$ and published in [2], but for a better comparison with the optimised multi-variate analysis the fit for this thesis was carried out again for $6\,\text{ab}^{-1}$, and with SMEFT Wilson coefficient parametrisation. Thus harmonising it with the results of the rest of the thesis. The fits were done in the $C_\phi - C_{q\phi}$ plane shown the top plots of Figure 4.9. As well as the $C_{u\phi} - C_{d\phi}$ one in the low panel of the same figure. We see that even with the traditional technique, two-parameter fits were possible. However, the bounds obtained on the trilinear self-coupling modifier are weaker than the projected bounds for the HL-LHC, made by ATLAS and CMS [107, 115, 232], which is expected due to the dilution of these bounds by adding Light Yukawa coupling modifiers and the loss of some signal due to the analysis technique. For the $C_{u\phi} - C_{d\phi}$ combined fit, no correlation between the two parameters is seen.
To demonstrate the power of multi-variate (MV) analysis, we compare the fit results from single parameter fits of this analysis to the cut-and count technique (CC) for both up and down quark coupling modifiers at 68% CL/CI

$$\begin{aligned} C_{u\phi}^{MV}\left(\kappa_u^{MV}\right) = [-0.09, 0.10]\ ([-466, 454]), \quad C_{u\phi}^{CC}(\kappa_u^{CC}) = [-0.18, 0.17]\ ([-841, 820]), \\ C_{d\phi}^{MV}(\kappa_d^{MV}) = [-0.16, 0.16]\ ([-360, 360]), \quad C_{d\phi}^{CC}(\kappa_d^{CC}) = [-0.18, 0.18]\ ([-405, 405]). \end{aligned} \tag{4.39}$$

A significant improvement of the bounds from using MV analysis over CC one of two-fold for $C_{u\phi}$, but a mild one for $C_{d\phi}$ with $\mathcal{O}(10\%)$ improvement.

In order to compare the ML multi-variate analysis used to other sensitivity projections, the projections on the trilinear coupling modifier C_ϕ are shown in Figure 4.10. These bounds are obtained by using the we pe BDT classification showcased in Table 4.3. These bounds are similar or slightly better than the results quoted by the experimental sensitivity analysis quoted before. This was achieved by optimising the BDT with spearating the signal and background channels, as well as the exclusion of less-important features. The projected 1σ bound on C_ϕ is $[-1.57, 1.00]$ at HL-LHC. Another advantage

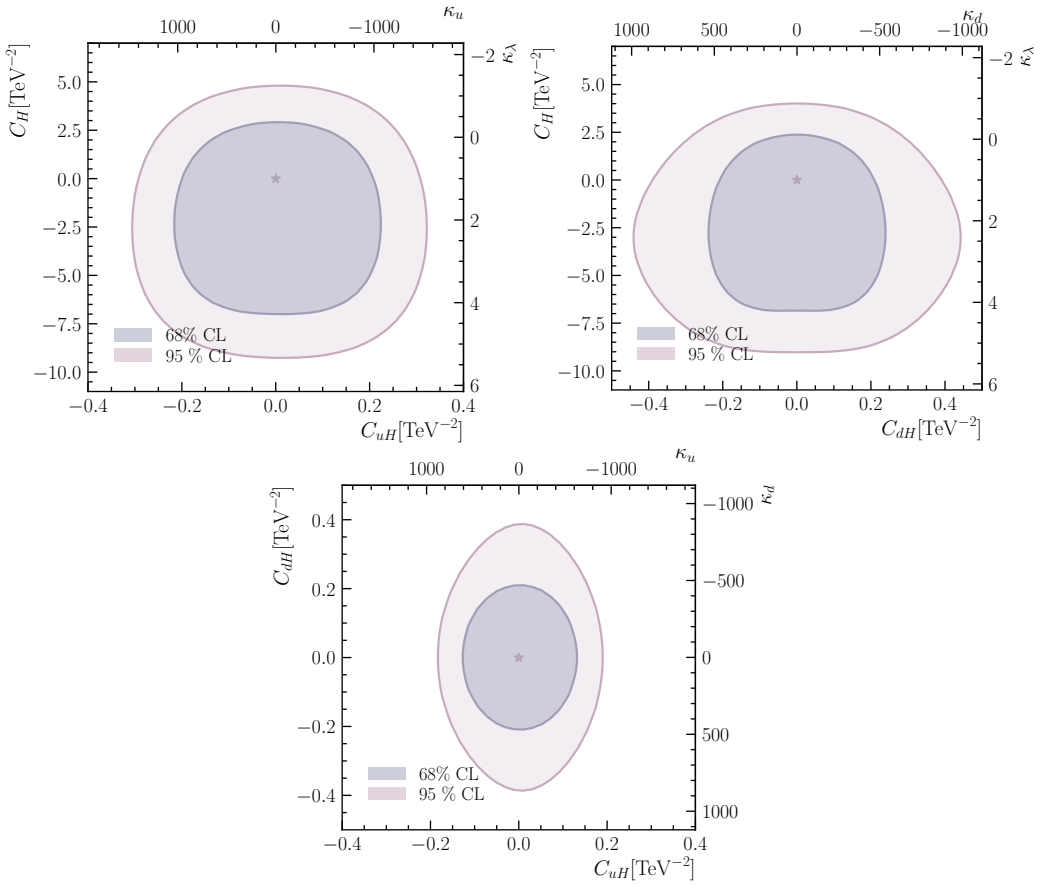

Figure 4.9. The 68% and 95% CL contours of the constraints on up and down Yukawa coupling modifiers as well as C_ϕ from two-parameter fits using the results of the cut-based analysis for the HL-LHC at 14 TeV and $6\mathrm{ab}^{-1}$ integrated luminosity.

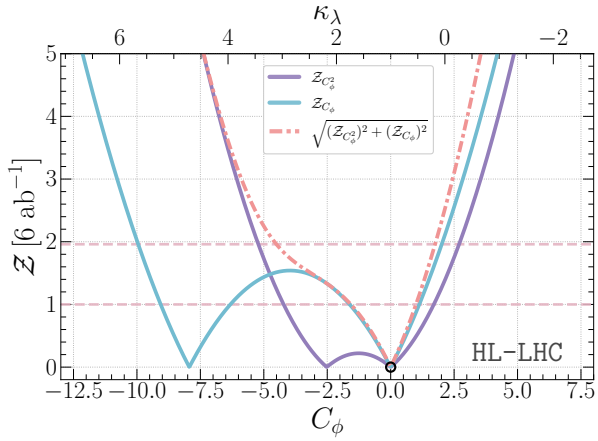

Figure 4.10. Bounds on C_ϕ (or κ_λ) at the HL-LHC from single parameter fit. The solid blue lines are the constraints coming from the hh^{ggF}_{int} contribution which scales linearly with the modified coupling and the solid purple line is that from the hh^{ggF}_{tri} contribution that scales quadratically with the modified coupling. The red dashed line is the combination of the quadratic and linear channel. The horizontal light red dashed lines marks the 68% and 95%CI's.

of the optimised multi-variate analysis is the ability to preform two-parameter fits in the same planes described above, shown in Figure 4.11 while maintaining the improvement over the cut-based one. Since the BDT training was able to achieve sufficient accuracy for seven-channel classifier, including up and down $q\bar{q}$A, the three ggF topologies and the backgrounds. It was possible to resolve all of the signal channels strata and their parametric dependence on the three Wilson coefficients $C_{u\phi}$, $C_{d\phi}$ and C_ϕ. A three-parameter fit is possible without degeneracies, as seen in Figure 4.12. However, the posterior distribution of the three-parameter fit show no marked correlations amongst the Wilson coefficients. In both two- and three-parameter fits degeneracy in the $C_{d\phi}$ direction is observed at 99.7$ CI. This due to the reduction of the Higgs pair signal when the $h \to d\bar{d}$ decay channel is opened, particularly for high values of this Wilson coefficient as highlighted by Figure 4.5. In fact, when this analysis is applied for the strange quark, the overall effect of enhanced strange quark is a reduction in the $b\bar{b}\gamma\gamma$ signal, making this Higgs pair final state insensitive to strange Yukawa enhancements, more details on this were discussed in [2]. Comparing with the constraints on C_ϕ from a single parameter fit in Figure 4.10, it can be seen from the two- and three-parameter fits in Figure 4.11 and Figure 4.12, respectively, that, the constraints on C_ϕ become diluted when the light-quark Yukawa coupling modifiers $C_{q\phi}$ are taken into an account. This effect is somewhat more prominent for $C_{d\phi}$ than for $C_{u\phi}$ and stems from the fact that away from $C_{u\phi,d\phi} = 0$ larger negative values of C_ϕ are allowed by the crescent shaped curves of the HDP contours. The bounds on $C_{u\phi}$ and $C_{d\phi}$ from the fit with two-parameters including C_ϕ remain the same as the bounds on these Wilson coefficient from the single parameter $C_{u\phi,d\phi}$ fits. The fit results are summarised in Table 4.4.

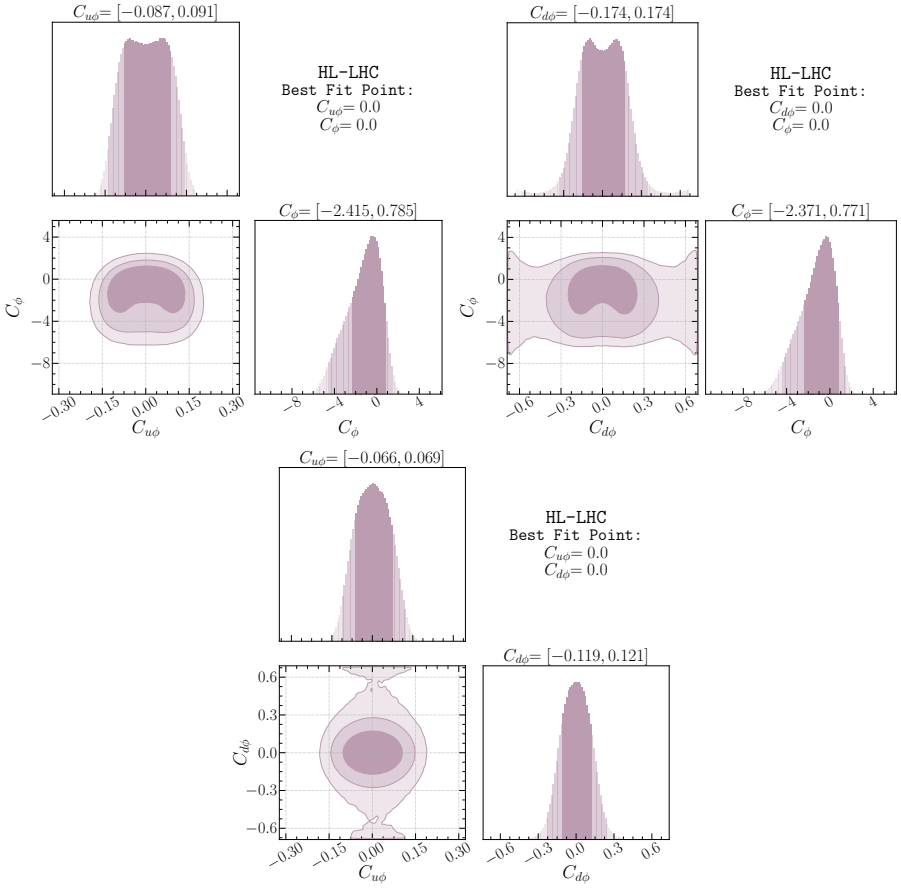

Figure 4.11. The 68%, 95% and 99.7% HDP contours, for Bayesian fits preformed on pairs of Wilson coefficients for C_ϕ, $C_{u\phi}$ and $C_{d\phi}$ form the multi-variate analysis output.

Operators	$C_{u\phi}$	$C_{d\phi}$	C_ϕ	κ_u	κ_d	κ_λ
HL-LHC 14 TeV 6 ab^{-1} @ 68% CI						
$\mathcal{O}_\phi$	–	–	[-1.57, 1.00]	–	–	[0.53, 1.73]
$\mathcal{O}_{u\phi}$	[-0.09, 0.10]	–	–	[-477, 431]	–	–
$\mathcal{O}_{d\phi}$	–	[-0.16, 0.16]	–	–	[-360, 360]	–
$\mathcal{O}_{u\phi}$ & $\mathcal{O}_\phi$	[-0.087, 0.091]	–	[-2.42, 0.79]	[-434, 417]	–	[0.63, 2.13]
$\mathcal{O}_{d\phi}$ & $\mathcal{O}_\phi$	–	[-0.17, 0.17]	[-2.73, 0.77]	–	[-381, 379]	[0.63, 2.27]
$\mathcal{O}_{u\phi}$ & $\mathcal{O}_{d\phi}$	[-0.065, 0.069]	[-0.12, 0.12]	–	[-331, 312]	[-268, 272]	–
All	[-0.077, 0.084]	[-0.160, 0.162]	[-2.77, 0.43]	[-400, 369]	[-362, 359]	[0.79, 2.30]

Table 4.4. Summary of the 68% projected bounds on $C_{u\phi}$, $C_{d\phi}$ and C_ϕ from single-, two- and three-parameter fits for HL-LHC with 6 ab^{-1} of data and FCC-hh with 30 ab^{-1} of data. The corresponding bounds on the rescaling of the effective couplings, κ_u, κ_d and κ_λ are presented on the right side of the table.

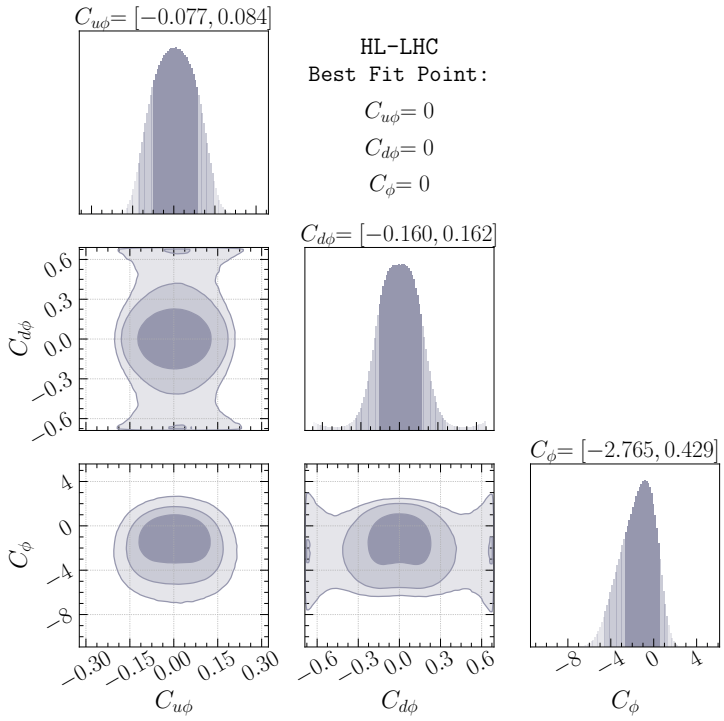

Figure 4.12. Three parameter Bayesian fits with $C_{u\phi}$, $C_{d\phi}$ and C_{ϕ}, the HDP contours are the same as Figure 4.11 .

4.7 Overview of Light Yukawa searches

There are additional measurements of the light-quark Yukawa couplings that might become relevant at HL-LHC or FCC-hh, a careful study of which is beyond the scope of the current work. Yet we attempt to include a discussion here, so as to provide a comparison with our study and to put it into proper context, or to serve as proposal for further studies. The channel $pp \to h+j$ has been suggested as a probe for charm Yukawa coupling [233] with charm-tagged jet having a potential bound of $\kappa_c \sim 1$ for the HL-LHC, depending on the charm-tagging scheme. This process could be used for the first and second generations Yukawa couplings by looking at the shapes of kinematic distributions, the most important one being the p_T distribution [234–236]. The expected HL-LHC 95% CL bounds are $\kappa_c \in [-0.6, 3.0]$, $|\kappa_u| \lesssim 170$ and $|\kappa_d| \lesssim 990$. The use of $h + j$ process along with other single Higgs processes have also been suggested as indirect probes for Higgs self coupling [90–94, 237], due to the contribution of the trilinear coupling to NLO electroweak corrections to these processes. In addition, experimental fits have been carried out for the trilinear coupling from single Higgs observables [238, 239].

It seems that for the HL-LHC, an optimal bound for the trilinear coupling can be obtained by combing both the data from single-Higgs process as well as Higgs pair production [95], with 68% CL bound on $\kappa_\lambda \in [0.1, 2.3]$, compared to the expected bound

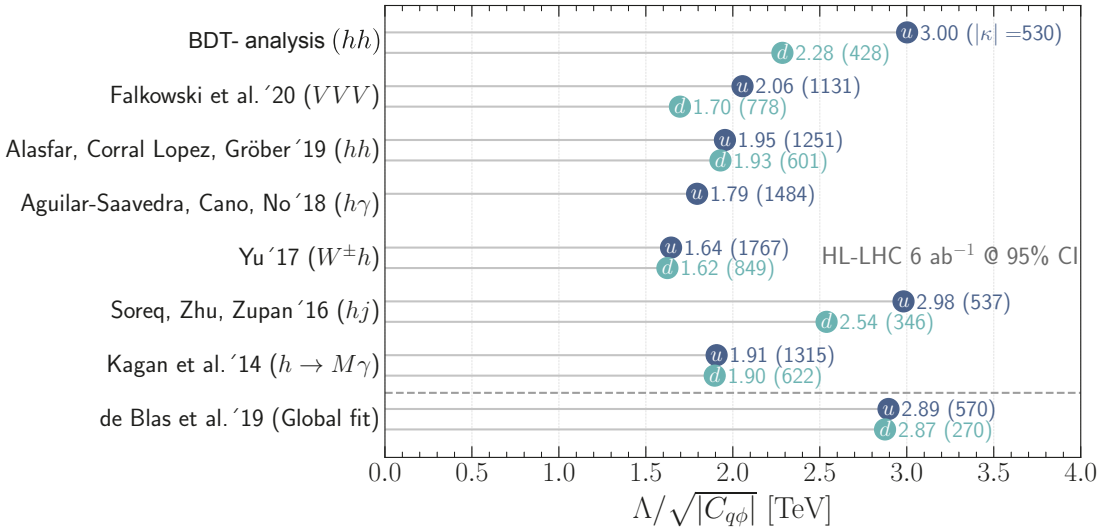

Figure 4.13. Summary of the 95% CI/CL sensitivity bounds on the SMEFT Wilson coefficients $C_{u\phi}$ (blue), and $C_{d\phi}$ (green). The bounds are interpreted in terms of the NP scale Λ that can be reached through the measurements of the Wilson coefficient at the HL-LHC at 6 ab^{-1}, the corresponding κ_q's are shown inside the parentheses. Single parameter fit 95% CI bounds are used from this analysis for comparison with previous studies.

of $\kappa_\lambda \in [0.0, 2.5] \cup [4.9, 7.4]$ coming from using di-Higgs measurements alone. Moreover, single Higgs processes, namely Zh and $W^{\pm}h$ production, could also be useful in probing charm-Yukawa coupling using a mixture of b- and c-tagging schemes leveraging the mistagging probability of c-jets as b-jets in b-tagging working points, and vice-versa, in order to break the degeneracy in the signal strength [240]. The use of this technique could probe $\kappa_c \sim 1$ in the FCC-hh. Of course, for the charm-Yukawa coupling, the constraints are set to improve significantly, as there has been recent direct observation of $h \to c\bar{c}$ [178]. Therefore, from here on, we will mainly concentrate on the process with more potential for constraining Yukawa couplings of the first generation quarks.

Rare Higgs decays to mesons, $h \to M + V$, $M = \Upsilon, J/\Psi, \phi \ldots$, were also suggested as a probe for light-quark Yukawa couplings [241–243], and there have been experimental searches for these decays [178, 244] with bounds on the branching ratios, $\mathcal{B}(h \to X, \gamma,\ X = \Upsilon, J/\Psi,) \sim 10^{-4} - 10^{-6}$ at 95% CL. It was shown in Ref. [245], that the charge asymmetry of the process $pp \to hW^+$ vs $pp \to hW^-$ can be used as a probe for light-quark Yukawa couplings as well as to break the degeneracy amongst quark flavours. Moreover, the rare process $pp \to h\gamma$ is also a possible way to distinguish between enhancements of the up- and down-Yukawa couplings [246] where the authors have estimated the bounds on the up-Yukawa coupling of $\kappa_u \sim 2000$ at the HL-LHC. Despite some processes appearing more sensitive than others, one should think of these processes as complementary to each other.

One of the main features of the effective couplings $hhq\bar{q}$ and $hhhq\bar{q}$ emerging from SMEFT operator $\mathcal{O}_{q\phi}$, or the Chiral Lagrangian for that matter, is that these couplings

are either free from propagator suppression for $hhq\bar{q}$ or scale with energy for $hhhq\bar{q}$ while being safe from strong unitarity constraints. This feature gives processes with multiple Higgs and/or vector bosons $V = W^{\pm}, Z$ an advantage in constraining $\mathcal{O}_{q\phi}$. The latter constrains come from the longitudinal degrees of freedom of the gauge bosons which can be understood from the Goldstone boson equivalence theorem. The use of the final state VV as a probe for $\mathcal{O}_{q\phi}$ is difficult due to the large SM background. However, the three-boson final state VVV was shown to give strong projected bounds for light-quark Yukawa couplings for HL-LHC with 95% CL bounds on $\kappa_u \sim 1600$, and $\kappa_d \sim 1100$. A ten fold improvement is expected at FCC-hh [247] with bounds of order $\kappa_d \sim 30$. Higgs pair production has a smaller SM background compared to VV production, but it has a significantly smaller cross section too, even when compared to VVV, as the latter process has already been observed at the LHC [248, 249].

On the contrary, Higgs pair production is inaccessible with the runs I-III of the LHC, but it is potentially accessible at the HL-LHC [250] having a $\sigma \cdot BR \sim 1\text{fb}^{-1}$. However, Higgs pair production, particularly the channel $h \to b\bar{b}\gamma\gamma$, is of significant interest as it has unique features. The first being the ability to constrain the trilinear and light-quark Yukawa couplings simultaneously, as we have already seen in the previous sections. Secondly, Higgs pair production could probe non-linear relations between Yukawa interaction and $hhq\bar{q}$ couplings [251]. Lastly, Higgs pair production is expected to be significant enhanced in certain models involving modification of light-quark Yukawa couplings (cf. [252–254]) A numerical comparison of the strongest bounds from HL-LHC on the first-generation Yukawa couplings from the studies discussed above in Figure 4.13. In comparison to the global fit bounds that have been obtained with no invisible or untagged Higgs decays allowed [255]. For $C_{d\phi}$, the most stringent bound comes from the global fit, and the $h + j$ channel, as a model-independent bound, while this analysis provides the second most stringent model-independent bound. For $C_{u\phi}$ this analysis provides the most stringent constraint while the bound from $h + j$ and the global analysis are comparable. The figure is interpreted in terms of the reach of NP scale Λ that can be achieved by the measurement of these Wilson coefficients. For future colliders, like the FCC-hh at 100 TeV, in addition to Higgs pair production, triple Higgs production might be an interesting channel for constraining the operators with Wilson coefficient $C_{u\phi}$ and $C_{d\phi}$ due to the energy increase of a Feynman diagram coupling the quarks to three Higgs bosons.
Finally, it should be noted that there are also non collider signatures for enhanced light-quark Yukawa couplings, manifesting in frequency shifts in atomic clocks from Higgs forces at the atomic level [256].

4.8 Discussion and conclusion

The chapter walked through the potential of Higgs pair production to glean information about the elusive Yukawa couplings of the first generation quarks, from the final state $b\bar{b}\gamma\gamma$. This has been done in two different approaches: The first is the traditional cut and count method. Afterwards, significant improvement of the analysis has been

achieved using interpretable machine learning. In order maintain harmony with other chapters of this thesis, the enhancements of light Yukawa couplings were parametrised within the SMEFT framework

Despite the limitations of the cut-based analysis for Higgs pair, it was still possible to estimate notable sensitivity for both up- and down- type Yukawa coupling to the Higgs boson, comparable with other channels and the model-dependent global fit. Superior estimated bounds, in particular for the up quark, emanated from the full exploitation of the kenimatical shapes and their correlations in a multi-variate analysis. This was achieved by using a High-level kenimatical distributions as features in a BDT classification. then interfacing it with an explainer based on Shapley values.

The precedence of using an interpretable ML framework over DNN's stems from the ability to optimise the training procedure by means of physics-motivated dimensionality reduction by excluding less important features. Interpretable ML not only outperforms black-box models, but also provides physics understanding of the processes at hand, pointing to kinematic variables like H_T and $m_{\gamma\gamma}$ as being important variables that instrument this separation. Lastly, but most importantly, interpretable models provide higher confidence in the results of their classification or regression.

The use of a BDT classifier was not only beneficial for increasing the hh signal selection efficiency, but also to classify the signal channels strata, such that it is possible to parametrise it in terms of C_ϕ, $C_{u\phi}$ and $C_{d\phi}$. By decomposing the ggF channel into its sub-topologies depending on their C_ϕ parametrisation cross-section into the box topologies which do not depend on the trilinear coupling, the triangle scaling quadratically with C_ϕ. Lastly the interference between the two, which has a linear dependence on C_ϕ. The $q\overline{q}$A, is considered exclusively a NP channel. It scales quadratically with $C_{q\phi}$. The outcome of this technique is the ability to preform, two and three-parameter fits including all of the Wilson coefficients in question.

With the HL-LHC Higgs pair searches, it is expected to constrain the Higgs trilinear coupling to $\mathcal{O}(1\%)$. A result match by other sensitivity analysis based on ML analysis done by experimentalists at the CMS and ATLAS [107, 115, 232]. This clearly indicates the desideratum of Higgs pair production observation for understanding the Higgs potential. In spite of light Yukawa modifiers like $C_{q\phi}$ being typically overlooked when studying Higgs pair production, this study showed that they can dilute the bounds on the trilinear Higgs coupling, and thus these coefficients need to be considered in any phenomenological studies of Higgs pair. Particularly that these Wilson coefficients are weakly bounded from other measurements, unlike other coefficients that can be constrained from single-Higgs, EWPO or top data.

There exist a handful of potential UV-complete models in which both light Yukawa as well as the Higgs trilinear couplings are enhanced. For example, a model proposed in ref [252] based on vector-like quarks (VLQ) with AFV assumptions. The original assumption of this model is excluded, as the authors assumed an enhancement of all light quark-Higgs couplings to be equal to the beauty Yukawa. One could still get significant enhancement to light Yukawa fro VLQ masses of ~ 2 TeV, which is well above the current direct searches excluding VLQ of masses $M_{VLQ} < 1.6$ TeV [257, 258] for the hadronic

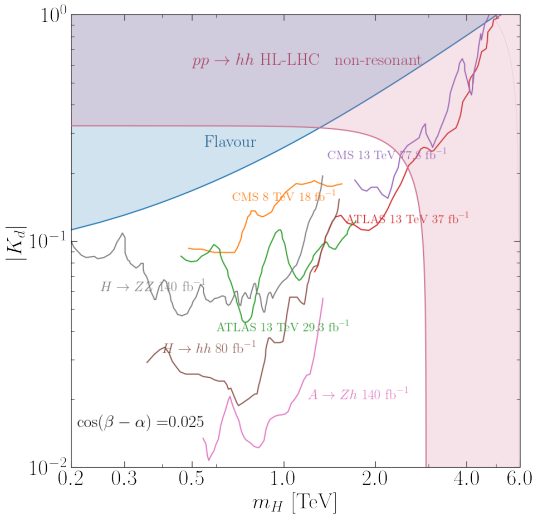

Figure 4.14. Example of constraints on the 2HDM with SFV presented in [254, 263] from flavour observables, LHC dijet , Zh,ZZ and resonant hh searches. The region shaded in Red is the bounds projected for the HL-LHC from the analysis presented in this chapter. This plot was inspired by the plots found in ref. [254].

final state, and $M_{VLQ} < 1.2$ TeV for the leptonic one [259]. Due to the AFV manifested in this model, the VLQ could be made not to couple to the third generation quarks, and evade the tree-level EWPO bounds [260]. In addition,the trilinear Higgs coupling could be modified by the inclusion of an additional scalar singlet cf. [106, 261, 262]. Another example of models with enhanced light Yukawa is a two-Higgs-doublet model (2HDM) model proposed in refs. [254, 263]. This model has a special kind of AFV, known as spontaneous flavour violation (SFV). Enhancements to light Yukawa couplings come from the second Higgs Yukawa couplings, which made diagonal in the flavour space K_q ($q = u, d$). SFV has the constraint that either the up-type or the down-type couplings can be enhanced, while the couplings of the other type maintain the SM hierarchy. The Higgs potential is modified by the addition of the second doublet, and consequently the Higgs self-coupling will be modified as well. Like any other 2HDM, the parameter space is rather large. The bounds on this model will depend on the region of its parameter space we are interested in. Figure 4.14 shows the bounds on this model for a point near the alignment limit. For small mass of the " heavy" Higgs H and large Yukawa coupling K_d flavour bounds dominate, while for larger m_H the dijet searches [264–266] would dominate due to the decay $H \to d\bar{d}$. On the contrary, the decay $H \to hh$ would become dominant from smaller values of K_d and larger H mass, but still $m_H < 2$ TeV. In this regime, resonant Higgs pair searches give string constraints for light Yukawa enhancement [267, 268]. Similar light Yukawa bounds in this region of the parameter space could also be derived from Zh [269] and ZZ [270, 271] searches. Lastly, for $m_H > 2$ TeV, the non-resonant Higgs pair production will become the dominant bound on light Yukawa enhancement, coming from the analysis of this chapter.

Part IV

Flavour physics

5 Flavour anomalies and Electroweak precision tests

Recent results from B-factories including Belle and Babar as well as the LHCb-experiment involving the semileptonic decays of the beauty mesons $B^0, B^{\pm}, B_s \ldots$ point to marked deviation of $\sim 2.5\sigma$ from the SM prediction, particularly in the branching fractions ratios

$$R_{K^{(*)}} \equiv \frac{Br(B \to K^{(*)}\mu^+\mu^-)}{Br(B \to K^{(*)}e^+e^-)}, \tag{5.1}$$

in the low dilepton mass bins [272–276] [1]. In addition to the results of angular analysis of the decay $B \to K^*\mu^+\mu^-$ [277, 278], with the observable P_5' showing similar deviation from the SM, the most recent measurement was published by LHCb [279]. Other observables derived from the branching fractions of semileptonic and full leptonic final states of B mesons decays, e.g. $B_s \to e^+e^-$ also showed deviations from the SM with the $2\sigma - 3\sigma$ range [280–283]. These observables have in common the FCNC transition $b \to s\ell\ell$ $\ell = e, \mu$, and are in conflict with the SM lepton universality of EW couplings. This tension could be translated into a strong case for the evidence of BSM physics with lepton flavour universality violation (LUV) [284–286].
When these aberrant results are added to the recent muon anomalous magnetic moment $g-2$ measurement by Fermilab [287] or measurements of differential dilepton braching fractions of B-mesons, grounds for the muons being the source of LUV are established, i.e. the NP degrees of freedom contain muon-flavoured couplings. However, long-distant effects present in the decay amplitudes ir $g-2$ corrections [288–292] – involving hadronic contributions that are theoretically difficult to handle [293–296] – make such a conclusion debatable, see, e.g. [297, 298].
Another class of B decays involving the tree-level $b \to c\tau\nu_\tau$ transitions has shown similar tension with the SM [299–302]. Amongst other, the observable $R_{D^{(*)}} \equiv Br(B \to D^{(*)}\tau\nu)/Br(B \to D^{(*)}\ell\nu)$, originally found at Babar [303] and subsequently measured at Belle [304] and LHCb [305] has shown a $\sim 20\%$ deviation from the SM. All of the anomalous flavour observables as summarised in Figure 5.1 with their pull in σ's shown in blue, compared the standard model predictions with their uncertainties in orange.
The simultaneous resolution for the anomalies emerging from $b \to s\ell\ell$ and the semileptonic $b \to c$ transitions, requires models with complicated flavour structure [307–316], as such models need to accommodate for imilar deviations from the SM for both classes albeit these two transitions occur at different orders in the SM. Such models are often

[1] The data from the most recent measurement of the R_{K^*} [276] has not been used in this work, as the fits shown in this chapter predates these results.

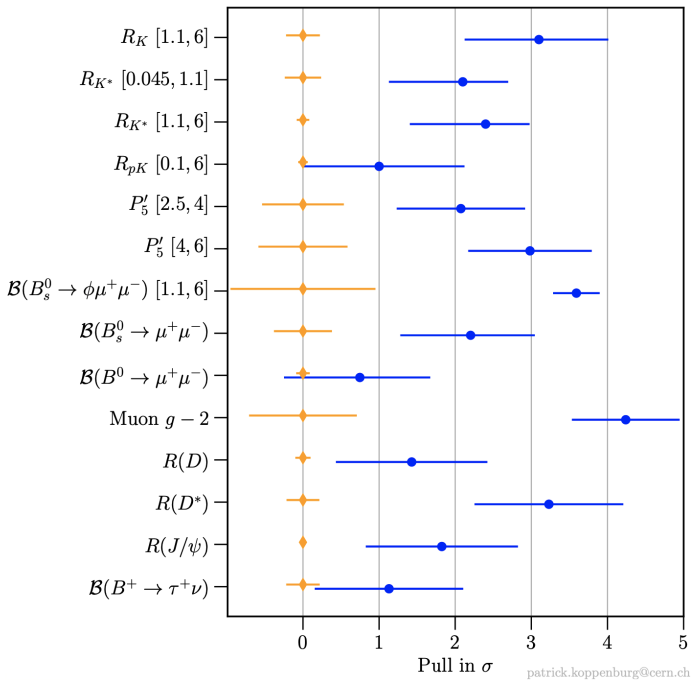

Figure 5.1. Forest plot summarising the flavour observables in tension with the SM predictions, the experimental pull in terms of standard deviations σ is shown in blue, while the SM prediction with the theoretical uncertainties is highlighted in orange. This figure is made by P. Koppenburg [306].

being at the edge of flavour physics constraints [110, 317] and collider bounds [318, 319]. On the other hand, most up-to-date measurements of $R_{D^{(*)}}$ from the Belle collaboration [320, 321] turns out to be in good agreement with the SM [322–325]. This fact may cast some doubt on the effective role one should really attribute to $b \to c$ transitions in the interpretation of the depicted *B-physics crisis*. Furthermore, the ratios of branching fractions of decays involving the FCNC $b \to s\ell\ell$ transitions have a much lower dependence on the long distance non-perturbative QCD effects, that $g-2$, and differential distributions of semileptonic B-decays [326–329] . Therefore, the LUV information extracted from such "clean" observables have the highest potential for extracting LUV insights, see [330] for more details.

The $b \to s\ell\ell$ anomalies have been studied in a model-independent manner, in particular SMEFT framework in refs. [331–335] and more recently revisited in refs. [336–342]. Additionally, many UV-complete models were investigated, particularly leptoquarks (LQ), like in refs. [343–347]. Another class of models of special interest are Z' models, in which the B anomalies can be realised at loop-level. The simplest of these models has been proposed in ref. [348], extending the SM with a single new Abelian gauge group, together with the presence of top- and muon-partners, resulting in a top-philic Z' boson capable of evading present collider constraints [349] and responsible for the required LUV signatures. This model has the advantage of not introducing extra flavour spurions to the

SM, i.e. similar to the MFV ansatz [186, 350, 351]. More general set of models with the same features can be found in ref. [352], and subsequently elaborated upon in greater detail in the phenomenological study of ref. [353].
While evading flavour constraints, models with top-philic Z' are in strong tension with the Z-pole measurements [353, 354]. In fact, it has been shown in [336], that in spite of large hadronic uncertainties for the amplitude of the $B \to K^* \mu^+ \mu^-$ decay, a tension of at the 3σ level at least would persist between B data and EWPO for muonic LUV effects, and an even stronger tension would be found in the case of LUV scenarios involving electron couplings. This elucidates the interplay between B-physics and EWPO's [336, 337, 345–347, 352, 355, 356].
This fact has been brought to light recently [357] to abandon *ii)*, and reformulate the original proposal addressing B anomalies at one loop adding specific BSM sources of flavour violation in order to reconcile B data with EW precision tests in this context. However, as briefly advertised in ref. [336], an important caveat of this EW tension versus B anomalies concerns the assumption of no tree-level NP contributions to EWPO.
This chapter aims to extend the theme of this thesis of interconnectivity between different SMEFT sectors to the flavour anomalies, by exploring the cross-talk between B-physics observables and EWPO's via SMEFT fits. This can be achieved by first studying the one-loop operator mixing effects seen in the RGE evolution of SMEFT operators [81, 82], followed by a global fit of flavour and EWPO SMEFT operators to the available data on both. Lastly, a set of potential UV-complete models, based on ones some present in the literature [348, 349, 352], that accommodate the resulting fit constraints are investigated. This work is an extension of several studies done by some of my collaborators [294, 297, 334, 336, 358–360], and published in [3].

This chapter is organized as follows: in section 5.1 a theoretical review the ingredients of the EFT analysis is presented; in section 5.2 details on the strategy adopted for the combined EW+flavour fit in the SMEFT are discussed, the results from which are collected in section 5.3; in section 5.4 I discuss the most economic viable Z' model in relation to our EFT results and also mention possible alternative leptoquark scenarios. Lastly, the conclusions are summarised in section 5.5.

5.1 Flavour anomalies in SMEFT

Global fits from $b \to s\ell\ell$ anomalies show that if NP degrees of freedom enter at tree-level, they would have an energy scale $\Lambda \sim 10$ TeV [331–335]. Highlighting that for LHC phenomenology, the use of SMEFT is justified. The operators of interest for the explanation of these B anomalies are [336, 337, 352]:

$$\mathcal{O}^{\ell\ell 23}_{LQ^{(1)}},\ (\mathcal{O}^{(1,3)}_{LQ})^{\ell\ell 23},\ \mathcal{O}^{23\ell\ell}_{Qe},\ \mathcal{O}^{\ell\ell 23}_{Ld},\ \mathcal{O}^{\ell\ell 23}_{ed}. \tag{5.2}$$

Following the same convention for the SM fields in **??** and operator definitions in the Warsaw basis presented in **??**. Current data, taking non-perturbative QCD effects into an account using light-cone sum rules, both left- and right-handed operators are permit-

ted [336, 338–340]. Nevertheless, the statistical significance for the right-handed $b \to s$ interaction remains small, coming only from $R_{K^*}/R_K \neq 1$ [335, 336]. Hence, one can effective only consider the left-handed operators $(\mathcal{O}_{LQ}^{(1,3)})^{2223}$ and $\mathcal{O}_{Qe}^{2322}$ for addressing the flavour anomalies. Additionally, when conservative hadronic uncertainties are considered [293–295], the preference of NP coupling to the muons exclusively becomes mitigated and the inclusion of electron interactions becomes viable as well [334]. From these considerations, we conclude that the operator $(\mathcal{O}_{LQ}^{(1,3)})^{\ell\ell 23}$ with either or both$\ell = e, \mu$ offers the minimal resolution of these anomalies within the SMEFT framework [336].
Introducing these operators at tree-level will lead to flavour violation beyond the SM, as these operators are flavour spurions unrelated to the SM ones. This can be avoided if they get generated at loop level from the RGE of operators involving the leptons and the Higgs [352]

$$(\mathcal{O}_{\phi L}^{(1,3)})^{\ell\ell}, \;\; \mathcal{O}_{\phi e}^{\ell\ell}, \tag{5.3}$$

or alternatively, from the semileptonic four-fermion (SL-4F) operators with right-handed top-quark currents:

$$\mathcal{O}_{Lu}^{\ell\ell 33}, \;\; \mathcal{O}_{eu}^{\ell\ell 33} \tag{5.4}$$

The leading log solution of the RGE for these operators [81, 82], with the matching conditions for the left-handed quark-current operators in eq. (5.2) at the EW scale $\mu_{\rm EW} \sim v$ are:[2]

$$\begin{aligned}
C_{LQ}^{(1)\;\ell\ell 23} &= V_{ts}^* V_{tb} \left(\frac{y_t}{4\pi}\right)^2 \log\left(\frac{\Lambda}{\mu_{\rm EW}}\right) \left(C_{Lu}^{\ell\ell 33} - C_{\phi L}^{(1)\;\ell\ell}\right) , \\
C_{LQ}^{(3)\;\ell\ell 23} &= V_{ts}^* V_{tb} \left(\frac{y_t}{4\pi}\right)^2 \log\left(\frac{\Lambda}{\mu_{\rm EW}}\right) C_{\phi L}^{(3)\;\ell\ell} , \\
C_{Qe}^{23\ell\ell} &= V_{ts}^* V_{tb} \left(\frac{y_t}{4\pi}\right)^2 \log\left(\frac{\Lambda}{\mu_{\rm EW}}\right) \left(C_{eu}^{\ell\ell 33} - C_{\phi e}^{\ell\ell}\right) .
\end{aligned} \tag{5.5}$$

In heavy quark physics, B decays are typically studied within the low energy weak effective theory [363–365], in which we have the vector and axial currents defined as

$$\begin{aligned}
\mathcal{O}_{9V,\ell} &= \frac{\alpha_e}{8\pi} (\bar{s}\gamma_\mu(1-\gamma_5)b)(\bar{\ell}\gamma^\mu \ell) , \\
\mathcal{O}_{10A,\ell} &= \frac{\alpha_e}{8\pi} (\bar{s}\gamma_\mu(1-\gamma_5)b)(\bar{\ell}\gamma^\mu\gamma_5 \ell) ,
\end{aligned} \tag{5.6}$$

[2] similar to the previous chapters, for one-loop effects, the NP scale is set to be $\Lambda = 1$ TeV. The renormalisation scale is set to $\mu_{\rm EW} = m_t \simeq v/\sqrt{2}$ to minimise the matching-scale dependence with the inclusion of the NLO corrections [361, 362].

and matched at the EW scale $\mu_{\rm EW}$ with the SMEFT operators in eq. (5.3) - (5.4) follow:

$$\begin{aligned} C^{\rm NP}_{9,\ell} &= \frac{\pi v^2}{\alpha\Lambda^2}\left(\frac{y_t}{4\pi}\right)^2 \log\left(\frac{\Lambda}{\mu_{\rm EW}}\right)\left(C^{(3)\ \ell\ell}_{\phi L} - C^{(1)\ \ell\ell}_{\phi L} - C^{\ell\ell}_{\phi e} + C^{\ell\ell 33}_{Lu} + C^{\ell\ell 33}_{eu}\right), \\ C^{\rm NP}_{10,\ell} &= \frac{\pi v^2}{\alpha\Lambda^2}\left(\frac{y_t}{4\pi}\right)^2 \log\left(\frac{\Lambda}{\mu_{\rm EW}}\right)\left(C^{(1)\ \ell\ell}_{\phi L} - C^{(1)\ \ell\ell}_{\phi L} - C^{\ell\ell}_{\phi e} - sC^{\ell\ell 33}_{Lu} + C^{\ell\ell 33}_{eu}\right). \end{aligned} \tag{5.7}$$

The overall normalization in the weak Hamiltonian follows the standard conventions adopted in refs. [294, 334, 336]. As anticipated, the set of operators of interest for the study of $R_{K^{(*)}}$ in eq. (5.5) is also sensitive to EWPO. The operators involving the Higgs field and lepton bilinears in the SMEFT induce tree-level modifications to EW-boson couplings, while modifications of the Z couplings to the leptons can be also induced via top-loop contribution [71]. In the leading-log approximation and at the leading order in the top Yukawa coupling, LUV effects can be generated by:

$$\begin{aligned} \Delta g^{\ell\ell}_{Z,L}\Big|_{\rm LUV} &= -\frac{1}{2}\left(C^{(1)\ \ell\ell}_{\phi L} + C^{(3)\ \ell\ell}_{\phi L}\right)\frac{v^2}{\Lambda^2} - 3\left(\frac{y_t\, v}{4\pi\Lambda}\right)^2 \log\left(\frac{\Lambda}{\mu_{\rm EW}}\right) C^{\ell\ell 33}_{Lu}, \\ \Delta g^{\ell\ell}_{Z,R}\Big|_{\rm LUV} &= -\frac{1}{2}C^{\ell\ell}_{\phi e}\frac{v^2}{\Lambda^2} - 3\left(\frac{y_t\, v}{4\pi\Lambda}\right)^2 \log\left(\frac{\Lambda}{\mu_{\rm EW}}\right) C^{\ell\ell 33}_{eu}, \end{aligned} \tag{5.8}$$

where $\Delta g^{\ell\ell}_{Z,L(R)} \equiv g^{\ell\ell}_{Z,L(R)} - g^{\ell\ell,{\rm SM}}_{Z,L(R)}$ is the deviation with respect to the left-handed (right-handed) leptonic couplings to the Z boson in the SM theory. Since EW couplings to leptons have been precisely measured at LEP/SLC, they provide an important test bed for lepton universality [354, 366].

These observations motivates a global SMEFT fit of the operators explaining the B-anomalies, as well as their interplay with EWPO. Assuming that the LUV affects are generated by NP via radiative effects, matching what is see in eq. (5.7). Consequently, the NP will contribute to EWPO at tree-level, whilst other SMEFT operators appearing from the REG mixing are assumed to be small or constrained from other processes. In order for these assumptions to be fulfilled within SMEFT, the operators modifying the EW coupling of the quarks need to be included as well

$$\mathcal{O}^{(1)\ qq}_{\phi Q},\ \mathcal{O}^{(3)\ qq}_{\phi Q},\ \mathcal{O}^{qq}_{\phi u},\ \mathcal{O}^{qq}_{\phi d}, \tag{5.9}$$

where $q = 1, 2, 3$ identifies quark generations. These operators are considered to be flavour aligned, in a similar fashion to $C_{q\phi}$ of the previous chapter, in particular they are assumed to be aligned with the down-quark basis. This is needed to avoid pathological tree-level FCNC [110]. The same holds for the leptonic operators, being aligned with the charged lepton mass bases.
The EWPO have a degeneracy between the first and second generation quarks, particularly in the down-type quarks sector. Therefore, it is natural to impose a $U(2)^3$ symmetry between first and second generator quark operators, thus imposing $C^{(1,3)\ 11}_{\phi Q} = C^{(1,3)\ 22}_{\phi Q}$, $C^{11}_{\phi u} = C^{22}_{\phi u}$. This also helps to suppress large FCNC contributions from these operators.

Additionally, the RGE boundary condition $C_{\phi u}^{33} = 0$ is assumed. This is motivated by the fact that this Wilson coefficient cannot be constraint by EWPO, as modifications to Z-coupling to right-handed top quarks cannot be probed by by Z-pole measurements. Finally, for completeness, the four-lepton operator is also included in the fit:

$$O_{LL}^{1221} = (\overline{L}_1\gamma^\mu L_2)(\overline{L}_2\gamma_\mu L_1) \ , \tag{5.10}$$

which contributes to the muon decay amplitude, and therefore alters the extraction of the value of the Fermi constant, G_F, which is one of the inputs of the SM EW sector.

The operators in eqs. (5.3), (5.9) and (5.10), with the assumptions mentioned before, saturate all the 17 degrees of freedom, i.e. combinations of operators, that can be constrained in a fit to EWPO in the dimension-six SMEFT framework while keeping flavour changing neutral currents in the light quark sector under control. Together with the 4 four-fermion operators from eq. (5.4), this completes a total of 21 operators, which is included in the fit setup described in the next section.

5.2 Analysis technique

The global fit combining both flavour observables related to the $b \to s\ell\ell$ anomalies, in addition to EWPO is carried out in a Bayesian statistical framework. The experimental observables are modelled via state-of-the-art theoretical information already implemented and described in ref. [336] for flavour physics, and for EW and Higgs physics in ref. [367] and, more recently, in ref. [366]. EWPO are extended by flavour non-universal SMEFT contributions described in ref. [354, 368]. The statistical and physics frameworks are both available within the publicly available `HEPfit` [99] package, a Markov Chain Monte Carlo (MCMC) framework built using the Bayesian Analysis Toolkit [369] [3]
The experimental input used for the global is summarised in the following, which are also implemented in `HEPfit`code :

- The set of EWPO including the Z-pole measurements from LEP/SLD, the measurements of the W properties at LEP-II, as well as several related inputs from the Tevatron and LHC measurements of the properties of the EW bosons [370–376]. The following lists the bulk of the EWPO included in the fits:

$$\begin{gathered} M_H,\ m_t,\ \alpha_S(M_Z),\ \Delta\alpha^{(5)}_{\rm had}(M_Z), \\ M_Z,\ \Gamma_Z,\ R_{e,\mu,\tau},\ \sigma_{\rm had},\ A_{FB}^{e,\mu,\tau},\ A_{e,\mu,\tau},\ A_{e,\tau}(P_\tau),\ R_{c,b},\ A_{FB}^{c,b},\ A_{s,c,b},\ R_{u+c}, \\ M_W, \Gamma_W,\ {\rm BR}_{W\to e\nu,\mu\nu,\tau\nu},\ \Gamma_{W\to cs}/\Gamma_{W\to ud+cs},\ |V_{tb}| \, ; \end{gathered}$$

- The angular distribution of $B \to K^{(*)}\ell^+\ell^-$ decays for both μ and e final states in the large-recoil region.These include data from ATLAS [377], Belle [328], CMS [378, 379] and LHCb [380, 381]; in addition to the branching fractions from LHCb [382],

[3] `HEPfit`is developed by some of my collaborators, who have co-authored this work

and of $B \to K^* \gamma$[4] for which the HFLAV average is used [384];

- Branching ratios for $B^{(+)} \to K^{(+)} \mu^+ \mu^-$ decays in the large-recoil region measured by LHCb [385];
- The angular distribution of $B_s \to \phi \mu^+ \mu^-$ [386] and the branching ratio of the decay $B_s \to \phi \gamma$ [387], measured by LHCb;
- The LUV ratios R_K [274] and R_{K^*} [273] from LHCb and Belle [275];
- Branching ratio of $B_{(s)} \to \mu^+ \mu^-$ measured by LHCb [281], CMS [280], and ATLAS [282]; we also use the upper limit on $B_s \to e^+ e^-$ decay reported recently by LHCb [283].

The measurements of $B \to K^{(*)} \ell^+ \ell^-$ decays in the low di-lepton invariant mass region are plagued by large uncertainties for the charmonium resonance, and thus not included win the fit. Moreover, the rare beauty baryonic decay $\Lambda_b \to \Lambda \, \mu^+ \mu^-$ is not considered as well.
Modelling the decays of hadrons involves factorisable (in terms of decay constant) and non-factorisable non-perturbative QCD effects. The non-factorisable effects emerge from long-distance hadronic contributions to [288, 289, 293] QCD loops appearing in radiative corrections to these decays. In this analysis, the $B \to K^* \ell^+ \ell^-$ has two different scenarios to describe these hadronic effects, discussed also in other previous works of my collaborators [297, 334, 336, 358–360]. The first is a conservative approach (Phenomenological Data Driven or PDD) as originally proposed in [294], and refined in ref. [297], whilst the second is a more optimistic one based on the results in [288] (Phenomenological Model Driven or PMD). The PDD scenario is based on a generic model of the hadronic effects, which is simultaneously fitted to $b \to s\ell\ell$ data alongside the NP effects. Contrary to PDD approach, the PMD scenario the dispersion relations specified in [288] is used constrain the hadronic contributions in the entire large-recoil region considered in the analysis, ergo PMD has smaller hadronic effects in the $B \to K^* \ell^+ \ell^-$ amplitudes [358]. Th choice of the hadronic uncertainties model significantly affects the outcome of the fits to the B-decays observables [336].
In order to be as general as possible, the SMEFT global fit is done for four different scenarios, described as follows:

- **EW**: Using EWPO data only with the assumptions discussed in section 5.1. This fit includes the operators in eqs. (5.3), (5.9), and (5.10), summing up to a total of 17 Wilson coefficients.
- **EW (SL-4F Only)**: This refers to a fit done with the Wilson coefficients of the SL-4F operators involving the right-handed top current, reported in eq. (5.4). This scenario incorporates the assumption that BSM enters the modifications of the Z couplings to muons and electrons through top-quark loops only.

[4] NP effects from dipole operators are strongly constrained as extensively investigated in ref. [383]. However, radiative exclusive B decays still provide relevant information about hadronic effects [297].

- **EW & Flavour**: Wilson coefficients of all the 21 operators given in eq. (5.3), (5.9), and eq. (5.10), together with eq. (5.4) are varied.
  All of the EW data as well as the flavour observables listed above are used. This scenario comes in two varieties, PDD and PMD, as explained above.
- **Flavour**: These fits exclusively include the Wilson coefficients of the *4 operators* (both electrons and muons) appearing in eq. (5.4), and are done including only flavour data, i.e. excluding EW measurements. Results are again distinguished for the PDD and PMD cases. This fit is typically done when flavour anomalies are discussed in the literature. Hence, it was included here to emphasize the importance of including EWPO .

5.3 Results from the SMEFT

5.3.1 Analysis of EW and $b \to s\ell\ell$ data

As a first step in our analysis, we reproduced the outcome of the EW fit originally obtained in ref. [354] using `HEPfit`, briefly revisited in section A.3. Then, we expanded upon the standard EW results through the study of the **EW** scenario introduced in the previous section, yielding constraints on the Wilson coefficients of the SMEFT operators involving, in particular, dimension-six operators with a Higgs-doublet current, and including also leading-loop effects under the working hypotheses stated in section 5.1. The subset of these operators containing leptonic currents can give rise to non-universal modifications of EW gauge-boson couplings. Assuming NP integrated out at the heavy scale $\Lambda > v$, these operators also contribute via RGE flow to $b \to s\ell\ell$ observables at one loop, see eq. (5.5).

On the left side of Figure 5.2, we show in orange the bounds from the **EW** fit on the Wilson coefficients of the operators with leptonic currents in terms of mean and standard deviation of the marginalized posterior probability density function. We observe compatibility with the SM within the 2σ level. Note that EW data strongly correlate the operators under consideration among themselves, as can be seen in the correlation matrix presented in Figure 5.3

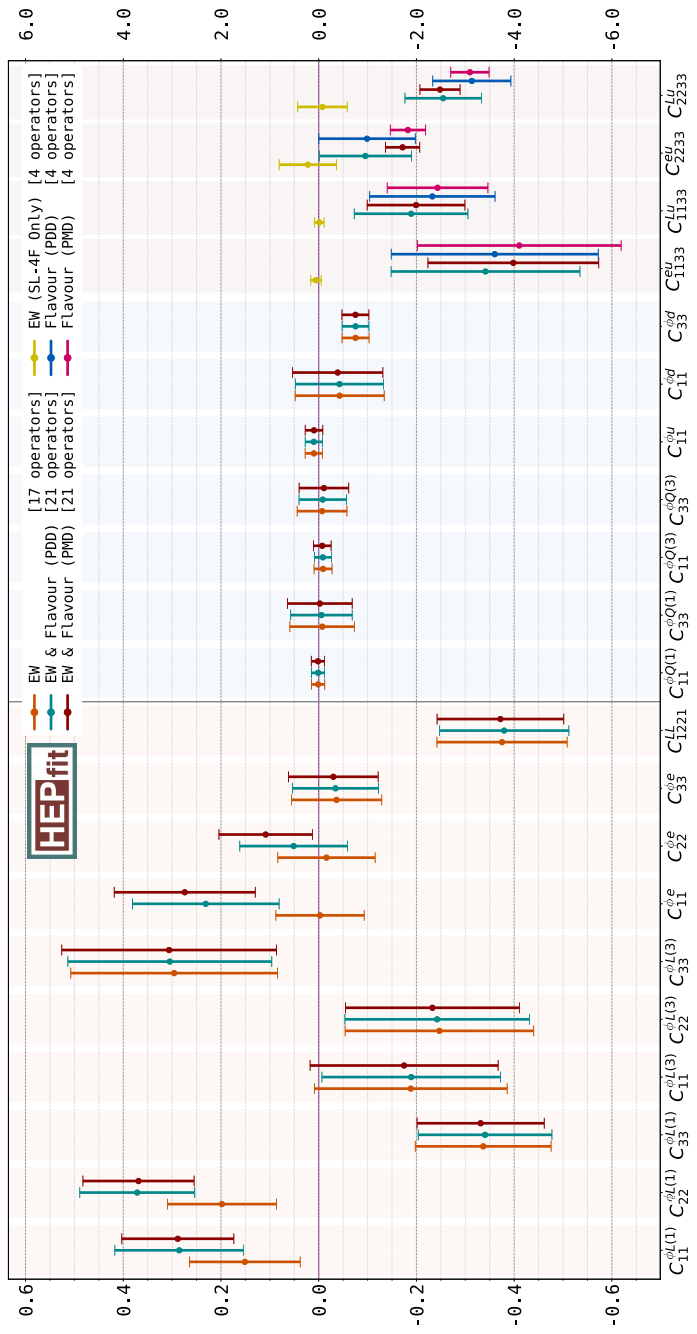

Figure 5.2. Mean and standard deviation of the marginalized posterior distributions for each of the Wilson coefficients (in TeV^{-2}) considered in the different fits described in section 5.2. Note that each fit assumes a different set of non-zero operators: EW – 17 operators presented in eqs. (5.3), (5.9) and (5.10); EW(SL-4F Only) – four-fermion operators in eq.(5.4); Flavour (PDD) and (PMD) are the fits with the operators in eq.(5.4), where (PDD) and (PMD) refer to the various assumptions on the hadronic long-distance effects in the flavour sector; EW & Flavour (PDD) and (PMD) stand for the fits including the 21 operators in eqs. (5.3), (5.4), (5.9) and (5.10). (Note the different scaling in the axes quantifying the size of the bounds presented in each half of the figure.)

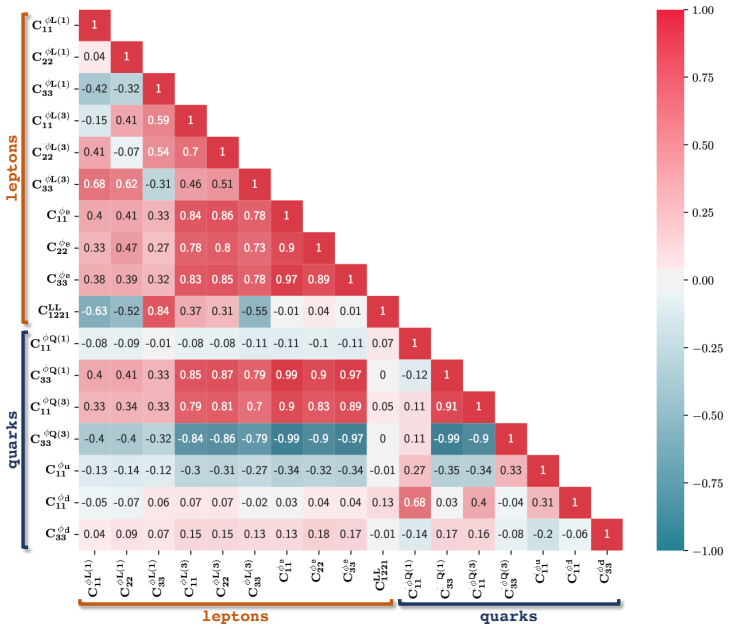

Figure 5.3. *The correlation matrix extracted from the SMEFT analysis of the set of independent operators in eqs. (5.3), (5.9), (5.10) in the **EW** scenario introduced in section 5.2. The two distinct groups of Wilson coefficients associated to leptonic and quark interactions are remarked as "leptons" and "quarks", respectively.*

where away from the photon pole, $R^{\rm SM}_{K^{(*)}}$ are predicted to be unity at percent level [286].

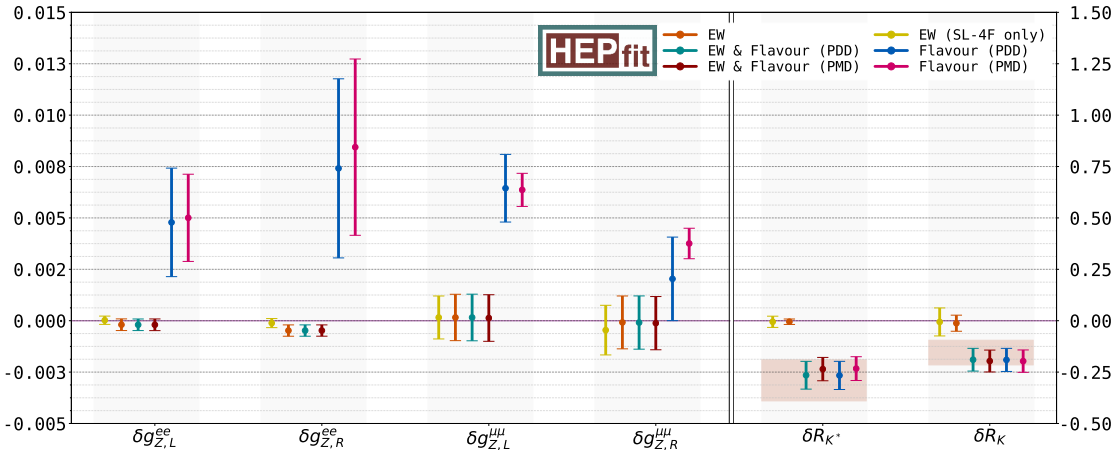

Figure 5.4. *Mean and standard deviation of the marginalized posterior of the key set of observables for this work, in relation to the tension between $b \to s\ell\ell$ anomalies and LEP/SLD measurements. In particular, the left panel shows the deviations in the effective $Z\ell\ell$ couplings, normalized by SM values. The right panel, on the other hand, shows the deviation from the nominal SM values of the lepton universality violating ratios, see eq. (5.11), with the red boxes indicating the region selected by the experimental measurements of $R_{K,(K^*)}$.*

In particular, the strong correlation between the operators with quarks and leptons is introduced by the non-negligible one-loop universal contribution of the operator $\mathcal{O}_{33}^{HQ^{(1)}}$ to all the EW couplings, as anticipated at the end of section 5.3. With the direct bound on $C_{33}^{HQ^{(1)}}$ being relatively weak compared to the limits on the leptonic operators, such effects in the leptonic couplings can be sizable.

This leads to a relaxation of the naive bounds on $C_{\ell\ell}^{HL^{(1)}}$, $C_{\ell\ell}^{HL^{(3)}}$ and $C_{\ell\ell}^{He}$ that one would obtain in a tree-level analysis. To illustrate this, we present in section A.3 a comparison with the results from such a tree level analysis of the EW fit. The results in Figure 5.3 can then be compared to those in Figure A.1 where, as it is apparent, there is a substantial decoupling between the dimension-six operators made of Higgs doublets and quark bilinears from the leptonic ones.

The impact of these operators on the key observables for the present discussion is reported in Figure 5.4. There, we collect mean and standard deviation on the shift in the Z coupling to light leptons (normalized to the corresponding SM value),and on the effect on $R_{K^{(*)}}$ in the dilepton-mass range $[1.0, 6.0]$ GeV^2:

$$\delta g_{Z,L(R)}^{ee(\mu\mu)} \equiv g_{Z,L(R)}^{ee(\mu\mu)} / g_{Z,L(R)}^{ee(\mu\mu),\mathrm{SM}} - 1 \ , \ \delta R_{K^{(*)}} \equiv R_{K^{(*)}} - R_{K^{(*)}}^{\mathrm{SM}} \ , \tag{5.11}$$

Note that EW measurements tightly constrain NP effects modifying the EW gauge boson couplings to electrons, and also forbid deviations beyond the per-mille level in the case of couplings to muons. This translates into strong bounds on the Wilson coefficients $C_{\ell\ell}^{HL^{(1,3)},He}$. Hence, the one-loop contribution to $R_{K^{(*)}}$ from $O_{\ell\ell}^{HL^{(1,3)},He}$ comes out to be tiny. We can then move our attention to the **EW (SL-4F Only)** scenario, reported in yellow in Figure 5.2 and Figure 5.4, and find a similar conclusion. Indeed, EW data once again strongly constrain the NP Wilson coefficients related to $O_{\ell\ell 33}^{eu,Lu}$ – the SL-4F operators – implying all the four NP Wilson coefficients to be compatible with 0. However, note that unlike the previous case, $C_{\ell\ell 33}^{Lu,eu}$ only contribute at one loop to $\delta g_{Z,L(R)}^{\ell\ell}$ and $\delta R_{K^{(*)}}$ in eq. (5.11). Consequently, the resulting impact on $b \to s\ell\ell$ flavour observables can be larger than the one in the **EW** scenario. As depicted in Figure 5.4, however, there is still an overall tension between EWPO bounds (in yellow) and the experimental measurements of R_K and R_{K^*} (indicated by the shaded red boxes in the right side of the figure) at the 3σ level.

To frame this tension from a different perspective, let us now focus on the set of flavour measurements as previously done in ref. [336]. In Figure 5.2 we also show the constraints on the four Wilson coefficients of eq. (5.4) coming from $b \to s\ell\ell$ data, in what we dubbed as the **Flavour** scenario. We present the PMD case, corresponding to an optimistic approach to QCD power corrections, in pink, while the more conservative PDD case is shown in blue. We observe that in both cases a muonic solution to B anomalies stands out, with C_{2233}^{Lu} different from 0 at more than 3σ in the PDD case, and at roughly 6σ in the PMD one.

We stress that the difference between the results obtained in the PMD and in the PDD case is substantially driven by the angular analysis of $B \to K^*\mu\mu$. In particular, only within the PDD approach the fully left-handed solution to B anomalies, $C_{9,\ell} = -C_{10,\ell}$,

is favoured by data (signalled here by the Wilson coefficient of $O^{eu}_{\ell\ell 33}$ being compatible with 0 at 1σ, see the results in blue in Figure 5.2). In addition, an electron resolution of B anomalies is, once again, viable only within PDD [334, 336].

In the **Flavour** scenario one can also predict the induced shift in the Z-boson couplings according to eq. (5.8), and these are shown in Figure 5.4. As can be seen, $\delta g^{\ell\ell}_{Z,L,R}$ would receive large contributions at one loop from $O^{Lu,eu}_{\ell\ell 33}$ in correspondence to the one-loop MFV-like resolution of B anomalies. Such contribution would be, however, now in tension with the results from EW precision tests. In particular, as a reflection of the main role played by O^{Lu}_{2233} in the **Flavour** fit to the four NP Wilson coefficients considered, $g^{\mu\mu}_{Z,L}$ shows the most important deviation from the SM value. Also, the prediction of $g^{\mu\mu}_{Z,L(R)}$ becomes indirectly sensitive to the underlying treatment of hadronic uncertainties adopted for the study of $b \to s$ data. Therefore, we observe that within the PMD approach, the inconsistency between what is needed to address B anomalies and what is required by EW measurements is even more severe than the 3σ established in the **EW (SL-4F Only)** scenario, and imprinted also in the **Flavour** fit with the PDD approach. In fact, we stress once again that adopting light-cone sum-rule results [288] for the long-distant effects in $B \to K^*\ell\ell$ decay, the tension between B anomalies and EW data reaches the 6σ level.

So, how do we reach a consensus between $b \to s\ell\ell$ measurements and EWPO? Succinctly, an obvious solution which satisfies these constraints is a class of models where $R_{K^{(*)}}$ anomalies are addressed at tree level and where modifications to Z-lepton-lepton vertices are at the same time suppressed. However, these models would not offer a solution to B anomalies of the MFV type envisaged so far, namely they would rely on the existence of sizeable new sources of flavour violation. At this point, we would like to emphasize that a combined fit of EW and flavour observables offers a new insight into this matter: it highlights strong correlations between the dimension-six operators $O^{Lu(eu)}_{\ell\ell 33}$ and $O^{HL^{(1)}(He)}_{\ell\ell}$ as is evident from Figure 5.5. This figure presents a pictorial representation of the correlations between the leptonic operators included in the different fits.

Apart from the fits introduced in the previous section, for illustration purposes we also show in Figure 5.5 the correlations obtained in a variant of the **EW** fit including also the four-fermion operators $O^{Lu(eu)}_{\ell\ell 33}$, labelled as **EW (including SL-4F operators)**. This is shown in the upper-right corner of the figure. As can be seen in that panel, and one could deduce from the relations in eq. (5.8), in a pure EW fit adding the four-fermion operators would simply introduce 4 flat directions. These are illustrated by the links connecting the $C^{eu}_{\ell\ell 33}$ ($C^{Lu}_{\ell\ell 33}$) and $C^{He}_{\ell\ell}$ ($C^{HL^{(1)}}_{\ell\ell}$) operators, corresponding to 100% anti-correlation. Such flat directions are lifted upon the introduction of the flavour measurements of R_K and R_{K^*}, as can be seen in the lower panels of Figure 5.5 for the **EW & Flavour** fits. Even then, due again to relations in eq. (5.5) and (5.8) and the comparatively different precision of the EW and flavour measurements, sizable correlations remain.

In Figure 5.2 the imprint of these correlations is a shift of central values and an increase on the bounds on the corresponding Wilson coefficients, with red and green bars representing the outcome of the fit in the **EW & Flavour** scenario within the **PMD** and

PDD approaches, respectively. The interplay between $O_{\ell\ell 33}^{Lu(eu)}$ and $O_{\ell\ell}^{HL^{(1)}(He)}$ is evident when comparing the reported red and green bounds versus the orange EW constraints on $C_{\ell\ell}^{HL^{(1)}(He)}$, and the yellow ones for $C_{\ell\ell 33}^{Lu(eu)}$. Consequently, as clearly depicted in Figure 5.4, looking at the red and green ranges reported for the **EW & Flavour** scenario, $R_{K^{(*)}}$ puzzles are solved with EW precision being respected. It is important to emphasize that, despite the significant correlation between quark and lepton operators introduced by the one-loop effects of $C_{33}^{HQ^{(1)}}$, quark operators play no significant role in reconciling the EWPO constraints with the solution to B anomalies. This will become clearer in the next section, but can be easily understood from the fact that, as mentioned before, quark and lepton constraints are somewhat uncorrelated in the tree-level EW fit, and the fact that the one-loop corrections effect induced by $C_{33}^{HQ^{(1)}}$ are flavour universal.

5.3.2 A minimal EFT picture

Finally, let us draw what would be the minimal picture for NP out of the general analysis obtained with the 21 operators considered in the **EW & Flavour** scenario. Indeed, a simpler picture will serve as a guideline for the UV models discussed in section 5.4. As mentioned before, given the hadronic uncertainties at hand, the most economic explanation addressing in particular $R_{K^{(*)}}$ anomalies resides in the NP contribution from the fully left-handed operator, $O_{\ell\ell 23}^{LQ}$. In the present context this operator is generated at one loop by $O_{\ell\ell 33}^{Lu}$, according to eq. (5.5).

Then, in Figure 5.6 we show in orange the overall constraint from $b \to s\ell\ell$ data on $C_{\ell\ell 33}^{Lu}$ within the most conservative approach to long-distance effects, i.e. the PDD one. In particular, in the left (right) panel we report the constraint on the muonic (electronic) scenario. In the same figure, we highlight with the vertical gray band the bound derived from the full correlated set of EWPO on the same operator. From the comparison of the orange and gray single-operator bounds, the tension between flavour and EW measurements is manifest at the 3σ level in the left panel of Figure 5.6. It gets even more pronounced in the right panel due to the precise probe of NP that EW gauge-boson couplings to electrons provide. In the same Figure 5.6, we also show with the horizontal gray band the result of the EWPO constraints applied this time on the NP contribution coming exclusively from the operator $C_{\ell\ell}^{HL^{(1)}}$. Note that this operator would also contribute to $R_{K^{(*)}}$ at one loop, but the size needed would be $\mathcal{O}(1)$ and it is out of scale in the vertical axis of the plot.

Most importantly, in the same figure we display in (dashed) magenta the $1(2)\sigma$ contour where EW data are reconciled with the one-loop MFV explanation of B anomalies when a combined fit of the NP contributions from these two operators is performed. Therefore, heavy BSM degrees of freedom that, once integrated out, generate sizeable contributions both to the Wilson coefficient of $O_{\ell\ell}^{HL^{(1)}}$ and of $C_{\ell\ell 33}^{Lu}$ are the key aspect of this scenario that addresses B anomalies without requiring sources of flavour violation beyond SM ones.

Finally, note that the role played here by $O_{\ell\ell 33}^{Lu}$ could be shared, in part, with $O_{\ell\ell 33}^{eu}$, depending on how much departure is actually required from the fully left-handed solution

to B anomalies. As already noted, this fact critically depends on the information stemming from $B \to K^* \mu\mu$ [336]. On general grounds, to relieve the bounds from EWPO, the presence of $O^{eu}_{\ell\ell 33}$ would also necessitate sizeable NP effects from $O^{He}_{\ell\ell}$.

As a last comment of this section we would also like to highlight that in the class of models considered the prediction for the LUV observable R_K is always close to the one for R_{K^*}: any hint of NP coming from $R_{K^*}/R_K \neq 1$ [284, 285, 335, 388] would not be addressed within the NP models considered here, mainly involving the operators in eq. (5.3) and (5.4). In the following sections we will put our focus on the economic EFT scenario captured in Figure 5.6 to build up simple UV scenarios realizing the EFT picture here delineated.

5.4 Directions for UV models

In this section we discuss how the lesson derived from the SMEFT picture illustrated, in particular, in Figure 5.6, can be realized in a minimal extension of the SM. Here, we explicitly show how models involving a new Z' gauge boson around the TeV scale provide the most economic example of the correlations advertised in the previous section. This can be achieved if we have a Z' coupled both to top and lepton SM fields. These couplings can be obtained introducing vector-like top and muon/electron partners reasonably close to the EW scale [348, 349], making this class of models potentially interesting also from the point of view of naturalness in the Higgs sector. Finally, we will also briefly comment on possible alternative scenarios that can be obtained with leptoquarks.

5.4.1 Z′ with vector-like partners

Let us start with the baseline presented originally in ref. [348]. A simple extension of the SM, able to address B anomalies, and that does not introduce any explicit new source of flavour violation, can be conceived as follows:

- The SM gauge group, $SU(3)_c \otimes SU(2)_L \otimes U(1)_Y$, is extended by a new Abelian gauge group, $U(1)_X$, under which SM fields are neutral;
- There is a new complex scalar field $\mathcal{S}$ that spontaneously breaks $U(1)_X$, giving a mass to the gauge boson X_μ equal to $m_{Z'} = g_X \langle \mathcal{S} \rangle$;
- A coloured vector-like top partner, $\mathcal{T}$, properly charged under $U(1)_X$ and $U(1)_Y$ can mix with the right-handed top-quark field u_3 via a Yukawa interaction with $\mathcal{S}$;
- A vector-like muonic partner, $\mathcal{M}$, doublet of $SU(2)_L$ and charged under $U(1)_{X,Y}$, can mix with the muonic doublet L_2 via another Yukawa coupling of $\mathcal{S}$;
- The couplings controlling the kinetic-mixing term, $X_{\mu\nu} B^{\mu\nu}$, and the quadratic scalar mixing, $\mathcal{S}^\dagger \mathcal{S} H^\dagger H$, are set to be phenomenologically negligible.[5]

[5] Using naive dimensional analysis, both kinetic and scalar quadratic mixing should appear beyond the tree level suppressed at least by a loop factor and the corresponding SM-partner rotation angles.

Then, the UV model is completely characterized by eight new parameters: the gauge coupling g_X, the mass $\mu_{\mathcal{S}}$ and quartic $\lambda_{\mathcal{S}}$ of the renormalizable potential of $\mathcal{S}$, the new Yukawa couplings $Y_{\mathcal{T},\mathcal{M}}$, here taken to be real, and the vector-like mass-term parameters $M_{\mathcal{T},\mathcal{M}}$. In particular, the Lagrangian of the model contains the following terms:

$$M_{\mathcal{T}}\overline{\mathcal{T}_R}\mathcal{T}_L+M_{\mathcal{M}}\overline{\mathcal{M}}_R\mathcal{M}_L+Y_t\overline{u}_3\tilde{H}^\dagger Q_3+Y_{\mathcal{T}}\overline{u}_3\mathcal{T}_L\mathcal{S}+Y_\mu\overline{e}_2H^\dagger L_2+Y_{\mathcal{M}}\overline{\mathcal{M}}_R L_2\mathcal{S}+\text{h.c.}\,, \quad (5.12)$$

that characterize the mixing pattern of SM fields and vector-like partners.[6] Symmetry breaking of $U(1)_X$ is triggered by $\langle\mathcal{S}\rangle^2=-\mu_{\mathcal{S}}^2/(2\lambda_{\mathcal{S}})\equiv\eta^2\neq 0$, that implies the following fermionic mixing patterns:

$$\text{top sector:}\quad \begin{pmatrix}\overline{u}_3 & \overline{\mathcal{T}}_R\end{pmatrix}\begin{pmatrix}\frac{Y_t\,v}{\sqrt{2}} & \frac{Y_{\mathcal{T}}\eta}{\sqrt{2}}\\ 0 & M_{\mathcal{T}}\end{pmatrix}\begin{pmatrix}U_3\\ \mathcal{T}_L\end{pmatrix}+\text{h.c.}\,, \quad (5.13)$$

$$\text{muon sector:}\quad \begin{pmatrix}\overline{e}_2 & \overline{\mathcal{M}}_R\end{pmatrix}\begin{pmatrix}\frac{Y_\mu v}{\sqrt{2}} & 0\\ \frac{Y_{\mathcal{M}}\eta}{\sqrt{2}} & M_{\mathcal{M}}\end{pmatrix}\begin{pmatrix}E_2\\ \mathcal{M}_L\end{pmatrix}+\text{h.c.}\,,$$

where U_i (E_i) indicates the Q_i-component (L_i-component) with weak isospin 1/2 (-1/2). Using the determinant and trace of the squared mass matrices, one can easily show that the eigenvalues $m_{t,\mathcal{T}}$ and $m_{\mu,\mathcal{M}}$ must satisfy [348]:

$$\begin{aligned} m_{t,\mu}\,m_{\mathcal{T},\mathcal{M}} &= \frac{1}{\sqrt{2}}Y_{t,\mu}vM_{\mathcal{T},\mathcal{M}}\,, \quad (5.14)\\ m_{t,\mu}^2+m_{\mathcal{T},\mathcal{M}}^2 &= M_{\mathcal{T},\mathcal{M}}^2+\frac{1}{2}(Y_{t,\mu}\,v)^2+\frac{1}{2}(Y_{\mathcal{T},\mathcal{M}}\,\eta)^2\,, \end{aligned}$$

that in the decoupling limit clearly yield: $m_{t,\mu}\simeq Y_{t,\mu}v/\sqrt{2}$, $m_{\mathcal{T},\mathcal{M}}\simeq M_{\mathcal{T},\mathcal{M}}$.

Defining for the top sector the rotation matrix from the interaction to the mass basis following the convention:

$$\begin{pmatrix}t_{R(L)}\\ \mathcal{T}'_{R(L)}\end{pmatrix}=\begin{pmatrix}\cos\theta^t_{R(L)} & -\sin\theta^t_{R(L)}\\ \sin\theta^t_{R(L)} & \cos\theta^t_{R(L)}\end{pmatrix}\begin{pmatrix}u_3(U_3)\\ \mathcal{T}_{R(L)}\end{pmatrix}\,, \quad (5.15)$$

and doing similarly for the muonic sector, the mixing angles between SM fields, t and μ, and their partner mass eigenstates, $\mathcal{T}'$ and $\mathcal{M}'$, can be conveniently expressed in terms of the dimensionless ratios $\xi_{\mathcal{T},\mathcal{M}}$ and $\varepsilon_{t,\mu}$:

$$\begin{aligned} &\tan 2\theta^t_R=\tfrac{2\xi_{\mathcal{T}}}{\xi_{\mathcal{T}}^2-\varepsilon_t^2-1}\,,\quad \tan 2\theta^t_L=\tfrac{2\varepsilon_t}{\xi_{\mathcal{T}}^2-\varepsilon_t^2+1}\,,\ \text{with}\ \varepsilon_t\equiv\tfrac{Y_t v}{Y_{\mathcal{T}}\eta},\ \xi_{\mathcal{T}}\equiv\tfrac{\sqrt{2}M_{\mathcal{T}}}{\eta Y_{\mathcal{T}}}\,; \quad (5.16)\\ &\tan 2\theta^\mu_R=\tfrac{2\varepsilon_\mu}{\xi_{\mathcal{M}}^2-\varepsilon_\mu^2+1}\,,\ \tan 2\theta^t_L=\tfrac{2\xi_{\mathcal{M}}}{\xi_{\mathcal{M}}^2-\varepsilon_\mu^2-1}\,,\ \text{with}\ \varepsilon_\mu\equiv\tfrac{Y_\mu v}{Y_{\mathcal{M}}\eta},\ \xi_{\mathcal{M}}\equiv\tfrac{\sqrt{2}M_{\mathcal{M}}}{\eta Y_{\mathcal{M}}}\,. \end{aligned}$$

In a perturbative expansion in $\varepsilon_{t,\mu}$, eq. (5.16) clearly shows that the mixing in the top sector proceeds mainly through $\tan\theta^t_R\simeq 1/\xi_{\mathcal{T}}$, while in the muonic sector one has

[6] Note that upon an opposite $U(1)_X$ charge assignment for the vector-like fermionic partners than the one implicitly assumed, one should replace in eq. (5.12) $\mathcal{S}$ with $S^\dagger$.

$\tan\theta_L^\mu \simeq 1/\xi_{\mathcal{M}}$ and very tiny $\tan\theta_R^\mu$.

Hence, for $\varepsilon_{t,\mu}/\xi_{\mathcal{T},\mathcal{M}} = Y_{t,\mu}v/\sqrt{2}M_{\mathcal{T},\mathcal{M}} < 1$, the leading couplings of the Z' boson to the SM fields correspond to right-handed tops and to left-handed muons as well as neutrinos according to:[7]

$$g_{Z't_R} = g_X \sin^2\theta_R^t = \frac{g_X}{1+\xi_{\mathcal{T}}^2} + \mathcal{O}\left(\varepsilon_t^2/\xi_{\mathcal{T}}^2\right) , \tag{5.17}$$

$$g_{Z'\mu_L(\nu)} = g_X \sin^2\theta_L^\mu = \frac{g_X}{1+\xi_{\mathcal{M}}^2} + \mathcal{O}\left(\varepsilon_\mu^2/\xi_{\mathcal{M}}^2\right) , \tag{5.18}$$

with $g_{Z't_L(\mu_R)}$ being non-negligible only at order $\varepsilon_{t(\mu)}^2/\xi_{\mathcal{T}(\mathcal{M})}^2$. Consequently, integrating out the Z' relevantly generates the operator O_{2233}^{Lu} with Wilson coefficient:

$$C_{2233}^{Lu} = -\frac{g_{Z't_R}g_{Z'\mu_L}}{m_{Z'}^2} \simeq -\frac{1}{(1+\xi_{\mathcal{T}}^2)(1+\xi_{\mathcal{M}}^2)\,\eta^2} , \tag{5.19}$$

together with four-fermion operators built of t_R or μ_L, ν fields that can be potentially probed at collider and by experimental signatures like ν-trident production.

From eq. (5.19) it is clear that in order to have $|C_{2233}^{Lu}| \sim 2$ TeV^{-2} as highlighted in Figure 5.6, one needs to rely on a relatively low symmetry-breaking scale $\eta \lesssim$ TeV;[8] for $m_{Z'} \sim$ TeV this implies $g_X \gtrsim 1$. In Figure 5.7 we show the 1σ region corresponding to the explanation of B anomalies via eq. (5.19) in the parameter space $\xi_{\mathcal{T},\mathcal{M}}$, fixing the gauge coupling $g_X = m_{Z'}/\eta$ for a tentative Z' gauge boson at the TeV scale and the VEV of the new scalar field $\mathcal{S}$ set to $\eta = 250$ GeV and $\eta = 500$ GeV in the left and right panel, respectively. In the same plot, we re-interpret in our scenario the most relevant collider constraints originally identified in ref. [353].

For small values of $\xi_{\mathcal{M}}$, the measurement of neutrino-trident production performed in [389] is effective, and its constraint is reported at the 2σ level with the orange vertical band. Under the reasonable assumption that the Z' boson is mainly produced at tree level in association with the $t\bar{t}$ pair, in the blue region we show the 95% high-p_T constraint stemming from the recasting of the $pp \to \mu^-\mu^+t\bar{t}$ search at ATLAS [390], while in cyan we report the expected constraint on the model from the 4-tops analysis of CMS [391], see ref. [353] for further details. From the same work, we also adopt the expected collider constraints for future projected luminosity corresponding to 300 fb^{-1}, shown with dashed lines. Note that these projections become of fundamental importance when it comes to probe the interesting 1σ region connected to B anomalies. In particular, the right panel in Figure 5.7 captures the benchmark for a promising discovery at the High-Luminosity LHC.

Finally, in the same figure, fixing the partner Yukawa coupling to $\mathcal{O}(1)$ values as reported in the two panels, we mark in gray the region corresponding to the bound on the mass of the vector-like partner expected from collider, taken to be $m_{\mathcal{T}} = 1.4$ TeV

[7] In what follows, for $\eta \sim \mathcal{O}(v)$ we will have $\xi_T \sim \mathcal{O}(1)$; consequently, $\varepsilon_t \sim \mathcal{O}(v/M_{\mathcal{T}})$.

[8] Note that even for masses as low as $\mu_{\mathcal{S}} \sim \mathcal{O}(v)$, for $\eta \simeq v$ and $\lambda_{\mathcal{S}} \sim \mathcal{O}(1)$, the interactions of $\mathcal{S}$ do not alter the phenomenology discussed here since the largest $\mathcal{S}$-generated effects are still suppressed as $\mathcal{O}(\varepsilon_t^2/\xi_{\mathcal{T}}^2)$.

from the search at ATLAS in ref. [392], and $m_{\mathcal{M}} = 0.8$ TeV from the CMS analysis of ref. [393].

As already discussed, the scenario depicted in Figure 5.7 remains viable under the lens of EW precision as long as we also have some heavy new dynamics yielding at the EW scale an imprint of $O_{22}^{HL^{(1)}}$ consistently with the correlation obtained in the left panel of Figure 5.6.

A simple way to obtain such NP contribution would be to consider the joint effect that the leptonic mixing of the vector-like partner would have together with the kinetic mixing of the Z', so far neglected. The Z-Z' mixing could also originate from charging the new scalar field $\mathcal{S}$ under both Abelian gauge groups, introducing a small misalignment with the standard hypercharge $U(1)_Y$ in the UV. However, the required mixing of the Z' would end up mediating light-quark pair annihilation into muons: the typical size of the Wilson coefficient of this four-fermion operator would be $\mathcal{O}(g_Y^2/m_{Z'}^2)$, in net tension with the di-muon bound from ATLAS [390], probing NP scales as high as 20 - 40 TeV for $\mathcal{O}(1)$ (dimensionless) couplings. Hence, we rule out here this possibility.

Interestingly, it is still possible to generate $O_{22}^{HL^{(1)}}$ without relying on the Z-Z' mixing, but rather invoking the presence in the UV theory of additional new vector-like leptonic states [394, 395]. These ones may be phenomenologically interesting in relation to the problem of the origin of neutrino masses as well as for the prediction of the anomalous magnetic moment $(g-2)_\mu$ [396], and may give peculiar multi-lepton signatures at colliders [397, 398].

In the most economic scenario, we may consider the presence in the UV theory of a pair of new vector-like muonic partners: a singlet of $SU(2)_L$, S_Y, and a triplet of $SU(2)_L$, T_Y, where in both cases the subscript Y denotes the hypercharge of the fermion. These fields would have their own mass terms controlled by the parameters M_{S_Y,T_Y}, and interact with the SM doublet L_2 via the Yukawa couplings $\mathcal{Y}_{S_Y,T_Y}$ according to:

$$\mathcal{Y}_{S_0}\overline{S}_{0,R}\tilde{H}^\dagger L_2 + \mathcal{Y}_{T_0}\overline{T}^A_{0,R}\tau^A\tilde{H}^\dagger L_2 + \text{h.c.}\ , \tag{5.20}$$

where we have reported the case of vector-like muonic partners with hypercharge $Y = 0$. We assume the new Yukawa couplings to be real. Another possibility of interest may be the one of replacing in eq. (5.20) $\tilde{H} = i\tau^2 H^*$ with the Higgs doublet, H, and involve then the pair of vector-like partners with hypercharge $Y = 1$.

Integrating out these vector-like states from the theory would generate contributions related to $\mathcal{O}^{HL^{(1,3)}}$ [395, 396] of the form:

$$\begin{aligned} C_{22}^{HL^{(1)}} &= \frac{\mathcal{Y}_{S_0}^2}{4M_{S_0}^2} - \frac{\mathcal{Y}_{S_1}^2}{4M_{S_1}^2} + \frac{3\mathcal{Y}_{T_0}^2}{4M_{T_0}^2} - \frac{3\mathcal{Y}_{T_1}^2}{4M_{T_1}^2}\ , \\ C_{22}^{HL^{(3)}} &= -\frac{\mathcal{Y}_{S_0}^2}{4M_{S_0}^2} - \frac{\mathcal{Y}_{S_1}^2}{4M_{S_1}^2} + \frac{\mathcal{Y}_{T_0}^2}{4M_{T_0}^2} + \frac{\mathcal{Y}_{T_1}^2}{4M_{T_1}^2}\ . \end{aligned} \tag{5.21}$$

Clearly, in order to have $C_{22}^{HL^{(1)}} \sim 0.1$ and negligible $C_{22}^{HL^{(3)}}$[9], one would need to rely on a tuning of the $Y = 0$ triplet Wilson coefficient with one of the contributions coming from the singlet vector-like muonic partner. However, once generated at the NP scale $\Lambda \sim \mathcal{O}(M_{T_0}) \gg v$, we observe that the relation established between the triplet and singlet contributions to $O^{HL^{(1,3)}}$ would be stable under the RG flow of the SMEFT.

A final comment is needed for the electron scenario reported in the right panel of Figure 5.6, that involves opposite signs for the Wilson coefficients of O^{Lu} and $O^{HL^{(1)}}$ discussed so far. For the former, we note that the sign highlighted in the matching in eq. (5.19) follows from having assumed the same sign for the charge of the vector-like top and muon partners under $U(1)_X$. Hence, assuming the vector-like electron partner to have the opposite $U(1)_X$ charge of the top-partner one would be sufficient to accomplish $C_{1133}^{Lu} > 0$. (Of course, this would also imply a distinct use in eq. (5.12) of $\mathcal{S}$ and $\mathcal{S}^\dagger$ couplings in the Yukawa terms of the vector-like partners involved to keep the theory invariant under $U(1)_X$.) For what concerns the generation of $C_{11}^{HL^{(1)}} < 0$, according to eq. (5.21) one needs to correlate once again the contribution stemming from S_0, or from S_1, with the effect coming from a $SU(2)_L$ triplet, that now needs to be identified with T_1, namely the triplet of hypercharge $Y = 1$.

Eventually, we wish also to comment on the possible role of the O^{eu} operator, so far neglected in this discussion, but of potential relevance more in general. In fact, as mentioned earlier, the presence of O^{eu} would be particularly needed in the case where hadronic corrections entering in the amplitude of $B \to K^* \ell\ell$ would be of the size originally estimated in [288]. In that case, a solution to flavour anomalies would be preferred in the muonic channel with NP Wilson coefficient C_{2233}^{eu} also substantially deviating from 0, as already discussed in subsection 5.3.1. Then, one would need to involve also the operator C_{22}^{He} to relieve possible tensions with EW precision. In a general picture, the required NP effects from $O_{11,22}^{He}$ can be obtained integrating out heavy vector-like $SU(2)_L$ leptonic doublets.

5.4.2 Leptoquark scenarios

An alternative way to reproduce the minimal EFT scenario of Figure 5.6 would be via *leptoquarks* (LQ), particles generically predicted in grand unified theories (GUTs) [399, 400]. Notoriously, LQ-induced dimension-six operators could be potentially dangerous as they would lead to proton decay at tree level, forcing to push their scale up to the GUT scale. However, the outcome may drastically change in models where the couplings of the LQs would be non-universal with respect to lepton and/or quark flavours. In such a case their mass could be much lower than what typically expected in GUTs and their signatures may actually be probed at present colliders. Interestingly, such LQs are candidates that could explain the lepton flavour universality violation – even at the loop level here considered [353, 357] – hinted in the recent LHCb and Belle data. However,

[9] We have indeed verified that a scenario involving at the same time C^{Lu} and $C^{HL^{(1,3)}}$ would not alter what already highlighted in Figure 5.6, with the best-fit value for $|C^{HL^{(3)}}|$ turning out to be of $\mathcal{O}(10^{-2})$.

this would imply generically a rather non-trivial flavour structure in the theory [401]. For a comprehensive survey of LQ models, see for instance [112, 344, 402–404].

Here, we limit ourselves to the case of toy models that specifically generate the operators of interest, namely $C^{Lu}_{\ell\ell 33}$ and $C^{eu}_{\ell\ell 33}$, for $\ell = 1$ (electron) or $\ell = 2$ (muon). In these peculiar LQ models we then assume that couplings between right-handed top quarks and light leptons are the only ones that actually matter for TeV phenomenology.

In Table 5.1 we list the vector and scalar LQs that constitute the potential LQ candidates able to generate the solutions for $b \to s\ell\ell$ anomalies at one loop under scrutiny.

Vector LQ: $\mathcal{V}^\mu$	$SU(3)_c \otimes SU(2)_L \otimes U(1)_Y$	Comments
$\overline{L}_\ell \gamma_\mu (\tau^A) Q_3 \, \mathcal{V}^{\mu(A)}$	$(\overline{\mathbf{3}}, \mathbf{1} \text{ or } \mathbf{3}, -2/3)$	not of interest
$(\mathcal{V}^\mu)^\dagger \, \overline{e}^c_\ell \gamma_\mu Q_3$	$(\overline{\mathbf{3}}, \mathbf{2}\,, 5/6)$	not of interest
$\overline{L}^c_\ell \gamma_\mu u_3 \, i\tau^2 \, \mathcal{V}^\mu$	$(\overline{\mathbf{3}}, \mathbf{2}, -1/6)$	generates $C^{Lu}_{\ell\ell 33} > 0$
$\overline{e}_\ell \gamma_\mu u_3 \, \mathcal{V}^\mu$	$(\overline{\mathbf{3}}, \mathbf{1}, -5/3)$	generates $C^{eu}_{\ell\ell 33} < 0$
Scalar LQ: $\mathcal{S}$		
$\overline{L}_\ell (\tau^A)(i\tau^2) \, Q^c_3 \, \mathcal{S}^{\dagger(A)}$	$(\overline{\mathbf{3}}, \mathbf{1} \text{ or } \mathbf{3}, 1/3)$	not of interest
$\overline{e}_\ell Q_3 \, i\tau^2 \mathcal{S}$	$(\overline{\mathbf{3}}, \mathbf{2}, -7/6)$	not of interest
$\overline{L}_\ell u_3 \, \mathcal{S}$	$(\overline{\mathbf{3}}, \mathbf{2}, -7/6)$	generates $C^{Lu}_{\ell\ell 33} < 0$
$\overline{e}^c_\ell u_3 \, \mathcal{S}$	$(\overline{\mathbf{3}}, \mathbf{1}, 1/3)$	generates $C^{eu}_{\ell\ell 33} > 0$

Table 5.1. Scalar and vector LQ interactions under scrutiny: LQs of interest for our analysis have to generate the dimension-six operators $O^{Lu,eu}_{\ell\ell 33}$.

Looking back at Figure 5.6, from the table above we recognize as the most economic LQ scenario for the resolution of B anomalies at one loop, the case of the vector LQ $\mathcal{V}^\mu \sim (\overline{\mathbf{3}}, \mathbf{2}, -1/6)$ for LUV effects originating from electron couplings, and the scalar $\mathcal{S} \sim (\overline{\mathbf{3}}, \mathbf{2}, -7/6)$ for the ones associated to muons. The interaction terms of interest are:

$$\mathcal{L}_{\mathcal{V}\overline{f}f} = \tilde{\lambda}_{te} \, \overline{L}^c_1 \gamma_\mu u_3 \, i\tau^2 \mathcal{V}^\mu + \text{h.c.} \quad , \quad \mathcal{L}_{\mathcal{S}\overline{f}f} = \lambda_{t\mu} \, \overline{L}_2 u_3 \mathcal{S} + \text{h.c.}, \tag{5.22}$$

leading to the corresponding matching condition:

$$C^{Lu}_{1133} = + \frac{|\tilde{\lambda}_{te}|^2}{M^2_{\mathcal{V}}} \quad , \quad C^{Lu}_{2233} = - \frac{|\lambda_{t\mu}|^2}{2M^2_{\mathcal{S}}} \, . \tag{5.23}$$

In Figure 5.8 we report in (lighter) magenta the underlying $1(2)\sigma$ region where B anomalies are addressed in concordance with the minimal EFT picture of Figure 5.6. In the same plot, we also show a conservative estimate of the present LHC constraint on the mass of the LQ states considered, based on the dedicated collider study of ref. [405].

We conclude noting that from the point of view of realizing the economic EFT result in Figure 5.6, these leptoquark models should again be supplied by the combination of a singlet and a triplet $SU(2)_L$ muon/electron partners. Otherwise, in these models the leading contribution to $C^{HL^{(1)}}_{\ell\ell}$ would appear only at the loop level, in net distinction

with the Z' scenario, where the Z-Z' mixing could be a priori exploited.

5.5 Summary

In this work we have revisited the analysis of $b \to s\ell\ell$ anomalies looking for NP solutions that generate these FCNC processes at one loop and do not involve any new source of flavour violation beyond the SM ones. To this end, we have performed a broad analysis with dimension-six operators in the SMEFT, combining the experimental data on B-physics with measurements of EWPO. The general outcome of our study is summarized in Figure 5.2 and, supported with Figure 5.4, shows that a resolution of B anomalies of the MFV nature can be made fully compatible with EW precision.

From the SMEFT results derived we have then proceeded to identifying a minimal EFT scenario as captured in Figure 5.6, that served as a simple guidance for SM UV completions. In this regard, we have explored in some detail the top-phillic and muon/electron-phillic Z', interesting for direct searches at collider as highlighted in Figure 5.7. We have also commented on the viable leptoquark scenarios, collected in Table 5.1. For both Z' and leptoquark solutions we have found that additional contributions were necessary in order to maintain Z coupling measurements under control: in particular, we have shown that a correlated pair of vector-like leptons, a $SU(2)_L$ singlet and a triplet, can realize the minimal EFT scenario depicted on Figure 5.6. We observe that the existence of these particles may be independently motivated by the heavy new dynamics underlying the origin of neutrino masses and/or by a tentative explanation of the $(g-2)_\mu$ anomaly [396].

We conclude by noting that the measurement of B decays at the scale of a few GeV is expected to reach a precision regime with the completion of the future runs at LHC and SuperKEKB. Hence, better measurements of the LUV observables and angular distributions of $b \to s\ell\ell$ will be available in the next few years from Belle II [330] and LHCb [406]. These will add a fundamental verification of the current interpretation of B anomalies and of the direction in our search for NP signatures. Along these lines, should these signals of LUV persist, their interplay with EW precision measurements could be further tested at future e^+e^- colliders. In particular, circular e^+e^- colliders running at the Z pole, such as the FCC-ee [407, 408] or CEPC [409], could test deviations in the lepton universality of neutral weak currents with more than one order of magnitude improvement in precision compared to current data. At linear colliders, like the ILC [410] or CLIC [411], where there is no proposed run at the Z pole, it would still be possible to obtain a significant improvement in the measurements of EWPO via radiative return to the Z [412]. Furthermore, the high-energy regime achievable at linear colliders would allow, after crossing the $t\bar{t}$ threshold, to directly test the effects of the interactions $O_{1133}^{Lu,eu}$ via $e^+e^- \to t\bar{t}$. For the muon case, on the other hand, to test $O_{2233}^{Lu,eu}$ one would still need to rely on more complicated signals, such as $t\bar{t}\mu^+\mu^-$, which would be in any case cleaner than at the LHC. (However, ideal optimal tests of these 4-fermion operators in 2-to-2 scattering processes would require a high-energy muon collider.) All of these could represent valuable additions from a "flavour" perspective in the interpretation of EW (and Higgs) measurements at these future machines within the EFT framework [255,

368].

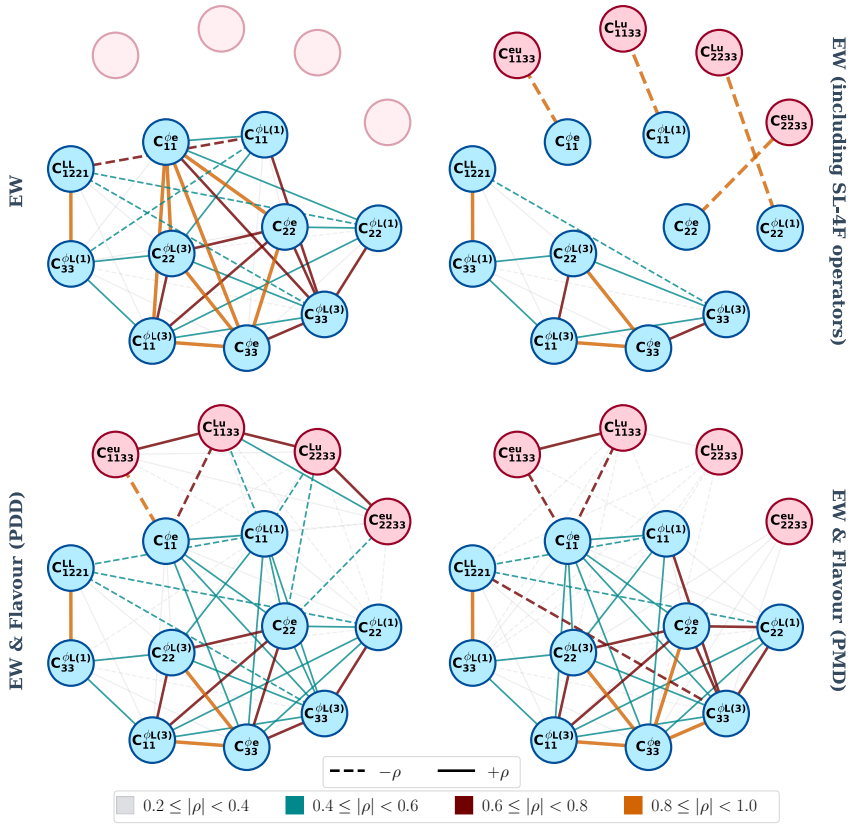

Figure 5.5. *Correlations among dimension-six operators involving leptonic currents in different scenarios. In the upper side we show the* ***EW*** *fit (upper-left panel), and the scenario where in the same setup the SL-4F operators are also included (upper-right panel), highlighting the anti-correlation among the set of Wilson coefficients* $C_{\ell\ell}^{HL^{(1)}}$, $C_{\ell\ell}^{He}$ *and* $C_{\ell\ell 33}^{Lu,eu}$. *In the lower-side panels we show how* $b \to s\ell\ell$ *measurements break these degeneracies, showing the* ***Flavour*** *fit for the PDD case (lower-left panel), and the PMD one (lower-right panel).*

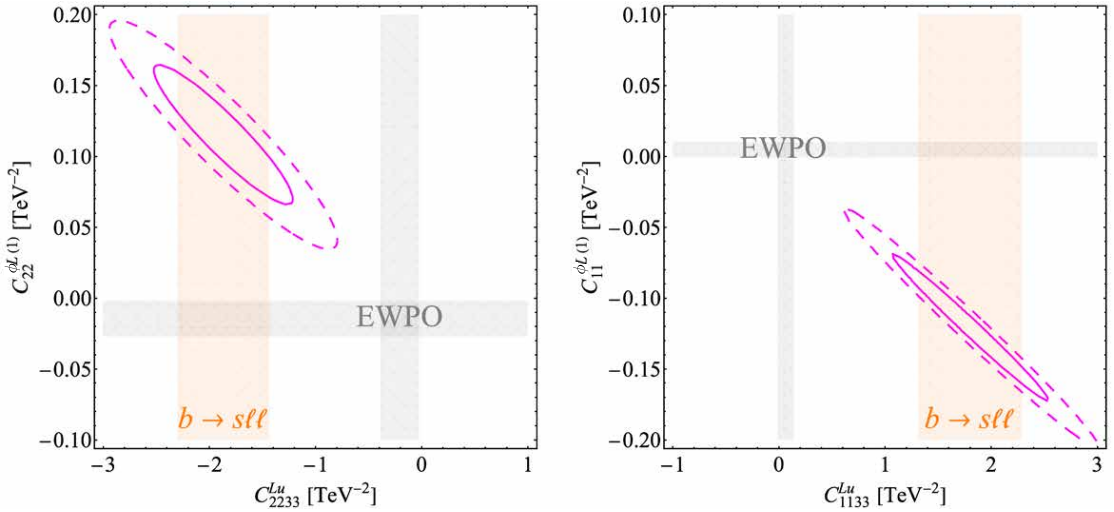

Figure 5.6. *The most economic EFT picture where B anomalies can be reconciled at one loop with EWPO. In (dashed) magenta the 1(2)σ correlation between the Wilson coefficients of the operators responsible of addressing B anomalies without any source of flavour violation beyond the Yukawa couplings of the SM. The minimal scenario involves LUV effects in the (electron) muon sector as highlighted by the 1σ orange band in the (right) left panel, originated from* $b \to s\ell\ell$ *data analyzed with a conservative approach to hadronic uncertainties. In same figure, the 1σ region allowed by EWPO within a single-operator analysis, horizontal and vertical grey bands.*

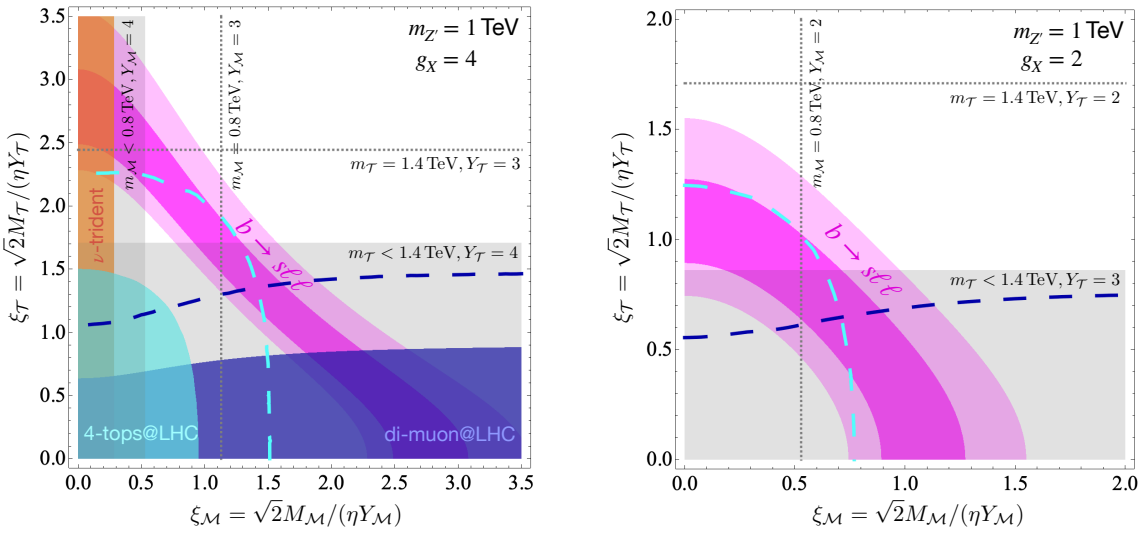

Figure 5.7. *68% (95%) probability region in (lighter) magenta for the minimal Z' model that addresses B anomalies in the parameter space identified by eq. (5.19), with $\eta = m_{Z'}/4$ (left panel), and $\eta = m_{Z'}/2$ (right panel), for $m_{Z'} = 1$ TeV. Relevant LHC constraints are reported in blue and cyan regions according to the analysis originally performed in ref. [353], together with the corresponding collider projections at 300 fb^{-1}. Finally, the gray regions underlie the parameter space where the mass of the vector-like partner lies below current collider limits for a fixed Yukawa coupling as explicitly reported, while dashed lines show the corresponding shift of the limit due to a smaller value of the same type of Yukawa coupling.*

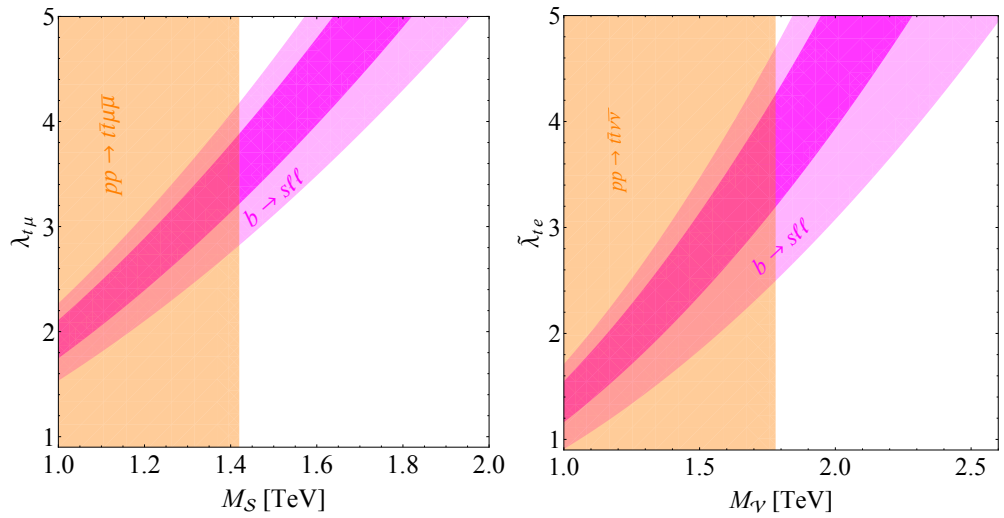

Figure 5.8. 68% (95%) probability region in magenta for the LQ candidates addressing $b \to s\ell\ell$ anomalies at one loop. The scalar (vector) LQ corresponds to a solution with LUV effects related to muon (electron) couplings. A conservative bound on the corresponding LQ mass is reported according to the analysis of ref. [405].

Appendices

A Details of Zh calculation

A.1 Orthogonal Projectors in $gg \to ZH$

In this appendix I present the explicit expressions of the projectors $\mathcal{P}_i^{\mu\nu\rho}$ appearing in eq.(**??**). The projectors are all normalized to 1. They are:

$$\begin{aligned}
\mathcal{P}_1^{\mu\nu\rho} &= \frac{m_Z}{\sqrt{2}s'p_T^2}\Big[p_1^\nu\epsilon^{\mu\rho p_1 p_2} - p_2^\mu\epsilon^{\nu\rho p_1 p_2} + q_t^\mu\epsilon^{\nu\rho p_2 p_3} && \text{(A.1)}\\
&+ q_u^\nu\epsilon^{\mu\rho p_1 p_3} + s'\epsilon^{\mu\nu\rho p_2} - s'\epsilon^{\mu\nu\rho p_1}\Big], && \text{(A.2)}\\
\mathcal{P}_2^{\mu\nu\rho} &= \frac{1}{\sqrt{2}s'p_T}\Big[q_u^\nu\epsilon^{\mu\rho p_1 p_3} + q_t^\mu\epsilon^{\nu\rho p_2 p_3}\Big], && \text{(A.3)}\\
\mathcal{P}_3^{\mu\nu\rho} &= \frac{\sqrt{3}}{2s'p_T}\Big[s'\epsilon^{\mu\nu\rho p_1} + s'\epsilon^{\mu\nu\rho p_2} - p_1^\nu\epsilon^{\mu\rho p_1 p_2} - p_2^\mu\epsilon^{\nu\rho p_1 p_2}\\
&+ (q_u^\nu\epsilon^{\mu\rho p_1 p_3} - q_t^\mu\epsilon^{\nu\rho p_2 p_3})\left(\frac{1}{3} + \frac{m_Z^2}{p_T^2}\right)\\
&+ \frac{m_Z^2}{p_T^2}(q_t^\mu\epsilon^{\nu\rho p_2 p_1} - q_u^\nu\epsilon^{\mu\rho p_1 p_2})\Big], && \text{(A.4)}\\
\mathcal{P}_4^{\mu\nu\rho} &= \frac{m_Z}{\sqrt{2}s'p_T^2}\Big[q_t^\mu(\epsilon^{\nu\rho p_2 p_1} - \epsilon^{\nu\rho p_2 p_3}) - q_u^\nu(\epsilon^{\mu\rho p_1 p_2} - \epsilon^{\mu\rho p_1 p_3})\Big], && \text{(A.5)}\\
\mathcal{P}_5^{\mu\nu\rho} &= \frac{1}{\sqrt{6}s'p_T}\Big[q_t^\mu\epsilon^{\nu\rho p_2 p_3} - q_u^\nu\epsilon^{\mu\rho p_1 p_3}\Big], && \text{(A.6)}\\
\mathcal{P}_6^{\mu\nu\rho} &= \frac{1}{s'p_T}\Big[g^{\mu\nu}\epsilon^{\rho p_1 p_2 p_3} + s'\epsilon^{\mu\nu\rho p_3} + p_1^\nu\epsilon^{\mu\rho p_2 p_3} - p_2^\mu\epsilon^{\nu\rho p_1 p_3} - \frac{s'}{2}\epsilon^{\mu\nu\rho p_2}\\
&+ \frac{1}{2}\left(p_1^\nu\epsilon^{\mu\rho p_1 p_2} + p_2^\mu\epsilon^{\nu\rho p_1 p_2} + q_u^\nu\epsilon^{\mu\rho p_1 p_3} - q_t^\mu\epsilon^{\nu\rho p_2 p_3} - s'\epsilon^{\mu\nu\rho p_1}\right)\\
&+ \frac{m_Z^2}{2p_T^2}(q_t^\mu\epsilon^{\nu\rho p_2 p_1} - q_u^\nu\epsilon^{\mu\rho p_1 p_2} + q_u^\nu\epsilon^{\mu\rho p_1 p_3} - q_t^\mu\epsilon^{\nu\rho p_2 p_3})\Big], && \text{(A.7)}
\end{aligned}$$

where we defined $q_t^\mu = (p_3^\mu - \frac{t'}{s'}p_2^\mu)$ and $q_u^\nu = (p_3^\nu - \frac{u'}{s'}p_1^\nu)$ and we used the shorthand notation $\epsilon^{\mu\nu\rho p_2} \equiv \epsilon^{\mu\nu\rho\sigma}p_2^\sigma$.

Using these projectors we obtained the relations between the form factors $\mathcal{A}_i$ defined

in in eq.(**??**) and those defined in section 2 of ref.[38]:

$$\mathcal{A}_1 = \frac{p_T^2}{2\sqrt{2}m_Z(p_T^2+m_Z^2)}\Big[(t'+u')F_{12}^+ - (t'-u')F_{12}^-\Big], \tag{A.8}$$

$$\mathcal{A}_2 = -\frac{p_T}{2\sqrt{2}(p_T^2+m_Z^2)}\Big[(t'+u')F_{12}^+ - (t'-u')F_{12}^- - \frac{p_T^2+m_Z^2}{2s'}((t'+u')F_3^+ - (t'-u')F_3^-)\Big], \tag{A.9}$$

$$\mathcal{A}_3 = \frac{p_T}{2\sqrt{3}(p_T^2+m_Z^2)}\Big[(t'+u')F_{12}^- - (t'-u')F_{12}^+ + (p_T^2+m_Z^2)(F_2^- + F_4)\Big], \tag{A.10}$$

$$\mathcal{A}_4 = -\frac{m_Z}{2\sqrt{2}(p_T^2+m_Z^2)}\Big[(t'+u')F_{12}^- - (t'-u')F_{12}^+ + (p_T^2+m_Z^2)\left((1-\frac{p_T^2}{m_Z^2})F_2^- + 2F_4\right)\Big], \tag{A.11}$$

$$\mathcal{A}_5 = \frac{p_T}{2\sqrt{6}(p_T^2+m_Z^2)}\Big[(t'+u')F_{12}^- - (t'-u')F_{12}^+ + (p_T^2+m_Z^2)\left(4(F_2^- + F_4) + \frac{3}{2s'}\left((t'+u')F_3^- - (t'-u')F_3^+\right)\right)\Big], \tag{A.12}$$

$$\mathcal{A}_6 = \frac{p_T}{2}F_4. \tag{A.13}$$

A.2 Two-loop Results

The NLO amplitude can be written in terms of three contributions, namely the two-loop 1PI triangle, the two-loop 1PI box and the reducible double-triangle diagrams,

$$\mathcal{A}_i^{(1)} = \mathcal{A}_i^{(1,\triangle)} + \mathcal{A}_i^{(1,\square)} + \mathcal{A}_i^{(1,\bowtie)} \ . \tag{A.14}$$

In this section, the exact analytic results for the triangle and double triangle topologies are presented.

The two-loop triangle results are

$$\mathcal{A}_1^{(1,\triangle)} = \frac{p_T^2\ (\hat{s}-\Delta_m)}{4\sqrt{2}m_Z}\frac{\mathcal{K}_t^{(2l)}}{(p_T^2+m_Z^2)}, \tag{A.15}$$

$$\mathcal{A}_2^{(1,\triangle)} = -\frac{p_T\ (\hat{s}-\Delta_m)}{4\sqrt{2}}\frac{\mathcal{K}_t^{(2l)}}{(p_T^2+m_Z^2)}, \tag{A.16}$$

$$\mathcal{A}_3^{(1,\triangle)} = \frac{p_T\ (\hat{t}-\hat{u})}{4\sqrt{3}}\frac{\mathcal{K}_t^{(2l)}}{(p_T^2+m_Z^2)}, \tag{A.17}$$

$$\mathcal{A}_4^{(1,\triangle)} = -\frac{m_Z\ (\hat{t}-\hat{u})}{4\sqrt{2}}\frac{\mathcal{K}_t^{(2l)}}{(p_T^2+m_Z^2)}, \tag{A.18}$$

$$\mathcal{A}_5^{(1,\triangle)} = -\frac{p_T\ (\hat{t}-\hat{u})}{4\sqrt{6}}\frac{\mathcal{K}_t^{(2l)}}{(p_T^2+m_Z^2)}, \tag{A.19}$$

$$\mathcal{A}_6^{(1,\triangle)} = 0, \tag{A.20}$$

where the $\mathcal{K}_t^{(2l)}$ function is defined in eq.(4.11) of ref.[413]. While the double-triangle for-factors are found to be.

$$\mathcal{A}_1^{(1,\bowtie)} = -\frac{m_t^2 p_T^2}{4\sqrt{2}\ m_Z\left(m_Z^2+p_T^2\right)^2}\left[F_t(\hat{t})\left(G_t(\hat{t},\hat{u})-G_b(\hat{t},\hat{u})\right)+(\hat{t}\leftrightarrow\hat{u})\right], \tag{A.21}$$

$$\mathcal{A}_2^{(1,\bowtie)} = \frac{m_t^2 p_T}{4\sqrt{2}\left(m_Z^2+p_T^2\right)^2}\left[F_t(\hat{t})\left(G_t(\hat{t},\hat{u})-G_b(\hat{t},\hat{u})\right)+(\hat{t}\leftrightarrow\hat{u})\right], \tag{A.22}$$

$$\mathcal{A}_3^{(1,\bowtie)} = \frac{m_t^2 p_T}{4\sqrt{3}\ \hat{s}\left(m_Z^2+p_T^2\right)^2}\left[\left(m_h^2-\hat{t}\right)F_t(\hat{t})\left(G_t(\hat{t},\hat{u})-G_b(\hat{t},\hat{u})\right)-(\hat{t}\leftrightarrow\hat{u})\right], \tag{A.23}$$

$$\mathcal{A}_4^{(1,\bowtie)} = -\frac{m_t^2}{4\sqrt{2}\ m_Z\hat{s}^2\left(m_Z^2+p_T^2\right)^2}\Bigg[\Big(m_Z^2\left(m_h^2-\hat{t}\right)^2 - \hat{t}\left(m_Z^2-\hat{u}\right)^2\Big)F_t(\hat{t})\left(G_t(\hat{t},\hat{u})-G_b(\hat{t},\hat{u})\right)-(\hat{t}\leftrightarrow\hat{u})\Bigg], \tag{A.24}$$

$$\mathcal{A}_5^{(1,\bowtie)} = -\frac{m_t^2 p_T}{4\sqrt{6}\ \hat{s}\left(m_Z^2+p_T^2\right)^2}\Bigg[\left(4m_Z^2-\hat{s}-4\hat{u}\right)F_t(\hat{t})\left(G_t(\hat{t},\hat{u})-G_b(\hat{t},\hat{u})\right) - (\hat{t}\leftrightarrow\hat{u})\Bigg], \tag{A.25}$$

$$\mathcal{A}_6^{(1,\bowtie)} = 0, \tag{A.26}$$

where

$$\begin{aligned} F_t(\hat{t}) &= \frac{1}{\left(m_h^2-\hat{t}\right)^2}\Bigg[2\hat{t}\Big(B_0\left(\hat{t},m_t^2,m_t^2\right)-B_0\left(m_h^2,m_t^2,m_t^2\right)\Big) \\ &+ \left(m_h^2-\hat{t}\right)\Big(\left(m_h^2-4m_t^2-\hat{t}\right)C_0\left(0,m_h^2,\hat{t},m_t^2,m_t^2,m_t^2\right)-2\Big)\Bigg], \end{aligned} \tag{A.27}$$

$$\begin{aligned} G_x(\hat{t},\hat{u}) &= \left(m_Z^2-\hat{u}\right)\Bigg[m_Z^2\Big(B_0\left(\hat{t},m_x^2,m_x^2\right)-B_0\left(m_Z^2,m_x^2,m_x^2\right)\Big) \\ &+ \left(\hat{t}-m_Z^2\right)\Big(2m_x^2C_0\left(0,\hat{t},m_Z^2,m_x^2,m_x^2,m_x^2\right)+1\Big)\Bigg]. \end{aligned} \tag{A.28}$$

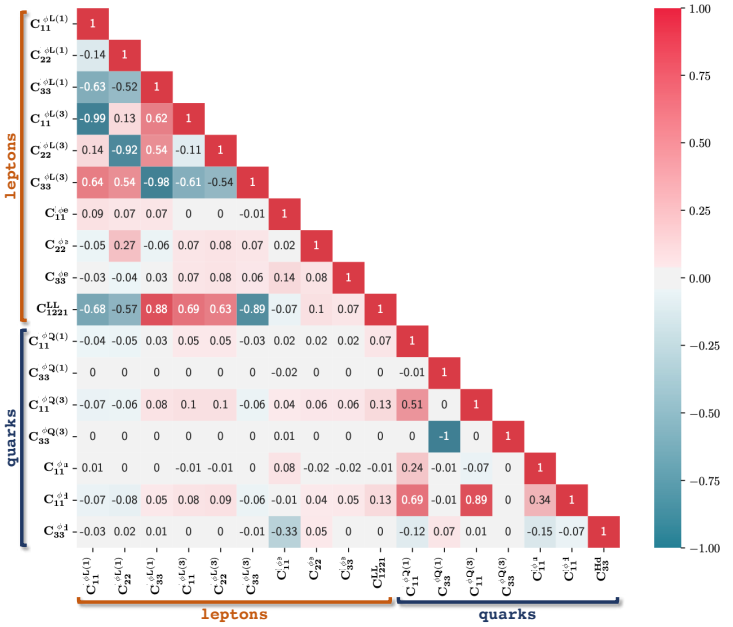

Figure A.1. *The correlation matrix extracted from the SMEFT analysis of the set of independent operators in eqs. (5.3), (5.9), (5.10), including only their effects at tree-level. The two distinct groups of correlated Wilson coefficients associated to leptonic and quark interactions are remarked as "leptons" and "quarks", respectively. Note that, compared to Figure 5.3, in this tree-level analysis there is a significant decorrelation between the constraints on quarks and lepton operators.*

A.3 Discussions on EW fits

Here we revisit the constraints set by EWPO on the parameter space of the SMEFT. We make minimal flavour assumptions and include all quark and lepton operators described in the **EW** fit presented in section 5.2. Measurements of EWPO have been extensively studied in the literature [354, 367, 414–422] within the SMEFT framework. The purpose here is to provide further details on the correlation between quark and lepton sectors constrained by EWPO, illustrating some of the effects when going beyond the tree-level analysis.

The experimental inputs are the same considered for the **EW** fit in section 5.2, and include, in particular, the full set measurements taken at LEP/SLD at the Z pole, as well as the measurements of the W boson obtained at LEP II, the Tevatron and the LHC (e.g. mass, width, branching ratios as well as the determination of $|V_{tb}|$ at the LHC [1]). For these fits we use the `HEPfit`package [99] as for the rest of the work.

We first consider the case of the **EW** fit at the tree level. In this case, the results

[1]The extraction of $|V_{tb}|$ could be, a priori, affected by other SMEFT effects entering in single-top production, e.g. 4-fermion operators. Such effects are neglected in our analysis. The only effect of this input in the EW fits in this paper is to lift a flat direction that would otherwise appear between $C_{33}^{HQ^{(1)}}$ and $C_{33}^{HQ^{(3)}}$, had we excluded this measurement. Even with this input, these two coefficients are nearly 100% correlated, as can be seen in Figure A.1.

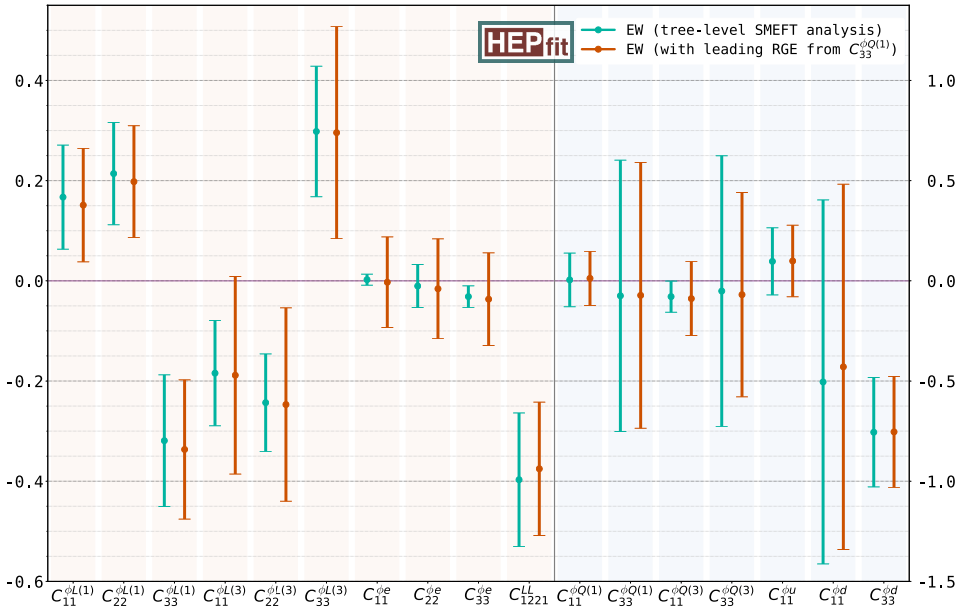

Figure A.2. *Comparison of the mean and standard deviation of the marginalized posterior for the Wilson coefficients (in TeV^{-2}) of the operators included in the* **EW** *fit under two different approximations: in green the results from a pure tree-level analysis; in orange we show the result including the dominant log-enhanced one-loop terms. See text for details.*

of the fit reveal that while there is sizable correlation between the left-handed leptonic operators, as well as between the different quark operators, both sector are however decoupled to a good extent in the fit as can be seen from Figure A.1.

For the main fits presented in section 5.3, however, we also consider the leading logarithmically enhanced contributions at one-loop level via RG running. For our purposes, and considering the size of the bounds on the different operators from the EW fit, the most important contribution comes from $C_{33}^{HQ^{(1)}}$. This induces an universal contribution that propagates into all EWPO. As a result of this, and similar to what was seen between the leptonic operators and the 4-fermion operators due to their interplay in eqs. (5.8), a non-trivial pattern of correlations between the lepton and quark operator sectors in the **EW** fit arises, as shown in Figure 5.3. Similar to the change in the bounds on the leptonic operators in the **EW+Flavour** fit once we included the RG effects of the four-fermion operators, the bounds on the leptonic operators also relax in the EW fit once we include the RG effects from $C_{33}^{HQ^{(1)}}$. This is shown in Figure A.2. However, unlike in the **EW+Flavour** fit, such effects do not induce a significant shift in the central values of the Wilson coefficients, which is simply due to the fact that the data selects $C_{33}^{HQ^{(1)}}$

to be centered around zero.

As can be seen in Figure A.2, the relaxation of the bounds can be in some cases rather dramatic, which brings about the question of what could be the impact of further effects not included in our analysis. We estimated that including the main RG effects for all the other operators in the EW fit amounts to changes of at most $\sim 25\%$. One should also note that finite terms involving the Wilson coefficients of the quark coupling may become relevant at this point. As can be deduced from the full NLO results presented in [422], these are not expected to significantly change the picture. In any case, the overall conclusions on this paper regarding the reconciliation between EW data and B anomalies hold true.

Bibliography

[1] L. Alasfar, G. Degrassi, P. P. Giardino, R. Gröber, and M. Vitti, "Virtual corrections to $gg \to ZH$ via a transverse momentum expansion," *JHEP* **05** (2021) 168, arXiv:2103.06225 [hep-ph].

[2] L. Alasfar, R. Corral Lopez, and R. Gröber, "Probing Higgs couplings to light quarks via Higgs pair production," *JHEP* **11** (2019) 088, arXiv:1909.05279 [hep-ph].

[3] L. Alasfar, A. Azatov, J. de Blas, A. Paul, and M. Valli, "B anomalies under the lens of electroweak precision," *JHEP* **12** (2020) 016, arXiv:2007.04400 [hep-ph].

[4] M. Bonetti, K. Melnikov, and L. Tancredi, "Higher order corrections to mixed QCD-EW contributions to Higgs boson production in gluon fusion," *Phys. Rev. D* **97** no. 5, (2018) 056017, arXiv:1801.10403 [hep-ph]. [Erratum: Phys.Rev.D 97, 099906 (2018)].

[5] X. Chen, T. Gehrmann, E. W. N. Glover, A. Huss, B. Mistlberger, and A. Pelloni, "Fully Differential Higgs Boson Production to Third Order in QCD," *Phys. Rev. Lett.* **127** no. 7, (2021) 072002, arXiv:2102.07607 [hep-ph].

[6] G. Billis, B. Dehnadi, M. A. Ebert, J. K. L. Michel, and F. J. Tackmann, "Higgs pT Spectrum and Total Cross Section with Fiducial Cuts at Third Resummed and Fixed Order in QCD," *Phys. Rev. Lett.* **127** no. 7, (2021) 072001, arXiv:2102.08039 [hep-ph].

[7] **ATLAS** Collaboration, "Measurements and interpretations of Higgs-boson fiducial cross sections in the diphoton decay channel using 139 fb^{-}1 of pp collision data at $\sqrt{s} = 13$ TeV with the ATLAS detector,".

[8] M. Bonetti, K. Melnikov, and L. Tancredi, "Three-loop mixed QCD-electroweak corrections to Higgs boson gluon fusion," *Phys. Rev. D* **97** no. 3, (2018) 034004, arXiv:1711.11113 [hep-ph].

[9] M. Bonetti, E. Panzer, V. A. Smirnov, and L. Tancredi, "Two-loop mixed QCD-EW corrections to $gg \to Hg$," *JHEP* **11** (2020) 045, arXiv:2007.09813 [hep-ph].

[10] M. Becchetti, R. Bonciani, V. Del Duca, V. Hirschi, F. Moriello, and A. Schweitzer, "Next-to-leading order corrections to light-quark mixed QCD-EW

contributions to Higgs boson production," *Phys. Rev. D* **103** no. 5, (2021) 054037, arXiv:2010.09451 [hep-ph].

[11] M. L. Czakon and M. Niggetiedt, "Exact quark-mass dependence of the Higgs-gluon form factor at three loops in QCD," *JHEP* **05** (2020) 149, arXiv:2001.03008 [hep-ph].

[12] M. Czakon, R. V. Harlander, J. Klappert, and M. Niggetiedt, "Exact Top-Quark Mass Dependence in Hadronic Higgs Production," *Phys. Rev. Lett.* **127** no. 16, (2021) 162002, arXiv:2105.04436 [hep-ph].

[13] F. Maltoni, E. Vryonidou, and M. Zaro, "Top-quark mass effects in double and triple Higgs production in gluon-gluon fusion at NLO," *JHEP* **11** (2014) 079, arXiv:1408.6542 [hep-ph].

[14] K. Kudashkin, K. Melnikov, and C. Wever, "Two-loop amplitudes for processes $gg \to Hg, qg \to Hq$ and $q\bar{q} \to Hg$ at large Higgs transverse momentum," *JHEP* **02** (2018) 135, arXiv:1712.06549 [hep-ph].

[15] J. M. Lindert, K. Kudashkin, K. Melnikov, and C. Wever, "Higgs bosons with large transverse momentum at the LHC," *Phys. Lett. B* **782** (2018) 210–214, arXiv:1801.08226 [hep-ph].

[16] S. P. Jones, M. Kerner, and G. Luisoni, "Next-to-leading-order qcd corrections to higgs boson plus jet production with full top-quark mass dependence," *Phys. Rev. Lett.* **120** (Apr, 2018) 162001. https://link.aps.org/doi/10.1103/PhysRevLett.120.162001.

[17] **LHC Higgs Cross Section Working Group** Collaboration, D. de Florian *et al.*, "Handbook of LHC Higgs Cross Sections: 4. Deciphering the Nature of the Higgs Sector," arXiv:1610.07922 [hep-ph].

[18] V. Hankele, G. Klämke, D. Zeppenfeld, and T. Figy, "Anomalous higgs boson couplings in vector boson fusion at the cern lhc," *Physical Review D* **74** no. 9, (2006) 095001.

[19] T. Han, G. Valencia, and S. Willenbrock, "Structure function approach to vector boson scattering in p p collisions," *Phys. Rev. Lett.* **69** (1992) 3274–3277, arXiv:hep-ph/9206246.

[20] T. Figy, C. Oleari, and D. Zeppenfeld, "Next-to-leading order jet distributions for Higgs boson production via weak boson fusion," *Phys. Rev. D* **68** (2003) 073005, arXiv:hep-ph/0306109.

[21] E. L. Berger and J. M. Campbell, "Higgs boson production in weak boson fusion at next-to-leading order," *Phys. Rev. D* **70** (2004) 073011, arXiv:hep-ph/0403194.

[22] M. Gomez-Bock, M. Mondragon, M. Muhlleitner, M. Spira, and P. M. Zerwas, "Concepts of Electroweak Symmetry Breaking and Higgs Physics," in *4th CERN-CLAF School of High-Energy Physics*, pp. 177–238. 12, 2007. arXiv:0712.2419 [hep-ph].

[23] P. Bolzoni, F. Maltoni, S.-O. Moch, and M. Zaro, "Higgs production via vector-boson fusion at NNLO in QCD," *Phys. Rev. Lett.* **105** (2010) 011801, arXiv:1003.4451 [hep-ph].

[24] A. Denner, S. Dittmaier, S. Kallweit, and A. Mück, "HAWK 2.0: A Monte Carlo program for Higgs production in vector-boson fusion and Higgs strahlung at hadron colliders," *Comput. Phys. Commun.* **195** (2015) 161–171, arXiv:1412.5390 [hep-ph].

[25] T. Han and S. Willenbrock, "QCD correction to the p p —> W H and Z H total cross-sections," *Phys. Lett. B* **273** (1991) 167–172.

[26] O. Brein, A. Djouadi, and R. Harlander, "NNLO QCD corrections to the Higgs-strahlung processes at hadron colliders," *Phys. Lett. B* **579** (2004) 149–156, arXiv:hep-ph/0307206.

[27] S. Amoroso *et al.*, "Les Houches 2019: Physics at TeV Colliders: Standard Model Working Group Report," in *11th Les Houches Workshop on Physics at TeV Colliders: PhysTeV Les Houches*. 3, 2020. arXiv:2003.01700 [hep-ph].

[28] M. Cepeda *et al.*, "Report from Working Group 2: Higgs Physics at the HL-LHC and HE-LHC," *CERN Yellow Rep. Monogr.* **7** (2019) 221–584, arXiv:1902.00134 [hep-ph].

[29] C. Englert, M. McCullough, and M. Spannowsky, "Gluon-initiated associated production boosts Higgs physics," *Phys. Rev. D* **89** no. 1, (2014) 013013, arXiv:1310.4828 [hep-ph].

[30] C. Englert, R. Rosenfeld, M. Spannowsky, and A. Tonero, "New physics and signal-background interference in associated $pp \to HZ$ production," *EPL* **114** no. 3, (2016) 31001, arXiv:1603.05304 [hep-ph].

[31] B. A. Kniehl, "Associated Production of Higgs and Z Bosons From Gluon Fusion in Hadron Collisions," *Phys. Rev. D* **42** (1990) 2253–2258.

[32] D. A. Dicus and C. Kao, "Higgs Boson - Z^0 Production From Gluon Fusion," *Phys. Rev. D* **38** (1988) 1008. [Erratum: Phys.Rev.D 42, 2412 (1990)].

[33] L. Altenkamp, S. Dittmaier, R. V. Harlander, H. Rzehak, and T. J. Zirke, "Gluon-induced Higgs-strahlung at next-to-leading order QCD," *JHEP* **02** (2013) 078, arXiv:1211.5015 [hep-ph].

[34] R. V. Harlander, A. Kulesza, V. Theeuwes, and T. Zirke, "Soft gluon resummation for gluon-induced Higgs Strahlung," *JHEP* **11** (2014) 082, arXiv:1410.0217 [hep-ph].

[35] A. Hasselhuhn, T. Luthe, and M. Steinhauser, "On top quark mass effects to $gg \to ZH$ at NLO," *JHEP* **01** (2017) 073, arXiv:1611.05881 [hep-ph].

[36] R. Harlander, J. Klappert, C. Pandini, and A. Papaefstathiou, "Exploiting the WH/ZH symmetry in the search for New Physics," *Eur. Phys. J. C* **78** no. 9, (2018) 760, arXiv:1804.02299 [hep-ph].

[37] B. Hespel, F. Maltoni, and E. Vryonidou, "Higgs and Z boson associated production via gluon fusion in the SM and the 2HDM," *JHEP* **06** (2015) 065, arXiv:1503.01656 [hep-ph].

[38] J. Davies, G. Mishima, and M. Steinhauser, "Virtual corrections to $gg \to ZH$ in the high-energy and large-m_t limits," arXiv:2011.12314 [hep-ph].

[39] L. Chen, G. Heinrich, S. P. Jones, M. Kerner, J. Klappert, and J. Schlenk, "ZH production in gluon fusion: two-loop amplitudes with full top quark mass dependence," arXiv:2011.12325 [hep-ph].

[40] R. Bonciani, G. Degrassi, P. P. Giardino, and R. Gröber, "Analytical Method for Next-to-Leading-Order QCD Corrections to Double-Higgs Production," *Phys. Rev. Lett.* **121** no. 16, (2018) 162003, arXiv:1806.11564 [hep-ph].

[41] A. Broggio, A. Ferroglia, R. Frederix, D. Pagani, B. D. Pecjak, and I. Tsinikos, "Top-quark pair hadroproduction in association with a heavy boson at NLO+NNLL including EW corrections," *JHEP* **08** (2019) 039, arXiv:1907.04343 [hep-ph].

[42] A. Kulesza, L. Motyka, D. Schwartländer, T. Stebel, and V. Theeuwes, "Associated top quark pair production with a heavy boson: differential cross sections at NLO+NNLL accuracy," *Eur. Phys. J. C* **80** no. 5, (2020) 428, arXiv:2001.03031 [hep-ph].

[43] G. Bevilacqua, H.-Y. Bi, H. B. Hartanto, M. Kraus, and M. Worek, "The simplest of them all: $t\bar{t}W^{\pm}$ at NLO accuracy in QCD," *JHEP* **08** (2020) 043, arXiv:2005.09427 [hep-ph].

[44] A. Denner and G. Pelliccioli, "NLO QCD corrections to off-shell $\mathrm{t\bar{t}W^{+}}$ production at the LHC," *JHEP* **11** (2020) 069, arXiv:2007.12089 [hep-ph].

[45] G. Bevilacqua, H.-Y. Bi, H. B. Hartanto, M. Kraus, J. Nasufi, and M. Worek, "NLO QCD corrections to off-shell $t\bar{t}W^{\pm}$ production at the LHC: correlations and asymmetries," *Eur. Phys. J. C* **81** no. 7, (2021) 675, arXiv:2012.01363 [hep-ph].

[46] A. Denner and G. Pelliccioli, "Combined NLO EW and QCD corrections to off-shell $\mathrm{t\bar{t}W}$ production at the LHC," *Eur. Phys. J. C* **81** no. 4, (2021) 354, arXiv:2102.03246 [hep-ph].

[47] F. F. Cordero, M. Kraus, and L. Reina, "Top-quark pair production in association with a $W^{\pm}$ gauge boson in the POWHEG-BOX," *Phys. Rev. D* **103** no. 9, (2021) 094014, arXiv:2101.11808 [hep-ph].

[48] G. Bevilacqua, H. Y. Bi, F. Febres Cordero, H. B. Hartanto, M. Kraus, J. Nasufi, L. Reina, and M. Worek, "Modeling uncertainties of $t\bar{t}W^{\pm}$ multilepton signatures," *Phys. Rev. D* **105** no. 1, (2022) 014018, arXiv:2109.15181 [hep-ph].

[49] A. Denner, J.-N. Lang, and M. Pellen, "Full NLO QCD corrections to off-shell $\mathrm{tt}^{-}\mathrm{bb}^{-}$ production," *Phys. Rev. D* **104** no. 5, (2021) 056018, arXiv:2008.00918 [hep-ph].

[50] G. Bevilacqua, H.-Y. Bi, H. B. Hartanto, M. Kraus, M. Lupattelli, and M. Worek, "$t\bar{t}b\bar{b}$ at the LHC: on the size of corrections and b-jet definitions," *JHEP* **08** (2021) 008, arXiv:2105.08404 [hep-ph].

[51] A. Denner, J.-N. Lang, M. Pellen, and S. Uccirati, "NLO QCD + electroweak predictions for off-shell ttH production at the LHC," in *12th International Workshop on Top Quark Physics*. 12, 2019. arXiv:1912.08493 [hep-ph].

[52] F. Maltoni, E. Vryonidou, and C. Zhang, "Higgs production in association with a top-antitop pair in the Standard Model Effective Field Theory at NLO in QCD," *JHEP* **10** (2016) 123, arXiv:1607.05330 [hep-ph].

[53] F. Dulat, A. Lazopoulos, and B. Mistlberger, "iHixs 2 — Inclusive Higgs cross sections," *Comput. Phys. Commun.* **233** (2018) 243–260, arXiv:1802.00827 [hep-ph].

[54] S. Alioli, P. Nason, C. Oleari, and E. Re, "NLO Higgs boson production via gluon fusion matched with shower in POWHEG," *JHEP* **04** (2009) 002, arXiv:0812.0578 [hep-ph].

[55] P. Nason and C. Oleari, "NLO Higgs boson production via vector-boson fusion matched with shower in POWHEG," *JHEP* **02** (2010) 037, arXiv:0911.5299 [hep-ph].

[56] E. Bagnaschi, G. Degrassi, P. Slavich, and A. Vicini, "Higgs production via gluon fusion in the POWHEG approach in the SM and in the MSSM," *JHEP* **02** (2012) 088, arXiv:1111.2854 [hep-ph].

[57] J. M. Campbell, R. K. Ellis, R. Frederix, P. Nason, C. Oleari, and C. Williams, "NLO Higgs Boson Production Plus One and Two Jets Using the POWHEG

BOX, MadGraph4 and MCFM," *JHEP* **07** (2012) 092, arXiv:1202.5475 [hep-ph].

[58] G. Luisoni, P. Nason, C. Oleari, and F. Tramontano, "$HW^{\pm}$/HZ + 0 and 1 jet at NLO with the POWHEG BOX interfaced to GoSam and their merging within MiNLO," *JHEP* **10** (2013) 083, arXiv:1306.2542 [hep-ph].

[59] B. Jäger, F. Schissler, and D. Zeppenfeld, "Parton-shower effects on Higgs boson production via vector-boson fusion in association with three jets," *JHEP* **07** (2014) 125, arXiv:1405.6950 [hep-ph].

[60] H. B. Hartanto, B. Jager, L. Reina, and D. Wackeroth, "Higgs boson production in association with top quarks in the POWHEG BOX," *Phys. Rev. D* **91** no. 9, (2015) 094003, arXiv:1501.04498 [hep-ph].

[61] J. Alwall, R. Frederix, S. Frixione, V. Hirschi, F. Maltoni, O. Mattelaer, H. S. Shao, T. Stelzer, P. Torrielli, and M. Zaro, "The automated computation of tree-level and next-to-leading order differential cross sections, and their matching to parton shower simulations," *JHEP* **07** (2014) 079, arXiv:1405.0301 [hep-ph].

[62] "Higgs corss-sections working group." https://twiki.cern.ch/twiki/bin/view/LHCPhysics/LHCHWG?redirectedfrom=LHCPhysics.LHCHXSWG.

[63] C. Degrande, G. Durieux, F. Maltoni, K. Mimasu, E. Vryonidou, and C. Zhang, "Automated one-loop computations in the standard model effective field theory," *Phys. Rev. D* **103** no. 9, (2021) 096024, arXiv:2008.11743 [hep-ph].

[64] R. Frederix, D. Pagani, and M. Zaro, "Large NLO corrections in $t\bar{t}W^{\pm}$ and $t\bar{t}t\bar{t}$ hadroproduction from supposedly subleading EW contributions," *JHEP* **02** (2018) 031, arXiv:1711.02116 [hep-ph].

[65] **CMS** Collaboration, A. M. Sirunyan *et al.*, "Search for the production of four top quarks in the single-lepton and opposite-sign dilepton final states in proton-proton collisions at $\sqrt{s} = 13$ TeV," *JHEP* **11** (2019) 082, arXiv:1906.02805 [hep-ex].

[66] **ATLAS** Collaboration, G. Aad *et al.*, "Evidence for $t\bar{t}t\bar{t}$ production in the multilepton final state in proton–proton collisions at $\sqrt{s} = 13$ TeV with the ATLAS detector," *Eur. Phys. J. C* **80** no. 11, (2020) 1085, arXiv:2007.14858 [hep-ex].

[67] **CMS** Collaboration, A. M. Sirunyan *et al.*, "Measurement of the cross section for $t\bar{t}$ production with additional jets and b jets in pp collisions at $\sqrt{s} = 13$ TeV," *JHEP* **07** (2020) 125, arXiv:2003.06467 [hep-ex].

[68] **ATLAS** Collaboration, "Measurements of fiducial and differential cross-sections of $t\bar{t}$ production with additional heavy-flavour jets in proton-proton collisions at $\sqrt{s} = 13$ TeV with the ATLAS detector," Tech. Rep. ATLAS-CONF-2018-029, 2018.

[69] J. D'Hondt, A. Mariotti, K. Mimasu, S. Moortgat, and C. Zhang, "Learning to pinpoint effective operators at the LHC: a study of the $t\bar{t}b\bar{b}$ signature," *JHEP* **11** (2018) 131, arXiv:1807.02130 [hep-ph].

[70] N. P. Hartland, F. Maltoni, E. R. Nocera, J. Rojo, E. Slade, E. Vryonidou, and C. Zhang, "A Monte Carlo global analysis of the Standard Model Effective Field Theory: the top quark sector," *JHEP* **04** (2019) 100, arXiv:1901.05965 [hep-ph].

[71] J. de Blas, M. Chala, and J. Santiago, "Renormalization Group Constraints on New Top Interactions from Electroweak Precision Data," *JHEP* **09** (2015) 189, arXiv:1507.00757 [hep-ph].

[72] L. Alasfar, J. de Blas, and R. Gröber, "Higgs probes of top quark contact interactions and their interplay with the Higgs self-coupling," arXiv:2202.02333 [hep-ph].

[73] **SMEFiT** Collaboration, J. J. Ethier, G. Magni, F. Maltoni, L. Mantani, E. R. Nocera, J. Rojo, E. Slade, E. Vryonidou, and C. Zhang, "Combined SMEFT interpretation of Higgs, diboson, and top quark data from the LHC," *JHEP* **11** (2021) 089, arXiv:2105.00006 [hep-ph].

[74] A. Dedes, W. Materkowska, M. Paraskevas, J. Rosiek, and K. Suxho, "Feynman rules for the Standard Model Effective Field Theory in R_ξ -gauges," *JHEP* **06** (2017) 143, arXiv:1704.03888 [hep-ph].

[75] H. Patel, "Package-X: A Mathematica package for the analytic calculation of one-loop integrals," *Comput. Phys. Commun.* **197** (2015) 276–290, arXiv:1503.01469 [hep-ph].

[76] P. Maierhöfer, J. Usovitsch, and P. Uwer, "Kira—A Feynman integral reduction program," *Comput. Phys. Commun.* **230** (2018) 99–112, arXiv:1705.05610 [hep-ph].

[77] T. Hahn, "Generating Feynman diagrams and amplitudes with FeynArts 3," *Comput. Phys. Commun.* **140** (2001) 418–431, arXiv:hep-ph/0012260.

[78] A. Alloul, N. D. Christensen, C. Degrande, C. Duhr, and B. Fuks, "FeynRules 2.0 - A complete toolbox for tree-level phenomenology," *Comput. Phys. Commun.* **185** (2014) 2250–2300, arXiv:1310.1921 [hep-ph].

[79] A. Smirnov, "Algorithm FIRE – Feynman Integral REduction," *JHEP* **10** (2008) 107, arXiv:0807.3243 [hep-ph].

[80] S. Dawson and P. P. Giardino, "Higgs decays to ZZ and $Z\gamma$ in the standard model effective field theory: An NLO analysis," *Phys. Rev. D* **97** no. 9, (2018) 093003, arXiv:1801.01136 [hep-ph].

[81] E. E. Jenkins, A. V. Manohar, and M. Trott, "Renormalization Group Evolution of the Standard Model Dimension Six Operators I: Formalism and lambda Dependence," *JHEP* **10** (2013) 087, arXiv:1308.2627 [hep-ph].

[82] E. E. Jenkins, A. V. Manohar, and M. Trott, "Renormalization Group Evolution of the Standard Model Dimension Six Operators II: Yukawa Dependence," *JHEP* **01** (2014) 035, arXiv:1310.4838 [hep-ph].

[83] R. Gauld, B. D. Pecjak, and D. J. Scott, "One-loop corrections to $h \to b\bar{b}$ and $h \to \tau\overline{\tau}$ decays in the Standard Model Dimension-6 EFT: four-fermion operators and the large-m_t limit," *JHEP* **05** (2016) 080, arXiv:1512.02508 [hep-ph].

[84] G. Ossola, C. G. Papadopoulos, and R. Pittau, "Reducing full one-loop amplitudes to scalar integrals at the integrand level," *Nucl. Phys. B* **763** (2007) 147–169, arXiv:hep-ph/0609007.

[85] G. Ossola, C. G. Papadopoulos, and R. Pittau, "CutTools: A Program implementing the OPP reduction method to compute one-loop amplitudes," *JHEP* **03** (2008) 042, arXiv:0711.3596 [hep-ph].

[86] G. Ossola, C. G. Papadopoulos, and R. Pittau, "On the Rational Terms of the one-loop amplitudes," *JHEP* **05** (2008) 004, arXiv:0802.1876 [hep-ph].

[87] R. D. Ball *et al.*, "Parton distributions with LHC data," *Nucl. Phys. B* **867** (2013) 244–289, arXiv:1207.1303 [hep-ph].

[88] I. Brivio, Y. Jiang, and M. Trott, "The SMEFTsim package, theory and tools," *JHEP* **12** (2017) 070, arXiv:1709.06492 [hep-ph].

[89] R. Alonso, E. E. Jenkins, A. V. Manohar, and M. Trott, "Renormalization Group Evolution of the Standard Model Dimension Six Operators III: Gauge Coupling Dependence and Phenomenology," *JHEP* **04** (2014) 159, arXiv:1312.2014 [hep-ph].

[90] M. Gorbahn and U. Haisch, "Indirect probes of the trilinear Higgs coupling: $gg \to h$ and $h \to \gamma\gamma$," *JHEP* **10** (2016) 094, arXiv:1607.03773 [hep-ph].

[91] G. Degrassi, P. P. Giardino, F. Maltoni, and D. Pagani, "Probing the Higgs self coupling via single Higgs production at the LHC," *JHEP* **12** (2016) 080, arXiv:1607.04251 [hep-ph].

[92] W. Bizon, M. Gorbahn, U. Haisch, and G. Zanderighi, "Constraints on the trilinear Higgs coupling from vector boson fusion and associated Higgs production at the LHC," *JHEP* **07** (2017) 083, arXiv:1610.05771 [hep-ph].

[93] F. Maltoni, D. Pagani, A. Shivaji, and X. Zhao, "Trilinear Higgs coupling determination via single-Higgs differential measurements at the LHC," *Eur. Phys. J. C* **77** no. 12, (2017) 887, arXiv:1709.08649 [hep-ph].

[94] G. Degrassi, B. Di Micco, P. P. Giardino, and E. Rossi, "Higgs boson self-coupling constraints from single Higgs, double Higgs and Electroweak measurements," *Phys. Lett. B* **817** (2021) 136307, arXiv:2102.07651 [hep-ph].

[95] S. Di Vita, C. Grojean, G. Panico, M. Riembau, and T. Vantalon, "A global view on the Higgs self-coupling," *JHEP* **09** (2017) 069, arXiv:1704.01953 [hep-ph].

[96] "Guidelines for extrapolation of cms and atlas lhc/hl-lhc couplings projections to he-lhc." https://twiki.cern.ch/twiki/bin/view/LHCPhysics/GuidelinesCouplingProjections2018#Details%20of%20the%20CMS%20projections.

[97] J. Salvatier, T. V. Wiecki, and C. Fonnesbeck, "Probabilistic programming in python using PyMC3," *PeerJ Computer Science* **2** (Apr, 2016) e55. https://doi.org/10.7717/peerj-cs.55.

[98] R. Kumar, C. Carroll, A. Hartikainen, and O. Martin, "Arviz a unified library for exploratory analysis of bayesian models in python," *Journal of Open Source Software* **4** no. 33, (2019) 1143. https://doi.org/10.21105/joss.01143.

[99] J. de Blas *et al.*, "HEPfit: a Code for the Combination of Indirect and Direct Constraints on High Energy Physics Models," *Eur. Phys. J. C* **80** no. 5, (2020) 456, arXiv:1910.14012 [hep-ph].

[100] J. Ellis, M. Madigan, K. Mimasu, V. Sanz, and T. You, "Top, Higgs, Diboson and Electroweak Fit to the Standard Model Effective Field Theory," *JHEP* **04** (2021) 279, arXiv:2012.02779 [hep-ph].

[101] I. Brivio, S. Bruggisser, F. Maltoni, R. Moutafis, T. Plehn, E. Vryonidou, S. Westhoff, and C. Zhang, "O new physics, where art thou? A global search in the top sector," *JHEP* **02** (2020) 131, arXiv:1910.03606 [hep-ph].

[102] C. Zhang, "Constraining *qqtt* operators from four-top production: a case for enhanced EFT sensitivity," *Chin. Phys. C* **42** no. 2, (2018) 023104, arXiv:1708.05928 [hep-ph].

[103] S. Dawson and P. P. Giardino, "Flavorful Electroweak Precision Observables in the Standard Model Effective Field Theory," arXiv:2201.09887 [hep-ph].

[104] **ATLAS** Collaboration, "Search for Higgs boson pair production in the two bottom quarks plus two photons final state in *pp* collisions at $\sqrt{s} = 13$ TeV with the ATLAS detector," Tech. Rep. ATLAS-CONF-2021-016, 2021.

[105] L. Alasfar, R. Gröber, C. Grojean, A. Paul, and Z. Qian, "Machine learning augmented probes of light-quark Yukawa and trilinear couplings from Higgs pair production," *In preparation* (2021) .

[106] L. Di Luzio, R. Gröber, and M. Spannowsky, "Maxi-sizing the trilinear Higgs self-coupling: how large could it be?," *Eur. Phys. J. C* **77** no. 11, (2017) 788, arXiv:1704.02311 [hep-ph].

[107] **CMS Collaboration** Collaboration, "Sensitivity projections for Higgs boson properties measurements at the HL-LHC," tech. rep., CERN, Geneva, 2018. https://cds.cern.ch/record/2647699.

[108] J. Alison *et al.*, "Higgs boson potential at colliders: Status and perspectives," *Rev. Phys.* **5** (2020) 100045, arXiv:1910.00012 [hep-ph].

[109] **CMS** Collaboration, "Prospects for HH measurements at the HL-LHC," *CMS-PAS-FTR-18-019* (2018) .

[110] L. Silvestrini and M. Valli, "Model-independent Bounds on the Standard Model Effective Theory from Flavour Physics," *Phys. Lett. B* **799** (2019) 135062, arXiv:1812.10913 [hep-ph].

[111] G. Banelli, E. Salvioni, J. Serra, T. Theil, and A. Weiler, "The Present and Future of Four Top Operators," *JHEP* **02** (2021) 043, arXiv:2010.05915 [hep-ph].

[112] J. de Blas, J. C. Criado, M. Perez-Victoria, and J. Santiago, "Effective description of general extensions of the Standard Model: the complete tree-level dictionary," *JHEP* **03** (2018) 109, arXiv:1711.10391 [hep-ph].

[113] Anisha, S. D. Bakshi, S. Banerjee, A. Biekötter, J. Chakrabortty, S. K. Patra, and M. Spannowsky, "Effective limits on single scalar extensions in the light of recent LHC data," arXiv:2111.05876 [hep-ph].

[114] "High-Luminosity Large Hadron Collider (HL-LHC) : Preliminary Design Report,".

[115] **ATLAS Collaboration** Collaboration, "Measurement prospects of the pair production and self-coupling of the Higgs boson with the ATLAS experiment at the HL-LHC,".

[116] T. Plehn and M. Rauch, "The quartic higgs coupling at hadron colliders," *Phys. Rev.* **D72** (2005) 053008, arXiv:hep-ph/0507321 [hep-ph].

[117] O. Eboli, G. Marques, S. Novaes, and A. Natale, "Twin higgs-boson production," *Physics Letters B* **197** no. 1, (1987) 269–272.

[118] E. Glover and J. van der Bij, "Higgs boson pair production via gluon fusion," *Nuclear Physics B* **309** no. 2, (1988) 282–294.

[119] D. A. Dicus, C. Kao, and S. S. D. Willenbrock, "Higgs Boson Pair Production From Gluon Fusion," *Phys. Lett.* **B203** (1988) 457–461.

[120] T. Plehn, M. Spira, and P. M. Zerwas, "Pair production of neutral Higgs particles in gluon-gluon collisions," *Nucl. Phys.* **B479** (1996) 46–64, arXiv:hep-ph/9603205 [hep-ph]. [Erratum: Nucl. Phys.B531,655(1998)].

[121] S. Dawson, S. Dittmaier, and M. Spira, "Neutral Higgs boson pair production at hadron colliders: QCD corrections," *Phys. Rev. D* **58** (1998) 115012, arXiv:hep-ph/9805244.

[122] J. Grigo, K. Melnikov, and M. Steinhauser, "Virtual corrections to Higgs boson pair production in the large top quark mass limit," *Nucl. Phys.* **B888** (2014) 17–29, arXiv:1408.2422 [hep-ph].

[123] D. de Florian and J. Mazzitelli, "Two-loop virtual corrections to Higgs pair production," *Phys. Lett. B* **724** (2013) 306–309, arXiv:1305.5206 [hep-ph].

[124] J. Grigo, J. Hoff, K. Melnikov, and M. Steinhauser, "On the Higgs boson pair production at the LHC," *Nucl. Phys.* **B875** (2013) 1–17, arXiv:1305.7340 [hep-ph].

[125] J. Grigo, J. Hoff, and M. Steinhauser, "Higgs boson pair production: top quark mass effects at NLO and NNLO," *Nucl. Phys. B* **900** (2015) 412–430, arXiv:1508.00909 [hep-ph].

[126] G. Degrassi, P. P. Giardino, and R. Gröber, "On the two-loop virtual QCD corrections to Higgs boson pair production in the Standard Model," *Eur. Phys. J. C* **76** no. 7, (2016) 411, arXiv:1603.00385 [hep-ph].

[127] D. Y. Shao, C. S. Li, H. T. Li, and J. Wang, "Threshold resummation effects in Higgs boson pair production at the LHC," *JHEP* **07** (2013) 169, arXiv:1301.1245 [hep-ph].

[128] S. Borowka, N. Greiner, G. Heinrich, S. P. Jones, M. Kerner, J. Schlenk, and T. Zirke, "Full top quark mass dependence in Higgs boson pair production at NLO," *JHEP* **10** (2016) 107, arXiv:1608.04798 [hep-ph].

[129] S. Borowka, N. Greiner, G. Heinrich, S. P. Jones, M. Kerner, J. Schlenk, U. Schubert, and T. Zirke, "Higgs Boson Pair Production in Gluon Fusion at Next-to-Leading Order with Full Top-Quark Mass Dependence," *Phys. Rev. Lett.* **117** no. 1, (2016) 012001, arXiv:1604.06447 [hep-ph]. [Erratum: Phys. Rev. Lett.117,no.7,079901(2016)].

[130] J. Baglio, F. Campanario, S. Glaus, M. Mühlleitner, M. Spira, and J. Streicher, "Gluon fusion into Higgs pairs at NLO QCD and the top mass scheme," *Eur. Phys. J.* **C79** no. 6, (2019) 459, arXiv:1811.05692 [hep-ph].

[131] X. Xu and L. L. Yang, "Towards a new approximation for pair-production and associated-production of the Higgs boson," *JHEP* **01** (2019) 211, arXiv:1810.12002 [hep-ph].

[132] G. Wang, Y. Wang, X. Xu, Y. Xu, and L. L. Yang, "Efficient computation of two-loop amplitudes for Higgs boson pair production," *Phys. Rev. D* **104** no. 5, (2021) L051901, arXiv:2010.15649 [hep-ph].

[133] J. Davies, R. Gröber, A. Maier, T. Rauh, and M. Steinhauser, "Top quark mass dependence of the Higgs boson-gluon form factor at three loops," *Phys. Rev.* **D100** no. 3, (2019) 034017, arXiv:1906.00982 [hep-ph].

[134] M. Grazzini, G. Heinrich, S. Jones, S. Kallweit, M. Kerner, J. M. Lindert, and J. Mazzitelli, "Higgs boson pair production at NNLO with top quark mass effects," *JHEP* **05** (2018) 059, arXiv:1803.02463 [hep-ph].

[135] D. de Florian, M. Grazzini, C. Hanga, S. Kallweit, J. M. Lindert, P. Maierhöfer, J. Mazzitelli, and D. Rathlev, "Differential Higgs Boson Pair Production at Next-to-Next-to-Leading Order in QCD," *JHEP* **09** (2016) 151, arXiv:1606.09519 [hep-ph].

[136] D. de Florian and J. Mazzitelli, "Higgs Boson Pair Production at Next-to-Next-to-Leading Order in QCD," *Phys. Rev. Lett.* **111** (2013) 201801, arXiv:1309.6594 [hep-ph].

[137] D. de Florian and J. Mazzitelli, "Higgs pair production at next-to-next-to-leading logarithmic accuracy at the LHC," *JHEP* **09** (2015) 053, arXiv:1505.07122 [hep-ph].

[138] S. Jones and S. Kuttimalai, "Parton Shower and NLO-Matching uncertainties in Higgs Boson Pair Production," *JHEP* **02** (2018) 176, arXiv:1711.03319 [hep-ph].

[139] G. Heinrich, S. P. Jones, M. Kerner, G. Luisoni, and L. Scyboz, "Probing the trilinear Higgs boson coupling in di-Higgs production at NLO QCD including parton shower effects," *JHEP* **06** (2019) 066, arXiv:1903.08137 [hep-ph].

[140] G. Heinrich, S. P. Jones, M. Kerner, G. Luisoni, and E. Vryonidou, "NLO predictions for Higgs boson pair production with full top quark mass dependence matched to parton showers," *JHEP* **08** (2017) 088, arXiv:1703.09252 [hep-ph].

[141] G. Heinrich, S. P. Jones, M. Kerner, and L. Scyboz, "A non-linear EFT description of $gg \to HH$ at NLO interfaced to POWHEG," *JHEP* **10** (2020) 021, arXiv:2006.16877 [hep-ph].

[142] L. Bellafronte, G. Degrassi, P. P. Giardino, R. Gröber, and M. Vitti, "Gluon Fusion Production at NLO: Merging the Transverse Momentum and the High-Energy Expansions," arXiv:2202.12157 [hep-ph].

[143] R. Gröber and M. Mühlleitner, "Composite Higgs Boson Pair Production at the LHC," *JHEP* **06** (2011) 020, arXiv:1012.1562 [hep-ph].

[144] R. Grober, M. Muhlleitner, M. Spira, and J. Streicher, "NLO QCD Corrections to Higgs Pair Production including Dimension-6 Operators," *JHEP* **09** (2015) 092, arXiv:1504.06577 [hep-ph].

[145] R. Grober, M. Muhlleitner, and M. Spira, "Higgs Pair Production at NLO QCD for CP-violating Higgs Sectors," *Nucl. Phys. B* **925** (2017) 1–27, arXiv:1705.05314 [hep-ph].

[146] D. de Florian, I. Fabre, and J. Mazzitelli, "Higgs boson pair production at NNLO in QCD including dimension 6 operators," *JHEP* **10** (2017) 215, arXiv:1704.05700 [hep-ph].

[147] G. Buchalla, M. Capozi, A. Celis, G. Heinrich, and L. Scyboz, "Higgs boson pair production in non-linear Effective Field Theory with full m_t-dependence at NLO QCD," *JHEP* **09** (2018) 057, arXiv:1806.05162 [hep-ph].

[148] S. Dittmaier *et al.*, "Handbook of LHC Higgs Cross Sections: 2. Differential Distributions," arXiv:1201.3084 [hep-ph].

[149] **LHC Higgs Cross Section Working Group** Collaboration, D. de Florian *et al.*, "Handbook of LHC Higgs Cross Sections: 4. Deciphering the Nature of the Higgs Sector," arXiv:1610.07922 [hep-ph].

[150] A. D. Martin, W. J. Stirling, R. S. Thorne, and G. Watt, "Uncertainties on alpha(S) in global PDF analyses and implications for predicted hadronic cross sections," *Eur. Phys. J.* **C64** (2009) 653–680, arXiv:0905.3531 [hep-ph].

[151] F. Demartin, S. Forte, E. Mariani, J. Rojo, and A. Vicini, "The impact of PDF and alphas uncertainties on Higgs Production in gluon fusion at hadron colliders," *Phys. Rev.* **D82** (2010) 014002, arXiv:1004.0962 [hep-ph].

[152] J. Baglio, F. Campanario, S. Glaus, M. Mühlleitner, J. Ronca, and M. Spira, "$gg \to HH$: Combined uncertainties," *Phys. Rev. D* **103** no. 5, (2021) 056002, arXiv:2008.11626 [hep-ph].

[153] L.-B. Chen, H. T. Li, H.-S. Shao, and J. Wang, "Higgs boson pair production via gluon fusion at N^{3}LO in QCD," *Phys. Lett. B* **803** (2020) 135292, arXiv:1909.06808 [hep-ph].

[154] L.-B. Chen, H. T. Li, H.-S. Shao, and J. Wang, "The gluon-fusion production of Higgs boson pair: N^{3}LO QCD corrections and top-quark mass effects," *JHEP* **03** (2020) 072, arXiv:1912.13001 [hep-ph].

[155] J. Baglio, A. Djouadi, R. Gröber, M. M. Mühlleitner, J. Quevillon, and M. Spira, "The measurement of the Higgs self-coupling at the LHC: theoretical status," *JHEP* **04** (2013) 151, arXiv:1212.5581 [hep-ph].

[156] L.-S. Ling, R.-Y. Zhang, W.-G. Ma, L. Guo, W.-H. Li, and X.-Z. Li, "NNLO QCD corrections to Higgs pair production via vector boson fusion at hadron colliders," *Phys. Rev. D* **89** no. 7, (2014) 073001, arXiv:1401.7754 [hep-ph].

[157] F. A. Dreyer and A. Karlberg, "Vector-Boson Fusion Higgs Pair Production at N^{3}LO," *Phys. Rev. D* **98** no. 11, (2018) 114016, arXiv:1811.07906 [hep-ph].

[158] F. A. Dreyer and A. Karlberg, "Fully differential Vector-Boson Fusion Higgs Pair Production at Next-to-Next-to-Leading Order," *Phys. Rev. D* **99** no. 7, (2019) 074028, arXiv:1811.07918 [hep-ph].

[159] H. T. Li and J. Wang, "Fully Differential Higgs Pair Production in Association With a W Boson at Next-to-Next-to-Leading Order in QCD," *Phys. Lett. B* **765** (2017) 265–271, arXiv:1607.06382 [hep-ph].

[160] H. T. Li, C. S. Li, and J. Wang, "Fully differential Higgs boson pair production in association with a Z boson at next-to-next-to-leading order in QCD," *Phys. Rev. D* **97** no. 7, (2018) 074026, arXiv:1710.02464 [hep-ph].

[161] R. Frederix, S. Frixione, V. Hirschi, F. Maltoni, O. Mattelaer, P. Torrielli, E. Vryonidou, and M. Zaro, "Higgs pair production at the LHC with NLO and parton-shower effects," *Phys. Lett. B* **732** (2014) 142–149, arXiv:1401.7340 [hep-ph].

[162] **CMS Collaboration** Collaboration, "Search for Higgs boson pair production in the four b quark final state," tech. rep., CERN, Geneva, 2021. https://cds.cern.ch/record/2771912.

[163] **CMS Collaboration** Collaboration, "Search for Higgs boson pair production via vector boson fusion with highly Lorentz-boosted Higgs bosons in the four b quark final state at $\sqrt{s} = 13$ TeV," tech. rep., CERN, Geneva, 2021. http://cds.cern.ch/record/2776802.

[164] **ATLAS** Collaboration, G. Aad *et al.*, "Search for the $HH \to b\bar{b}b\bar{b}$ process via vector-boson fusion production using proton-proton collisions at $\sqrt{s} = 13$ TeV with the ATLAS detector," *JHEP* **07** (2020) 108, arXiv:2001.05178 [hep-ex]. [Erratum: JHEP 01, 145 (2021), Erratum: JHEP 05, 207 (2021)].

[165] **ATLAS** Collaboration, G. Aad *et al.*, "Search for non-resonant Higgs boson pair production in the $bb\ell\nu\ell\nu$ final state with the ATLAS detector in pp collisions at $\sqrt{s} = 13$ TeV," *Phys. Lett. B* **801** (2020) 135145, arXiv:1908.06765 [hep-ex].

[166] **CMS Collaboration** Collaboration, "Search for nonresonant Higgs boson pair production in the 4 leptons plus 2 b jets final state in proton-proton collisions at $\sqrt{s} = 13$ TeV," tech. rep., CERN, Geneva, 2020. https://cds.cern.ch/record/2725691.

[167] **ATLAS Collaboration** Collaboration, "Combination of searches for non-resonant and resonant Higgs boson pair production in the $b\bar{b}\gamma\gamma$, $b\bar{b}\tau^+\tau^-$ and $b\bar{b}b\bar{b}$ decay channels using pp collisions at $\sqrt{s} = 13$ TeV with the ATLAS detector," tech. rep., CERN, Geneva, Oct, 2021. https://cds.cern.ch/record/2786865. All figures including auxiliary figures are available at https://atlas.web.cern.ch/Atlas/GROUPS/PHYSICS/CONFNOTES/ATLAS-CONF-2021-052.

[168] **CMS** Collaboration, A. M. Sirunyan *et al.*, "Search for nonresonant Higgs boson pair production in final states with two bottom quarks and two photons in proton-proton collisions at $\sqrt{s} = 13$ TeV," *JHEP* **03** (2021) 257, arXiv:2011.12373 [hep-ex].

[169] A. Azatov, R. Contino, G. Panico, and M. Son, "Effective field theory analysis of double Higgs boson production via gluon fusion," *Phys. Rev.* **D92** no. 3, (2015) 035001, arXiv:1502.00539 [hep-ph].

[170] U. Baur, T. Plehn, and D. L. Rainwater, "Probing the Higgs selfcoupling at hadron colliders using rare decays," *Phys. Rev.* **D69** (2004) 053004, arXiv:hep-ph/0310056 [hep-ph].

[171] F. Kling, T. Plehn, and P. Schichtel, "Maximizing the significance in Higgs boson pair analyses," *Phys. Rev.* **D95** no. 3, (2017) 035026, arXiv:1607.07441 [hep-ph].

[172] V. Barger, L. L. Everett, C. B. Jackson, and G. Shaughnessy, "Higgs-Pair Production and Measurement of the Triscalar Coupling at LHC(8,14)," *Phys. Lett.* **B728** (2014) 433–436, arXiv:1311.2931 [hep-ph].

[173] A. Adhikary, S. Banerjee, R. K. Barman, B. Bhattacherjee, and S. Niyogi, "Revisiting the non-resonant Higgs pair production at the HL-LHC," *JHEP* **07** (2018) 116, arXiv:1712.05346 [hep-ph].

[174] A. Alves, T. Ghosh, and K. Sinha, "Can We Discover Double Higgs Production at the LHC?," *Phys. Rev. D* **96** no. 3, (2017) 035022, arXiv:1704.07395 [hep-ph].

[175] S. Weinberg, "Models of Lepton and Quark Masses," *Phys. Rev. D* **101** no. 3, (2020) 035020, arXiv:2001.06582 [hep-th].

[176] **ATLAS** Collaboration, G. Aad *et al.*, "A search for the dimuon decay of the Standard Model Higgs boson with the ATLAS detector," *Phys. Lett. B* **812** (2021) 135980, arXiv:2007.07830 [hep-ex].

[177] **CMS** Collaboration, A. M. Sirunyan *et al.*, "Evidence for Higgs boson decay to a pair of muons," *JHEP* **01** (2021) 148, arXiv:2009.04363 [hep-ex].

[178] **ATLAS** Collaboration, "Direct constraint on the Higgs-charm coupling from a search for Higgs boson decays to charm quarks with the ATLAS detector,".

[179] **ATLAS** Collaboration, G. Aad *et al.*, "Direct constraint on the Higgs-charm coupling from a search for Higgs boson decays into charm quarks with the ATLAS detector," arXiv:2201.11428 [hep-ex].

[180] **CMS** Collaboration, A. M. Sirunyan *et al.*, "A search for the standard model Higgs boson decaying to charm quarks," *JHEP* **03** (2020) 131, arXiv:1912.01662 [hep-ex].

[181] **CMS** Collaboration, V. Khachatryan *et al.*, "Search for a standard model-like Higgs boson in the $\mu^+\mu^-$ and e^+e^- decay channels at the LHC," *Phys. Lett.* **B744** (2015) 184–207, arXiv:1410.6679 [hep-ex].

[182] Y. Nakai, D. Shih, and S. Thomas, "Strange Jet Tagging," arXiv:2003.09517 [hep-ph].

[183] B. Grzadkowski, M. Iskrzynski, M. Misiak, and J. Rosiek, "Dimension-Six Terms in the Standard Model Lagrangian," *JHEP* **10** (2010) 085, arXiv:1008.4884 [hep-ph].

[184] R. Contino, M. Ghezzi, C. Grojean, M. Muhlleitner, and M. Spira, "Effective Lagrangian for a light Higgs-like scalar," *JHEP* **07** (2013) 035, arXiv:1303.3876 [hep-ph].

[185] G. Blankenburg, J. Ellis, and G. Isidori, "Flavour-Changing Decays of a 125 GeV Higgs-like Particle," *Phys. Lett.* **B712** (2012) 386–390, arXiv:1202.5704 [hep-ph].

[186] G. D'Ambrosio, G. F. Giudice, G. Isidori, and A. Strumia, "Minimal flavor violation: An Effective field theory approach," *Nucl. Phys.* **B645** (2002) 155–187, arXiv:hep-ph/0207036 [hep-ph].

[187] A. Pich and P. Tuzon, "Yukawa Alignment in the Two-Higgs-Doublet Model," *Phys. Rev. D* **80** (2009) 091702, arXiv:0908.1554 [hep-ph].

[188] A. Pich, "Flavour constraints on multi-Higgs-doublet models: Yukawa alignment," *Nucl. Phys. B Proc. Suppl.* **209** (2010) 182–187, arXiv:1010.5217 [hep-ph].

[189] D. Egana-Ugrinovic, S. Homiller, and P. Meade, "Aligned and Spontaneous Flavor Violation," *Phys. Rev. Lett.* **123** no. 3, (2019) 031802, arXiv:1811.00017 [hep-ph].

[190] P. M. Ferreira, L. Lavoura, and J. P. Silva, "Renormalization-group constraints on Yukawa alignment in multi-Higgs-doublet models," *Phys. Lett. B* **688** (2010) 341–344, arXiv:1001.2561 [hep-ph].

[191] M. Jung, A. Pich, and P. Tuzon, "Charged-Higgs phenomenology in the Aligned two-Higgs-doublet model," *JHEP* **11** (2010) 003, arXiv:1006.0470 [hep-ph].

[192] F. J. Botella, G. C. Branco, A. M. Coutinho, M. N. Rebelo, and J. I. Silva-Marcos, "Natural Quasi-Alignment with two Higgs Doublets and RGE Stability," *Eur. Phys. J. C* **75** (2015) 286, arXiv:1501.07435 [hep-ph].

[193] R. Contino, C. Grojean, M. Moretti, F. Piccinini, and R. Rattazzi, "Strong Double Higgs Production at the LHC," *JHEP* **05** (2010) 089, arXiv:1002.1011 [hep-ph].

[194] D. Dicus, T. Stelzer, Z. Sullivan, and S. Willenbrock, "Higgs boson production in association with bottom quarks at next-to-leading order," *Phys. Rev.* **D59** (1999) 094016, arXiv:hep-ph/9811492 [hep-ph].

[195] C. Balazs, H.-J. He, and C. P. Yuan, "QCD corrections to scalar production via heavy quark fusion at hadron colliders," *Phys. Rev.* **D60** (1999) 114001, arXiv:hep-ph/9812263 [hep-ph].

[196] R. V. Harlander and W. B. Kilgore, "Higgs boson production in bottom quark fusion at next-to-next-to leading order," *Phys. Rev.* **D68** (2003) 013001, arXiv:hep-ph/0304035 [hep-ph].

[197] S. Dawson, C. Kao, Y. Wang, and P. Williams, "QCD Corrections to Higgs Pair Production in Bottom Quark Fusion," *Phys. Rev.* **D75** (2007) 013007, arXiv:hep-ph/0610284 [hep-ph].

[198] A. H. Ajjath, P. Banerjee, A. Chakraborty, P. K. Dhani, P. Mukherjee, N. Rana, and V. Ravindran, "Higgs pair production from bottom quark annihilation to NNLO in QCD," *JHEP* **05** (2019) 030, arXiv:1811.01853 [hep-ph].

[199] M. Spira, "Higgs Boson Production and Decay at Hadron Colliders," *Prog. Part. Nucl. Phys.* **95** (2017) 98–159, arXiv:1612.07651 [hep-ph].

[200] V. N. Gribov and L. N. Lipatov, "Deep inelastic e p scattering in perturbation theory," *Sov. J. Nucl. Phys.* **15** (1972) 438–450. [Yad. Fiz.15,781(1972)].

[201] G. Altarelli and G. Parisi, "Asymptotic Freedom in Parton Language," *Nucl. Phys.* **B126** (1977) 298–318.

[202] Y. L. Dokshitzer, "Calculation of the Structure Functions for Deep Inelastic Scattering and e+ e- Annihilation by Perturbation Theory in Quantum Chromodynamics.," *Sov. Phys. JETP* **46** (1977) 641–653. [Zh. Eksp. Teor. Fiz.73,1216(1977)].

[203] **NNPDF** Collaboration, R. D. Ball *et al.*, "Parton distributions from high-precision collider data," *Eur. Phys. J.* **C77** no. 10, (2017) 663, arXiv:1706.00428 [hep-ph].

[204] A. Buckley, J. Ferrando, S. Lloyd, K. Nordström, B. Page, M. Rüfenacht, M. Schönherr, and G. Watt, "LHAPDF6: parton density access in the LHC precision era," *Eur. Phys. J.* **C75** (2015) 132, arXiv:1412.7420 [hep-ph].

[205] A. Denner, S. Dittmaier, and L. Hofer, "COLLIER - A fortran-library for one-loop integrals," *PoS* **LL2014** (2014) 071, arXiv:1407.0087 [hep-ph].

[206] A. Djouadi, J. Kalinowski, and M. Spira, "HDECAY: A Program for Higgs boson decays in the standard model and its supersymmetric extension," *Comput. Phys. Commun.* **108** (1998) 56–74, arXiv:hep-ph/9704448 [hep-ph].

[207] A. Djouadi, J. Kalinowski, M. Muehlleitner, and M. Spira, "HDECAY: Twenty$_{++}$ years after," *Comput. Phys. Commun.* **238** (2019) 214–231, arXiv:1801.09506 [hep-ph].

[208] T. Sjostrand, S. Mrenna, and P. Z. Skands, "PYTHIA 6.4 Physics and Manual," *JHEP* **05** (2006) 026, arXiv:hep-ph/0603175 [hep-ph].

[209] D. C. Hall, "RootTuple: A library enabling ROOT n-tuple output from FORTRAN HEP programs," http://roottuple.hepforge.org.

[210] T. Sjöstrand, S. Ask, J. R. Christiansen, R. Corke, N. Desai, P. Ilten, S. Mrenna, S. Prestel, C. O. Rasmussen, and P. Z. Skands, "An introduction to PYTHIA 8.2," *Comput. Phys. Commun.* **191** (2015) 159–177, arXiv:1410.3012 [hep-ph].

[211] **DELPHES 3** Collaboration, J. de Favereau, C. Delaere, P. Demin, A. Giammanco, V. Lemaître, A. Mertens, and M. Selvaggi, "DELPHES 3, A modular framework for fast simulation of a generic collider experiment," *JHEP* **02** (2014) 057, arXiv:1307.6346 [hep-ex].

[212] C. Grojean, A. Paul, and Z. Qian, "Resurrecting $b\bar{b}h$ with kinematic shapes," *JHEP* **04** (2021) 139, arXiv:2011.13945 [hep-ph].

[213] W. Beenakker, S. Dittmaier, M. Kramer, B. Plumper, M. Spira, and P. M. Zerwas, "Higgs radiation off top quarks at the Tevatron and the LHC," *Phys. Rev. Lett.* **87** (2001) 201805, arXiv:hep-ph/0107081.

[214] D. Fäh and N. Greiner, "Diphoton production in association with two bottom jets," *Eur. Phys. J. C* **77** no. 11, (2017) 750, arXiv:1706.08309 [hep-ph].

[215] F. Campanario, R. Roth, and D. Zeppenfeld, "QCD radiation in WH and WZ production and anomalous coupling measurements," *Phys. Rev. D* **91** (2015) 054039, arXiv:1410.4840 [hep-ph].

[216] S. Dawson, C. Jackson, L. Reina, and D. Wackeroth, "Higgs production in association with bottom quarks at hadron colliders," *Mod. Phys. Lett. A* **21** (2006) 89–110, arXiv:hep-ph/0508293.

[217] M. Cacciari, G. P. Salam, and G. Soyez, "FastJet User Manual," *Eur. Phys. J.* **C72** (2012) 1896, arXiv:1111.6097 [hep-ph].

[218] **CMS** Collaboration, S. Chatrchyan *et al.*, "Inclusive b-jet production in pp collisions at $\sqrt{s} = 7$ TeV," *JHEP* **04** (2012) 084, arXiv:1202.4617 [hep-ex].

[219] **CMS** Collaboration, "Performance of b tagging at sqrt(s)=8 TeV in multijet, ttbar and boosted topology events," Tech. Rep. CMS-PAS-BTV-13-001, CERN, Geneva, 2013. https://cds.cern.ch/record/1581306.

[220] **ATLAS** Collaboration, "Performance assumptions based on full simulation for an upgraded ATLAS detector at a High-Luminosity LHC," Tech. Rep. ATL-PHYS-PUB-2013-009, CERN, Geneva, 2013. http://cds.cern.ch/record/1604420.

[221] **CMS** Collaboration, "Photon ID performance with 19.6 fb^{-1} of data collected at $\sqrt{s} = 8$ TeV with the CMS detector," Tech. Rep. CMS-DP-2013-010, CERN, Geneva, 2013. http://cds.cern.ch/record/1542855.

[222] G. Cowan, K. Cranmer, E. Gross, and O. Vitells, "Asymptotic formulae for likelihood-based tests of new physics," *Eur. Phys. J.* **C71** (2011) 1554, arXiv:1007.1727 [physics.data-an]. [Erratum: Eur. Phys. J.C73,2501(2013)].

[223] L. Heinrich, M. Feickert, and G. Stark, "pyhf: v0.6.3." https://doi.org/10.5281/zenodo.1169739. https://github.com/scikit-hep/pyhf/releases/tag/v0.6.3.

[224] L. Heinrich, M. Feickert, G. Stark, and K. Cranmer, "pyhf: pure-python implementation of histfactory statistical models," *Journal of Open Source Software* **6** no. 58, (2021) 2823. https://doi.org/10.21105/joss.02823.

[225] T. Chen and C. Guestrin, "XGBoost: A Scalable Tree Boosting System," in *Proceedings of the 22nd ACM SIGKDD International Conference on Knowledge Discovery and Data Mining*, KDD '16, p. 785–794. Association for Computing Machinery, New York, NY, USA, 2016. https://dl.acm.org/doi/10.1145/2939672.2939785.

[226] L. S. Shapley, "Notes on the n-Person Game-II: The Value of an n-Person Game," *Rand Corporation* (1951) . https://www.rand.org/pubs/research_memoranda/RM0670.html.

[227] D. Alvestad, N. Fomin, J. Kersten, S. Maeland, and I. Strümke, "Beyond Cuts in Small Signal Scenarios - Enhanced Sneutrino Detectability Using Machine Learning," arXiv:2108.03125 [hep-ph].

[228] A. S. Cornell, W. Doorsamy, B. Fuks, G. Harmsen, and L. Mason, "Boosted decision trees in the era of new physics: a smuon analysis case study," arXiv:2109.11815 [hep-ph].

[229] S. M. Lundberg and S.-I. Lee, "A unified approach to interpreting model predictions," in *Advances in Neural Information Processing Systems*, I. Guyon, U. V. Luxburg, S. Bengio, H. Wallach, R. Fergus, S. Vishwanathan, and R. Garnett, eds., vol. 30, pp. 4765–4774. Curran Associates, Inc., 2017. 1705.07874. https://proceedings.neurips.cc/paper/2017/file/8a20a8621978632d76c43dfd28b67767-Paper.pdf.

[230] S. M. Lundberg, G. G. Erion, and S.-I. Lee, "Consistent Individualized Feature Attribution for Tree Ensembles," *arXiv e-prints* (Feb., 2018) , arXiv:1802.03888 [cs.LG].

[231] S. M. Lundberg, G. Erion, H. Chen, A. DeGrave, J. M. Prutkin, B. Nair, R. Katz, J. Himmelfarb, N. Bansal, and S.-I. Lee, "From local explanations to global understanding with explainable AI for trees," *Nature Machine Intelligence* **2** no. 1, (2020) 56–67. https://www.nature.com/articles/s42256-019-0138-9.

[232] **ATLAS** Collaboration, "Measurement prospects of the pair production and self-coupling of the Higgs boson with the ATLAS experiment at the HL-LHC,".

[233] I. Brivio, F. Goertz, and G. Isidori, "Probing the Charm Quark Yukawa Coupling in Higgs+Charm Production," *Phys. Rev. Lett.* **115** no. 21, (2015) 211801, arXiv:1507.02916 [hep-ph].

[234] Y. Soreq, H. X. Zhu, and J. Zupan, "Light quark Yukawa couplings from Higgs kinematics," *JHEP* **12** (2016) 045, arXiv:1606.09621 [hep-ph].

[235] F. Bishara, U. Haisch, P. F. Monni, and E. Re, "Constraining Light-Quark Yukawa Couplings from Higgs Distributions," *Phys. Rev. Lett.* **118** no. 12, (2017) 121801, arXiv:1606.09253 [hep-ph].

[236] G. Bonner and H. E. Logan, "Constraining the Higgs couplings to up and down quarks using production kinematics at the CERN Large Hadron Collider," arXiv:1608.04376 [hep-ph].

[237] M. McCullough, "An Indirect Model-Dependent Probe of the Higgs Self-Coupling," *Phys. Rev. D* **90** no. 1, (2014) 015001, arXiv:1312.3322 [hep-ph]. [Erratum: Phys.Rev.D 92, 039903 (2015)].

[238] **CMS** Collaboration, "Constraints on the Higgs boson self-coupling from ttH+tH, H to gamma gamma differential measurements at the HL-LHC," Tech. Rep. CMS-PAS-FTR-18-020, 2018.

[239] **ATLAS** Collaboration, "Constraints on the Higgs boson self-coupling from the combination of single-Higgs and double-Higgs production analyses performed with the ATLAS experiment," Tech. Rep. ATLAS-CONF-2019-049, 2019.

[240] G. Perez, Y. Soreq, E. Stamou, and K. Tobioka, "Prospects for measuring the Higgs boson coupling to light quarks," *Phys. Rev.* **D93** no. 1, (2016) 013001, arXiv:1505.06689 [hep-ph].

[241] G. T. Bodwin, F. Petriello, S. Stoynev, and M. Velasco, "Higgs boson decays to quarkonia and the $H\bar{c}c$ coupling," *Phys. Rev.* **D88** no. 5, (2013) 053003, arXiv:1306.5770 [hep-ph].

[242] A. L. Kagan, G. Perez, F. Petriello, Y. Soreq, S. Stoynev, and J. Zupan, "Exclusive Window onto Higgs Yukawa Couplings," *Phys. Rev. Lett.* **114** no. 10, (2015) 101802, arXiv:1406.1722 [hep-ph].

[243] M. König and M. Neubert, "Exclusive Radiative Higgs Decays as Probes of Light-Quark Yukawa Couplings," *JHEP* **08** (2015) 012, arXiv:1505.03870 [hep-ph].

[244] **CMS** Collaboration, A. M. Sirunyan *et al.*, "Search for rare decays of Z and Higgs bosons to J/ψ and a photon in proton-proton collisions at $\sqrt{s} = 13$ TeV," *Eur. Phys. J. C* **79** no. 2, (2019) 94, arXiv:1810.10056 [hep-ex].

[245] F. Yu, "Light Quark Yukawa Couplings and the $W^{\pm}h$ Charge Asymmetry," *Nucl. Part. Phys. Proc.* **285-286** (2017) 123–125.

[246] J. A. Aguilar-Saavedra, J. M. Cano, and J. M. No, "More light on Higgs flavor at the LHC: Higgs boson couplings to light quarks through $h + \gamma$ production," *Phys. Rev. D* **103** no. 9, (2021) 095023, arXiv:2008.12538 [hep-ph].

[247] A. Falkowski, S. Ganguly, P. Gras, J. M. No, K. Tobioka, N. Vignaroli, and T. You, "Light quark Yukawas in triboson final states," *JHEP* **04** (2021) 023, arXiv:2011.09551 [hep-ph].

[248] **ATLAS** Collaboration, A. Sciandra, "Measurement of Triboson Production and aQGCs with the ATLAS detector,".

[249] **CMS** Collaboration, "Observation of heavy triboson production in leptonic final states in proton-proton collisions at $\sqrt{s} = 13$ TeV,".

[250] T. Binoth, S. Karg, N. Kauer, and R. Ruckl, "Multi-Higgs boson production in the Standard Model and beyond," *Phys. Rev.* **D74** (2006) 113008, arXiv:hep-ph/0608057 [hep-ph].

[251] R. Contino, M. Ghezzi, M. Moretti, G. Panico, F. Piccinini, and A. Wulzer, "Anomalous Couplings in Double Higgs Production," *JHEP* **08** (2012) 154, arXiv:1205.5444 [hep-ph].

[252] S. Bar-Shalom and A. Soni, "Universally enhanced light-quarks Yukawa couplings paradigm," *Phys. Rev.* **D98** no. 5, (2018) 055001, arXiv:1804.02400 [hep-ph].

[253] M. Bauer, M. Carena, and A. Carmona, "Higgs Pair Production as a Signal of Enhanced Yukawa Couplings," *Phys. Rev. Lett.* **121** no. 2, (2018) 021801, arXiv:1801.00363 [hep-ph].

[254] D. Egana-Ugrinovic, S. Homiller, and P. Meade, "Multi-Higgs Production Probes Higgs Flavor," *Phys. Rev. D* **103** (2021) 115005, arXiv:2101.04119 [hep-ph].

[255] J. De Blas *et al.*, "Higgs Boson Studies at Future Particle Colliders," arXiv:1905.03764 [hep-ph].

[256] C. Delaunay, R. Ozeri, G. Perez, and Y. Soreq, "Probing Atomic Higgs-like Forces at the Precision Frontier," *Phys. Rev.* **D96** no. 9, (2017) 093001, arXiv:1601.05087 [hep-ph].

[257] **ATLAS Collaboration** Collaboration, M. Unal, "Searches for vector-like quarks with the ATLAS Detector,". http://cds.cern.ch/record/2777832.

[258] **CMS** Collaboration, A. M. Sirunyan *et al.*, "Search for pair production of vectorlike quarks in the fully hadronic final state," *Phys. Rev. D* **100** no. 7, (2019) 072001, arXiv:1906.11903 [hep-ex].

[259] **CMS** Collaboration, A. M. Sirunyan *et al.*, "Search for vector-like quarks in events with two oppositely charged leptons and jets in proton-proton collisions at $\sqrt{s} = 13$ TeV," *Eur. Phys. J. C* **79** no. 4, (2019) 364, arXiv:1812.09768 [hep-ex].

[260] S. Dawson, S. Homiller, and S. D. Lane, "Putting SMEFT Fits to Work," arXiv:2007.01296 [hep-ph].

[261] A. Falkowski and R. Rattazzi, "Which EFT," arXiv:1902.05936 [hep-ph].

[262] S. Chang and M. A. Luty, "The Higgs Trilinear Coupling and the Scale of New Physics," *JHEP* **03** (2020) 140, arXiv:1902.05556 [hep-ph].

[263] D. Egana-Ugrinovic, S. Homiller, and P. R. Meade, "Higgs bosons with large couplings to light quarks," arXiv:1908.11376 [hep-ph].

[264] **ATLAS** Collaboration, M. Aaboud *et al.*, "Search for low-mass resonances decaying into two jets and produced in association with a photon using pp collisions at $\sqrt{s} = 13$ TeV with the ATLAS detector," *Phys. Lett. B* **795** (2019) 56–75, arXiv:1901.10917 [hep-ex].

[265] **ATLAS** Collaboration, G. Aad *et al.*, "Search for new resonances in mass distributions of jet pairs using 139 fb^{-1} of pp collisions at $\sqrt{s} = 13$ TeV with the ATLAS detector," *JHEP* **03** (2020) 145, arXiv:1910.08447 [hep-ex].

[266] **CMS** Collaboration, A. M. Sirunyan *et al.*, "Search for high mass dijet resonances with a new background prediction method in proton-proton collisions at $\sqrt{s} = 13$ TeV," *JHEP* **05** (2020) 033, arXiv:1911.03947 [hep-ex].

[267] **CMS** Collaboration, A. M. Sirunyan *et al.*, "Combination of searches for Higgs boson pair production in proton-proton collisions at $\sqrt{s} = 13$ TeV," *Phys. Rev. Lett.* **122** no. 12, (2019) 121803, arXiv:1811.09689 [hep-ex].

[268] **ATLAS** Collaboration, G. Aad *et al.*, "Combination of searches for Higgs boson pairs in pp collisions at $\sqrt{s}$ =13 TeV with the ATLAS detector," arXiv:1906.02025 [hep-ex].

[269] **ATLAS** Collaboration, "Search for heavy resonances decaying into a Z boson and a Higgs boson in final states with leptons and b-jets in 139 fb^{-1} of pp collisions at $\sqrt{s} = 13TeV$ with the ATLAS detector,".

[270] **ATLAS** Collaboration, G. Aad *et al.*, "Search for heavy resonances decaying into a pair of Z bosons in the $\ell^+\ell^-\ell'^+\ell'^-$ and $\ell^+\ell^-\nu\overline{\nu}$ final states using 139 fb^{-1} of proton-proton collisions at $\sqrt{s} = 13$ TeV with the ATLAS detector," arXiv:2009.14791 [hep-ex].

[271] **CMS** Collaboration, A. M. Sirunyan *et al.*, "Search for a new scalar resonance decaying to a pair of Z bosons in proton-proton collisions at $\sqrt{s} = 13$ TeV," *JHEP* **06** (2018) 127, arXiv:1804.01939 [hep-ex]. [Erratum: JHEP 03, 128 (2019)].

[272] **LHCb** Collaboration, R. Aaij *et al.*, "Test of lepton universality using $B^+ \to K^+\ell^+\ell^-$ decays," *Phys. Rev. Lett.* **113** (2014) 151601, arXiv:1406.6482 [hep-ex].

[273] **LHCb** Collaboration, R. Aaij *et al.*, "Test of lepton universality with $B^0 \to K^{*0}\ell^+\ell^-$ decays," *JHEP* **08** (2017) 055, arXiv:1705.05802 [hep-ex].

[274] **LHCb** Collaboration, R. Aaij *et al.*, "Search for lepton-universality violation in $B^+ \to K^+\ell^+\ell^-$ decays," *Phys. Rev. Lett.* **122** no. 19, (2019) 191801, arXiv:1903.09252 [hep-ex].

[275] **Belle** Collaboration, A. Abdesselam *et al.*, "Test of lepton flavor universality in $B \to K^*\ell^+\ell^-$ decays at Belle," arXiv:1904.02440 [hep-ex].

[276] **LHCb** Collaboration, R. Aaij *et al.*, "Test of lepton universality in beauty-quark decays," arXiv:2103.11769 [hep-ex].

[277] S. Descotes-Genon, J. Matias, and J. Virto, "Understanding the $B \to K^*\mu^+\mu^-$ Anomaly," *Phys. Rev.* **D88** (2013) 074002, arXiv:1307.5683 [hep-ph].

[278] S. Descotes-Genon, L. Hofer, J. Matias, and J. Virto, "Global analysis of $b \to s\ell\ell$ anomalies," *JHEP* **06** (2016) 092, arXiv:1510.04239 [hep-ph].

[279] **LHCb** Collaboration, R. Aaij *et al.*, "Measurement of CP-Averaged Observables in the $B^0 \to K^{*0}\mu^+\mu^-$ Decay," *Phys. Rev. Lett.* **125** no. 1, (2020) 011802, arXiv:2003.04831 [hep-ex].

[280] **CMS** Collaboration, S. Chatrchyan *et al.*, "Measurement of the $B_s^0 \to \mu^+\mu^-$ Branching Fraction and Search for $B^0 \to \mu^+\mu^-$ with the CMS Experiment," *Phys. Rev. Lett.* **111** (2013) 101804, arXiv:1307.5025 [hep-ex].

[281] **LHCb** Collaboration, R. Aaij *et al.*, "Measurement of the $B_s^0 \to \mu^+\mu^-$ branching fraction and effective lifetime and search for $B^0 \to \mu^+\mu^-$ decays," *Phys. Rev. Lett.* **118** no. 19, (2017) 191801, arXiv:1703.05747 [hep-ex].

[282] **ATLAS** Collaboration, M. Aaboud *et al.*, "Study of the rare decays of B_s^0 and B^0 mesons into muon pairs using data collected during 2015 and 2016 with the ATLAS detector," *JHEP* **04** (2019) 098, arXiv:1812.03017 [hep-ex].

[283] **LHCb** Collaboration, R. Aaij *et al.*, "Search for the rare decays $B_s^0 \to e^+e^-$ and $B^0 \to e^+e^-$," *Phys. Rev. Lett.* **124** no. 21, (2020) 211802, arXiv:2003.03999 [hep-ex].

[284] G. Hiller and M. Schmaltz, "R_K and future $b \to s\ell\ell$ physics beyond the standard model opportunities," *Phys. Rev.* **D90** (2014) 054014, arXiv:1408.1627 [hep-ph].

[285] G. Hiller and M. Schmaltz, "Diagnosing lepton-nonuniversality in $b \to s\ell\ell$," *JHEP* **02** (2015) 055, arXiv:1411.4773 [hep-ph].

[286] M. Bordone, G. Isidori, and A. Pattori, "On the Standard Model predictions for R_K and R_{K^*}," *Eur. Phys. J. C* **76** no. 8, (2016) 440, arXiv:1605.07633 [hep-ph].

[287] **Muon g-2** Collaboration, B. Abi *et al.*, "Measurement of the Positive Muon Anomalous Magnetic Moment to 0.46 ppm," *Phys. Rev. Lett.* **126** no. 14, (2021) 141801, arXiv:2104.03281 [hep-ex].

[288] A. Khodjamirian, T. Mannel, A. A. Pivovarov, and Y. M. Wang, "Charm-loop effect in $B \to K^{(*)}\ell^+\ell^-$ and $B \to K^*\gamma$," *JHEP* **09** (2010) 089, arXiv:1006.4945 [hep-ph].

[289] J. Lyon and R. Zwicky, "Resonances gone topsy turvy - the charm of QCD or new physics in $b \to s\ell^+\ell^-$?," arXiv:1406.0566 [hep-ph].

[290] V. Chobanova, T. Hurth, F. Mahmoudi, D. Martinez Santos, and S. Neshatpour, "Large hadronic power corrections or new physics in the rare decay $B \to K^*\mu^+\mu^-$," *JHEP* **07** (2017) 025, arXiv:1702.02234 [hep-ph].

[291] T. Blake, U. Egede, P. Owen, K. A. Petridis, and G. Pomery, "An empirical model to determine the hadronic resonance contributions to $\overline{B}^0 \to \overline{K}^{*0}\mu^+\mu^-$ transitions," *Eur. Phys. J. C* **78** no. 6, (2018) 453, arXiv:1709.03921 [hep-ph].

[292] C. Bobeth, M. Chrzaszcz, D. van Dyk, and J. Virto, "Long-distance effects in $B \to K^*\ell\ell$ from analyticity," *Eur. Phys. J. C* **78** no. 6, (2018) 451, arXiv:1707.07305 [hep-ph].

[293] S. Jäger and J. Martin Camalich, "Reassessing the discovery potential of the $B \to K^*\ell^+\ell^-$ decays in the large-recoil region: SM challenges and BSM opportunities," *Phys. Rev. D* **93** no. 1, (2016) 014028, arXiv:1412.3183 [hep-ph].

[294] M. Ciuchini, M. Fedele, E. Franco, S. Mishima, A. Paul, L. Silvestrini, and M. Valli, "$B \to K^*\ell^+\ell^-$ decays at large recoil in the Standard Model: a theoretical reappraisal," *JHEP* **06** (2016) 116, arXiv:1512.07157 [hep-ph].

[295] A. Arbey, T. Hurth, F. Mahmoudi, and S. Neshatpour, "Hadronic and New Physics Contributions to $b \to s$ Transitions," *Phys. Rev. D* **98** no. 9, (2018) 095027, arXiv:1806.02791 [hep-ph].

[296] M. Chrzaszcz, A. Mauri, N. Serra, R. Silva Coutinho, and D. van Dyk, "Prospects for disentangling long- and short-distance effects in the decays $B \to K^*\mu^+\mu^-$," *JHEP* **10** (2019) 236, arXiv:1805.06378 [hep-ph].

[297] M. Ciuchini, A. M. Coutinho, M. Fedele, E. Franco, A. Paul, L. Silvestrini, and M. Valli, "Hadronic uncertainties in semileptonic $B \to K^*\mu^+\mu^-$ decays," *PoS* **BEAUTY2018** (2018) 044, arXiv:1809.03789 [hep-ph].

[298] T. Hurth, F. Mahmoudi, and S. Neshatpour, "On the new LHCb angular analysis of $B \to K^*\mu^+\mu^-$: Hadronic effects or New Physics?," arXiv:2006.04213 [hep-ph].

[299] A. Azatov, D. Bardhan, D. Ghosh, F. Sgarlata, and E. Venturini, "Anatomy of $b \to c\tau\nu$ anomalies," *JHEP* **11** (2018) 187, arXiv:1805.03209 [hep-ph].

[300] A. K. Alok, D. Kumar, S. Kumbhakar, and S. Uma Sankar, "Solutions to R_D-R_{D^*} in light of Belle 2019 data," *Nucl. Phys. B* **953** (2020) 114957, arXiv:1903.10486 [hep-ph].

[301] C. Murgui, A. Peñuelas, M. Jung, and A. Pich, "Global fit to $b \to c\tau\nu$ transitions," *JHEP* **09** (2019) 103, arXiv:1904.09311 [hep-ph].

[302] R.-X. Shi, L.-S. Geng, B. Grinstein, S. Jäger, and J. Martin Camalich, "Revisiting the new-physics interpretation of the $b \to c\tau\nu$ data," *JHEP* **12** (2019) 065, arXiv:1905.08498 [hep-ph].

[303] **BaBar** Collaboration, J. Lees *et al.*, "Measurement of an Excess of $\overline{B} \to D^{(*)}\tau^-\overline{\nu}_\tau$ Decays and Implications for Charged Higgs Bosons," *Phys. Rev. D* **88** no. 7, (2013) 072012, arXiv:1303.0571 [hep-ex].

[304] **Belle** Collaboration, M. Huschle *et al.*, "Measurement of the branching ratio of $\overline{B} \to D^{(*)}\tau^-\overline{\nu}_\tau$ relative to $\overline{B} \to D^{(*)}\ell^-\overline{\nu}_\ell$ decays with hadronic tagging at Belle," *Phys. Rev. D* **92** no. 7, (2015) 072014, arXiv:1507.03233 [hep-ex].

[305] **LHCb** Collaboration, R. Aaij *et al.*, "Measurement of the ratio of the $B^0 \to D^{*-}\tau^+\nu_\tau$ and $B^0 \to D^{*-}\mu^+\nu_\mu$ branching fractions using three-prong τ-lepton decays," *Phys. Rev. Lett.* **120** no. 17, (2018) 171802, arXiv:1708.08856 [hep-ex].

[306] P. Koppenburg, "Penguin B decays. Seminario de physica, USACH,". http://cds.cern.ch/record/2767155.

[307] L. Di Luzio, A. Greljo, and M. Nardecchia, "Gauge leptoquark as the origin of B-physics anomalies," *Phys. Rev. D* **96** no. 11, (2017) 115011, arXiv:1708.08450 [hep-ph].

[308] L. Calibbi, A. Crivellin, and T. Li, "Model of vector leptoquarks in view of the B-physics anomalies," *Phys. Rev. D* **98** no. 11, (2018) 115002, arXiv:1709.00692 [hep-ph].

[309] M. Bordone, C. Cornella, J. Fuentes-Martin, and G. Isidori, "A three-site gauge model for flavor hierarchies and flavor anomalies," *Phys. Lett. B* **779** (2018) 317–323, arXiv:1712.01368 [hep-ph].

[310] R. Barbieri and A. Tesi, "B-decay anomalies in Pati-Salam SU(4)," *Eur. Phys. J. C* **78** no. 3, (2018) 193, arXiv:1712.06844 [hep-ph].

[311] N. Assad, B. Fornal, and B. Grinstein, "Baryon Number and Lepton Universality Violation in Leptoquark and Diquark Models," *Phys. Lett. B* **777** (2018) 324–331, arXiv:1708.06350 [hep-ph].

[312] J. Heeck and D. Teresi, "Pati-Salam explanations of the B-meson anomalies," *JHEP* **12** (2018) 103, arXiv:1808.07492 [hep-ph].

[313] B. Fornal, S. A. Gadam, and B. Grinstein, "Left-Right SU(4) Vector Leptoquark Model for Flavor Anomalies," *Phys. Rev. D* **99** no. 5, (2019) 055025, arXiv:1812.01603 [hep-ph].

[314] A. Crivellin, C. Greub, D. Müller, and F. Saturnino, "Importance of Loop Effects in Explaining the Accumulated Evidence for New Physics in B Decays with a Vector Leptoquark," *Phys. Rev. Lett.* **122** no. 1, (2019) 011805, arXiv:1807.02068 [hep-ph].

[315] A. Crivellin, D. Müller, and F. Saturnino, "Flavor Phenomenology of the Leptoquark Singlet-Triplet Model," *JHEP* **06** (2020) 020, arXiv:1912.04224 [hep-ph].

[316] M. Bordone, O. Catà, and T. Feldmann, "Effective Theory Approach to New Physics with Flavour: General Framework and a Leptoquark Example," *JHEP* **01** (2020) 067, arXiv:1910.02641 [hep-ph].

[317] **UTfit** Collaboration, M. Bona *et al.*, "Model-independent constraints on $\Delta F = 2$ operators and the scale of new physics," *JHEP* **03** (2008) 049, arXiv:0707.0636 [hep-ph].

[318] A. Greljo and D. Marzocca, "High-p_T dilepton tails and flavor physics," *Eur. Phys. J.* **C77** no. 8, (2017) 548, arXiv:1704.09015 [hep-ph].

[319] M. J. Baker, J. Fuentes-Martín, G. Isidori, and M. König, "High- p_T signatures in vector–leptoquark models," *Eur. Phys. J.* **C79** no. 4, (2019) 334, arXiv:1901.10480 [hep-ph].

[320] **Belle** Collaboration, S. Hirose *et al.*, "Measurement of the τ lepton polarization and $R(D^*)$ in the decay $\overline{B} \to D^* \tau^- \overline{\nu}_\tau$," *Phys. Rev. Lett.* **118** no. 21, (2017) 211801, arXiv:1612.00529 [hep-ex].

[321] **Belle** Collaboration, A. Abdesselam *et al.*, "Measurement of $\mathcal{R}(D)$ and $\mathcal{R}(D^*)$ with a semileptonic tagging method," arXiv:1904.08794 [hep-ex].

[322] D. Bigi and P. Gambino, "Revisiting $B \to D\ell\nu$," *Phys. Rev. D* **94** no. 9, (2016) 094008, arXiv:1606.08030 [hep-ph].

[323] F. U. Bernlochner, Z. Ligeti, M. Papucci, and D. J. Robinson, "Combined analysis of semileptonic B decays to D and D^*: $R(D^{(*)})$, $|V_{cb}|$, and new physics," *Phys. Rev. D* **95** no. 11, (2017) 115008, arXiv:1703.05330 [hep-ph]. [Erratum: Phys.Rev.D 97, 059902 (2018)].

[324] D. Bigi, P. Gambino, and S. Schacht, "$R(D^*)$, $|V_{cb}|$, and the Heavy Quark Symmetry relations between form factors," *JHEP* **11** (2017) 061, arXiv:1707.09509 [hep-ph].

[325] S. Jaiswal, S. Nandi, and S. K. Patra, "Extraction of $|V_{cb}|$ from $B \to D^{(*)}\ell\nu_\ell$ and the Standard Model predictions of $R(D^{(*)})$," *JHEP* **12** (2017) 060, arXiv:1707.09977 [hep-ph].

[326] B. Capdevila, S. Descotes-Genon, J. Matias, and J. Virto, "Assessing lepton-flavour non-universality from $B \to K^* \ell\ell$ angular analyses," *JHEP* **10** (2016) 075, arXiv:1605.03156 [hep-ph].

[327] N. Serra, R. Silva Coutinho, and D. van Dyk, "Measuring the breaking of lepton flavor universality in $B \to K^* \ell^+ \ell^-$," *Phys. Rev. D* **95** no. 3, (2017) 035029, arXiv:1610.08761 [hep-ph].

[328] **Belle** Collaboration, S. Wehle *et al.*, "Lepton-Flavor-Dependent Angular Analysis of $B \to K^* \ell^+ \ell^-$," *Phys. Rev. Lett.* **118** no. 11, (2017) 111801, arXiv:1612.05014 [hep-ex].

[329] M. Algueró, B. Capdevila, S. Descotes-Genon, P. Masjuan, and J. Matias, "What R_K and Q_5 can tell us about New Physics in $b \to s\ell\ell$ transitions?," *JHEP* **07** (2019) 096, arXiv:1902.04900 [hep-ph].

[330] **Belle-II** Collaboration, W. Altmannshofer *et al.*, "The Belle II Physics Book," *PTEP* **2019** no. 12, (2019) 123C01, arXiv:1808.10567 [hep-ex]. [Erratum: PTEP 2020, 029201 (2020)].

[331] G. D'Amico, M. Nardecchia, P. Panci, F. Sannino, A. Strumia, R. Torre, and A. Urbano, "Flavour anomalies after the R_{K^*} measurement," *JHEP* **09** (2017) 010, arXiv:1704.05438 [hep-ph].

[332] L.-S. Geng, B. Grinstein, S. Jäger, J. Martin Camalich, X.-L. Ren, and R.-X. Shi, "Towards the discovery of new physics with lepton-universality ratios of $b \to s\ell\ell$ decays," *Phys. Rev. D* **96** no. 9, (2017) 093006, arXiv:1704.05446 [hep-ph].

[333] B. Capdevila, A. Crivellin, S. Descotes-Genon, J. Matias, and J. Virto, "Patterns of New Physics in $b \to s\ell^+\ell^-$ transitions in the light of recent data," *JHEP* **01** (2018) 093, arXiv:1704.05340 [hep-ph].

[334] M. Ciuchini, A. M. Coutinho, M. Fedele, E. Franco, A. Paul, L. Silvestrini, and M. Valli, "On Flavourful Easter eggs for New Physics hunger and Lepton Flavour Universality violation," *Eur. Phys. J.* **C77** no. 10, (2017) 688, arXiv:1704.05447 [hep-ph].

[335] G. Hiller and I. Nisandzic, "R_K and R_{K^*} beyond the standard model," *Phys. Rev. D* **96** no. 3, (2017) 035003, arXiv:1704.05444 [hep-ph].

[336] M. Ciuchini, A. M. Coutinho, M. Fedele, E. Franco, A. Paul, L. Silvestrini, and M. Valli, "New Physics in $b \to s\ell^+\ell^-$ confronts new data on Lepton Universality," *Eur. Phys. J.* **C79** no. 8, (2019) 719, arXiv:1903.09632 [hep-ph].

[337] J. Aebischer, W. Altmannshofer, D. Guadagnoli, M. Reboud, P. Stangl, and D. M. Straub, "B-decay discrepancies after Moriond 2019," *Eur. Phys. J.* **C80** no. 3, (2020) 252, arXiv:1903.10434 [hep-ph].

[338] A. K. Alok, A. Dighe, S. Gangal, and D. Kumar, "Continuing search for new physics in $b \to s\mu\mu$ decays: two operators at a time," *JHEP* **06** (2019) 089, arXiv:1903.09617 [hep-ph].

[339] M. Algueró, B. Capdevila, A. Crivellin, S. Descotes-Genon, P. Masjuan, J. Matias, M. Novoa, and J. Virto, "Emerging patterns of New Physics with and without Lepton Flavour Universal contributions," *Eur. Phys. J. C* **79** no. 8, (2019) 714, arXiv:1903.09578 [hep-ph].

[340] K. Kowalska, D. Kumar, and E. M. Sessolo, "Implications for new physics in $b \to s\mu\mu$ transitions after recent measurements by Belle and LHCb," *Eur. Phys. J. C* **79** no. 10, (2019) 840, arXiv:1903.10932 [hep-ph].

[341] A. Arbey, T. Hurth, F. Mahmoudi, D. M. Santos, and S. Neshatpour, "Update on the b→s anomalies," *Phys. Rev. D* **100** no. 1, (2019) 015045, arXiv:1904.08399 [hep-ph].

[342] A. Datta, J. Kumar, and D. London, "The B anomalies and new physics in $b \to se^+e^-$," *Phys. Lett. B* **797** (2019) 134858, arXiv:1903.10086 [hep-ph].

[343] L. Calibbi, A. Crivellin, and T. Ota, "Effective Field Theory Approach to $b \to s\ell\ell^{(')}$, $B \to K^{(*)}\nu\overline{\nu}$ and $B \to D^{(*)}\tau\nu$ with Third Generation Couplings," *Phys. Rev. Lett.* **115** (2015) 181801, arXiv:1506.02661 [hep-ph].

[344] I. Doršner, S. Fajfer, A. Greljo, J. Kamenik, and N. Košnik, "Physics of leptoquarks in precision experiments and at particle colliders," *Phys. Rept.* **641** (2016) 1–68, arXiv:1603.04993 [hep-ph].

[345] D. Buttazzo, A. Greljo, G. Isidori, and D. Marzocca, "B-physics anomalies: a guide to combined explanations," *JHEP* **11** (2017) 044, arXiv:1706.07808 [hep-ph].

[346] J. Kumar, D. London, and R. Watanabe, "Combined Explanations of the $b \to s\mu^+\mu^-$ and $b \to c\tau^-\overline{\nu}$ Anomalies: a General Model Analysis," *Phys. Rev.* **D99** no. 1, (2019) 015007, arXiv:1806.07403 [hep-ph].

[347] C. Cornella, J. Fuentes-Martin, and G. Isidori, "Revisiting the vector leptoquark explanation of the B-physics anomalies," *JHEP* **07** (2019) 168, arXiv:1903.11517 [hep-ph].

[348] J. F. Kamenik, Y. Soreq, and J. Zupan, "Lepton flavor universality violation without new sources of quark flavor violation," *Phys. Rev.* **D97** no. 3, (2018) 035002, arXiv:1704.06005 [hep-ph].

[349] P. J. Fox, I. Low, and Y. Zhang, "Top-philic Z' forces at the LHC," *JHEP* **03** (2018) 074, arXiv:1801.03505 [hep-ph].

[350] A. Buras, P. Gambino, M. Gorbahn, S. Jager, and L. Silvestrini, "Universal unitarity triangle and physics beyond the standard model," *Phys. Lett. B* **500** (2001) 161–167, arXiv:hep-ph/0007085.

[351] A. L. Kagan, G. Perez, T. Volansky, and J. Zupan, "General Minimal Flavor Violation," *Phys. Rev. D* **80** (2009) 076002, arXiv:0903.1794 [hep-ph].

[352] A. Celis, J. Fuentes-Martin, A. Vicente, and J. Virto, "Gauge-invariant implications of the LHCb measurements on lepton-flavor nonuniversality," *Phys. Rev. D* **96** no. 3, (2017) 035026, arXiv:1704.05672 [hep-ph].

[353] J. E. Camargo-Molina, A. Celis, and D. A. Faroughy, "Anomalies in Bottom from new physics in Top," *Phys. Lett.* **B784** (2018) 284–293, arXiv:1805.04917 [hep-ph].

[354] A. Efrati, A. Falkowski, and Y. Soreq, "Electroweak constraints on flavorful effective theories," *JHEP* **07** (2015) 018, arXiv:1503.07872 [hep-ph].

[355] B. Bhattacharya, A. Datta, D. London, and S. Shivashankara, "Simultaneous Explanation of the R_K and $R(D^{(*)})$ Puzzles," *Phys. Lett. B* **742** (2015) 370–374, arXiv:1412.7164 [hep-ph].

[356] F. Feruglio, P. Paradisi, and A. Pattori, "Revisiting Lepton Flavor Universality in B Decays," *Phys. Rev. Lett.* **118** no. 1, (2017) 011801, arXiv:1606.00524 [hep-ph].

[357] R. Coy, M. Frigerio, F. Mescia, and O. Sumensari, "New physics in $b \to s\ell\ell$ transitions at one loop," *Eur. Phys. J. C* **80** no. 1, (2020) 52, arXiv:1909.08567 [hep-ph].

[358] M. Ciuchini, M. Fedele, E. Franco, S. Mishima, A. Paul, L. Silvestrini, and M. Valli, "$B \to K^*\ell^+\ell^-$ in the Standard Model: Elaborations and Interpretations," *PoS* **ICHEP2016** (2016) 584, arXiv:1611.04338 [hep-ph].

[359] M. Ciuchini, M. Fedele, E. Franco, S. Mishima, A. Paul, L. Silvestrini, and M. Valli, "Knowns and Unknowns in the Predictions for $B \to K^*\mu^+\mu^-$," *Nucl. Part. Phys. Proc.* **285-286** (2017) 45–49.

[360] M. Ciuchini, A. M. Coutinho, M. Fedele, E. Franco, A. Paul, L. Silvestrini, and M. Valli, "On hadronic uncertainties polluting the New Physics hunt in $b \to s$ transitions," *Nucl. Part. Phys. Proc.* **303-305** (2018) 8–13.

[361] J. Aebischer, A. Crivellin, M. Fael, and C. Greub, "Matching of gauge invariant dimension-six operators for $b \to s$ and $b \to c$ transitions," *JHEP* **05** (2016) 037, arXiv:1512.02830 [hep-ph].

[362] C. Bobeth, A. J. Buras, A. Celis, and M. Jung, "Yukawa enhancement of Z-mediated new physics in $\Delta S = 2$ and $\Delta B = 2$ processes," *JHEP* **07** (2017) 124, arXiv:1703.04753 [hep-ph].

[363] G. Buchalla, A. J. Buras, and M. E. Lautenbacher, "Weak decays beyond leading logarithms," *Rev. Mod. Phys.* **68** (1996) 1125–1144, arXiv:hep-ph/9512380.

[364] A. J. Buras, "Weak Hamiltonian, CP violation and rare decays," in *Les Houches Summer School in Theoretical Physics, Session 68: Probing the Standard Model of Particle Interactions*, pp. 281–539. 6, 1998. arXiv:hep-ph/9806471.

[365] L. Silvestrini, "Effective Theories for Quark Flavour Physics," in *Les Houches summer school: EFT in Particle Physics and Cosmology*. 5, 2019. arXiv:1905.00798 [hep-ph].

[366] J. de Blas, M. Ciuchini, E. Franco, S. Mishima, M. Pierini, L. Reina, and L. Silvestrini, "Electroweak precision observables and Higgs-boson signal strengths in the Standard Model and beyond: present and future," *JHEP* **12** (2016) 135, arXiv:1608.01509 [hep-ph].

[367] M. Ciuchini, E. Franco, S. Mishima, and L. Silvestrini, "Electroweak Precision Observables, New Physics and the Nature of a 126 GeV Higgs Boson," *JHEP* **08** (2013) 106, arXiv:1306.4644 [hep-ph].

[368] J. de Blas, G. Durieux, C. Grojean, J. Gu, and A. Paul, "On the future of Higgs, electroweak and diboson measurements at lepton colliders," *JHEP* **12** (2019) 117, arXiv:1907.04311 [hep-ph].

[369] A. Caldwell, D. Kollár, and K. Kröninger, "BAT - The Bayesian analysis toolkit," *Computer Physics Communications* **180** no. 11, (Nov., 2009) 2197–2209, arXiv:0808.2552 [physics.data-an].

[370] **ALEPH, DELPHI, L3, OPAL, SLD, LEP Electroweak Working Group, SLD Electroweak Group, SLD Heavy Flavour Group** Collaboration, S. Schael *et al.*, "Precision electroweak measurements on the Z resonance," *Phys. Rept.* **427** (2006) 257–454, arXiv:hep-ex/0509008 [hep-ex].

[371] **SLD** Collaboration, K. Abe *et al.*, "First direct measurement of the parity violating coupling of the Z0 to the s quark," *Phys. Rev. Lett.* **85** (2000) 5059–5063, arXiv:hep-ex/0006019 [hep-ex].

[372] **CDF, D0** Collaboration, T. E. W. Group, "2012 Update of the Combination of CDF and D0 Results for the Mass of the W Boson," arXiv:1204.0042 [hep-ex].

[373] **ALEPH, DELPHI, L3, OPAL, LEP Electroweak** Collaboration, S. Schael *et al.*, "Electroweak Measurements in Electron-Positron Collisions at W-Boson-Pair Energies at LEP," *Phys. Rept.* **532** (2013) 119–244, arXiv:1302.3415 [hep-ex].

[374] **ATLAS** Collaboration, M. Aaboud *et al.*, "Measurement of the W-boson mass in pp collisions at $\sqrt{s} = 7$ TeV with the ATLAS detector," *Eur. Phys. J. C* **78** no. 2, (2018) 110, arXiv:1701.07240 [hep-ex]. [Erratum: Eur.Phys.J.C 78, 898 (2018)].

[375] **CMS** Collaboration, V. Khachatryan *et al.*, "Measurement of the t-channel single-top-quark production cross section and of the $| V_{tb} |$ CKM matrix element in pp collisions at $\sqrt{s}$= 8 TeV," *JHEP* **06** (2014) 090, arXiv:1403.7366 [hep-ex].

[376] **D0** Collaboration, V. Abazov *et al.*, "Measurement of $\sin^2\theta^{\ell}_{\text{eff}}$ and Z-light quark couplings using the forward-backward charge asymmetry in $p\overline{p} \to Z/\gamma^* \to e^+e^-$

events with $\mathcal{L} = 5.0$ fb^{-1} at $\sqrt{s} = 1.96$ TeV," *Phys. Rev. D* **84** (2011) 012007, arXiv:1104.4590 [hep-ex].

[377] **ATLAS** Collaboration, M. Aaboud *et al.*, "Angular analysis of $B_d^0 \to K^* \mu^+ \mu^-$ decays in pp collisions at $\sqrt{s} = 8$ TeV with the ATLAS detector," *JHEP* **10** (2018) 047, arXiv:1805.04000 [hep-ex].

[378] **CMS** Collaboration, V. Khachatryan *et al.*, "Angular analysis of the decay $B^0 \to K^{*0} \mu^+ \mu^-$ from pp collisions at $\sqrt{s} = 8$ TeV," *Phys. Lett.* **B753** (2016) 424–448, arXiv:1507.08126 [hep-ex].

[379] **CMS** Collaboration, A. M. Sirunyan *et al.*, "Measurement of angular parameters from the decay $\mathrm{B}^0 \to \mathrm{K}^{*0} \mu^+ \mu^-$ in proton-proton collisions at $\sqrt{s} = 8$ TeV," *Phys. Lett.* **B781** (2018) 517–541, arXiv:1710.02846 [hep-ex].

[380] **LHCb** Collaboration, R. Aaij *et al.*, "Angular analysis of the $B^0 \to K^{*0} e^+ e^-$ decay in the low-q^2 region," *JHEP* **04** (2015) 064, arXiv:1501.03038 [hep-ex].

[381] **LHCb** Collaboration, R. Aaij *et al.*, "Measurement of *CP*-averaged observables in the $B^0 \to K^{*0} \mu^+ \mu^-$ decay," arXiv:2003.04831 [hep-ex].

[382] **LHCb** Collaboration, R. Aaij *et al.*, "Measurements of the S-wave fraction in $B^0 \to K^+ \pi^- \mu^+ \mu^-$ decays and the $B^0 \to K^*(892)^0 \mu^+ \mu^-$ differential branching fraction," *JHEP* **11** (2016) 047, arXiv:1606.04731 [hep-ex]. [Erratum: JHEP04,142(2017)].

[383] A. Paul and D. M. Straub, "Constraints on new physics from radiative B decays," *JHEP* **04** (2017) 027, arXiv:1608.02556 [hep-ph].

[384] **HFLAV** Collaboration, Y. S. Amhis *et al.*, "Averages of b-hadron, c-hadron, and τ-lepton properties as of 2018," arXiv:1909.12524 [hep-ex].

[385] **LHCb** Collaboration, R. Aaij *et al.*, "Differential branching fractions and isospin asymmetries of $B \to K^{(*)} \mu^+ \mu^-$ decays," *JHEP* **06** (2014) 133, arXiv:1403.8044 [hep-ex].

[386] **LHCb** Collaboration, R. Aaij *et al.*, "Angular analysis and differential branching fraction of the decay $B_s^0 \to \phi \mu^+ \mu^-$," *JHEP* **09** (2015) 179, arXiv:1506.08777 [hep-ex].

[387] **LHCb** Collaboration, R. Aaij *et al.*, "Measurement of the ratio of branching fractions $BR(B_0 \to K^{\star 0} \gamma)/BR(B_{s0} \to \phi\gamma)$ and the direct CP asymmetry in $B_0 \to K^{\star 0} \gamma$," *Nucl. Phys.* **B867** (2013) 1–18, arXiv:1209.0313 [hep-ex].

[388] T. Hurth, F. Mahmoudi, and S. Neshatpour, "Global fits to $b \to s\ell\ell$ data and signs for lepton non-universality," *JHEP* **12** (2014) 053, arXiv:1410.4545 [hep-ph].

[389] **CCFR** Collaboration, S. Mishra *et al.*, "Neutrino tridents and W Z interference," *Phys. Rev. Lett.* **66** (1991) 3117–3120.

[390] **ATLAS** Collaboration, M. Aaboud *et al.*, "Search for new high-mass phenomena in the dilepton final state using 36 fb^{-1} of proton-proton collision data at $\sqrt{s} = 13$ TeV with the ATLAS detector," *JHEP* **10** (2017) 182, arXiv:1707.02424 [hep-ex].

[391] **CMS** Collaboration, A. M. Sirunyan *et al.*, "Search for standard model production of four top quarks with same-sign and multilepton final states in proton–proton collisions at $\sqrt{s} = 13\,\text{TeV}$," *Eur. Phys. J. C* **78** no. 2, (2018) 140, arXiv:1710.10614 [hep-ex].

[392] **ATLAS** Collaboration, M. Aaboud *et al.*, "Search for pair production of heavy vector-like quarks decaying into high-p_T gy bosons and top quarks in the lepton-plus-jets final state in pp collisions at $\sqrt{s} = 13$ TeV with the ATLAS detector," *JHEP* **08** (2018) 048, arXiv:1806.01762 [hep-ex].

[393] **CMS** Collaboration, A. M. Sirunyan *et al.*, "Search for vector-like leptons in multilepton final states in proton-proton collisions at $\sqrt{s} = 13$ TeV," *Phys. Rev. D* **100** no. 5, (2019) 052003, arXiv:1905.10853 [hep-ex].

[394] S. D. Thomas and J. D. Wells, "Phenomenology of Massive Vectorlike Doublet Leptons," *Phys. Rev. Lett.* **81** (1998) 34–37, arXiv:hep-ph/9804359.

[395] F. del Aguila, J. de Blas, and M. Perez-Victoria, "Effects of new leptons in Electroweak Precision Data," *Phys. Rev. D* **78** (2008) 013010, arXiv:0803.4008 [hep-ph].

[396] K. Kannike, M. Raidal, D. M. Straub, and A. Strumia, "Anthropic solution to the magnetic muon anomaly: the charged see-saw," *JHEP* **02** (2012) 106, arXiv:1111.2551 [hep-ph]. [Erratum: JHEP10,136(2012)].

[397] N. Kumar and S. P. Martin, "Vectorlike Leptons at the Large Hadron Collider," *Phys. Rev. D* **92** no. 11, (2015) 115018, arXiv:1510.03456 [hep-ph].

[398] P. N. Bhattiprolu and S. P. Martin, "Prospects for vectorlike leptons at future proton-proton colliders," *Phys. Rev. D* **100** no. 1, (2019) 015033, arXiv:1905.00498 [hep-ph].

[399] J. C. Pati and A. Salam, "Lepton Number as the Fourth Color," *Phys. Rev. D* **10** (1974) 275–289. [Erratum: Phys.Rev.D 11, 703–703 (1975)].

[400] H. Georgi and S. L. Glashow, "Unity of all elementary-particle forces," *Phys. Rev. Lett.* **32** (Feb, 1974) 438–441. https://link.aps.org/doi/10.1103/PhysRevLett.32.438.

[401] D. Bečirević and O. Sumensari, "A leptoquark model to accommodate $R_K^{\rm exp} < R_K^{\rm SM}$ and $R_{K^*}^{\rm exp} < R_{K^*}^{\rm SM}$," *JHEP* **08** (2017) 104, arXiv:1704.05835 [hep-ph].

[402] W. Buchmuller, R. Ruckl, and D. Wyler, "Leptoquarks in Lepton - Quark Collisions," *Phys. Lett. B* **191** (1987) 442–448. [Erratum: Phys.Lett.B 448, 320–320 (1999)].

[403] F. del Aguila, J. de Blas, and M. Perez-Victoria, "Electroweak Limits on General New Vector Bosons," *JHEP* **09** (2010) 033, arXiv:1005.3998 [hep-ph].

[404] R. Alonso, B. Grinstein, and J. Martin Camalich, "Lepton universality violation and lepton flavor conservation in B-meson decays," *JHEP* **10** (2015) 184, arXiv:1505.05164 [hep-ph].

[405] A. Angelescu, D. Beˇ cirević, D. Faroughy, and O. Sumensari, "Closing the window on single leptoquark solutions to the B-physics anomalies," *JHEP* **10** (2018) 183, arXiv:1808.08179 [hep-ph].

[406] **LHCb** Collaboration, R. Aaij *et al.*, "Physics case for an LHCb Upgrade II - Opportunities in flavour physics, and beyond, in the HL-LHC era," arXiv:1808.08865 [hep-ex].

[407] **FCC** Collaboration, A. Abada *et al.*, "FCC Physics Opportunities: Future Circular Collider Conceptual Design Report Volume 1," *Eur. Phys. J. C* **79** no. 6, (2019) 474.

[408] **FCC** Collaboration, A. Abada *et al.*, "FCC-ee: The Lepton Collider: Future Circular Collider Conceptual Design Report Volume 2," *Eur. Phys. J. ST* **228** no. 2, (2019) 261–623.

[409] **CEPC Study Group** Collaboration, M. Dong *et al.*, "CEPC Conceptual Design Report: Volume 2 - Physics & Detector," arXiv:1811.10545 [hep-ex].

[410] P. Bambade *et al.*, "The International Linear Collider: A Global Project," arXiv:1903.01629 [hep-ex].

[411] J. de Blas *et al.*, "The CLIC Potential for New Physics," arXiv:1812.02093 [hep-ph].

[412] **LCC Physics Working Group** Collaboration, K. Fujii *et al.*, "Tests of the Standard Model at the International Linear Collider," arXiv:1908.11299 [hep-ex].

[413] U. Aglietti, R. Bonciani, G. Degrassi, and A. Vicini, "Analytic Results for Virtual QCD Corrections to Higgs Production and Decay," *JHEP* **01** (2007) 021, arXiv:hep-ph/0611266.

[414] Z. Han and W. Skiba, "Effective theory analysis of precision electroweak data," *Phys. Rev. D* **71** (2005) 075009, arXiv:hep-ph/0412166.

[415] F. del Aguila and J. de Blas, "Electroweak constraints on new physics," *Fortsch. Phys.* **59** (2011) 1036–1040, arXiv:1105.6103 [hep-ph].

[416] J. de Blas, "Electroweak limits on physics beyond the Standard Model," *EPJ Web Conf.* **60** (2013) 19008, arXiv:1307.6173 [hep-ph].

[417] A. Falkowski and F. Riva, "Model-independent precision constraints on dimension-6 operators," *JHEP* **02** (2015) 039, arXiv:1411.0669 [hep-ph].

[418] L. Berthier and M. Trott, "Towards consistent Electroweak Precision Data constraints in the SMEFT," *JHEP* **05** (2015) 024, arXiv:1502.02570 [hep-ph].

[419] J. de Blas, M. Ciuchini, E. Franco, S. Mishima, M. Pierini, L. Reina, and L. Silvestrini, "Electroweak precision constraints at present and future colliders," *PoS* **ICHEP2016** (2017) 690, arXiv:1611.05354 [hep-ph].

[420] J. de Blas, M. Ciuchini, E. Franco, S. Mishima, M. Pierini, L. Reina, and L. Silvestrini, "The Global Electroweak and Higgs Fits in the LHC era," *PoS* **EPS-HEP2017** (2017) 467, arXiv:1710.05402 [hep-ph].

[421] J. Ellis, C. W. Murphy, V. Sanz, and T. You, "Updated Global SMEFT Fit to Higgs, Diboson and Electroweak Data," *JHEP* **06** (2018) 146, arXiv:1803.03252 [hep-ph].

[422] S. Dawson and P. P. Giardino, "Electroweak and QCD corrections to Z and W pole observables in the standard model EFT," *Phys. Rev. D* **101** no. 1, (2020) 013001, arXiv:1909.02000 [hep-ph].